# Solvothermal crystallization and performance degradation mechanism of high-voltage cobalt-phosphate cathodes for Li-ion batteries

Moohyun Woo

260804030

Department of Mining and Materials Engineering,
McGill University


**Submitted:** August 2024

A thesis submitted to McGill University in partial fulfillment of the requirements for the degree of Doctor in Engineering in the Department of Mining and Materials Engineering

# Table of Content

# Abstract

Enhancing energy density is a crucial yet challenging goal for advancing the development of next generation Li-ion batteries. Achieving high energy densities necessitates the development of novel synthesis techniques and defect engineering methods for creating high-voltage (high-V) cathode materials. Lithium cobalt phosphate ($LiCoPO_4$, LCP), a high-V polyanionic compound, has been identified as a promising next-generation cathode material due to its theoretical greater energy density compared to the commercial lithium iron phosphate ($LiFePO_4$, LFP). However, the development of LCP faces obstacles, such as lower capacities than the theoretical value due to defected crystal structure as well as severe capacity fade due to high-V induced electrolyte interfacial degradation reactions. This thesis focuses on LCP crystal-controlled material synthesis, characterization, electrochemical evaluation, post-mortem analysis, and surface modification seeking to understand and control occurrence of defects and interphasial phenomena limiting attainment of full discharge capacity, high rate and stable performance.

Single-crystal LCP material was first successfully synthesized using hydrothermal (HT) synthesis with water as an eco-friendly solvent. By controlling the supersaturation with an over-stoichiometric ratio of lithium ($Li:Co:PO_4 = 2.5:1:1$) and maintaining a pH of 9 at 220 ºC, high-quality crystals were obtained. Post-synthesis treatments, such as nanosizing through planetary-milling and carbon coating, aimed to improve the discharge capacity by reducing diffusion distances and enhancing electronic conductivity, but achieved only partial success. Detailed surface and bulk crystal characterizations, along with electrochemical analysis, revealed two previously non-identified issues: The formation of a resistive $Co(OH)_2$ surface passivation layer and the presence of abundant anti-site defects due to excess Co, both of which hinder Li-ion intercalation.

To overcome these issues, the water solvent was replaced with ethylene glycol (EG) as the synthesis medium and an Argon (Ar)-annealing treatment was applied. This novel solvothermal (ST) synthesis method yielded defect-free crystals with a shorter Li-ion diffusion pathway. Molecular simulations and surface energy calculations established that EG promotes the preferential anisotropic crystal growth of LCP. Adjusting the Li content and using Ar-annealing minimized anti-site defects, resulting in improved Li-ion diffusivity, approaching the nearly theoretical full capacity (163.0 mAh $g^{-1}$ at C/10), superior rate capability (151.6 mAh $g^{-1}$ at 1 C), and relatively stabilized capacity retention (61.7 % after 100 cycles at 1 C).

Post-mortem analysis of cycled electrodes in different cycling-aging conditions identified that high-V operation of LCP leads to the growth of an irreversible cathode-electrolyte interphase (CEI) layer associated with increased charge-transfer overpotential, and redox metal (RM) dissolution, all contributing to capacity fade. This understanding led to the development of a facile one-step sucrose-derived reduced graphene oxide (RGO) coating, aimed at enhancing charge exchange and mitigating progressive side reactions at the cathode-electrolyte interface. This approach helps to decelerate and ideally prevent the evolution of the CEI layer and RM dissolution, which are responsible for increased charge-transfer overpotential and loss of RM-related capacity. Utilizing this innovative coating strategy, the electrochemical performance was further improved, with the discharge capacity reaching up to 163.0 mAh $g^{-1}$ (equivalent to 771.2 Wh $kg^{-1}$ in energy density), along with the enhanced retention rate of 76.4 % after 100 cycles at 1 C.

# Résumé

L'amélioration de la densité énergétique est un objectif crucial mais difficile à atteindre pour faire progresser le développement de la prochaine génération de batteries Li-ion. L'obtention de densités d'énergie élevées nécessite le développement de nouvelles techniques de synthèse et de méthodes d'ingénierie des défauts pour créer des matériaux cathodiques à haute tension. Le phosphate de lithium et de cobalt ($LiCoPO_4$, LCP), un composé polyanionique à haute tension, a été identifié comme un matériau cathodique prometteur de la prochaine génération en raison de sa densité énergétique théoriquement supérieure à celle du phosphate de lithium et de fer commercial ($LiFePO_4$, LFP). Cependant, le développement du LCP se heurte à des obstacles, tels que des capacités inférieures à la valeur théorique en raison d'une structure cristalline défectueuse, ainsi qu'une forte diminution de la capacité due à des réactions de dégradation interfaciale de l'électrolyte induites par des tensions élevées. Cette thèse se concentre sur la synthèse, la caractérisation, l'évaluation électrochimique, l'analyse post-mortem et la modification de la surface des cristaux de LCP afin de comprendre et de contrôler l'apparition de défauts et de phénomènes interphasiques limitant l'obtention d'une pleine capacité de décharge, d'un taux élevé et d'une performance stable.

Le matériau LCP monocristallin a d'abord été synthétisé avec succès par voie hydrothermale (HT) avec de l'eau comme solvant respectueux de l'environnement. En contrôlant la sursaturation avec un rapport surstœchiométrique de lithium ($Li:Co:PO_4 = 2,5:1:1$) et en maintenant un pH de 9 à 220 ºC, des cristaux de haute qualité ont été obtenus. Les traitements post-synthèse, tels que la nanosynthèse par broyage planétaire et l'enrobage de carbone, visaient à améliorer la capacité de décharge en réduisant les distances de diffusion et en améliorant la conductivité électronique, mais ils n'ont eu qu'un succès partiel. Des caractérisations détaillées de la surface et du cristal en vrac, ainsi qu'une analyse électrochimique, ont révélé deux problèmes qui n'avaient pas été identifiés auparavant : La formation d'une couche de passivation de surface résistive en $Co(OH)_2$ et la présence d'abondants défauts antisites dus à l'excès de Co, qui entravent tous deux l'intercalation des Li-ion.

Pour résoudre ces problèmes, le solvant eau a été remplacé par de l'éthylène glycol (EG) comme milieu de synthèse et un traitement de recuit à l'argon (Ar) a été appliqué. Cette nouvelle méthode de synthèse solvothermique (ST) a permis d'obtenir des cristaux sans défaut avec une voie de diffusion de l'ion lithium plus courte. Les simulations moléculaires et les calculs d'énergie de surface ont établi que l'EG favorise la croissance cristalline anisotrope préférentielle du LCP. L'ajustement de la teneur en Li et l'utilisation d'un recuit à l'Ar minimisent les défauts antisites, ce qui

améliore la diffusivité des ions Li- et permet d'approcher la pleine capacité presque théorique (163.0 mAh $g^{-1}$ à C/10), une capacité de débit supérieure (151.6 mAh $g^{-1}$ à 1 C) et une rétention de capacité relativement stabilisée (61.7 % après 100 cycles à 1 C).

L'analyse post-mortem d'électrodes cyclées dans différentes conditions de vieillissement a permis d'identifier que le fonctionnement à haute tension des LCP conduit à la croissance d'une couche d'interphase cathode-électrolyte (CEI) irréversible associée à une surpotentialité de transfert de charge accrue et à une dissolution de métal redox (RM), contribuant toutes à l'affaiblissement de la capacité. Cette compréhension a conduit au développement d'un revêtement d'oxyde de graphène réduit (RGO) en une seule étape, dérivé du saccharose, visant à améliorer l'échange de charge et à atténuer les réactions secondaires progressives à l'interface cathode-électrolyte. Cette approche permet de ralentir et, idéalement, d'empêcher l'évolution de la couche CEI et la dissolution du RM, qui sont responsables de l'augmentation de la surpuissance de transfert de charge et de la perte de capacité liée au RM. Grâce à cette stratégie de revêtement innovante, les performances électrochimiques ont encore été améliorées, la capacité de décharge atteignant 163.0 mAh $g^{-1}$ (équivalant à 771.2 Wh $kg^{-1}$ en densité énergétique), avec un taux de rétention amélioré de 76.4 % après 100 cycles à 1 C.

## Acknowledgements

First and foremost, I would like to express my utmost gratitude to my thesis advisor, Professor George P. Demopoulos for offering me this unique research opportunity under his supervision at McGill University. This thesis would not have been completed without his intellectual guidance and patience for my mistakes during my doctoral studies. His incredible passion always makes me inspired to overcome many obstacles in this project. Thanks to his intensive research trainings, I could be finally become an independent researcher who can bring contributions to original knowledge in materials science instead of just following someone's commands without doubts.

I also acknowledge the financial supports that enabled this project from McGill Engineering Doctoral Award program and Natural Sciences and Engineering Research Council (NSERC) Strategic Project grant program. I am also pleased to acknowledge the sponsorship of this project by Hydro-Québec's Centre of Excellence in Transportation Electrification and Energy Storage.

It would have been impossible to manage tough hours in the lab, failing experiments and personal matters if it was not for my incredible previous and current lab mates in the HydroMET group including Dr. Hsien-chieh Chiu, Dr. Zhuoran Wang, Dr. Fuqiang Guo, Dr. Huijing Wei, Dr. Marianna Uceda, Dr. Francois Larouche, Dr. Yan (Helen) Zeng, Dr. Majid Rasool, Dr. Konstantina Chalastara, Dr. Andrea La Monaca, Han Wang, Dr. Rana Yekani, Fan Yu, Dr. Senhao Wang, Arian Norouzi, Joon Kyung Koong, Krystal Davis, Aristya Marzuki, Philip Gamboa, Gökçe Kiliç, and Valentina Nunez Pava. As I reflect on our journey together in the lab, I am filled with gratitude for each and every one of you. Through long hours, countless experiments and shared challenges, we have formed a bond that goes beyond just colleagues - we are a team and a family. I want to take this opportunity to express my deepest appreciation for your unwavering support, encouragement, and dedication. Whether it was lending a helping hand during experiments, offering words of encouragement during setbacks, or simply sharing a laugh during the stressful moments, your presence has made all the difference. Together, we have faced numerous obstacles and celebrated many victories. It is through our collective effort, passion, and determination that we have been able to push the boundaries of knowledge and make meaningful contributions to our field of research. As we continue on our individual paths, let us carry with us the memories of our shared experiences and the lessons we have learned together. Thank you for being part of this incredible journey, and I look forward to many more exciting adventures ahead.

My sincere gratitude goes towards two professors Prof. Jinhyuk Lee and Prof. Dong-Hwa Seo and their students including Hoda Ahmed, Richie Fong, Greg Lazaris, and Sang-Wook Park for the invaluable guidance, support, and opportunities you have provided during our collaborative research endeavors. Working alongside you has been an enriching and rewarding experience, and I am deeply thankful for the knowledge and insights I have gained from your expertise. Your dedication to excellence and commitment to advancing research in our field have been truly inspiring. Your willingness to share your expertise, resources, and time has played a significant role in our collective growth and success. I am particularly grateful for the trust and confidence you have placed in me, allowing me to contribute to our research projects and fostering an environment of collaboration and innovation. As we continue our research journey together, I am excited about the possibilities that lie ahead and confident that our partnership will continue to yield meaningful contributions to our field. Thank you once again for your enthusiasm, creativity, support, and friendship. It has been an honor and privilege to work with you, and I look forward to our continued collaboration in the future.

Finishing my Ph. D. journey would not have been possible without my family in South Korea. I would like to express my heartfelt gratitude for your unwavering love, support, and encouragement throughout my academic journey and the completion of this thesis. Your guidance and belief in me have been the driving force behind my success, and I am truly grateful for everything you have done for me. I am blessed to have such an adorable family. Your love and support have shaped me into the person I am today, and I dedicate this achievement to each of you.

Thanks to all of you, I was able to successfully complete the long and challenging journey of my doctoral studies. Thank you and Merci beaucoup.

## Contribution of Authors

This thesis is structured in a manuscript-based format. Chapters 3 to 5 consist of separate manuscripts, which have been either published or being submitted for publication in journals. The research was conducted in the Department of Materials Engineering of McGill University under the research guidance of Prof. George P. Demopoulos, who served as the principal investigator and overseer of this thesis project, along with managing the associated funding. The contributions of each co-author involved in the manuscript chapters are explained below.

**Chapter 3 Manuscript: Moohyun Woo, Jinhyuk Lee and George P. Demopoulos, "*Surface and bulk defect formation during hydrothermal synthesis of $LiCoPO_4$ crystals and their electrochemical implications*", Mater. Adv., 2023, 4, 4823-4834, DOI: https://doi.org/10.1039/D3MA00455D**

M. Woo performed all the experiments, characterizations, interpretation of results under the supervision of G. P. Demopoulos. M. Woo prepared the first draft and J. Lee and G. P. Demopoulos reviewed it and made suggestions for revision. J. Lee contributed to the discussion and analysis of the results.

**Chapter 4 Manuscript: Moohyun Woo, Sang-Wook Park, Jinhyuk Lee, Dong-Hwa Seo and George P. Demopoulos, "*Attaining full Li-ion storage capacity in nearly defect-free and preferential orientation grown $LiCoPO_4$ via ab initio solvothermal crystallization control*", Adv. Energy Mater., 2024, 202404404, DOI: https://doi.org/10.1002/aenm.202404404**

The laboratory experiments, electrochemical studies and interpretation of results were carried out by M. Woo under the supervision of G. P. Demopoulos. S.-W Park conducted the computational simulation and calculation under the guidance of D.-H Seo. J. Lee contributed with the interpretation of the GITT electrochemical tests. M. Woo prepared the first draft, and all the authors contributed to writing the paper.

**Chapter 5 Manuscript: Moohyun Woo and George P. Demopoulos, "*Interfacial capacity fade mechanism of high-voltage $LiCoPO_4$ cathode and its mitigation*", Submitted, 2025**

M. Woo performed all experiments and fundamental post-mortem analysis under the supervision of G. P. Demopoulos. M. Woo prepared the first draft and G. P. Demopoulos reviewed it and suggested revisions.

I hereby give copyright clearance for the inclusion of above papers, of which I am corresponding author, into the Ph.D. dissertation of Moohyun Woo.

Signature: _____ Date: _____

Prof. George P. Demopoulos

Department of Mining and Materials Engineering

McGill University

Montréal, Québec

# List of Figures

## List of Tables

# List of Symbols and Abbreviations

**Symbols**

| | |
|---|---|
| $\gamma$ | Surface free energy per unit area |
| $\gamma_{net}$ | Net effective surface free energy |
| $\eta$ | Overpotential |
| $\theta$ | Angle of incidence |
| $\lambda$ | Wavelength |
| $\mu$ | Chemical potential |
| $A$ | Pre-exponential factor, or Surface area |
| $A_i$ | Aqueous species |
| $[A_i]$ | Activity of an aqueous specie, $A_i$ |
| $C$ | Coulomb or Concentration |
| $C_S$ | Critical supersaturation |
| $D^{Li}$ | Chemical diffusion coefficient of Li-ion |
| $E$ | Specific energy |
| $E_g$ | Thermodynamic stability window |
| $E_{slab}$ | Energy of slab supercell |
| $E_{bulk}$ | Energy of bulk structure per atom |
| $E_d$ | Adsorption energy |
| $f$ | Structural factor |
| $F$ | Faraday constant |
| $\Delta G$ | Total free energy change |
| $\Delta G_{critictal}$ | Critical energy |
| $\Delta G_S$ | Surface free energy change |
| $\Delta G_v$ | Bulk free energy change per unit volume |
| $I$ | Current or Intensity |
| $J$ | Nucleation rate or Current density |
| $J^{het}$ | Heterogeneous nucleation rate |
| $J^{homo}$ | Homogenous nucleation rate |
| $K_{SP}$ | Solubility product |
| $\gamma$ | Surface energy |

| | |
|---|---|
| $\gamma'$ | Surface energy after adsorption |
| $\Delta\gamma$ | Surface energy change |
| $M_w$ | Molar mass |
| $n$ | Number of charge |
| $n_M$ | Number of mole |
| $Q$ | Specific capacity |
| $Q_{dis}$ | Discharge capacity |
| $r$ | Radius of a sphere |
| $r_c$ | Critical nuclei size |
| $R_{MF}$ | Mid-Frequency resistance |
| $R_{wp}$ | Weighted reliability factor |
| $S$ | Supersaturation, or Specific surface area |
| $t$ | Time |
| $T$ | Absolute temperature |
| $V$ | Voltage, or Unit cell volume |
| $V_{dis}$ | Discharge voltage |
| $V_{OC}$ | Open circuit voltage |
| $V_M$ | Molar volume |
| $a$ | Lattice parameter of x aixs |
| $b$ | Lattice parameter of y aixs |
| $c$ | Lattice parameter of z aixs |
| $d$ | Lattice spacing |
| $\tau$ | Time duration |
| $k_B$ | Boltzmann's constant |
| $k_i$ | Stoichiometric coefficient |
| Ω | Resistance |

**Abbreviations**

| | |
|---|---|
| 1-D | One-dimensional |
| 2-D | Two-dimensional |
| 3-D | Three-dimensional |
| AIMD | *ab initio* molecular dynamics |

| | |
|---|---|
| Ar | Argon |
| BA | Benzyl alcohol |
| BET | Brunauer–Emmett–Teller |
| BM | Ball-milling |
| C | Carbon |
| CA | Citric acid |
| CE | Coulombic efficiency |
| CEI | Cathode-electrolyte interphase |
| CFE | Cold-field emission |
| CMC | Carboxymethylcellulose sodium salt. |
| CNT | Carbon nanotube |
| CPA | Crystallization by particle attachment |
| CS | Critical supersaturation |
| CTAB | Cetyltrimethylammonium bromide |
| CT/IR | Charge-transfer resistance and Ohmic drop |
| CV | Cyclic voltammetry |
| DEG | Diethylene glycol |
| DFT | Density functional theory |
| DMC | Dimethyl carbonate |
| DMD | Dissolution-migration-deposition |
| EA | Electric aircraft |
| EC | Ethylene carbonate |
| EDS | Energy-dispersive X-ray spectroscopy |
| EG | Ethylene glycol |
| EIS | Electrochemical impedance spectroscopy |
| EMC | Ethyl methyl carbonate |
| EVs | Electric vehicles |
| FTIR | Fourier transform infrared |
| FWHM | Full width at half maximum |
| GITT | Galvanostatic intermittent titration technique |
| HAADF | High-angle annular dark-field |
| High-V | High-voltage |

| | |
|---|---|
| HOMO | Highest occupied molecular orbital |
| HT | Hydrothermal |
| HR-TEM | High-resolution transmission electron microscopy |
| ICP -OES | Inductively coupled plasma optical emission spectroscopy |
| LCO | $LiCoO_2$ |
| LCP | $LiCoPO_4$ |
| LFP | $LiFePO_4$ |
| LIBs | Li-ion batteries |
| LMO | $LiMn_2O_4$ |
| LSV | Linear sweep voltammetry |
| LTO | $Li_2TiO_3$ |
| LUMO | Lowest unoccupied molecular orbital |
| MF | Mid-frequency |
| MH | Microwave heating |
| MP-AES | Microwave plasma atomic emission spectrometer |
| MT | Mass-transfer resistance |
| MWST | Microwave solvothermal |
| MWCNT | Nultiwalled carbon nanotube |
| $N_2$ | Nitrogen |
| NCA | $LiNi_xCo_yAl_zO_2$ (where x+y+z = 1) |
| NCM | $LiNi_xCo_yMn_zO_2$ (where x+y+z = 1) |
| NCM811 | $LiNi_{0.8}Co_{.1}Mn_{0.1}O_2$ |
| NMP | N-methyl pyrrolidinone |
| OCV | Open circuit voltage |
| PC | Propylene carbonate |
| PEG | Polyethylene glycol |
| PM | Planetary-milling |
| PTFE | Polytetrafluoroethylene |
| PVDF | Polyvinylidene fluoride |
| PVP | Polyvinylpyrrolidone |
| PXRD | Powder X-ray diffraction |
| RGO | Reduced graphene oxide |

| | |
|---|---|
| RM | Redox metal |
| SAED | Selected area electron diffraction |
| SEI | Solid electrolyte interphase |
| SEM | Scanning electron microscopy |
| SF | Supercritical fluid |
| SP | Spray pyrolysis |
| SS | Solid-state reaction |
| ST | Solvothermal |
| TEG | Triethylene glycol |
| TEM | Transmission electron microscopy |
| TGA | Thermogravimetric analysis |
| TM | Transition metal |
| TMSP | Tris(trimethylsilyl) phosphite |
| TTEG | Tetraethylene glycol |
| VASP | Vienna *ab initio* simulation package |
| XPS | X-ray photoelectron spectroscopy |
| XRD | X-ray diffraction |

# Chapter 1: Introduction

## 1.1 Motivation

Rechargeable Li-ion batteries (LIBs), initially introduced by Whittingham in 1976, have revolutionized energy storage with their remarkable capacity-to-weight and capacity-to-volume ratios.[1, 2] This high energy density of LIBs among the different secondary battery types has fueled progress across various technologies from portable electronic devices to large-scale applications such as electric vehicles (EVs) and stationary storage systems for renewable solar and wind energy.[3-5] Industry analysts at McKinsey & Company foresee strong increase in global LIB demand over the next decade.[6] From a baseline of 700 GWh in 2022, the demand is expected to soar to approximately 4.7 TWh by 2030, making a nearly sevenfold increase. Specifically, in EV sector, LIBs are predicted to dominate the market in 2030, with an estimated demand of around 4,300 GWh.

LIBs consist of three primary components: two electrodes (cathode and anode) and an electrolyte. Among these components, cathode materials play a crucial role in determining key performance metrics such as energy density, cycling stability, and good power capability.[7-10] Since the creation of the first modern LIB prototype in 1985 and their commercial launch by Sony in 1991, research on cathode materials has predominantly favoured oxide-based compounds with layered and spinel structures starting with the prototypical $LiCoO_2$ (LCO) and followed by $LiNi_xCo_yMn_zO_2$ (NCM, where $x+y+z = 1$), $LiNi_xCo_yAl_zO_2$ (NCA, where $x+y+z = 1$), $LiMn_2O_4$ (LMO), as well as polyanionic compounds with olivine structures such as $LiFePO_4$ (LFP).[11-13]

Despite the energy density above 600 Wh $kg^{-1}$ of LCO, it is hindered by high costs, cobalt's supply, and poor thermal stability, which can lead to explosion and fire hazards.[14] To address these issues, NCM and NCA cathodes have been developed by partially replacing cobalt with nickel and manganese or aluminum in the layered structure, which reduces costs and increases energy density. However, safety concerns like oxygen evolution remains.[15, 16] LMO with spinel structure offers a significant cost advantage over LCO, but its lower energy density and shorter cycle life limit its widespread use.[17] In contrast, LFP which is one of polyanionic compounds has emerged as a sustainable cathode material due to its make-up of abundant elements and the superior stability owed to the unique olivine-type robust crystal structure.[18] LFP occupies a large portion of LIBs market by overcoming the intrinsically sluggish kinetics with the carbon coating strategy developed by Hydro-

Québec.[19] Despite the nearly theoretical energy density of 590 Wh $kg^{-1}$ for commercially available LFP, this value is still relatively low and insufficient for the long-range requirements of EVs.[20-22] With this trend, the ever-growing demand for advanced rechargeable LIBs with greater energy density has triggered intensive research on other polyanionic compounds that operate at high-voltage (high-V), aiming to develop next-generation cathode materials.

Lithium cobalt phosphate ($LiCoPO_4$, LCP), sharing the olivine-type crystal structure with LFP, has emerged as a promising candidate for next-generation cathode materials in LIBs. LCP presents several advantages that make it an attractive option for overcoming current energy density limitations. It combines its very high-V of 4.8 V vs. $Li/Li^+$ (as compared to 3.5 V vs. $Li/Li^+$ for the commercially available LFP) and the equal theoretical capacity with LFP (~167 mAh $g^{-1}$), resulting in 800 Wh $kg^{-1}$ compared to 590 Wh $kg^{-1}$ of LFP. [23-25] Additionally, the strong P–O bonds similarly to LFP guarantee a robust host framework for Li-ion storage, offering excellent thermal safety. Despite these promising characteristics, LCP other than the high cost of Co that limits its application to niche markets, it faces several challenges to commercialization. The material's performance is hindered by multiple factors: sluggish Li-ion mobility, low electronic conductivity, structural imperfections induced by anti-site defects where cobalt ions occupy lithium sites.[26-31] Furthermore, it suffers from rapid capacity fade over repeated charge-discharge cycles, attributed to degradation of its crystal structure or the build-up of unwanted compounds formed by irreversible side reactions at the cathode-electrolyte interface, leading to a substantial decrease in Li-ion storage capacity.[32-35]

To enhance LCP kinetics, various methods such as nanosizing and doping have been intensively explored. Nanosizing by pulverization can achieve high charge-discharge capacity for a few initial cycles, but it introduces abundant anti-site defects in the bulk crystal structure and triggers severe side reactions with the electrolyte at the interface.[29-31, 35-37] These drawbacks are particularly detrimental in LCP due to its unique properties. As LCP is characterized by one-dimensional (1-D) diffusion channels, anti-site defects interrupt the Li-ion intercalation. This, combined with an increased surface area and high operating voltage, accelerates electrolyte decomposition, adversely impacting long-term cycling performance.[38, 39] Additionally, for large-scale applications, micron-sized particles are favored to enhance volumetric energy density, as opposed to nano-sized particles produced by pulverization.[40, 41]

Alternatively, doping strategies have emerged as an alternative approach to enhance the electrochemical performance of LCP. These methods aim to improve the structural features of LCP,

potentially suppressing anti-site defect formation upon cycling and enhancing kinetics by creating lithium and/or cobalt vacancies, particularly when applying aliovalent dopants.[42] While some experimental studies have shown promising results with LCP doping, this approach also presents certain limitations. Increased dopant concentration necessitates charge compensation, which can reduce capacity from the theoretical value. Additionally, the narrow cut-off voltage window (4.3-5.0 V vs $Li/Li^+$) required in the case of Fe doping to prevent the reduction of $Fe^{3+}$ that triggers instability may contribute to capacity limitations.[43] Therefore, further studies on LCP cathode materials are warranted.

To unlock the full potential of LCP, it is essential to develop novel synthesis and defect engineering approaches. Material synthesis plays a crucial role as it determines the properties of crystal structure, which in turn influence electrochemical performance. In this thesis, solution synthesis of LCP (Hydrothermal, HT & Solvothermal, ST) was implemented in order to probe the impact of various synthesis parameters on LCP crystal structure/morphology/purity and electrochemical storage properties. Particular attention was paid on characterization of the LCP materials regarding both particle surface composition inhomogeneities and bulk structure defects affecting their electrochemical performance. In addition, post-mortem analysis characterizing cycled electrodes in different aging conditions sought to shed light on the interfacial capacity fade mechanism linked to high-V operation and a coating strategy as mitigating measure was explored.

### 1.2. Objectives

The overall goal of this thesis is to investigate in depth the crystal and surface chemistry of LCP materials in order to shed light on its intercalation kinetics and interfacial reactivity aiming to unlock ultimately their full potential as high energy density cathodes for next generation LIBs. Following are the main objectives of this thesis:

1. Identifying the critical limitations of hydrothermal (HT) synthesis regarding both particle surface composition inhomogeneities and bulk structure defects affecting the electrochemical performance of LCP.
2. Designing novel LCP of defect-free crystal structure and shortened Li-ion diffusion pathway to achieve nearly theoretical full capacity via solvothermal (ST) synthesis and Argon (Ar)-annealing.

3. Understanding the core connection between capacity fade mechanism and irreversible interfacial chemistry triggered by high-V operation of LCP and propose a mitigating coating strategy.

### 1.3. Thesis Organization

This thesis consists of seven chapters, followed by Appendices of supporting information. Chapter 1 gives a general introduction to the motivation and objectives of this thesis. Chapter 2 provides a literature review on the fundamentals of LIBs with the focus on cathode materials, present research status and issues of LCP as a promising cathode material, and the basics of solution-based synthesis accompanied by its application in preparing materials for LIB cathodes.

In Chapter 3, impact of HT synthesis parameters but also post-synthesis modifications on LCP crystal structure/morphology/purity and electrochemical storage properties are investigated. Upon monitoring the evolution of surface and bulk structure during material fabrication, the formation of defects is characterized, and their consequence on Li-ion intercalation responsible for the exhibited low discharge capacity is determined.

In Chapter 4, micron-scale and preferentially-grown LCP particles incorporating the defect-free olivine crystal structure are designed via ST-synthesis and subsequent Ar-annealing. The morphological and structural advantages of utilizing EG as a solvent are elucidated by both experimental characterizations and computational approaches.

In Chapter 5, the relationship between capacity fade mechanism and irreversible side reactions at the interface with electrolyte is investigated by implementing post-mortem analysis characterizing cycled electrodes in different aging conditions. In addition, a reduced graphene oxide (RGO) coating strategy is described as potential mitigating tool.

Chapter 6 connects the overall findings of this thesis to the objectives laid out in Chapter 1 and topics discussed in Chapter 2, to offer a global discussion. The summary of the work conducted in this thesis is presented in Chapter 7 in terms of major conclusions, contributions to the original knowledge, and ideas for further work. The supplementary information for Chapters 3 to 5 is presented in the APPENDIX section.

## 1.4 References


1. M. S. Whittingham, Electrical energy storage and intercalation chemistry. *Science* **1976**, *192*, 1126-1127.
2. M. Armand, J. M. Tarascon, Building better batteries. *Nature* **2008**, *451*, 652-657.
3. D. Larcher, J. M. Tarascon, Towards greener and more sustainable batteries for electrical energy storage. *Nature Chemistry* **2015**, *7* (1), 19-29.
4. B. Dunn, H. Kamath, J. M. Tarascon, Electrical energy storage for the grid: A battery of choices. *Science* **2011**, *334* (6058), 928-935.
5. J. B. Goodenough, Y. Kim, Challenges for rechargeable Li batteries. *Chemistry of Materials* **2010**, *22* (3), 587-603.
6. McKinsey & Company, Battery 2030: Resilient, sustainable, and circular. **2023**.
7. J. M. Tarascon, M. Armand, Issues and challenges facing rechargeable lithium batteries. *Nature* **2001**, *414*, 359-367.
8. Whittingham, M. S., Lithium batteries and cathode materials. *Chemical Reviews* **2004**, *104* (10), 4271-4302.
9. V. Etacheri, R. Marom, R. Elazari, G. Salitra, D. Aurbach, Challenges in the development of advanced Li-ion batteries: a review. *Energy & Environmental Science* **2011**, *4* (9), 3243-3262.
10. A. Manthiram, X. Yu, S. Wang, Lithium battery chemistries enabled by solid-state electrolytes. *Nature Reviews Materials* **2017**, *2* (4), 16103.
11. K. Ozawa, Lithium-ion rechargeable batteries with $LiCoO_2$ and carbon electrodes: The $LiCoO_2$/C system. *Solid State Ionics* **1994**, *69*, 212-221.
12. N. Nitta, F. Wu, J. T. Lee, G. Yushin, Li-ion battery materials: Present and future. *Materials Today* **2015**, *18* (5), 252-264.
13. Q. Zhao, S. Stalin, C. Z. Zhao, L. A. Archer, Designing solid-state electrolytes for safe, energy-dense batteries. *Nature Reviews Materials* **2020**, *5* (3), 229-252.
14. Y. Furushima, C. Yanagisawa, T. Nakagawa, Y. Aoki, N. Muraki, Thermal stability and kinetics of delithiated $LiCoO_2$. *Journal of Power Sources* **2011**, *196* (4), 2260-2263.
15. W. Li, E. M. Erickson, A. Manthiram, High-nickel layered oxide cathodes for lithium-based automotive batteries. *Nature Energy* **2020**, *5* (1), 26-34.
16. W. Li, B. Song, A. Manthiram, High-voltage positive electrode materials for lithium-ion batteries. *Chemical Society Reviews* **2017**, *46* (10), 3006-3059.
17. Y. Huang, Y. Dong, S. Li, J. Lee, C. Wang, Z. Zhu, W. Xue, Y. Li, J. Li, Lithium manganese spinel cathodes for lithium-ion batteries. *Advanced Energy Materials* **2021**, *11* (2), 2000997.
18. A. Yamada, S. C. Chung, K. Hinokuma, Optimized $LiFePO_4$ for lithium battery cathodes. *Journal of The Electrochemical Society* **2001**, *148* (3), A224-A229.
19. K. Zaghib, J. Shim, A. Guerfi, P. Charest, K.A. Striebel, Effect of carbon source as additives in $LiFePO_4$ as positive electrode for lithium-ion batteries. *Electrochemical and Solid-State Letters* **2005**, *8* (4), A207-A210.
20. D. Lin, Y. Liu, Y. Cui, Reviving the lithium metal anode for high-energy batteries. *Nature Nanotechnology* **2017**, *12* (3), 194-206.
21. J. Lu, Z. Chen, Z. Ma, F. Pan, L. A. Curtiss, K. Amine, Challenges and opportunities towards fast-charging battery materials. *Nature Energy* **2018**, *3* (7), 512-523.
22. F. M. N. U. Khan, M. G. Rasul, A. S. M. Sayem, N. Mandal, Maximizing energy density of lithium-ion batteries for electric vehicles: A critical review. *Energy Reports* **2023**, *9*, 11-21.

23. D. Liu, W. Zhu, C. Kim, M. Cho, A. Guerfi, S. A. Delp, J. L. Allen, T. R. Jow, K. Zaghib, High-energy lithium-ion battery using substituted $LiCoPO_4$: From coin type to 1 Ah cell. *Journal of Power Sources* **2018**, *388*, 52-56.
24. D.-W. Han, Y.-M. Kang, R.-Z. Yin, M.-S. Song, H.-S. Kwon, Effects of Fe doping on the electrochemical performance of $LiCoPO_4$/C composites for high power-density cathode materials. *Electrochemistry Communications* **2009**, *11* (1), 137-140.
25. F. C. Strobridge, R. J. Clement, M. Leskes, D. S. Middlemiss, O. J. Borkiewicz, K. M. Wiaderek, K. W. Chapman, P. J. Chupas, C. P. Grey, Identifying the structure of the intermediate, $Li_{2/3}CoPO_4$, formed during electrochemical cycling of $LiCoPO_4$. *Chemistry of Materials* **2014**, *26* (21), 6193-6205.
26. X. Wu, F. Rohman, M. Meledina, H. Tempel, R. Schierholz, H. Kungl, J. Mayer, R.-A. Eichel, Analysis of the effects of different carbon coating strategies on structure and electrochemical behavior of $LiCoPO_4$ material as a high-voltage cathode electrode for lithium ion batteries. *Electrochimica Acta* **2018**, *279*, 108-117.
27. S. Y. Chung, J. T. Bloking, Y. M. Chiang, Electronically conductive phospho-olivines as lithium storage electrodes. *Nature Materials* **2002**, *1* (2), 123-128.
28. A. K. Padhi, K. S. Nanjundaswamy, J. B. Goodenough, Phospho-olivines as positive-electrode materials for rechargeable lithium batteries. *Journal of the Electrochemical Society* **1997**, *144* (4), 1188-1194.
29. A. Boulineau, T. Gutel, Revealing electrochemically induced antisite defects in $LiCoPO_4$: Evolution upon cycling. *Chemistry of Materials* **2015**, *27* (3), 802-807.
30. M. K. Devaraju, Q. D. Truong, T. Tomai, H. Hyodo, Y. Sasaki, I. Honma, Antisite defects in $LiCoPO_4$ nanocrystals synthesized via a supercritical fluid process. *RSC Advances* **2014**, *4* (94), 52410-52414.
31. Q. D. Truong, M. K. Devaraju, T. Tomai, I. Honma, Direct observation of antisite defects in $LiCoPO_4$ cathode materials by annular dark- and bright-field electron microscopy. *ACS Applied Materials & Interfaces* **2013**, *5* (20), 9926-32.
32. E. Markevich, R. Sharabi, H. Gottlieb, V. Borgel, K. Fridman, G. Salitra, D. Aurbach, G. Semrau, M. A. Schmidt, N. Schall, C. Bruenig, Reasons for capacity fading of $LiCoPO_4$ cathodes in $LiPF_6$ containing electrolyte solutions. *Electrochemistry Communications* **2012**, *15* (1), 22-25.
33. L. Dimesso, C. Spanheimer, D. Becker, W. Jaegermann, Properties of $LiCoPO_4$-non-graphitic carbon foam composites. *Journal of the European Ceramic Society* **2014**, *34* (4), 933-941.
34. J. L. Allen, T.R. Jow, J. Wolfenstine, Improved cycle life of Fe-substituted $LiCoPO_4$. *Journal of Power Sources* **2011**, *196* (20), 8656-8661.
35. S. Sreedeep, S. Natarajan, V. Aravindan, Recent advancements in $LiCoPO_4$ cathodes using electrolyte additives. *Current Opinion in Electrochemistry* **2022**, *31*, 100868.
36. A. Manthiram, K. Chemelewski, E. S. Lee, A perspective on the high-voltage $LiMn_{1.5}Ni_{0.5}O_4$ spinel cathode for lithium-ion batteries. *Energy & Environmental Science* **2014**, *7* (4), 1339-1350.
37. N. Tolganbek, Y. Yerkinbekova, S. Kalybekkyzy, Z. Bakenov, A. Mentbayeva, Current state of high voltage olivine structured $LiMPO_4$ cathode materials for energy storage applications: A review. *Journal of Alloys and Compounds* **2021**, *882*, 160774.
38. Q. D. Truong, M. K. Devaraju, Y. Ganbe, T. Tomai, I. Honma, Controlling the shape of $LiCoPO_4$ nanocrystals by supercritical fluid process for enhanced energy storage properties. *Scientific Reports* **2014**, *4*, 3975.
39. N. Boaretto, I. Garbayo, S. Valiyaveettil-SobhanRaj, A. Quintela, C. Li, M. Casas-Cabanas, F. Aguesse, Lithium solid-state batteries: State-of-the-art and challenges for materials, interfaces and processing. *Journal of Power Sources* **2021**, *502*, 229919.

40. R. Brow, A. Donakowski, A. Mesnier, D. J. Pereira, K. X. Steirer, S. Santhanagopalan, A. Manthiram, Mechanical pulverization of Co-free nickel-rich cathodes for improved high-voltage cycling of lithium-ion batteries. *ACS Applied Energy Materials* **2022**, *5* (6), 6996-7005.
41. R. Zhu, G. Liu, G. Qu, X. Li, X. Chen, W. Wan, C. Wang, Y. Huang, Enhancing volumetric energy density of $LiFePO_4$ battery using liquid metal as conductive agent. *Advanced Functional Materials* **2024**, 2409230.
42. K. J. Kreder, G. Assat, A. Manthiram, Aliovalent substitution of $V^{3+}$ for $Co^{2+}$ in $LiCoPO_4$ by a low-temperature microwave-assisted solvothermal process. *Chemistry of Materials* **2016**, *28* (6), 1847-1853.
43. N. Okita, K. Kisu, E. Iwama, Y. Sakai, Y. Lim, Y. Takami, M. T. Sougrati, T. Brousse, P. Rozier, P. Simon, W. Naoi, K. Naoi, Stabilizing the structure of $LiCoPO_4$ nanocrystals via addition of $Fe^{3+}$: Formation of $Fe^{3+}$ surface layer, creation of diffusion-enhancing vacancies, and enabling high-voltage battery operation. *Chemistry of Materials* **2018**, *30* (19), 6675-6683.

# Chapter 2: Literature Review

This chapter begins with an overview of the basic principles of LIBs and the different types of most prevalent cathode materials. This is followed by an overall review of lithium cobalt phosphate, $LiCoPO_4$ (LCP) emphasizing the limitations of conventional preparation methods and the importance of solution synthesis and reasons for prioritizing it. Subsequently, the concluding section of this chapter is concerned with unclear aspects in LCP solution synthesis that require further clarification to establish it as a functional cathode for advanced LIBs delivering enhanced energy density.

## 2.1. Rechargeable LIBs

### 2.1.1. Working principles of LIBs

Rechargeable LIBs consist of three main components, a positive electrode (cathode) and a negative electrode (anode) that are immersed in an electrolyte. The cathode and anode both act as source and sink for Li-ions during battery operation, while the electrolyte facilitates the transport of Li-ions between two electrodes. When fully charged LIBs are discharged, Li-ions are released (de-intercalation) from the anode and diffuse through the electrolyte towards the cathode (intercalation). Concurrently, electrons are produced through the de-intercalation reaction of Li-ions at the anode and flow from the anode to the cathode through the external circuit. The opposite process occurs during the charge step. Figure 2.1 illustrates the general configuration of a LIB employing $LiCoO_2$ (LCO) as the cathode and graphite as the anode. The conventional electrolyte comprises a lithium salt, like $LiPF_6$, dissolved in a non-aqueous solvent, such as a mixture of ethylene carbonate and dimethyl carbonate (EC/DMC). The separator consists of a porous polyethylene material that serves to prevent direct contact between the two electrodes, while it is both electrically insulating and facilitating the mobility of Li-ions. In the charge process, Li-ions are extracted from LCO, traveling through the electrolyte and separator, and are subsequently intercalated into anode. Simultaneously, electrons are provided by $Co^{3+}$ in the cathode and transferred to the graphite via the external circuit making electric current. Conversely, during discharge, the opposite reactions occur. The two half-reactions occurring in LIBs during charge can be depicted below:

$$Cathode: LiCoO_2 \rightarrow Li_{1-x}CoO_2 + xLi^+ + xe^- \quad (2.1)$$

$$Anode: C_6 + xLi^+ + xe^- \rightarrow Li_xC_6 \quad (2.2)$$

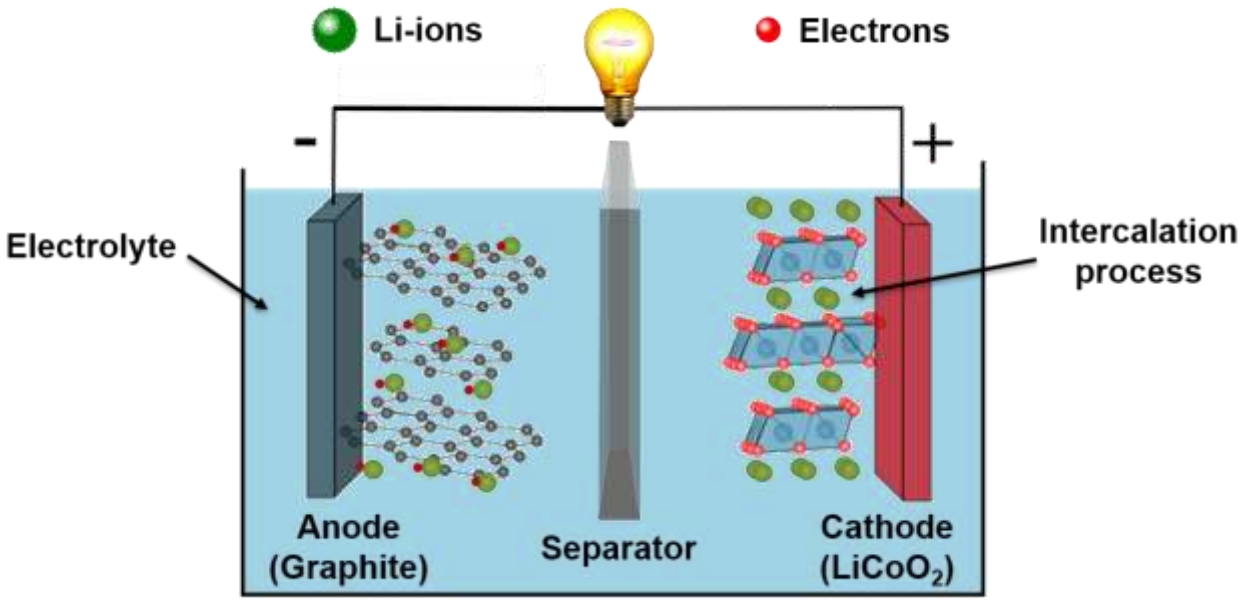


**Figure 2.1.** The schematic of a Li-ion battery illustrates a structure where the anode and cathode are positioned in a sandwich-like configuration, internally isolated by a porous membrane separator, submerged in an electrolyte, and externally connected through a circuit.

Selecting electrode materials play an important role in determining the performance of LIBs. The primary properties considered for batteries, including voltage, specific capacity, energy density, power density, cycle life, safety, and cost, are closely intertwined with the chemical composition and crystal/electronic structure of the cathode materials.

The energy density of LIBs refers to the amount of energy stored per unit volume ($W\,h\,L^{-1}$). It is also frequently described in terms of gravimetric or specific energy density, representing the battery's energy per unit mass ($W\,h\,kg^{-1}$). The energy density can be calculated as the product of the open circuit voltage ($V_{OC}$) and the specific capacity ($Q_c$), with the specific capacity denoting the quantity of charge stored per unit mass ($Ah\,g^{-1}$).

**Open circuit voltage** of a cell, denoted as $V_{OC}$ and measured in volts ($V$), represents the voltage across the cell terminals in the absence of any applied current.

$$V_{OC} = \frac{-(\mu_{Li}^{Cathode} - \mu_{Li}^{Anode})}{nF} \tag{2.3}$$

where $n$ is the number of electrons ($n$ = 1 for Li-ion) and $F$ is Faraday constant of 96,485 C mol$^{-1}$.

**Theoretical specific capacity** for a material can be determined using the equation (2.4), which involves the amount of charge transferred ($n$), Faraday's constant ($F$, measured in C mol$^{-1}$), and the molar mass ($M_w$, measured in g mol$^{-1}$) of the intercalation compound (cathode active material).

$$Q = \frac{nF}{M_w}\left(\frac{A \cdot s}{g}\right) \tag{2.4}$$

For example, the theoretical specific capacity of $LiCoPO_4$ (LCP) is calculated below:

$$Q_{LiCoPO_4} = \frac{1\ mol \cdot 96485\ C \cdot mol^{-1}}{160.85\ g} \cdot \left(\frac{1000}{3600}\right) = 166.6\ mA \cdot h \cdot g^{-1} \tag{2.5}$$

**Energy density** refers to the amount of energy contained within a given volume ($Wh\ L^{-1}$) or mass ($Wh\ kg^{-1}$). The produced energy density is calculated by the discharge capacity ($Q_{dis}$) and discharge voltage ($V_{dis}$) below:

$$E_{dis} = \int_0^{Q_{dis}} V_{dis}(q)dq = \int_0^{t_{dis}} V_{dis}(q)I_{dis}dt \tag{2.6}$$

where $q$ represents the specific capacity, $t$ is the discharge duration, and $I_{dis}$ signifies the constant current in the cell at the galvanostatic mode. It should be acknowledged that $V_{dis}$ is less than $V_{OC}$ due to the existence of internal resistance which is called overpotential ($\eta$).

Various terminologies for the field of LIBs are summarized as follows. **Power density** is defined as the quantity of energy ($W\ kg^{-1}$ or $W\ L^{-1}$) transferred by the material per unit time per unit mass or volume. **Rate capability** refers to the ability of LIBs to charge and discharge at different current applied for charge and discharge - this is denoted as the C-rate. 1 C means full charge or discharge in an hour. **Cycle life** pertains to the number of charge and discharge cycles, typically at a certain C-rate, that a battery can efficiently undergo before its performance declines below certain threshold. **Coulombic efficiency (CE)** of LIBs is determined by the ratio of the charge capacity to the discharge capacity of the electrode:

$$CE = \frac{Q_{dis}}{Q_{ch}} \tag{2.7}$$

In terms of the electrolyte, the utilization of suitable electrolytes is critical for the overall electrochemical performance of LIBs, particularly when considering high-voltage (high-V) cathode materials such as LCP. The stability window of the electrolyte, denoted as $E_g$, represents the energy difference between its lowest unoccupied molecular orbital (LUMO) and highest occupied molecular orbital (HOMO) as shown in Figure 2.2.[1] For enhanced energy density of LIBs, it is necessary to expand the stability window.

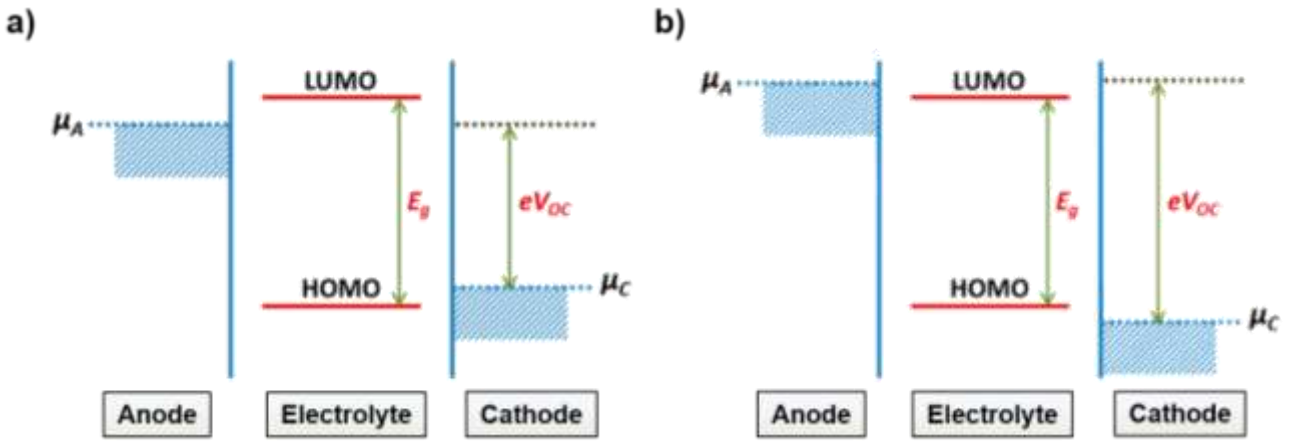


**Figure 2.2.** Schematic energy level diagram for (a) conventional and (b) high-V electrodes with electrolyte.[1] $E_g$ is the thermodynamic stability window of the electrolyte. $V_{OC}$ is the thermodynamic cell potential. $\mu_{anode}$ and $\mu_{cathode}$ are the theoretical electrochemical potentials of the anode and cathode, respectively.

When the anode has an electrochemical potential that is higher than the LUMO of the electrolyte, it will cause the electrolyte to reduce. This reduction process continues until a passivating layer known as the solid-electrolyte interphase (SEI) forms. The SEI layer acts as a barrier, preventing further electron transfer from the anode to the electrolyte, thereby stabilizing the system. On the other hand, if the cathode has an electrochemical potential lower than HOMO of the electrolyte, it will oxidize the electrolyte until a passivating cathode-electrolyte interphase (CEI) layer forms, creating a barrier to electron transfer from HOMO to the cathode. Therefore, for electrolyte stability, the theoretical electrochemical potentials of anode, $\mu_{anode}$ and cathode, $\mu_{cathode}$ must fall within the thermodynamic stability window ($E_g$) of the electrolyte. The theoretical expression for the electrolyte stability window is:

$$eV_{OC} = \mu_{Adnode} - \mu_{Cathode} \leq E_g \tag{2.8}$$

### 2.1.2. Various types of cathode materials for LIBs

As mentioned in Chapter 1, the cathode serves a key role in determining the overall properties of LIBs, including energy density, cycling stability, and cost. Therefore, the selection of cathode material significantly impacts how much energy can be stored, how long it can maintain performance over multiple charge and discharge cycles, and the overall cost of LIBs. As it is shown in Figure 2.3, different types of cathode materials occupy the market including $LiCoO_2$ (LCO), $LiMn_2O_4$ (LMO), $LiNi_xCo_yMn_zO_2$ (NCM, where x+y+z = 1), $LiNi_xCo_yAl_zO_2$ (NCA, where x+y+z = 1), and $LiFePO_4$

(LFP).[2] Among these candidates, LFP, NCM, and LCO currently dominate a significant portion of the total market share, and their market size is expected to grow steadily in 2030. Advantages and disadvantages of each cathode material are summarized in Figure 2.4 and Table 2.1.[3]

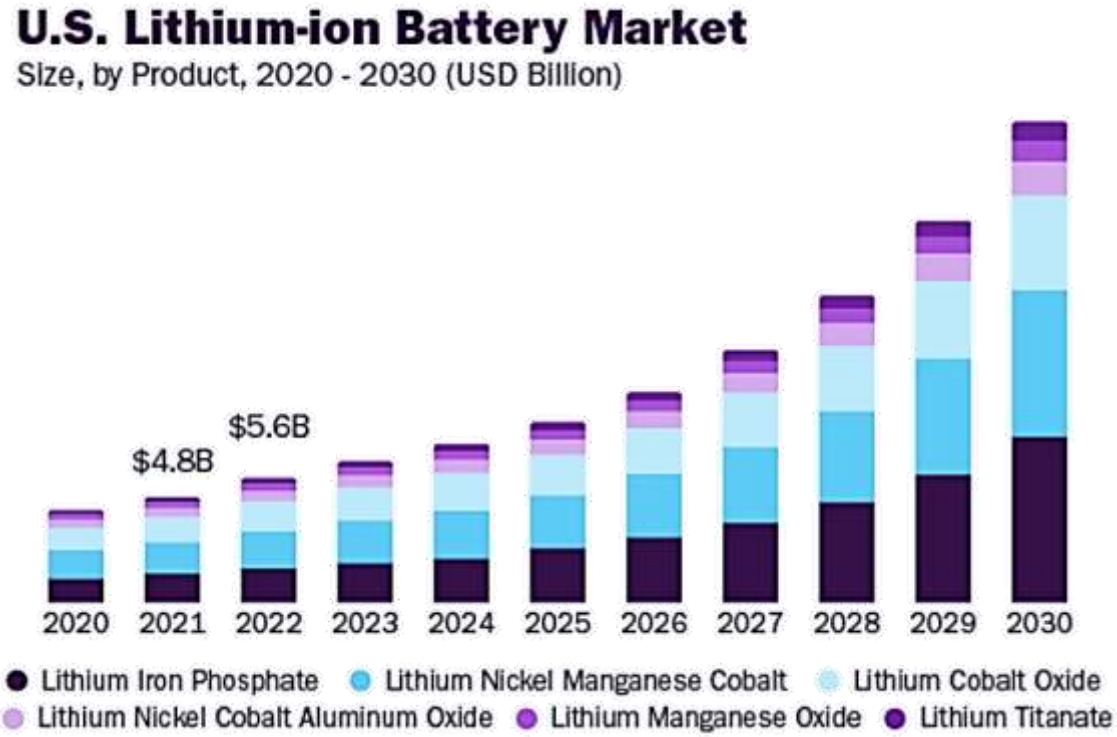


**Figure 2.3.** Present and future US Market share of Li-ion battery by product from 2020 to 2030.[2]

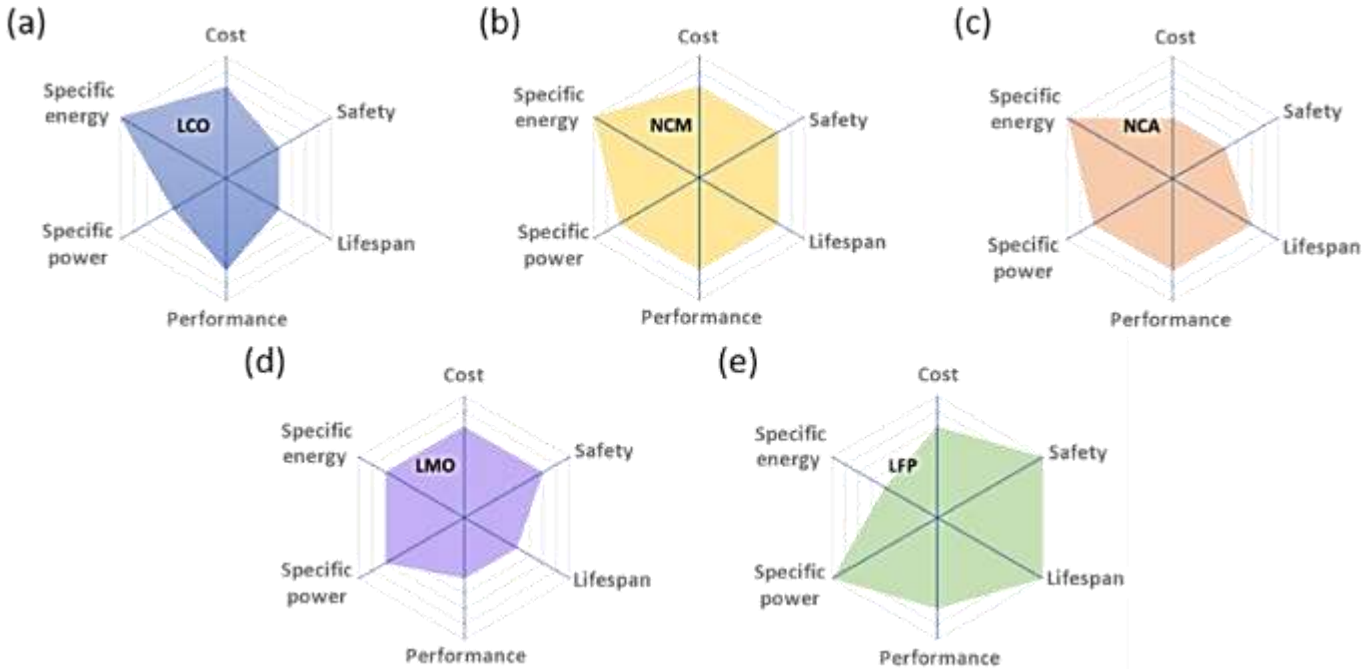


**Figure 2.4.** Spider web charts of key properties for comparison of five types of commercial cathode materials. (a) $LiCoO_2$, (b) $LiNi_xCo_yMn_{1-x-y}O_2$ (x+y+z = 1), (c) $LiNi_xCo_yAl_{1-x-y}O_2$ (where x+y+z = 1), (d) $LiMn_2O_4$, (e) $LiFePO_4$.[3]

The first commercial cathode material was LCO, developed by Sony in 1991.[4] The practical capacity of LCO is about 140 mAh $g^{-1}$, which is lower than its theoretical capacity of 270 mAh $g^{-1}$, at a redox voltage of 3.9 V vs. $Li/Li^+$.[5] Despite its high tap density, which allows for high volumetric energy densities ideal for small portable electronic devices, LCO has major drawbacks including poor thermal stability and the high cost of cobalt.[6] As depicted in Figure 2.5a, LCO possesses a layered structure where transition metal (TM) layers and lithium layers are stacked alternately, enabling Li-ion transport within two-dimensional (2-D) planes. In addition, charging above 4.2 V vs. $Li/Li^+$ can extract entire Li-ions to achieve higher capacity but will also induce irreversible structural change towards spinel, oxygen evolution, and electrolyte degradation.[7-9] These effects ultimately result in capacity degradation and safety concerns.[10-12]

**Table 2.1.** Properties of cathode materials in commercial LIBs.[13]

| Cathode | Redox potential ($Li/Li^+$) | Capacity (mA h $g^{-1}$) | Advantages | Disadvantages |
|---|---|---|---|---|
| LCO | 3.9 | 155 | - Energy density<br>- Long cycle life | - High cost<br>- Poor thermal stability |
| NCM | 3.8 | 160 | - Energy density<br>- Long cycle life | - Intergranular cracking |
| NCA | 3.7 | 180 | - Relatively higher capacity than NCM<br>- Long cycle life | - Moisture and $CO_2$ sensitivity |
| LMO | 4.0 | 120 | - Thermal stability<br>- Power density<br>- Low cost | - Low energy density<br>- Severe capacity fade |
| LFP | 3.4 | 160 | - Excellent thermal stability<br>- Power density<br>- Excellent long cycle life<br>- Low cost | - Low energy density |

NCM was developed by substituting cobalt with nickel and manganese, aiming to lower costs, increase energy density, and enhance thermal stability compared to LCO.[14-16] To obtain different electrochemical properties, the ratio of TM has been adjusted such as $LiNi_{0.33}Mn_{0.33}Co_{0.33}O_2$ (denoted as NCM111) for enhanced stability and $LiNi_{0.8}Mn_{0.1}Co_{0.1}O_2$ (denoted as NCM811) for higher capacity respectively. Nickel contributes to the capacity through dual redox reactions involving both $Ni^{2+}/Ni^{3+}$ and $Ni^{3+}/Ni^{4+}$ couples.[17] Cobalt not only prevents the occurrence of anti-site defects between TM layer and lithium layer but also provides additional capacity through $Co^{3+}/Co^{4+}$ redox reactions.[15, 18] Also, manganese enhances crystal stability by maintaining its oxidation state as $Mn^{4+}$, particularly under

higher oxidation potentials during the delithiation process.[19, 20] Currently, high-nickel NCM has been pursued for its higher energy density. However, high-nickel content above 80 % is intimately associated with poor thermal stability and capacity degradation due to intragranular cracking and TM dissolution.[21, 22]

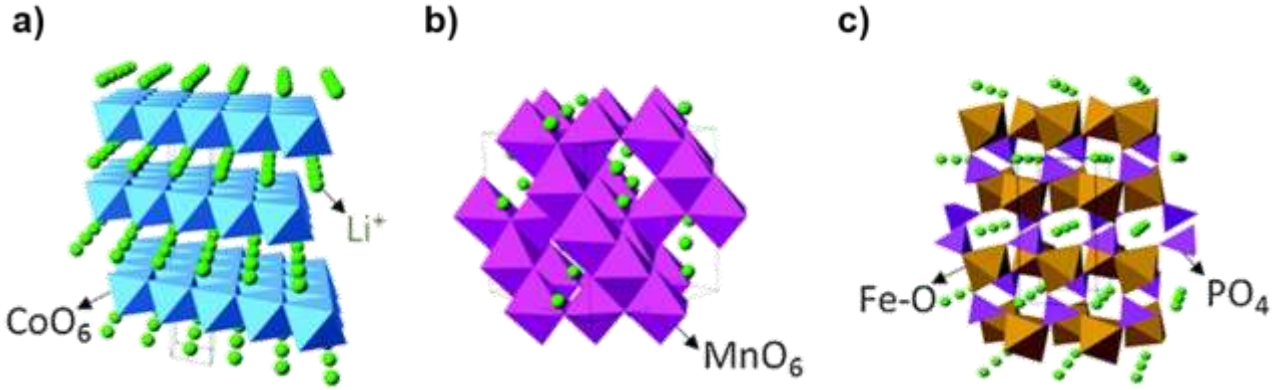


**Figure 2.5.** Crystal structures of representative intercalation cathode compounds with various dimensions of Li-ion diffusion pathways: (a) 2-D: layered ($LiCoO_2$), (b) 3-D: spinel ($LiMn_2O_4$), and (c) 1-D: olivine ($LiFePO_4$).[13]

NCA, another option within the same layered oxide category, substitutes aluminum for manganese to achieve higher energy density compared to NCM.[23] It has mostly been manufactured by Panasonic for its cooperative partner, Tesla, and by Samsung for applications such as EVs and cordless vacuum cleaners.[24] Yet, the surface of NCA particles is sensitive to moisture and $CO_2$, resulting in the formation of insulating layers containing LiOH and $Li_2CO_3$.[25] This sensitivity is particularly critical in long-term applications. Therefore, additional coating strategies are necessary to mitigate these issues effectively.

Unlike the layered oxides, LMO adopts a three-dimensional (3-D) spinel structure (Figure 2.5b) that facilitates Li-ion intercalation, resulting in higher power density.[26] In addition, the cost is reduced by replacing entire cobalt with relatively less expensive manganese. Furthermore, its inherently reliable thermal stability enhances safety during usage.[27] However, the application of LMO has been restricted because of Jahn–Teller distortion and manganese dissolution, resulting in structure degradation and short cycle life.[27, 28] Furthermore, the dissolved manganese can migrate and deposit on the other components in LIBs, inducing TM-related capacity loss.[29]

Apart from the oxide materials, LFP has been the most successful cathode so far due to its high safety, low cost, excellent cyclability, and high power capability.[30-33] The robust host framework of olivine crystal structure guarantees excellent thermal stability and enhanced cycling stability. However, it is widely recognized that LFP exhibits inherently poor ionic and electronic conductivity due to its 1-D Li-ion diffusion pathway (Figure 2.5c) and electronic structure.[34, 35] Despite intensive research and optimization on LFP cathodes via nanosizing and conductive carbon coating strategies, modified LFP still exhibits low energy density attributed to relatively low operating voltage (3.4 V vs $Li/Li^+$) and low tap density resulting from nano particle sizes.[36-38] This negative aspect limits its practical application to stationary storage, as higher energy density is demanded in EVs.

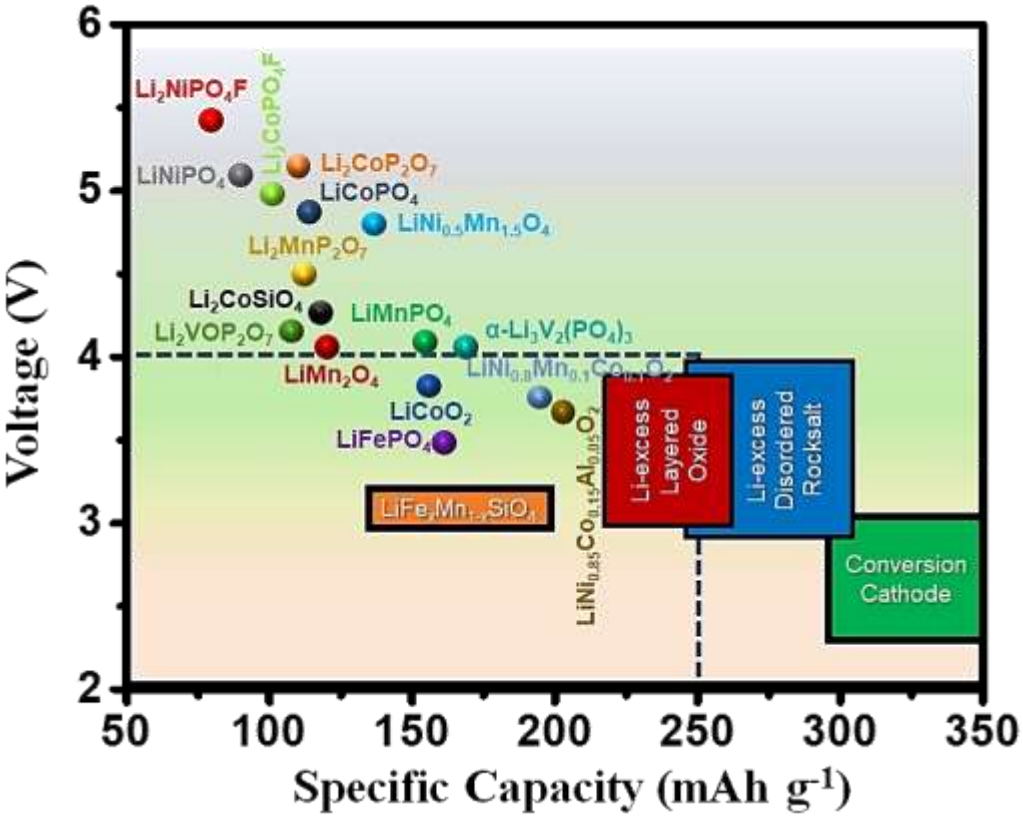


**Figure 2.6.** Distribution of cathode materials based on operating voltage and specific capacity. Dotted square is the guide line indicating 4 V vs. $Li/Li^+$ - 250 mAh $g^{-1}$ range.[39]

Therefore, there is a huge interest in research on next-generation cathode materials that offer higher energy density. Based on the equation (2.6), there are two options to enhance the energy density: either pushing capacity or uplifting voltage. Figure 2.6 illustrates the cathode materials positioning with different operating voltage and specific capacity.[39] Until now, cathode materials positioned within the dashed line representing 4 V - 250 mAh $g^{-1}$ have been developed and commercialized. However, ongoing research is focused on next-generation cathode materials to beyond the current

energy levels. While significant research has been dedicated to increasing capacity, such as Li-excess layered oxides and Li-excess disordered Rocksalt, studies on high-V cathodes are still missing.

In this regard, LCP has attracted attention due to its relatively higher potential to enhance the energy density while maintaining the robust crystal structure with LFP. However, fundamental studies on LCP itself are currently insufficient, necessitating deeper exploration before additional treatments such as surface coating and/or cation substitution are pursued. Thus, novel synthesis approaches focusing on precise crystal growth control and defect engineering aiming to achieve theoretical capacity values will be useful. Also, understanding capacity fade mechanisms during long-term cycling is crucial to enhance battery durability. Thus, while LCP shows promise, further research is essential to optimize its performance and address challenges in practical applications.

### 2.2. Lithium cobalt phosphate ($LiCoPO_4$, LCP)

The polyanion olivine-structured $LiMPO_4$ (M = Fe, Mn, Ni and Co) family discovered by Goodenough et al. in 1997 is particularly attractive because of the strong P–O bonds that make the olivine structure, a robust host for Li-ion storage, offering excellent thermal safety and good theoretical capacity of 167 mAh $g^{-1}$.[40] At first, LFP with a redox potential of 3.5 V vs. $Li/Li^+$ has been recognized as the safest commercial cathode material that is equally environmentally benign and can be produced at relatively low cost.[41, 42] However, this attention has been moved recently to another member in this family, LCP because it could provide higher energy density with its high redox voltage plateau up to 4.8 V vs. $Li/Li^+$ as opposed to 3.5 V vs. $Li/Li^+$ for the conventional LFP-liquid electrolyte syste. Thus, the energy density of LCP cathode could theoretically increase from 590 Wh $kg^{-1}$ to 800 Wh $kg^{-1}$.[43, 44] These characteristics make LCP an attractive candidate as one of cathode materials for advanced LIBs. In terms of energy cost, LCP can be more economical compared to other commercialized cathodes, aided by its enhanced energy density, despite the price of cobalt being more expensive than other transition metals such as iron, manganese, and nickel. In detail, when LCP applies in cylindrical batteries (18650 size cells), the estimated cost of LCP is to be 142 \$ $kW^{-1}$ $h^{-1}$ which is the lowest among the currently commercialized cathodes (shown in Figure 2.7).[45, 46] But leaving aside the cost issue, LCP is of interest as high-V cathode for niche applications where high energy density is essential.

U.S. Army Research Laboratory (ARL) and Hydro-Québec have collaborated on research involving LCP, resulting in significant advancements in battery technology. A key achievement is the

creation of a high energy density, 5.0 V Li-ion cell. Their joint efforts are evidenced by co-authored research publications and multiple patents, showcasing considerable progress in improving battery materials for diverse applications.[46-48] This partnership has established LCP as a crucial cathode material for aerospace and military applications, owing to its distinctive advantages. In aerospace, the high energy density of LCP, resulting from its operating voltage, enables satellites and space probes to operate for extended periods with more compact and lightweight batteries. This characteristic reduces mission costs and enhances feasibility. The chemical stability of this phosphate-based cathode material also ensures dependable performance under the extreme temperature fluctuations and radiation encountered in space environments.

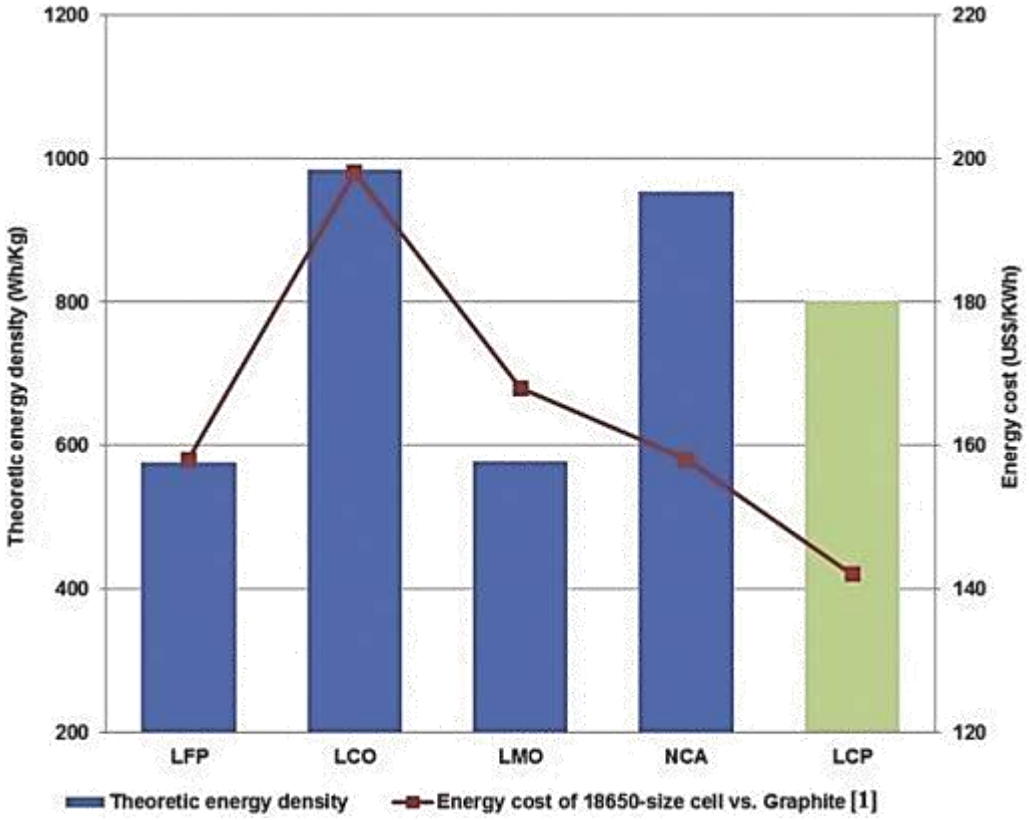


**Figure 2.7.** Theoretical energy density and energy cost comparison of cathode materials.[46]

### 2.2.1. Crystal structure and features of LCP

The LCP belongs to the olivine orthorhombic crystal system. As illustrated in the schematic diagram of LCP (Figure 2.8), $PO_4$ tetrahedra (Cyan colored) establish a 3-D framework where all cations including Co and Li occupy octahedral sites. More specifically, the crystal structure comprises two types of polyhedral, the $CoO_6$ octahedra (Purple colored) and $PO_4$ tetrahedra. The zigzag chains with $CoO_6$ octahedra run in parallel to the crystallographic *c*-axis.[49] These chains are linked by the

$PO_4$ tetrahedra, resulting in a three-dimensional structure. This robust polyanion framework provides excellent thermal and structural stability during Li-ion (de)intercalation. In this structure, Li-ions can theoretically move one-dimensionally along either [010] or [001]. But the [010] pathway is preferred because of the lower activation energy.[50-52] These 1-D diffusion pathways make the dynamics of Li-ion diffusion extremely sensitive to defects that would impede Li-ion diffusion. Furthermore, it is essential to consider the interference caused by the cathode-electrolyte interphase (CEI) layer, which evolves due to the high operating voltage of LCP required for Li-ion intercalation.[53]

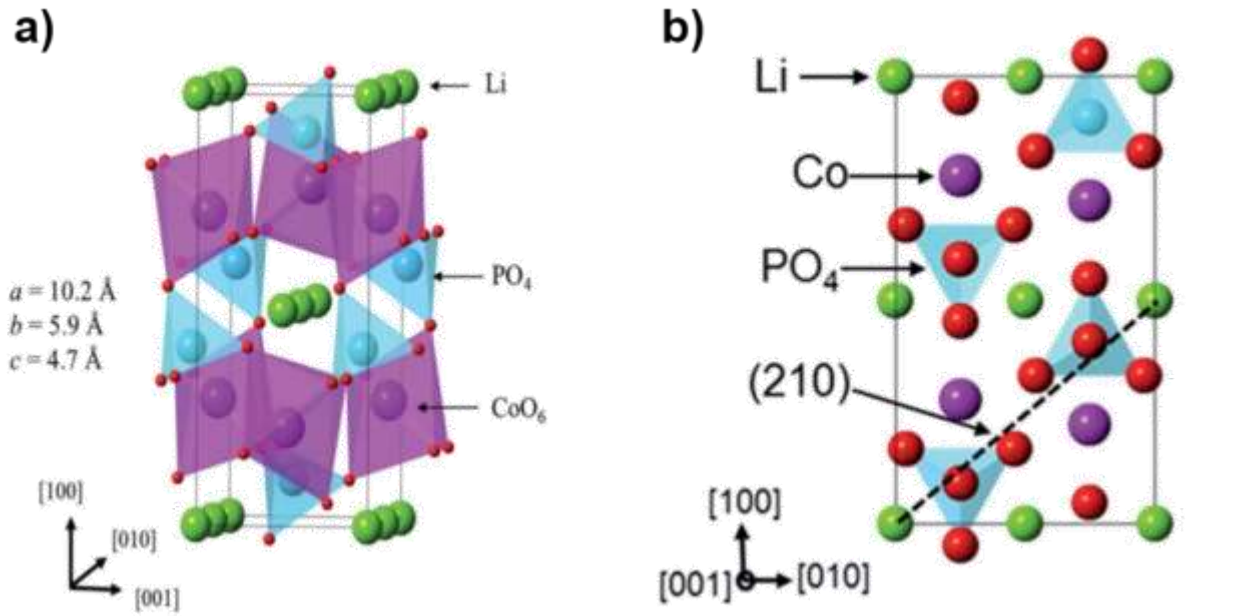


**Figure 2.8.** Illustration of (a) unit cell of *pnma*-LCP showing Li-ions in 1-D channels along [010] and (b) unit cell viewed down [001] showing the orientation of the (210) plane (dashed line) related to the Li positions.[49]

Until now, three different polymorphs of LCP have been reported (*pnma, pna2$_1$, and cmcm*). However, only *pnma* adopts the olivine structure and two other candidates (*pna2$_1$* and *cmcm*) have different structure type ($\delta_1$-$LiZnPO_4$ and $Na_2CrO_4$).[54] In addition, Kreder et al. studied the synthesis and characterization of these three polymorphs of LCP.[55] These polymorphs show different redox peaks, specifically at 4.8 and 4.9 V (*pnma*), 4.95 V (*pna2$_1$*), and 4.3 V (*cmcm*) as shown in Figure 2.9a. Additionally, LCP with *pnma* had the biggest discharge capacity, 67 mAh $g^{-1}$ compared to the other polymorphs, *pna2$_1$* and *cmcm* showing 33 and 6 mAh $g^{-1}$ which is corresponding to 40 %, 20 % and 4 % of the theoretical capacity respectively (Figure 2.9b). Even with the highest discharge capacity value, 67 mAh/g, it is still very low compared to theoretical capacity. Nevertheless, this data indicates that we should aim to obtain the *pnma* structure during LCP synthesis, which uniquely possesses the olivine structure among the three different polymorphs.

The electrochemical intercalation of LCP with the *pnma* space group goes through the intermediate phase, $Li_{2/3}Co^{2+}{}_{2/3}Co^{3+}{}_{1/3}PO_4$ as evident by two distinct oxidation-reduction peaks in CV curves and flat plateaus in charge-discharge curve. The existence of the intermediate phase has been confirmed by first-principles density functional theory (DFT) calculations and various characterizations.[56-58] This implies that one-third of Li-ions are initially extracted from pristine LCP, followed by the extraction of remaining Li-ions from the intermediate phase. This occurs at 4.8 and 4.9 V vs. $Li/Li^+$ upon charge and 4.7 and 4.8 V vs. $Li/Li^+$ upon discharge. The whole Li-ion intercalation process of LCP can be described by the equation 2.9 and 2.10 below.

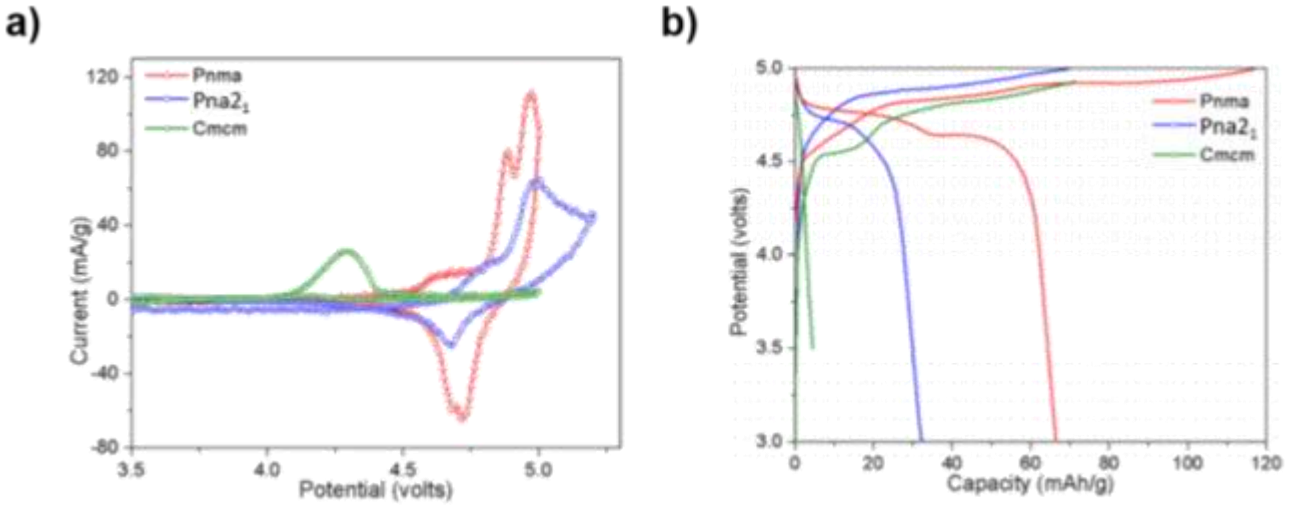


**Figure 2.9.** Electrochemical performance of three different LCP polymorphs, *pnma* (red colored), *pna2₁* (blue colored), and *cmcm* (green colored). (a) Cyclic voltammetry (CV) at slow scan rate of 0.05 mV/s and (b) initial charge-discharge curves at C/10.[55]

$$LiCoPO_4 \leftrightarrow Li_{2/3}Co^{2+}_{2/3}Co^{3+}_{1/3}PO_2 + \frac{1}{3}Li^+ + \frac{1}{3}e^- \quad (2.9)$$

$$Li_{2/3}Co^{2+}_{2/3}Co^{3+}_{1/3}PO_2 \leftrightarrow CoPO_4 + \frac{2}{3}Li^+ + \frac{2}{3}e^- \quad (2.10)$$

Another notable feature of LCP is the electrolyte decomposition that occurs due to high-V operation necessary for Li-ion intercalation. The conventional liquid electrolyte, which contains $LiPF_6$ in EC/DMC solvents, is prone to decomposition above 4.5 V vs. $Li/Li^+$. This decomposition contributes to the progressive capacity loss in LCP during repeated charge-discharge cycles.[59] Markevich et al. also reported that the nucleophilic attack of HF on the strong P-O bonding in LCP results from electrolyte decomposition.[60] Additionally, experimental studies and theoretical calculations have revealed that the delithiated phase, $CoPO_4$, exhibits energetic instability.[61-65] This instability is attributed to the presence of $Co^{3+}$ in a high-spin state within the octahedral coordination environment of $CoPO_4$. To date, various approaches have been employed to mitigates collateral issues

associated with the high-V operation of LCP as is the electrolyte and separator stabilities. These approaches have included the incorporation of electrolyte additives, and optimization of separator properties.[66, 67] The aforementioned strategies, however, lie beyond the scope of cathode material science and will not be elaborated in this review.

### 2.2.2. Synthesis of LCP

Various synthesis methods have been applied to produce LCP, each with advantages and limitations. The major routes include (1) solid-state reaction, which is suitable for large-scale production but lacks particle control; (2) sol-gel process, which yields uniform nano-sized particles but may raise environmental concerns due to the use organics; and (3) hydrothermal/solvothermal methods, which offer good control over particle homogeneity. Careful selection and optimization of these methods are necessary based on desired LCP properties such as particle size, morphology, purity, and scalability. The following paragraphs offers a comprehensive overview of these synthesis techniques.

Solid-state reaction, which is simple to operate and scalable finding industrial application, is the most conventional way to synthesize LCP. Typically, precursor chemicals containing Li, Co, $PO_4$ are firstly ground or milled thoroughly for better elemental intermixing then heated to 300-400 °C to evaporate crystalline water and expel decomposed gases like $CO_2$. After that, the mixture is ground again and annealed at elevated temperatures of 600-900 °C for 8-36 h. However, solid-state reactions possess drawbacks like unregulated particle growth and agglomeration due to repetitive grinding and calcination promoting diffusion and sintering. Another problem is the formation of unwanted impurities like $Co_3(PO_4)_2$, $Li_3PO_4$, $Co_2O_3$, $Co_3O_4$, and $Li_2O$ due to poor mixing.[68, 69] Solid-state synthesis can be combined relatively easily with carbon coating to boost electron conductivity but not amenable to advanced crystallization controls via the use of growth regulating inhibitors.[70, 71]

Sol-gel process is a popular–limited mostly to laboratory scale research–low-temperature wet-chemical method that has been used to synthesize LCP, as it is capable of providing high purity, good homogeneity, and small particle size due to the uniform mixing of reactants at the atomic or molecular level in solution.[72, 73] In this methodology, precursor chemicals containing Li, Co, $PO_4$ are dissolved in solvents and blended thoroughly to create a homogeneous sol. The sol is then dried to form a gel-like network. After drying, the gel is ground into a powder and undergoes calcination at high temperature, similar to the solid-state reactions. Despite its particle size control advantages, the sol-

gel method encounters challenges in scaling up for mass production. These challenges include its procedure complexity, extended processing times, and reliance on hazardous chemical substances, which can hinder its practical application on an industrial scale.

Hydrothermal/solvothermal methods offer a distinct advantage over solid-state reaction and sol-gel process in crystallizing LCP.[74] While the latter require high-temperature calcination, hydrothermal/solvothermal synthesis can produce highly crystalline LCP at comparatively lower temperatures, typically ranging from 150-250 °C. This process employs pressure reactors capable of sustaining both elevated temperatures and pressures, operating above the solvent's boiling point. The term 'Hydrothermal' is applied when water serves as the solvent, whereas 'Solvothermal' denotes the use of organic solvents in the reaction. Another significant advantage of this synthesis is its capability to produce nanoparticles with precisely controlled stoichiometry, high purity, tailored morphologies, and uniform size distributions. The desired outcome is accomplished through the manipulation of the nucleation-growth process, which is achieved by adjusting various synthesis parameters. These include managing supersaturation via chemical concentration control, regulating reaction temperature and duration, modifying agitation speed, and incorporating specific additives. Subsequent heat treatment, however, is required to either apply a carbon coating or reduce anti-site defects, addressing the sluggish ionic and electronic conductivity of LCP.

In addition to the aforementioned techniques for obtaining LCP, other alternative preparation methods have also been applied. These include spray pyrolysis[75-78], co-precipitation[79-81], polyol process[82, 83], supercritical fluid techniques[84-87], microwave-assisted synthesis[88-91], and carbo-thermal reduction approaches[92, 93]. Despite the application of various synthesis methodologies, the electrochemical performance of pristine LCP remains unsatisfactory for practical applications. Existing synthesis techniques alone cannot fully address the inherent limitations of LCP. Consequently, most research efforts have shifted towards applying strategies to enhance the electrochemical performance of LCP.

### 2.2.3. Strategies to enhance LCP performance

Olivine LCP cathodes exhibit several operating drawbacks in LIBs, including low attainable specific capacity, poor cycle stability, and inferior rate performance. These limitations originate from the intrinsic properties of olivine materials, such as their inadequate ionic and electronic conductivity but also their crystal structure and redox chemistry of the $Co^{3+}/Co^{2+}$ couple. Thanks to the experience

gained from the development and commercialization of LFP, the sluggish kinetics of LCP have been improved to some extent. This enhancement has been achieved through (1) surface coating with highly conductive carbon-based materials to improve electronic conductivity or inorganic layer to mitigate irreversible interfacial reactions with liquid electrolytes, (2) cation substitution to create vacancies for greater ionic diffusion, and (3) size reduction and morphology control to reduce Li-ion diffusion pathway.

#### 2.2.3.1. Surface coating

Surface coating with conductive carbon-based materials ensures enhanced electronic conductivity. Thermal treatment is commonly applied to decompose and carbonize carbon sources. This heat treatment concurrently improves the crystallinity through the reduction of anti-site defects. Proper application of carbon coating prevents particle aggregation and restricts crystal growth during calcination.[94-96] Furthermore, the carbon layer serves as a protective layer shielding LCP from direct exposure with electrolytes. This protection mitigates irreversible surface degradation caused by HF, a by-product of electrolyte decomposition.[83, 96, 97] However, it is imperative that the coating be thin, uniform, and intact to facilitate the effective Li-ion intercalation across the electrode-electrolyte interface by minimizing the activation energy required for Li-ion transport.[98, 99] Thus, selecting the right carbon source can have an impact on the quality of the carbon layer. Table 2.2 provides a comprehensive overview of various coating materials and their corresponding impacts on electrochemical performance.

For improved cycling stability, non-carbon materials such as LFP[100-102], NiO[103], $AlF_3$[104], $VO_x$[97], $Li_3V_2(PO_4)_3$[93, 105], and $Al_2O_3$[106] have been also reported so far. Örnek et al. reported the development of LCP with a nanoscale NiO surface coating, fabricated through a three-step process.[103] This approach combines the advantageous aspects of Stöber method, hydrothermal, and microwave synthesis techniques. The resulting LCP particles are encapsulated by a uniform NiO layer measuring 8–10 nm in thickness. This protective coating serves to mitigate the volumetric stresses and strains typically associated with Li-ion intercalation. It should be noted, however, that the preparation of these non-carbon materials necessitates multiple synthesis techniques, including a combination of dry coating, sol-gel process, microwave heating, etching, and calcination step.

**Table 2.2.** Surface coating strategies applied on LCP.[107]

| Synthesis method* | Carbon source | Initial discharge capacity (mAh $g^{-1}$, C-rate) | Capacity retention | Ref. |
|---|---|---|---|---|
| Solid-state fusion method | Super P | 123, C/10 | 109 mA h $g^{-1}$ at C/10 after 30 cycles | 108 |
| SS and BM | Sucrose, graphene oxide | 146, C/10 | 92 mA h $g^{-1}$ at C/10 after 40 cycles | 109 |
| MH | Acetylene black | 144, C/10 | 73 mA h $g^{-1}$ at C/10 after 30 cycles | 88 |
| Sol–gel process | Citric acid | 137, C/10 | 93 mA h $g^{-1}$ at C/10 after 30 cycles | 110 |
| Sol–gel process | Citric acid, acetylene black | 131, C/10 | 102 mA h $g^{-1}$ at C/10 after 40 cycles | 111 |
| Sol–gel process | Citric acid | 92, C/20 | 78 mA h $g^{-1}$ at C/10 after 35 cycles | 112 |
| HT | CMC, glucose, ascorbic acid | 135, C/10 | 70 mA h $g^{-1}$ at C/10 after 30 cycles | 94 |
| MWHT | Alginic acid | 160, C/5 | 95 mA h $g^{-1}$ at C/5 after 30 cycles | 113 |
| ST | Glucose | 136, C/10 | 124 mA h $g^{-1}$ at C/10 after 50 cycles | 114 |
| ST | Glucose, Mn doping | 105, C/5 | 95 mA h $g^{-1}$ at C/5 after 30 cycles | 115 |
| ST | Sucrose | 120, C/10 | 94 mA h $g^{-1}$ at C/10 after 20 cycles | 116 |
| ST | Sucrose | 124, C/10 | 103 mA h $g^{-1}$ at C/10 after 100 cycles | 95 |
| MWST | Tannic acid | 155, C/10 | 141 mA h $g^{-1}$ at C/10 after 80 cycles | 117 |
| ST | Sucrose, PVDF, and CTAB | 154.1, C/10 | 84.9 mA h $g^{-1}$ at 1 C after 1000 cycles | 118 |
| **Synthesis method** | **Non-carbon source** | **Initial discharge capacity (mAh $g^{-1}$, C-rate)** | **Capacity retention** | **Ref.** |
| SS | LFP coating | 132, C/10 | 92 mA h $g^{-1}$ at C/10 after 17 cycles | 101 |
| SS | LFP coating, Fe doping | 128, 0.1 mA $cm^{-2}$ | 90 mA h $g^{-1}$ at 0.1 mA $cm^{-2}$ after 17 cycles | 100 |
| MWST | LFP coating, V doping | 145, C/10 | 74 mA h $g^{-1}$ at C/10 after 20 cycles | 102 |
| MWHT | NiO coating | 159, C/10 | 135 mA h $g^{-1}$ at C/10 after 80 cycles | 103 |
| Sol–gel process | $AlF_3$ coating | 159, C/10 | 145 mA h $g^{-1}$ at C/10 after 50 cycles | 104 |

* BM: Ball-milling, CMC: carboxymethylcellulose sodium salt, HT: Hydrothermal, LFP: $LiFePO_4$, MH: Microwave heating, MWHT: Microwave hydrothermal, MWST: Microwave solvothermal, SS: Solid-state reaction, ST: Solvothermal.

### 2.2.3.2. Cation substitution

Another strategy to enhance the electrochemical performance of LCP is cation substitution, which involves the partial replacement of cobalt in the LCP crystal lattice with alternative cations. Firstly, it could enhance both ionic and electronic conductivity. The former is achieved through the creation of Li vacancies, while the latter results from reducing the energy barrier for polaron migration between adjacent TM sites.[116, 119] Additionally, this substitution can modify the coordination environment within the bulk structure and stabilize the delithiated LCP phase, $CoPO_4$.[120, 121] Consequently, cation substitution leads to improved overall electrochemical performance. Different elements have been investigated as dopants: (i) $Fe^{2+}$ [47, 120, 122-125], $Mn^{2+}$ [126, 127], $Mg^{2+}$ [128, 129], $Ca^{2+}$ [128, 130], $Cu^{2+}$ [131] that are isovalent and possess similar ionic radii with $Co^{2+}$ and (ii) $Fe^{3+}$ [24], $Si^{4+}$ [47], $Cr^{3+}$ [47, 131], $V^{3+}$ [132, 133], $Y^{3+}$ [134] that are aliovalent elements and have different ionic radii with $Co^{2+}$.

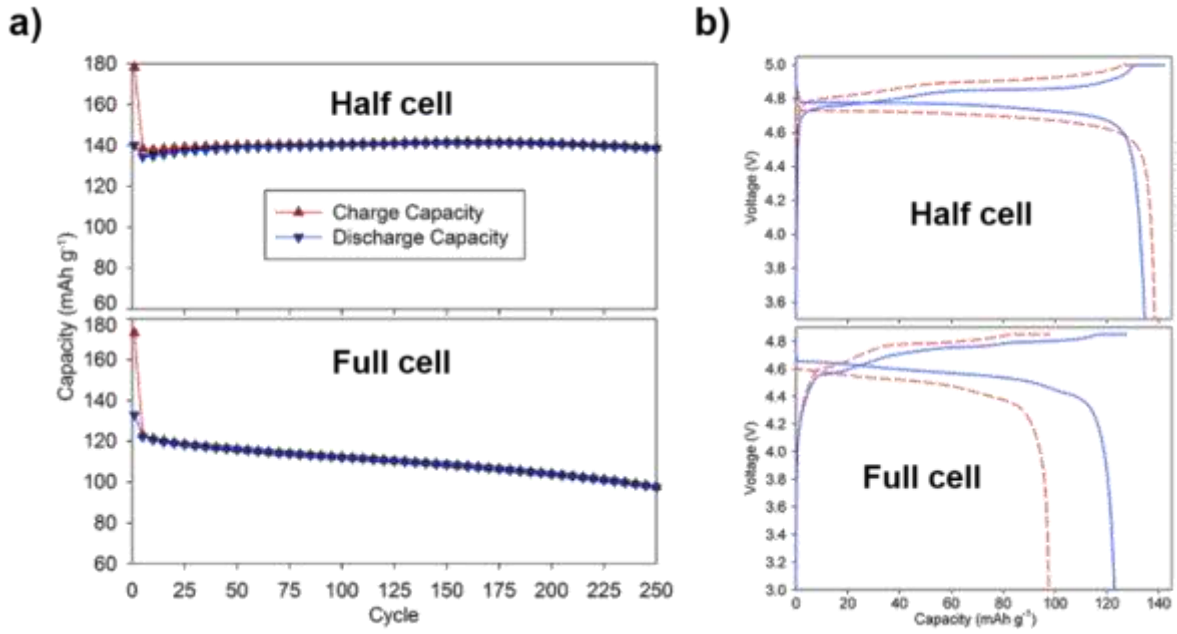


**Figure 2.10.** (a) Capacity retention and (b) charge-discharge curves of Cr, Si-$LiCo_{0.9}Fe_{0.1}PO_4$. Solid blue and dashed red lines indicate the 2nd and 250th cycle, respectively.[115]

Kang et al. utilized a combination of *ab initio* calculations and X-ray absorption spectroscopy to elucidate the effects of $Fe^{2+}$ substitution in LCP structure.[124] Their findings revealed that Fe substitution mitigates the anti-site mixing of Li and Co. This phenomenon is attributed to the higher stabilization energy of oxygen octahedra surrounding Fe, which preferentially occupy the cobalt sites. Optimizing the $Fe^{2+}$ doping content is crucial to achieving a balance between electrochemical performance and energy density, as it can enhance electrochemical performance but reduce the energy density of LCP. Besides, $Mn^{2+}$ doping has been observed to induce lattice distortion in LCP

structure.[135, 136] This distortion reduces the surface energy of LCP particles, consequently inhibiting crystal growth and resulting in smaller particle sizes.

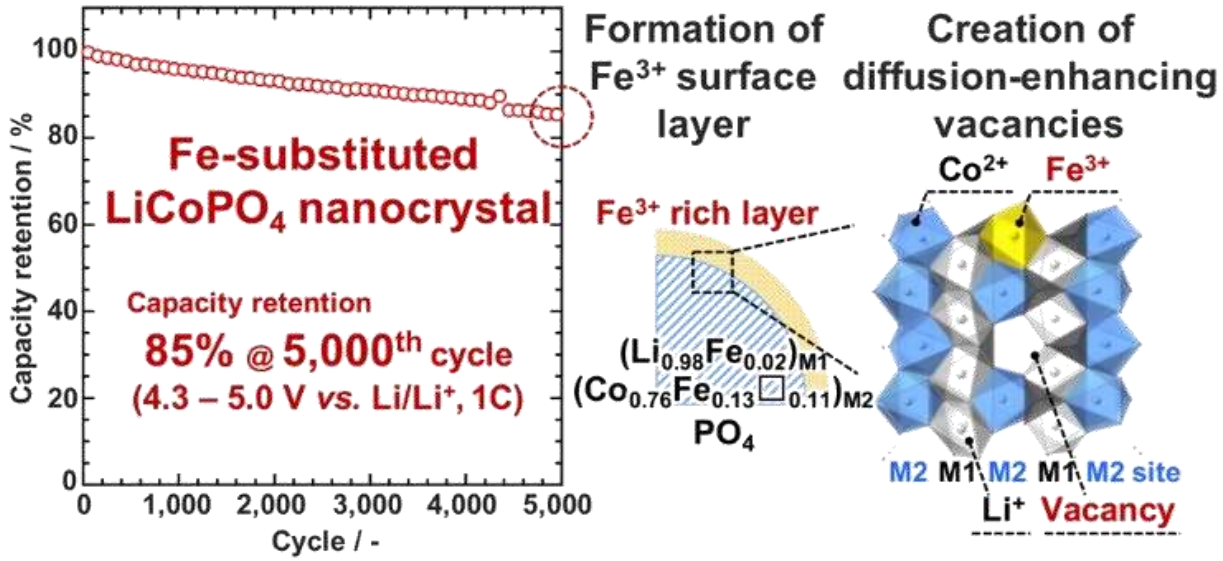


**Figure 2.11.** Capacity retention with the narrow cut-off voltage, 4.3-5.0 V vs. Li/Li$^+$ and the schematic diagrams demonstrating the surface and structural model of Fe-substituted $LiCoPO_4$/MWCNT composite.[137]

Aliovalent cation doping in cobalt site has been established as an effective way to improve both cycling stability and rate capability of LCP. The substitution process involves dopants with different oxidation state than that of the host cations. Such substitution is associated with the generation of vacancies within the crystal lattice to preserve charge neutrality, consequently improving rate capability and cycling stability.[47, 132, 137, 138] Allen et al. elucidated that $Fe^{3+}$ can stabilize LCP structure, when occupying both Li and Co sites.[59] In a follow-up study, their research group examined Fe, Cr, and Si co-substituted LCP, as depicted in Figure 2.10.[47] Their findings revealed that $Cr^{3+}$ further augmented energy density, cycling stability and rate capability. Additionally, $Si^{4+}$ was found to mitigate the reactivity with electrolyte, leading to extended cycling stability. Naoi et al. prepared the composite material with $LiCo_{0.8}Fe_{0.2}PO_4$ and multiwalled carbon nanotube (MWCNT).[137] In this composite, $Fe^{3+}$-rich phase layer on LCP surface was successfully formed. The oxidation of $Fe^{2+}$ to $Fe^{3+}$ facilitated the migration of Fe ions towards the surface, driven by the increased repulsive forces between $Fe^{3+}$ and $Co^{2+}$. This $Fe^{3+}$-rich phase layer stabilized the delithiated phase, preventing both the crystal structure deterioration and progressive SEI evolution. As long as the electrochemical reduction of $Fe^{3+}$ is avoided, this surface protection can persist. As shown in Figure 2.11, this electrode retained 85 % of the initial capacity in the narrow voltage range of 4.3-5.0 V vs. Li/Li$^+$ after 5000 cycles.

Applying cation substitution has been demonstrated to improve structural features, effectively suppressing anti-site defect formation upon cycling tests and upgrade the overall kinetics. While some LCP doping advances were experimentally verified, challenges still persist. Notably, charge compensation with increasing dopant concentration and narrow cut-off voltage (4.3-5.0 V vs $Li/Li^+$) leads to a reduction in capacity from the theoretical capacity value. Moreover, the body of research addressing the fundamental aspects of LCP prior to cation tailoring is markedly insufficient. Thus, the necessity for more intensive research on the material itself is emphasized to gain a complete understanding and maximize the utilization of LCP in high-energy density LIBs.

**Table 2.3.** Cation substitution strategies applied on LCP.

| **Material* (Synthesis method)*** | **Voltage range (V vs. $Li/Li^+$)** | **Initial discharge capacity (mAh $g^{-1}$, C-rate)** | **Capacity retention** | **Ref.** |
|---|---|---|---|---|
| $LiCo_{0.88}V_{0.08}\square_{0.04}PO_4$ (MWST) | 3-5 | 97, C/10 | 82 mA h $g^{-1}$ at C/10 after 20 cycles | 132 |
| C-$Li_{0.92}Co_{0.8}Fe^{2+}_{0.2}Fe^{3+}_{0.08}PO_4$ (MH) | 2.5-5.3 | 100, C/10 | 97 mA h $g^{-1}$ at C/10 after 500 cycles | 59 |
| C-$LiCo_{0.82}Fe_{0.0976}Cr_{0.0488}Si_{0.00976}PO_4$ (BM and annealing) | 3.5-5 | 140, C/3 | 140 mA h $g^{-1}$ at C/3 after 30 cycles | 46, 47 |
| C-$LiCo_{0.94}Cr_{0.04}PO_4$ (Sol-gel and annealing) | 3-5.3 | 144, C/10 | 102 mA h $g^{-1}$ at C/10 after 100 cycles | 138 |
| $LiCo_{0.8}Fe_{0.2}PO_4$ (HT and annealing) | 2.5-4.95 | 147, C/10 | 138 mA h $g^{-1}$ at C/10 after 300 cycles | 139 |
| $LiCo_{0.5}Fe_{0.5}PO_4$ (BM and annealing) | 3-5 | 120, C/10 | 100 mA h $g^{-1}$ at C/10 after 15 cycles | 92 |
| C-$Li_{1.025}Co_{0.95}V_{0.05}PO_4$ (SS) | 3.2-5.1 | 134, C/10 | 114 mA h $g^{-1}$ at C/10 after 25 cycles | 133 |
| $LiCo_{0.985}Y_{0.01}PO_4$ (Sol-gel) | 3-5.1 | 153.4, C/10 | 32 mA h $g^{-1}$ at C/10 after 30 cycles | 134 |
| $LiCo_{0.5}Mn_{0.5}PO_4$ (HT) | 3-5 | 126, C/20 | 110 mA h $g^{-1}$ at C/20 after 30 cycles | 140 |
| C-$LiCo_{0.95}Mn_{0.05}PO_4$ (Sol-gel and annealing) | 2.8-5.2 | 140, C/10 | 136 mA h $g^{-1}$ at C/10 after 60 cycles | 135 |
| $LiCo_{0.9}Ca_{0.1}PO_4$ (Sol-gel and annealing) | 3.5-5.3 | 68, C/10 | 15 mA h $g^{-1}$ at C/10 after 20 cycles | 141 |
| $LiCo_{0.9}Fe_{0.1}PO_4$ (ST and annealing) | 3.5-5 | 103, C/10 | X | 120 |

| | | | | |
|---|---|---|---|---|
| $LiCo_{0.975}Mg_{0.025}PO_4$ (Sol-gel and annealing) | 3.5-5.3 | 88, C/10 | 15 mA h $g^{-1}$ at C/10 after 20 cycles | 129 |
| $LiCo_{0.9}Ca_{0.1}PO_4$ (Sol-gel and annealing) | 3.5-5.3 | 104, C/10 | 15 mA h $g^{-1}$ at C/10 after 10 cycles | 142 |
| C-$LiCo_{0.5}Fe_{0.5}PO_4$ (MWST) | 2.5-5 | 94, C/2 | 82 mA h $g^{-1}$ at C/2 after 50 cycles | 143 |
| $Li_{0.98}Fe_{0.02}Co_{0.785}Fe_{0.13}\square_{0.085}PO_4$ with MWCNT (Sol-gel and annealing) | 4.3-5 | 130, C/5 | 128 mA h $g^{-1}$ at C/5 after 1000 cycles | 137 |
| $LiCo_{0.95}Fe_{0.05}PO_4$ (BM and microwave heating) | 3.5-5.2 | 120, C/5 | X | 124 |
| C-$LiCo_{0.95}Mn_{0.05}PO_4$ (SP, BM and annealing) | 2.5-5 | 132, C/20 | 87 mA h $g^{-1}$ at C/20 after 100 cycles | 77 |
| $LiCo_{0.97}V_{0.02}\square_{0.01}PO_4$ (MWST and annealing) | 3-5 | 145, C/10 | 74 mA h $g^{-1}$ at C/10 after 20 cycles | 102 |
| $LiCo_{0.95}Zn_{0.05}PO_4$ (Sol-gel and annealing) | 3-5 | 128.6, 1 C | 85.6 mA h $g^{-1}$ at 1 C after 200 cycles | 144 |
| C-$LiCo_{0.5}Mn_{0.5}PO_4$ (SF and HT) | 2.8-5.2 | 156.5, C/10 | 153 mA h $g^{-1}$ at C/10 after 100 cycles | 145 |
| $LiCo_{0.85}Fe_{0.1}Zn_{0.05}PO_4$ (Wet chemical synthesis and annealing) | 3-5.1 | 118, 1 C | 79 mA h $g^{-1}$ at 1 C after 300 cycles | 146 |

* BM: Ball-milling, C: Carbon, HT: Hydrothermal, MH: Microwave heating, MWST: Microwave solvothermal, SP: Spray pyrolysis, SS: Solid-state reaction, SF: Supercritical fluid, ST: Solvothermal

**2.2.3.3. Size reduction and morphology control**

Apart from the strategies discussed in the previous section, tailoring the size and morphology of the final product has attracted significant attention due to its ability to shorten the Li-ion diffusion pathway along the [010] direction, leading to enhanced discharge capacity and improved rate capability. For LCP nanosizing, several synthesis techniques and post-synthesis treatments such as pulverization (high-energy ball-milling) process have been employed so far.[76, 147] Taniguchi et al. fabricated LCP/C nanocomposite via a combined approach of spray pyrolysis and wet ball-lling. Their material exhibited agglomeration of LCP primary particles with an average size of approximately 87 nm. The initial discharge capacities were 142 and 109 mAh $g^{-1}$ at C/20 and 20 C, respectively. Nanosizing can enhance the initial charge-discharge capacity, but it also brings several drawbacks. This strategy increases the electrode-electrolyte interface area. The heightened interface promotes

detrimental side reactions with electrolyte, particularly in high-V cathode materials like LCP. These undesired reactions accelerate electrolyte decomposition, negatively affecting long-term battery cycling. Therefore, optimizing synthesis conditions to achieve micron-sized LCP particles with high volumetric energy density and cycling stability is crucial to meet the growing demand of higher volumetric energy density for various large-scale applications.

Crystallographic orientation control has emerged as a promising strategy to address the aforementioned challenges associated with the conventional nanosizing. This strategy can prioritize optimizing the length of Li-ion diffusion pathway while maintaining the particle size micron-scale, rather than reducing overall particle size. Solvothermal synthesis is widely recognized as the most effective method for achieving this goal due to its precise control over particle size and morphology. Recent investigations have revealed the crucial role of solvent selection in modulating particle dimensions. Notably, high-viscosity organic solvents such as ethylene glycol (EG), have demonstrated effectiveness in regulating the crystalline growth of LCP. As shown in Figure 2.12, Wu et al. reported the significance of EG-to-water ratio as a key parameter for controlling LCP particle size in solvothermal synthesis.[95]

The sample (R = 4, 80 vol.% of EG) exhibits 123.8 mAh $g^{-1}$ as initial discharge capacity, and 83 % capacity retention after 100 cycles at C/10. Likewise, Nilges et al. adopted a microwave solvothermal method for LCP synthesis with the 1:1 (v/v) mixture of water and EG.[148] The final product consists of single-crystal LCP with a unique hexagonal platelet morphology. This platelet measured roughly 700-800 nm in length, 400-600 nm in width, and only 100-220 nm in thickness. Interestingly, the thinnest dimension of these hexagonal platelets aligns perfectly with the [010] direction. This alignment coincides with the preferred pathway for Li-ion diffusion within the LCP crystal structure, potentially explaining the observed improvement in electrochemical performance. The synthesized platelet exhibits an initial discharge capacity of 137 mAh $g^{-1}$ at C/10 and retains 68 % of its capacity after 100 cycles at C/2.

Subsequent investigations by Nilges et al. explored the effects of various organic solvents as alternatives to EG in binary solvent systems.[149] This extended study aimed to elucidate the impact of these alternative solvents on modulating the morphological characteristics of LCP particles. The data presented in Figure 2.13 clearly elucidates the substantial impact of the binary solvents with water and various organic solvents on the size and morphology of LCP. These systems consist of water in combination with various organic solvents, specifically: ethylene glycol (EG), diethylene glycol

(DEG), triethylene glycol (TEG), tetraethylene glycol (TTEG), polyethylene glycol 400 (PEG), and benzyl alcohol (BA). This dependence on the type of solvent leads to a wide variety of particle geometries, including square, rhombic, and hexagonal platelets. The samples obtained from TEG exhibited the smallest dimension along the [010] direction. This favorable orientation, resulting in anisotropic crystals with enhanced Li-ion diffusion, delivers the best published initial discharge capacity of 141 mAh $g^{-1}$ at C/10 with 96 % capacity retention after 15 cycles at C/2.

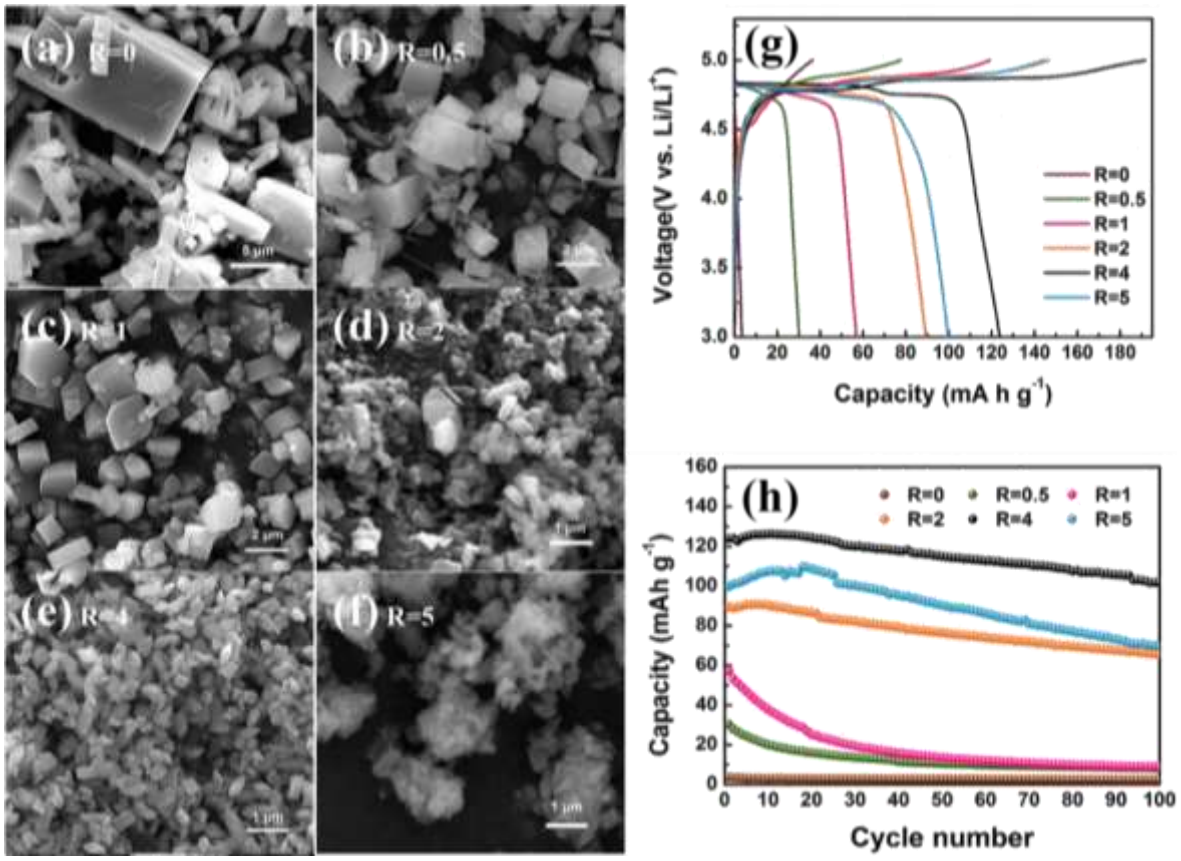


**Figure 2.12.** (a-f) SEM images of LCP samples with different volume ratios of EG to $H_2O$ denoted as R (R = 0, 0.5, 1, 2, 4, and 5); (g) initial charge-discharge curves and (h) capacity retention of the samples at C/10.[95]

In addition, the crystal growth orientation of LCP could be tailored by adding different additives. Eichel et al. utilized a combination of solvothermal techniques and subsequent air annealing to fabricate LCP materials exhibiting diverse morphologies including unstructured nanoparticles, nanorods, and microrods.[150] In Figure 2.14, the effect of additives including citric acid (CA), Polyvinylpyrrolidone (PVP), and Cetyltrimethylammonium bromide (CTAB) denoted as LCP-CA, LCP-PVP, and LCP-CTAB, on crystal morphology is shown. The pristine LCP without additives (Figure 2.14a-b) were well-dispersed nanospheres with an average size of 200 to 400 nm.

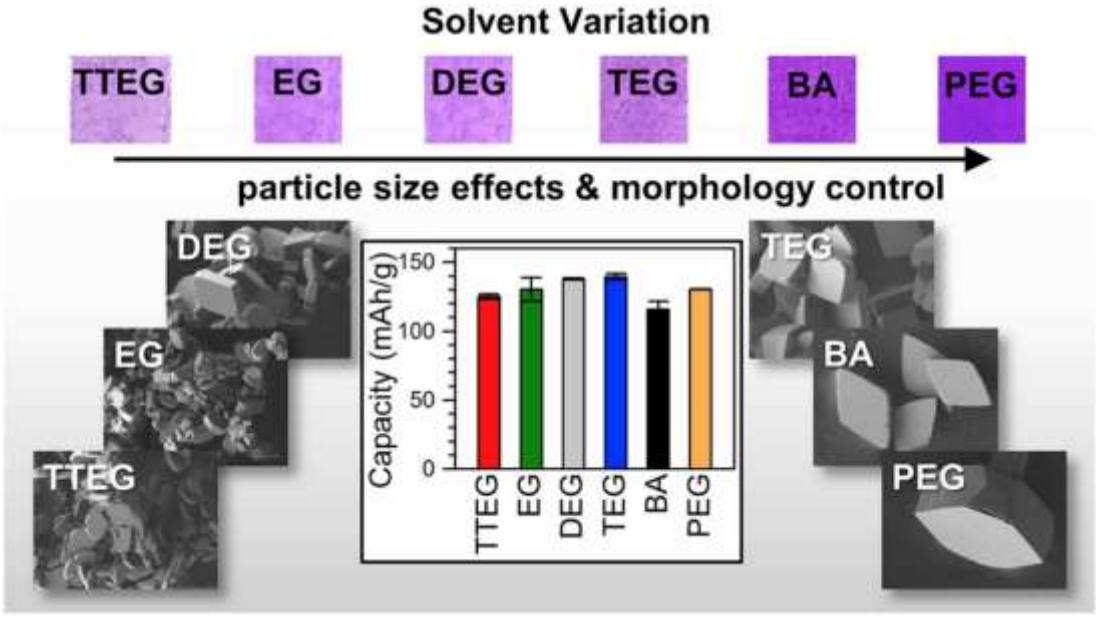


**Figure 2.13.** LCP particles synthesized in various water/organic binary solvent systems with the color of the powders from light pink to dark violet.[149]

In contrast, incorporating additives triggers a remarkable transformation in particle morphology, resulting in the formation of nanosheet and rod-shaped particles ranging from nano- to micro-scale. When citric acid was included in the solvothermal synthesis, LCP-CA shown in Figure 2.14 d-f transformed into thin nanosheets. These nanosheets have a thickness of tens of nanometers and exhibit irregular diameters in the sub-micrometer range. It is well-known that CA serves as a chelating agent which forms a strong bond between its carboxylic groups and $Co^{2+}$, influencing its behavior during the synthesis process.[151, 152] Furthermore, DEG solvent applied in the solvothermal synthesis plays a crucial role. It also exhibits strong bonding with $Co^{2+}$ on the group of (010) crystal planes, effectively hindering the growth of LCP crystals along the [010] direction. Contrarily, the introduction of PVP and CTAB as alternative additives induces a significant morphological shift in LCP from nanosheets to rod-shaped structure. This remarkable transformation can be attributed to the interplay between the variations in pH value of precursor solutions and chelating properties due to the polarity. Although LCP-CA displays the highest initial discharge capacity (123.4 mAh $g^{-1}$ at C/10), its capacity retention suffers significantly. This is due to the larger surface area of LCP-CA, which accelerates detrimental side reactions with the electrolyte at high-V. Conversely, LCP-PVP exhibits a

slightly lower initial capacity (112.6 mAh $g^{-1}$ at C/10) but demonstrates a somewhat better capacity retention (62 % after 50 cycles).

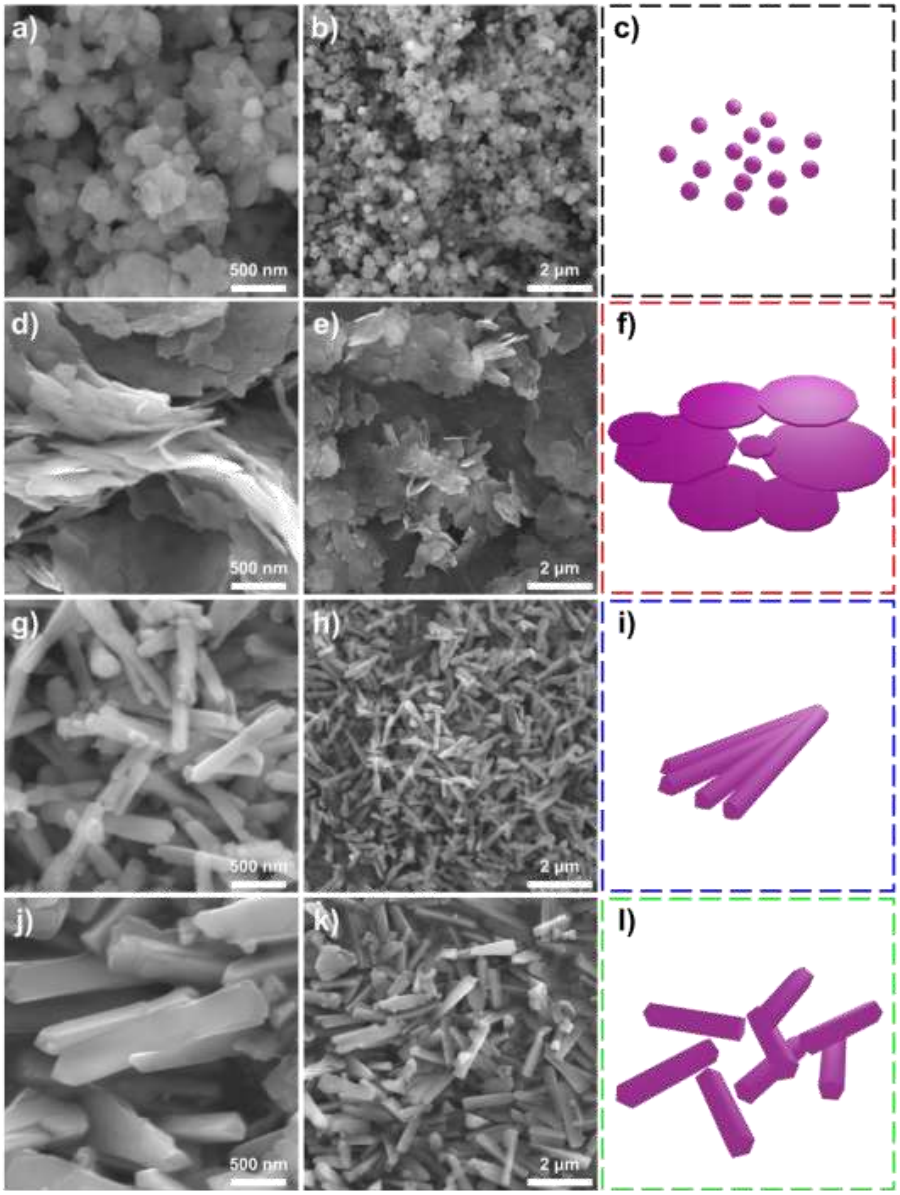


**Figure 2.14.** SEM images and the corresponding schematic models of pristine LCP and LCP with different additives: (a-c) LCP without surfactant; (d-f) LCP-CA; (g-i) LCP-PVP; (j-l) LCP-CTAB.[150]

As discussed in Sections 2.2.2 and 2.2.3.3, solvothermal synthesis proves to be a powerful methodology for precisely controlling LCP morphology. However, achieving ideal electrochemical performance, particularly reaching theoretical full capacity and enhanced capacity retention, necessitates further optimization. This optimization requires comprehensive studies rather than solely solvent and additive testing. It necessitates meticulous control over a wider range of parameters within the solvothermal process itself. Furthermore, incorporating post-synthesis treatments such as annealing process can be beneficial.

## 2.3. Hydrothermal/solvothermal synthesis

Hydrothermal/solvothermal synthesis is a technique for producing inorganic materials through chemical reactions in a closed pressure reactor. These reactions occur in solution, either water (Hydrothermal) or organic solvents (Solvothermal), at escalated temperatures exceeding the boiling point of the chosen solvent under pressure.[153] The technique distinguishes itself as a cost-efficient and environmentally benign process for the synthesis of diverse inorganic compounds such as LCP. This approach possesses the capability to modulate essential characteristics of the synthesized solids, such as purity, composition, crystal structure, particle size distribution, and morphological features. The synthesis of functional materials for energy storage applications necessitates a methodical approach to the selection of well-considered parameters that yield final products with the requisite quality and properties to achieve the desired functionality. To achieve this, it is essential to comprehend the fundamental mechanisms governing particle formation and growth in order to effectively manipulate the synthesis process. Hence, this section provides an overview of the fundamental principles underlying hydrothermal/solvothermal synthesis, as well as theories of particle formation and growth theory.

### 2.3.1. Principles of hydrothermal/solvothermal synthesis

Hydrothermal/solvothermal synthesis typically denotes heterogeneous reactions occurring in aqueous (or organic) solvents or mineralizers under elevated pressure and temperature conditions. This process facilitates the dissolution and subsequent re-precipitation of materials that exhibit low solubility under standard conditions.[154] The history of hydrothermal/solvothermal process is intimately closed with the emergence of nanotechnology. While the first use of hydrothermal methods to create submicron-sized quartz particles dates to the mid of 1800s, its widespread application failed to flourish until the 1990s. This delay can be attributed to two main factors: the lack of sophisticated tools to analyze nanoscale materials and a limited understanding of hydrothermal solution chemistry necessary for controlled crystal growth.[155] The revolution in nanoscience during the 1980s, coupled with the development of high-resolution microscopes, ignited a resurgence in hydrothermal techniques.[156] Additionally, advancements in understanding the chemical and physical properties of hydrothermal systems paved the way for solvothermal process. This variation utilizes organic solvents to achieve precise control over the morphology and size of nanomaterials.[157, 158]

Hydrothermal and solvothermal reactions occur within specialized containers called autoclaves. Typically made of metal for strength, they often have an inner lining of Teflon, special alloys, or even precious metals like platinum to shield the autoclave itself from the harsh conditions. This protection is essential because the reactions involve hot, corrosive conditions. For optimal control and monitoring, some autoclaves are equipped with pressure gauges like Parr Instrument Company (shown in Figure 2.15) to track pressure directly. Additionally, an agitator can be incorporated to ensure a uniform mix of reactants within the vessel.

**Figure 2.15.** Autoclave reactor for hydrothermal/solvothermal synthesis equipped with pressure monitoring gauge and agitation system supplied by Parr Instrument Company.[159]

### 2.3.2. Mechanisms of nucleation and growth of particles

The crystallization kinetics controls the size and morphology of particles produced by precipitation from solution.[160] Solid phases in a solution are formed through nucleation and growth processes. In the nucleation process, the molecules or ions in a solution aggregate to form clusters, which repeatedly form and dissolve until reach a critical size.[160] There are two types of nucleation mechanisms (homogeneous or heterogeneous nucleation) based on the location, where nucleation appears.[161] In detail, homogeneous nucleation occurs when nuclei form uniformly in the parent phase. On the other hand, heterogeneous nucleation occurs at surfaces of suspended particles or other foreign surfaces like impurities, bubbles etc.

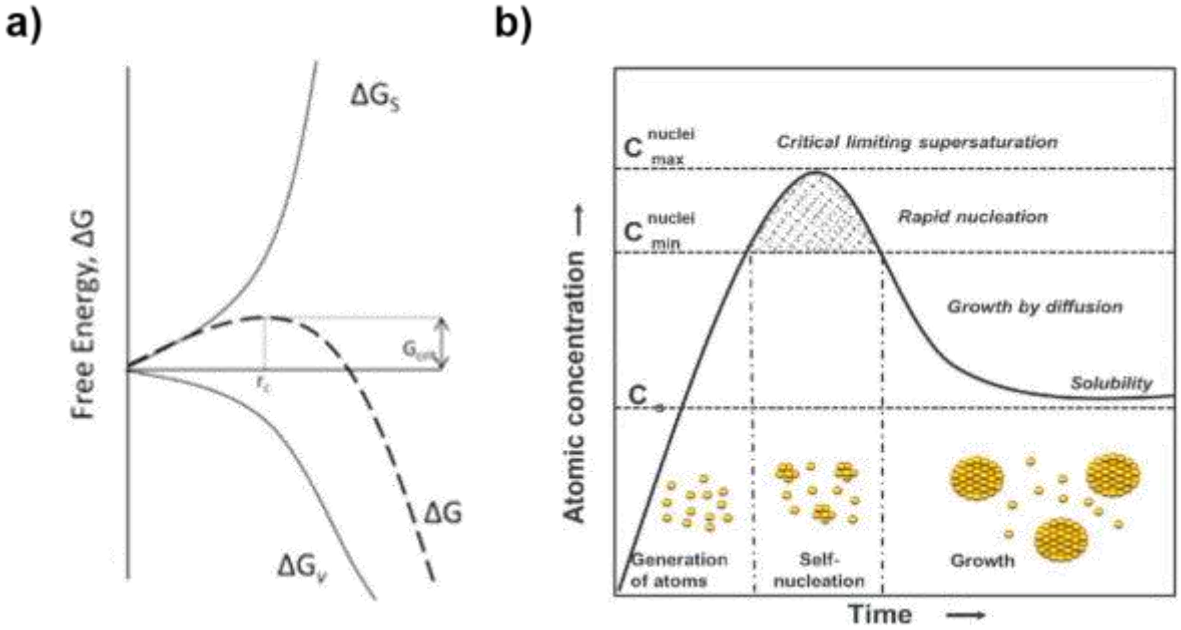


**Figure 2.16.** (a) Gibbs free energy changes depending on the radius r of a spherical cluster and (b) LaMer mechanism describing the classical crystal growth mechanism.[161, 162]

The driving force for nucleation is the total free energy change $\Delta G$, which is the sum of the surface free energy change $\Delta G_s$ associated with the generation of new surface; and the bulk free energy change $\Delta G_v$ associated with the variation in total volume, which can be given by:

$$\Delta \mathrm{G} = \Delta G_s + \Delta G_v \tag{2.11}$$

$$\Delta G_s = 4\pi r^2 \gamma \tag{2.12}$$

$$\Delta G_v = \frac{4}{3}\pi r^3 \Delta G_v = \frac{4}{3}\pi r^3 \left(-\frac{k_B T \ln S}{v}\right) \tag{2.13}$$

where $r$ is the radius of the cluster, $\gamma$ is the surface free energy per unit area, and $\Delta G_v$ is the bulk free energy change per unit volume, $k_B$ is Boltzmann's constant of $1.38\times10^{-23}$ J K$^{-1}$, $T$ is the absolute temperature, $S$ is supersaturation, and $v$ is the molecular volume.

The change of free energy as a function of the nuclei size is shown in Figure 2.16a. Because $\gamma$ is always positive and $\Delta G_v$ is always negative, there exists a maximum free energy, thus the clusters have to pass in order to form stable nuclei. The critical nuclei size $r_c$, corresponding to the maximum free energy, represents the minimum size of a stable nucleus. Particles smaller than $r_c$ will dissolve, and particles larger than $r_c$ will be growing to reduce the total free energy. $r_c$ is calculated using equation: $\frac{\mathrm{d}\Delta \mathrm{G}}{\mathrm{dr}} = 0$, which leads to

$$r_c = -\frac{2\gamma}{\Delta G_v} = \frac{2\gamma v}{k_B T \ln S} \tag{2.13}$$

The critical energy $\Delta G_{critical}$, which represents an activation energy barrier, is given by

$$\Delta G_{Critical} = \frac{16\pi\gamma^3}{3\Delta G_v{}^2} = \frac{16\pi\gamma^3 v^2}{3(k_B T \ln S)^2} \tag{2.14}$$

The homogeneous nucleation rate $J^{homo}$, measured in number of nuclei formed per unit time per unit volume, can be expressed as an Arrhenius-type equation:

$$J^{homo} = \mathrm{Aexp}\left(-\frac{\Delta G_{critical}}{k_B T}\right) = \mathrm{Aexp}(-\frac{16\pi\gamma^3 v^2}{3k_B{}^3 T^3 (\ln S)^2}) \tag{2.15}$$

where $A$ is a pre-exponential factor. It can be seen from equation (2.15) that there are three main experimental parameters that govern the nucleation rate, namely, temperature $T$, supersaturation $S$, and surface free energy $\gamma$. Among these factors, supersaturation plays the most critical role. For example, doubling the supersaturation level from 2 to 4 can significantly boost the nucleation rate, with an increase of up to $10^{70}$ times. Thus, supersaturation serves as the key driving force for the solid phase formation. For the following reaction,

$$k_1 A_1 + k_2 A_2 + \cdots + k_i A_i = [(A_1)_{k_1}(A_2)_{k_2} \cdots (A_1)_{k_i}] \tag{2.16}$$

where $A_i$ is an aqueous species, $k_i$ is the stoichiometric coefficient, and $[(A_1)_{k_1}(A_2)_{k_2} \cdots (A_1)_{k_i}]$ is the new phase.[163] Supersaturation can by expressed by

$$\mathrm{S} = \frac{\prod_i [A_i]^{k_i}}{K_{SP}} \tag{2.17}$$

where $[A_i]$ is the activity of an aqueous species, and $K_{SP}$ is the solubility product of the new phase. For simplicity, concentration might be used instead of activity for the calculation of supersaturation. The presence of heterogeneities, in the parent phase can significantly influence crystal formation. These imperfections act as a lowering the energy barrier needed for nucleation. This is known as heterogeneous nucleation.

$$J^{hetero} = \mathrm{Aexp}\left(-\frac{\Delta G_{critical}}{k_B T} f\right) = \mathrm{Aexp}(-\frac{16\pi\gamma^3 v^2 f}{3k_B{}^3 T^3 (\ln S)^2}) \tag{2.18}$$

The rate of heterogeneous nucleation can be described by considering a structural factor, denoted as $f$. This factor accounts for the specific influence of the imperfections on the nucleation process. Additionally, a concept of net effective surface free energy, $\gamma_{net}$ is employed to capture the overall energy involved in forming a new crystal surface on the imperfections.

Subsequent to the formation of stable nuclei, particle growth begins. The pathways of this growth are influenced by various parameters, including the level of supersaturation, the composition of the surrounding medium, and thermal conditions. Among classical crystallization theories, LaMer mechanism has emerged as a predominant model for elucidating the crystallization process of nanoparticles. This mechanism separates the process into three stages, as demonstrated in Figure 2.16b: (I) The system experiences a rapid escalation in free monomer concentration until it reaches a critical supersaturation (CS) point; (II) upon achieving $C_{min}$ saturation, the energy barrier for nucleation is overcome, initiating spontaneous self-nucleation of monomers; (III) the saturation level then declines below the threshold required for continued self-nucleation, transitioning the system to a growth phase characterized by diffusion-controlled accretion of monomers from the solution onto existing particles.

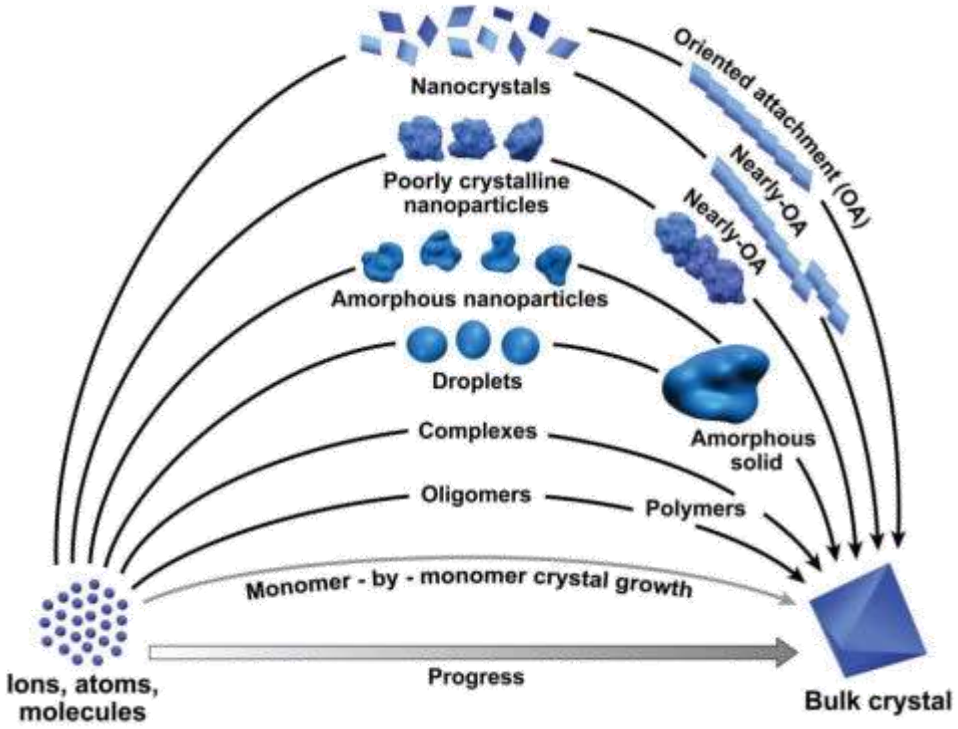


**Figure 2.17.** Various pathways to crystallization by particle attachment (CPA).[164]

Classical nucleation and growth models which focus solely on monomer-by-monomer crystal growth, are inconsistent with actual experimental results. In response to this discrepancy, a new paradigm has emerged based on extensive experimental evidence gathered from a wide array of solution-based systems. This new framework, termed crystallization by particle attachment (CPA), integrates a spectrum of nonclassical crystal nucleation and growth mechanisms. In Figure 2.17, the pathways of plausible building blocks are governed by the free-energy landscape and the reaction dynamics including particle diffusion and relaxation.[164]

## 2.4. Summary

$LiCoPO_4$ (LCP) is a promising high-V cathode material with an olivine crystal structure similar to $LiFePO_4$. This structure provides safety through strong P-O bonds but also results in lower energy density due to its lower operating voltage. Thus, LCP is seen as a potential high-V candidate within the olivine family, balancing safety and performance.

Various methodologies, including solid-state reaction, hydrothermal-solvothermal methods, and sol-gel techniques, have been used to synthesize LCP. Each method has its own advantages and disadvantages. However, the intrinsic properties of LCP, such as poor ionic and electronic conductivity, crystal structure defects and interfacial stability at high-V operation remain insufficiently addressed, highlighting the need for further post-synthesis treatments.

Several strategies have been proposed to overcome the limitations of LCP. Surface coating with carbon or inorganic materials enhances electronic conductivity and stability by reducing side reactions at the electrolyte interface, but this method complicates the synthesis process due to multiple steps. Another approach is cation substitution, which creates vacancies that improve Li-ion diffusion and stabilize the structure by suppressing anti-site formation during cycling tests. However, increased dopant concentration and narrow cut-off voltage ranges may lead to capacities below theoretical values.

Particle size reduction and morphology control have been proposed to address above-mentioned challenges. Both methods can shorten the Li-ion diffusion pathway, with nanosizing via ball-milling or preferential crystal growth. However, ball-milling leads to severe side reactions due to increased interface area with electrolyte and results in low tap density, causing poor volumetric energy density. As a result, the research aim has been shifted to solvothermal synthesis, which tailors LCP crystal morphology to retain micron-sized particles with shorter dimensions along the [010] direction, enhancing Li-ion diffusion. Despite these advancements, further research is needed to achieve theoretical full capacity and improved cycling stability.

This literature review has identified several gaps in LCP research. First, there is insufficient research on hydrothermal synthesis, requiring further studies to identify its fundamental limitations. Second, understanding the anisotropic growth mechanism in solvothermal synthesis needs collaborative efforts between experimental and computational research. Lastly, the mechanism of

capacity fade during cycling tests remains unclear. While anti-site defects in the bulk structure are known to contribute, the reasons for capacity fade at the electrolyte interface are still debated.

In conclusion, the subsequent research outlined in Chapters 3, 4, and 5 aims to address these points, providing a comprehensive understanding and potential solutions to enhance the electrochemical performance of LCP. This work is crucial for developing LCP as a high-energy density cathode material for LIBs, addressing current challenges and paving the way for future innovations.

## 2.5 References


1. J. B. Goodenough, K.-S Park, The Li-ion rechargeable battery: A perspective. *Journal of the American Chemical Society* **2013**, *135* (4), 1167-1176.
2. Grand View Research, Lithium-ion battery market size, share & growth Report, 2030. **2023**.
3. A. Heberta, E. McCalla, The role of metal substitutions in the development of Li batteries, part I: Cathodes. *Materials Advances* **2021**, *2* (11), 3474-3518.
4. A. Yoshino, Secondary Battery. **1987**, *US4668595A*.
5. K. Ozawa, Lithium-ion rechargeable batteries with $LiCoO_2$ and carbon electrodes: The $LiCoO_2$/C system. *Solid State Ionics* **1994**, *69*, 212-221.
6. Y. Furushima, C. Yanagisawa, T. Nakagawa, Y. Aoki, N. Muraki, Thermal stability and kinetics of delithiated $LiCoO_2$. *Journal of Power Sources* **2011**, *196* (4), 2260-2263.
7. H. Tan, S. Takeuchi, B. Kamala, I. Takeuchi, L. Bendersky, Microscopy study of structural evolution in epitaxial $LiCoO_2$ cathode films during electrochemical cycling. *ACS Applied Materials & Interfaces* **2016**, *8* (10), 6727-6735.
8. J. Chen, Z. Lin, W. Xiang, B. Wu, G. Zhang, X. Wen, Y. Che, D. Ruan, W. Li, M. Chen, Investigation of degradation mechanism of $LiCoO_2$/graphite batteries with multiscale characterization. *Electrochimica Acta* **2022**, *436*, 141374.
9. K. Ito, K. Tamura, K. Shimizu, N. L. Yamada, K. Watanabe, K. Suzuki, R. Kanno, M. Hirayama, Degradation of a lithium cobalt oxide cathode under high voltage operation at an interface with an oxide solid electrolyte. *RSC Applied Interfaces* **2024**, *1* (4) 790-799.
10. E. Wang, X. Ye, B. Zhang, B. Qu, J. Guo, S. Zheng, Enhancing the stability of 4.6 V $LiCoO_2$ cathode material via gradient doping. *Nanomaterials* **2024**, *14* (2), 147.
11. C. Wang, J. Weng, S. Wu, X. Zhang, Q. Tong, M. Zhu, A review – Exploring the performance degradation mechanisms of $LiCoO_2$ cathodes at high voltage conditions and some optimizing strategies. *Materials Chemistry Frontiers* **2022**, *6*, 2319-2337.
12. A. Yano, M. Shikano, A. Ueda, H. Sakaebe, Z. Ogumi, $LiCoO_2$ degradation behavior in the high-voltage phase transition region and improved reversibility with surface coating. *Journal of The Electrochemical Society* **2017**, *164* (1), A6116.
13. N. Nitta, F. Wu, J. T. Lee, G. Yushin, Li-ion battery materials: Present and future. *Materials Today* **2015**, *18* (5), 252-264.
14. S. Chen, X. Zhang, M. Xia, K. Wei, L. Zhang, X. Zhang, Y. Cui, J. Shu, Issues and challenges of layered lithium nickel cobalt manganese oxides for lithium-ion batteries. *Journal of Electroanalytical Chemistry* **2021**, *895*, 115412.

15. Z. Tang, D. Feng, Y. Xu, L. Chen, X. Zhang, Q. Ma, Safety issues of layered nickel-based cathode materials for lithium-ion batteries: Origin, Strategies and Prospects. *Batteries* **2023**, *9* (3), 156.
16. J. Xu, F. Lin, M. M. Doeff, W. Tong, A review of Ni-based layered oxides for rechargeable Li-ion batteries. *Journal of Materials Chemistry A* **2017**, *5* (3), 874-901.
17. E. Hu, X. Yu, R. Lin, X. Bi, J. Lu, S. Bak, K.-W. Nam, H. L. Xin, C. Jaye, D. A. Fischer, K. Amine, X.-Q. Yang, Evolution of redox couples in Li- and Mn-rich cathode materials and mitigation of voltage fade by reducing oxygen release. *Nature Energy* **2018**, *3*, 690-698.
18. J. Wang, X. Lei, L. Gu, X. Wang, D. Su, Structure modification of Ni-rich layered oxide cathode toward advanced lithium-ion batteries. *Journal of Materials Research* **2022**, *37*, 3250-3268.
19. J. Hu, H. Wang, B. Xiao, P. Liu, T. Huang, Y. Li, X. Ren, Q. Zhang, J. Liu, X. Ouyang, X. Sun, Challenges and approaches of single-crystal Ni-rich layered cathodes in lithium batteries. *National Science Review* **2023**, *10* (12), nwad252.
20. L. Nation, J. Li, C. James, Y. Qi, N. Dudney, B. W. Sheldon, *In situ* stress measurements during electrochemical cycling of lithium-rich cathodes. *Journal of Power Sources* **2017**, *364*, 383-391.
21. H.-H. Ryu, B. Namkoong, J.-H. Kim, I. Belharouak, C. S. Yoon, Y.-K. Sun, Capacity fading mechanisms in Ni-rich single-crystal NCM cathodes. *ACS Energy Letters* **2021**, *6* (8), 2726-2734.
22. X. Zhang, Z. Cui, E. Jo, A. Manthiram, Inhibition of transition-metal dissolution with advanced electrolytes in batteries with silicon-graphite anodes and high-nickel cathodes. *Energy Storage Materials* **2023**, *56*, 562-571.
23. K. Zhou, Q. Xie, B. Li, A. Manthiram, An in-depth understanding of the effect of aluminum doping in high-nickel cathodes for lithium-ion batteries. *Energy Storage Materials* **2021**, *34*, 229-240.
24. Petro Industry News, How are lithium NCA batteries used? **2022**.
25. H. Yu, D. Pei, A review of the origin, adverse influence and modification method of residual surface lithium in Ni-rich cathodes. *International Journal of Electrochemical Science* **2024**, *19* (1), 100391.
26. N. Takami, H. Inagaki, Y. Tatebayashi, H. Saruwatari, K. Honda, S. Egusa, High-power and long-life lithium-ion batteries using lithium titanium oxide anode for automotive and stationary power applications. *Journal of Power Sources* **2013**, *244*, 469-475.
27. M. Baazizi, M. Karbak, M. Aqil, S. Sayah, M. Dahbi, F. Ghamouss, High-valence surface-modified LMO cathode materials for lithium-ion batteries: Diffusion kinetics and *operando* thermal stability investigation. *ACS Applied Materials & Interfaces* **2023**, *15* (34), 40385-40396.
28. C. Zuo, Z. Hu, R. Qi, J. Liu, Z. Li, J. Lu, C. Dong, K. Yang, W. Huang, C. Chen, Z. Song, S. Song, Y. Yu, J. Zheng, F. Pan, Double the capacity of manganese spinel for lithium-ion storage by suppression of cooperative Jahn–Teller distortion. *Advanced Energy Materials* **2020**, *10* (34), 2000363.
29. T. Liu, A. Dai, J. Lu, T. Yuan, T. Xiao, L. Yu, M. Li, J. Gim, L. Ma, J. Liu, C. Zhan, L. Li, J. Zheng, Y. Ren, T. Wu, R. Shahbazian-Yassar, J. Wen, F. Pan, K. Amine, Correlation between manganese dissolution and dynamic phase stability in spinel-based lithium-ion battery. *Nature Communications* **2019**, *10* (1), 4721.
30. L.-X. Yuan, Z.-H. Wang, W.-X. Zhang, X.-L. Hu, J.-T. Chen, Y.-H. Huang, J. B. Goodenough, Development and challenges of $LiFePO_4$ cathode material for lithium-ion batteries. *Energy & Environmental Science* **2011**, *4* (2), 269-284.
31. B. Ramasubramanian, S. Sundarrajan, V. Chellappan, M. V. Reddy, S. Ramakrishna, K. Zaghib, Recent development in carbon-$LiFePO_4$ cathodes for lithium-ion batteries: A mini review. *Batteries* **2022**, *8* (10), 133.
32. A. K. Padhi, K. S. Nanjundaswamy, J. B. Goodenough, Phospho-olivines as positive-electrode materials for rechargeable lithium batteries. *Journal of The Electrochemical Society* **1997**, *144*, 1188.

33. H. Joachin, T. D. Kaun, K. Zaghib, J. Prakash, Electrochemical and thermal studies of carbon-coated $LiFePO_4$ cathode. *Journal of The Electrochemical Society* **2009**, *156* (6), A401-A406.
34. C. Wang, J. Hong, Ionic/electronic conducting characteristics of $LiFePO_4$ cathode materials: The determining factors for high-rate performance. *Electrochemical and Solid-State Letters* **2007**, *10*, A65.
35. B. L. Ellis, K. T. Lee, L. F. Nazar, Positive electrode materials for Li-ion and Li-batteries. *Chemistry of Materials* **2010**, *22* (3), 691-714.
36. M. Konarova, I. Taniguchi, Synthesis of carbon-coated $LiFePO_4$ nanoparticles with high-rate performance in lithium secondary batteries. *Journal of Power Sources* **2010**, *195* (11), 3661-3667.
37. Wang, B., Xu, B., Liu, T., Liu, P., Guo, C., Wang, S., Wang, Q., Xiong, Z., Wang, D., X. S. Zhao, Mesoporous carbon-coated $LiFePO_4$ nanocrystals co-modified with graphene and $Mg^{2+}$ doping as superior cathode materials for lithium-ion batteries. *Nanoscale* **2014**, *6* (2), 986-95.
38. J.-K. Kim, S. M. Jeong, Physico-electrochemical properties of carbon coated $LiFePO_4$ nanoparticles prepared by different preparation method. *Applied Surface Science* **2020**, *505*, 144630.
39. S. Ghosh, U. Bhattacharjee, S. Bhowmik, S. K. Martha, A review on high-capacity and high-voltage cathodes for next-generation lithium-ion batteries. *Journal of Energy and Power Technology* **2022**, *4* (1), 1-59.
40. K. Amine, H. Yasuda, M. Yamachi, Olivine $LiCoPO_4$ as 4.8 V electrode material for lithium batteries. *Electrochemical and Solid-State Letters* **2000**, *3* (4), 178-179.
41. L. Brückner, J. Frank, T. Elwert, Industrial recycling of lithium-ion batteries—A critical review of metallurgical process routes. *Metals* **2020**, *10* (8), 1107.
42. M. Bruno, S. Fiore, Material flow analysis of lithium-ion battery recycling in Europe: Environmental and economic implications. *Batteries* **2023**, *9* (4), 231.
43. A. K. Padhi, K. S. Nanjundaswamy, J. B. Goodenough, Phospho-olivines as positive-electrode materials for rechargeable lithium batteries. *Journal of the Electrochemical Society* **1997**, *144* (4), 1188-1194.
44. J. M. Lloris, C. P. Vicente, J. L. Tirado, Improvement of the electrochemical performance of $LiCoPO_4$ 5 V material using a novel synthesis procedure. *Electrochemical and Solid-State Letters* **2002**, *5* (10), A234-A237.
45. W. F. Howard, R. M. Spotnitz, Theoretical evaluation of high-energy lithium metal phosphate cathode materials in Li-ion batteries. *Journal of Power Sources* **2007**, *165* (2), 887-891.
46. D. Liu, W. Zhu, C. Kim, M. Cho, A. Guerfi, S. A. Delp, J. L. Allen, T. R. Jow, K. Zaghib, High-energy lithium-ion battery using substituted $LiCoPO_4$: From coin type to 1 Ah cell. *Journal of Power Sources* **2018**, *388*, 52-56.
47. J. L. Allen, J. L. Allen, T. Thompson, S. A. Delp, J. Wolfenstine, T. R. Jow, Cr and Si substituted-$LiCo_{0.9}Fe_{0.1}PO_4$: Structure, full and half Li-ion cell performance. *Journal of Power Sources* **2016**, *327*, 229-234.
48. J. L. Allen, J. L. Allen, S. A. Delp, J. Wolfenstine, T. R. Jow, High voltage lithium-ion positive electrode material. **2020**, *EP3291342A1*.
49. Y. H. Ikuhara, X. Gao, C. A. J. Fisher, A. Kuwabara, H. Moriwake, K. Kohama, H. Iba, Y. Ikuhara, Atomic level changes during capacity fade in highly oriented thin films of cathode material $LiCoPO_4$. *Journal of Materials Chemistry A* **2017**, *5* (19), 9329-9338.
50. D. Morgan, A. V. D. Ven, G. Ceder, Li Conductivity in $Li_xMPO_4$ (M = Mn, Fe, Co, Ni) olivine materials. *Electrochemical and Solid-State Letters* **2004**, *7* (2), A30.
51. M. S. Islam, D. J. Driscoll, C. A. J. Fisher, P. R. Slater, Atomic-scale investigation of defects, dopants, and lithium transport in the $LiFePO_4$ olivine-type battery material. *Chemistry of Materials* **2005**, *17* (20), 5085-5092.

52. S. Nishimura, G. Kobayashi, K. Ohoyama, R. Kanno, M. Yashima, A. Yamada, Experimental visualization of lithium diffusion in $Li_xFePO_4$. *Nature Materials* **2008**, *7* (9), 707-711.
53. D. Pritzl, A. E. Bumberger, M. Wetjen, J. Landesfeind, S. Solchenbach, H. A. Gasteiger, Identifying contact resistances in high-voltage cathodes by impedance spectroscopy. *Journal of The Electrochemical Society* **2019**, *166* (4), A582-A590.
54. J. Ludwig, T. Nilges, Recent progress and developments in lithium cobalt phosphate chemistry- Syntheses, polymorphism and properties. *Journal of Power Sources* **2018**, *382*, 101-115.
55. K. J. Kreder, G. Assat, A. Manthiram, Microwave-assisted solvothermal synthesis of three polymorphs of $LiCoPO_4$ and their electrochemical properties. *Chemistry of Materials* **2015**, *27* (16), 5543-5549.
56. M. Kaus, I. Issac, R. Heinzmann, S. Doyle, S. Mangold, H. Hahn, V. S. K. Chakravadhanula, C. Kübel, H. Ehrenberg, S. Indris, Electrochemical delithiation/relithiation of $LiCoPO_4$: A two-step reaction mechanism investigated by *in situ* X-ray diffraction, *in situ* X-ray absorption spectroscopy, and *ex situ* $^7Li/^{31}P$ NMR spectroscopy. *The Journal of Physical Chemistry C* **2014**, *118* (31), 17279-17290.
57. F. C. Strobridge, R. J. Clement, M. Leskes, D. S. Middlemiss, O. J. Borkiewicz, K. M. Wiaderek, K. W. Chapman, P. J. Chupas, C. P. Grey, Identifying the structure of the intermediate, $Li_{2/3}CoPO_4$, formed during electrochemical cycling of $LiCoPO_4$. *Chcemistry of Materials* **2014**, *26* (21), 6193-6205.
58. M. G. Palmer, J. T. Frith, A. L. Hector, A. W. Lodge, J. R. Owen, C. Nicklin, J. Rawle, *In situ* phase behaviour of a high capacity $LiCoPO_4$ electrode during constant or pulsed charge of a lithium cell. *Chemical Communications* **2016**, *52*, 14169.
59. J. L. Allen, T. R. Jow, J. Wolfenstine, Improved cycle life of Fe-substituted $LiCoPO_4$. *Journal of Power Sources* **2011**, *196* (20), 8656-8661.
60. E. Markevich, R. Sharabi, H. Gottlieb, V. Borgel, K. Fridman, G. Salitra, D. Aurbach, G. Semrau, M. A. Schmidt, N. Schall, C. Bruenig, Reasons for capacity fading of $LiCoPO_4$ cathodes in $LiPF_6$ containing electrolyte solutions. *Electrochemistry Communications* **2012**, *15* (1), 22-25.
61. N. N. Bramnik, K. Nikolowski, C. Baehtz, K. G. Bramnik, H. Ehrenberg, Phase transitions occurring upon lithium insertion−extraction of $LiCoPO_4$. *Chemistry of Materials* **2007**, *19* (4), 908-915.
62. N. N. Bramnik, K. Nikolowski, D. M. Trots, H. Ehrenberg, Thermal stability of $LiCoPO_4$ cathodes. *Electrochemical and Solid-State Letters* **2008**, *11*, A89.
63. D. Liu, C. Kim, A. Perea, D. Joël, W. Zhu, S. Collin-Martin, A. Forand, M. Dontigny, C. Gagnon, H. Demers, S. Delp, J. Allen, R. Jow, K. Zaghib, High-voltage lithium-ion battery using substituted $LiCoPO_4$: Electrochemical and safety performance of 1.2 Ah pouch cell. *Materials* **2020**, *13* (19), 4450.
64. H. Ehrenberg, N. N. Bramnik, A. Senyshyn, H. Fuess, Crystal and magnetic structures of electrochemically delithiated $Li_{1-x}CoPO_4$ phases. *Solid State Sciences* **2009**, *11* (1), 18-23.
65. A. Osnis, M. Kosa, D. Aurbach, D. T. Major, Systematic first-principles investigation of mixed transition metal olivine phosphates $LiM_{1-y}M'_yPO_4$ (M/M′ = Mn, Fe, and Co) as cathode materials. *Journal of Physical Chemistry C* **2013**, *117* (35), 17919-17926.
66. T. Fukutsuka, T. Nakagawa, K. Miyazaki, T. Abe, Electrochemical properties of $LiCoPO_4$-thin film electrodes in LiF-based electrolyte solution with anion receptors. *Journal of Power Sources* **2016**, *306*, 753-757.
67. Y. Maeyoshi, S. Miyamoto, H. Munakata, K. Kanamura, Enhanced cycle stability of $LiCoPO_4$ by using three-dimensionally ordered macroporous polyimide separator. *Journal of Power Sources* **2017**, *350*, 103-108.

68. N. N. Bramnik, K. G. Bramnik, T. Buhrmester, C. Baehtz, H. Ehrenberg, H. Fuess, Electrochemical and structural study of $LiCoPO_4$-based electrodes. *Journal of Solid-State Electrochemistry* **2004**, *8*, 558-564.
69. S. Sun, C. Du, J. Wu, Z. Tang, M. Yang, X. Zhang, Synthesis of $LiCoPO_4$ as cathode material for lithium-ion batteries by the rheological phase method. *Ionics* **2014**, *20*, 1627-1634.
70. J. M. Lloris, C. P. Vicente, J. L. Tirado, Improvement of the electrochemical performance of $LiCoPO_4$ 5 V material using a novel synthesis procedure. *Electrochemical and Solid-State Letters* **2002**, *5*, A234.
71. Q. Sun, J.-Y. Luo, Z.-W. Fu, Facile synthesis and electrochemical properties of carbon-coated $LiCoPO_4$ submicron particles as positive materials for lithium-ion batteries. *Electrochemical and Solid-State Letters* **2011**, *14*, A151.
72. N. Priyadharsini, S. Shanmugapriya, P. R. Kasturi, S. Surendran, R. K. Selvan, Morphology-dependent electrochemical properties of sol-gel synthesized $LiCoPO_4$ for aqueous hybrid capacitors. *Electrochimica Acta* **2018**, *289*, 516-526.
73. L. Dimesso, G. Cherkashinin, C. Spanheimer, W. Jaegermann, Preparation and characterization of carbon foams–$LiCoPO_4$ composites. *Journal of Alloys and Compounds* **2012**, *516*, 119-125.
74. S. Brutti, S. Panero, Recent advances in the development of $LiCoPO_4$ as high voltage cathode material for Li-ion batteries. *Nanotechnology for Sustainable Energy* **2013**, *1140*, 67-99.
75. J. Liu, T. E. Conry, X. Song, L. Yang, M. M. Doeff, T. J. Richardson, Spherical nanoporous $LiCoPO_4$/C composites as high-performance cathode materials for rechargeable lithium-ion batteries. *Journal of Materials Chemistry* **2011**, *21*, 9984-9987.
76. T. N. L. Doan, I. Taniguchi, Preparation of $LiCoPO_4$/C nanocomposite cathode of lithium batteries with high-rate performance. *Journal of Power Sources* **2011**, *196* (13), 5679-5684.
77. I. Taniguchi, T. N. L. Doan, B. Shao, Synthesis and electrochemical characterization of $LiCo_xMn_{1-x}PO_4$/C nanocomposites. *Electrochimica Acta* **2011**, *56* (22), 7680-7685.
78. T. N. L. Doan, I. Taniguchi, Effect of spray pyrolysis temperature on physical and electrochemical properties of $LiCoPO_4$/C nanocomposites. *Powder Technology* **2012**, *217*, 574-580.
79. J. Ni, L. Gao, L. Lu, Carbon coated lithium cobalt phosphate for Li-ion batteries: Comparison of three coating techniques. *Journal of Power Sources* **2013**, *221*, 35-41.
80. C. Delacourt, C. Wurm, P. Reale, M. Morcrette, C. Masquelier, Low temperature preparation of optimized phosphates for Li-battery applications. *Solid State Ionics* **2004**, *173* (1-4), 113-118.
81. D. Choi, X. Li, W. A. Henderson, Q. Huang, S. K. Nune, J. P. Lemmon, V. L. Sprenkle, $LiCoPO_4$ cathode from a $CoHPO_4 \cdot xH_2O$ nanoplate precursor for high voltage Li-ion batteries. *Heliyon* **2016**, *2* (2), e00081.
82. R. Vasanthi, D. Kalpana, N. G. Renganathan, Olivine-type nanoparticle for hybrid supercapacitors. *Journal of Solid State Electrochemistry* **2008**, *12*, 961-969.
83. P. R. Kumar, V. Madhusudhanrao, N. B, M. Venkateswarlu, N. Satyanarayana, Enhanced electrochemical performance of carbon-coated $LiMPO_4$ (M = Co and Ni) nanoparticles as cathodes for high-voltage lithium-ion battery. *Journal of Solid State Electrochemistry* **2016**, *20*, 1855-1863.
84. X. Rui, X. Zhao, Z. Lu, H. Tan, D. Sim, H. H. Hng, R. Yazami, T. M. Lim, Q. Yan, Olivine-type nanosheets for lithium-ion battery cathodes. *ACS Nano* **2013**, *7* (6), 5637-5646.
85. Q. D. Truong, M. K. Devaraju, Y. Ganbe, T. Tomai, I. Honma, Controlling the shape of $LiCoPO_4$ nanocrystals by supercritical fluid process for enhanced energy storage properties. *Scientific Reports* **2014**, *4*, 3975.
86. Q. D. Truong, M. K. Devarajua, I. Honma, Benzylamine-directed growth of olivine-type $LiMPO_4$ nanoplates by a supercritical ethanol process for lithium-ion batteries. *Journal of materials Chemistry A* **2014**, *2*, 17400-17407.

87. M. K. Devaraju, Q. D. Truong, H. Hyodo, T. Tomai, I. Honma, Supercritical fluid synthesis of $LiCoPO_4$ nanoparticles and their application to lithium ion battery. *Inorganics* **2014**, *2*, 233-247.
88. H. H. Li, J. Jin, J. P. Wei, Z. Zhou, J. Yan, Fast synthesis of core-shell $LiCoPO_4$/C nanocomposite via microwave heating and its electrochemical Li intercalation performances. *Electrochemistry Communications* **2009**, *11* (1), 95-98.
89. D.-W. Han, Y.-M. Kang, R.-Z. Yin, M.-S. Song, H.-S. Kwon, Effects of Fe doping on the electrochemical performance of $LiCoPO_4$/C composites for high power-density cathode materials. *Electrochemistry Communications* **2009**, *11* (1), 137-140.
90. R. E. Rogers, G. M. Clarke, O. N. Matthew, M. J. Ganter, R. A. DiLeo, J. W. Staub, M. W. Forney, B. J. Landi, Impact of microwave synthesis conditions on the rechargeable capacity of $LiCoPO_4$ for lithium-ion batteries. *Journal of Applied Electrochemistry* **2013**, *43*, 271-278.
91. S. Rosenberg, A. Hintennach, *In situ* carbon-coated $LiCoPO_4$ synthesized via a microwave-assisted path. *Russian Journal of Electrochemistry* **2015**, *51*, 305-309.
92. N. V. Kosova, O. A. Podgornova, E. T. Devyatkina, V. R. Podugolnikova, S. A. Petrov, Effect of $Fe^{2+}$ substitution on the structure and electrochemistry of $LiCoPO_4$ prepared by mechanochemically assisted carbothermal reduction. *Journal of Materials Chemistry A* **2014**, *2*, 20697-20705.
93. N. V. Kosova, O. A. Podgornova, I. A. Bobrikov, V. V. Kaichev, A. V. Bukhtiyarov, Approaching better cycleability of $LiCoPO_4$ by vanadium modification. *Materials Science and Engineering: B* **2016**, *213*, 105-113.
94. Y. Maeyoshi, S. Miyamoto, Y. Noda, H. Munakata, K. Kanamura, Effect of organic additives on characteristics of carbon-coated $LiCoPO_4$ synthesized by hydrothermal method. *Journal of Power Sources* **2017**, *337*, 92-99.
95. B. Wu, H. Xu, D. Mu, L. Shi, B. Jiang, L. Gai, L. Wang, Q. Liu, L. Ben, F. Wu, Controlled solvothermal synthesis and electrochemical performance of $LiCoPO_4$ submicron single crystals as a cathode material for lithium-ion batteries. *Journal of Power Sources* **2016**, *304*, 181-188.
96. S.-M. Oh, S.-T. Myung, Y.-K. Sun, Olivine $LiCoPO_4$–carbon composite showing high rechargeable capacity. *Journal of Materials Chemistry* **2012**, *22*, 14932-14937.
97. N. Laszczynski, A. Birrozzi, K. Maranski, M. Copley, M. E. Schuster, S. Passerini, Effect of coatings on the green electrode processing and cycling behaviour of $LiCoPO_4$. *Journal of Materials Chemistry A* **2016**, *4*, 17121-17128.
98. J. Yang, J. J. Xu, Synthesis and characterization of carbon-coated lithium transition metal phosphates $LiMPO_4$ (M = Fe, Mn, Co, Ni) prepared via a nonaqueous sol-gel route. *Journal of The Electrochemical Society* **2006**, *153*, A716.
99. P. N. Poovizhi, S. Selladurai, Study of pristine and carbon-coated $LiCoPO_4$ olivine material synthesized by modified sol–gel method. *Ionics* **2011**, *17*, 13-19.
100. I. C. Jang, C. G. Son, S. M. G. Yang, J. W. Lee, A. R. Cho, V. Aravindan, G. J. Park, K. S. Kang, W. S. Kim, W. I. Cho, Y. S. Lee, $LiFePO_4$ modified $Li_{1.02}(Co_{0.9}Fe_{0.1})_{0.98}PO_4$ cathodes with improved lithium storage properties. *Journal of Materials Chemistry* **2011**, *21*, 6510-6514.
101. I. C. Jang, H. H. Lim, S. B. Lee, K. Karthikeyan, V. Aravindan, K. S. Kang, W. S. Yoon, W. I. Cho, Y. S. Lee, Preparation of $LiCoPO_4$ and $LiFePO_4$ coated $LiCoPO_4$ materials with improved battery performance. *Journal of Alloys and Compounds* **2010**, *497* (1-2), 321-324.
102. K. J. Kreder III, A. Manthiram, Vanadium-substituted $LiCoPO_4$ core with a monolithic $LiFePO_4$ shell for high-voltage lithium-ion batteries. *ACS Energy Letters* **2017**, *2* (1), 64-69.
103. A. Örnek, An impressive approach to solving the ongoing stability problems of $LiCoPO_4$ cathode: Nickel oxide surface modification with excellent core–shell principle. *Journal of Power Sources* **2017**, *356*, 1-11.

104. Y. Wang, J. Qiu, Z. Yu, H. Ming, M. Li, S. Zhang, Y. Yang, $AlF_3$-modified $LiCoPO_4$ for an advanced cathode towards high energy lithium-ion battery. *Ceramics International* **2018**, *44* (2), 1312-1320.
105. L. Wu, S. Shi, X. Zhang, J. Liu, D. Chen, H. Ding, S. Zhong, Novel synthesis of $LiCoPO_4$–$Li_3V_2(PO_4)_3$ composite cathode material for Li-ion batteries. *Materials Letters* **2015**, *152*, 228-231.
106. A. Eftekhari, Surface modification of thin-film based $LiCoPO_4$ 5 V cathode with metal oxide. *Journal of The Electrochemical Society* **2004**, *151*, A1456.
107. M. Zhang, N. Garcia-Araez, A. L. Hector, Understanding and development of olivine $LiCoPO_4$ cathode materials for lithium-ion batteries. *Journal of Materials Chemistry A* **2018**, *6*, 14483-14517.
108. K. Gangulibabu, D. Nallathamby, M. M. Meyrick, Carbonate anion controlled growth of $LiCoPO_4$/C nanorods and its improved electrochemical behavior. *Electrochimica Acta* **2013**, *101*, 18-26.
109. H. Chen, M. Chen, C. Du, Y. Cui, P. Zuo, X. Cheng, G. Yin, Synthesis and electrochemical performance of hierarchical nanocomposite of carbon coated $LiCoPO_4$ crosslinked by graphene. *Materials Chemistry and Physics* **2016**, *171*, 6-10.
110. L. Y. Xing, M. Hu, Q. Tang, J. P. Wei, X. Qin, Z. Zhou, Improved cyclic performances of $LiCoPO_4$/C cathode materials for high-cell-potential lithium-ion batteries with thiophene as an electrolyte additive. *Electrochimica Acta* **2012**, *59*, 172-178.
111. J. Ni, H. Wang, L. Gao, L. Lu, A high-performance $LiCoPO_4$/C core/shell composite for Li-ion batteries. *Electrochimica Acta* **2012**, *70*, 349-354.
112. J. Xu, S.-L. Chou, M. Avdeev, M. Sale, H.-K. Liu, S.-X. Dou, Lithium rich and deficient effects in $LixCoPO_4$ (x = 0.90, 0.95, 1, 1.05) as cathode material for lithium-ion batteries. *Electrochimica Acta* **2013**, *88*, 865-870.
113. A. Örnek, A new and effective approach to 4.8 V cathode synthesis with superior electrochemical qualities for lithium-ion applications. *Journal of Alloys and Compounds* **2017**, *710*, 809-818.
114. F. Wang, J. Yang, Y. NuLi, J. Wang, Novel hedgehog-like 5 V $LiCoPO_4$ positive electrode material for rechargeable lithium battery. *Journal of Power Sources* **2011**, *196* (10), 4806-4810.
115. M. Li, Solvothermal synthesis of $LiCo_{1-x}Mn_xPO_4$/C cathode materials for lithium-ion batteries. *Ionics* **2012**, *18*, 507-512.
116. D. D. Lecce, J. Manzi, F. M. Vitucci, A. De Bonis, S. Panero, S. Brutti, Effect of the iron doping in $LiCoPO_4$ cathode materials for lithium cells. *Electrochimica Acta* **2015**, *185*, 17-27.
117. A. ÿrnek, A. YeĬildaĿ, M. Can, S. Aktürk, A practical and effective strategy for the thin and uniform carbon layer onto $LiCoPO_4$ cathode surface in terms of the rate capability and cycle stability. *Materials Research Bulletin* **2016**, *83*, 1-11.
118. W. Sun, S. Cui, Y. Xing, D. Sun, W. Liu, Y. Jin, Hight voltage lithium cobalt phosphate with nitrogen doped carbon coating layer for ultrahigh performance lithium-ion battery. *Journal of Power Sources* **2024**, *602*, 234378.
119. M. D. Johannes, K. Hoang, J. L. Allen, K. Gaskell, Hole polaron formation and migration in olivine phosphate materials. *Physical Review B* **2012**, *85*, 115106.
120. S. Brutti, J. Manzi, D. Meggiolaro, F. M. Vitucci, F. Trequattrini, A. Paolone, O. Palumbo, Interplay between local structure and transport properties in iron-doped $LiCoPO_4$ olivines. *Journal of Materials Chemistry A* **2017**, *5*, 14020-14030.
121. J. G. Lapping, S. A. Delp, J. L. Allen, J. L. Allen, J. W. Freeland, M. D. Johannes, L. Hu, D. T. Tran, T. R. Jow, J. Cabana, Changes in electronic structure upon Li deintercalation from $LiCoPO_4$ derivatives. *Chemistry of Materials* **2018**, *30* (6), 1898-1906.

122. N. V. Kosova, O. A. Podgornova, E. T. Devyatkina, V. R. Podugolnikov, S. A. Petrov, Effect of $Fe^{2+}$ substitution on the structure and electrochemistry of $LiCoPO_4$ prepared by mechanochemically assisted carbothermal reduction. *Journal of Materials Chemistry A* **2014**, *2* (48), 20697-20705.
123. R. Hanafusa, Y. Oka, T. Nakamura, Electrochemical and magnetic studies of Li-deficient $Li_{1-x}Co_{1-x}Fe_xPO_4$ olivine cathode compounds. *Journal of The Electrochemical Society* **2015**, *162* (2), A3045.
124. Y.-M. Kang, Y.-I. Kim, M.-W. Oh, R.-Z. Yin, Y. Lee, D.-W. Han, H.-S. Kwon, J. H. Kim, F. Ramanath, Structurally stabilized olivine lithium phosphate cathodes with enhanced electrochemical properties through Fe doping. *Energy & Environmental Science* **2011**, *4* (12), 4978.
125. J. L. Allen, T. R. Jow, J. Wolfenstine, Improved cycle life of Fe-substituted $LiCoPO_4$. *Journal of Power Sources* **2011**, *196* (20), 8656-8661.
126. R. Tussupbayev, I. Taniguchi, Physical and electrochemical properties of $LiCoPO_4$/C nanocomposites prepared by a combination of emulsion drip combustion and wet ball-milling followed by heat treatment. *Journal of Power Sources* **2013**, *236*, 276-284.
127. J. F. Ni, Y. Han, J. Liu, H. Wang, L. Gao, Improving electrochemical properties of $LiCoPO_4$ by Mn substitution: A case research on $LiCo_{0.5}Mn_{0.5}PO_4$. *ECS Electrochemistry Letters* **2013**, *2* (1), A3.
128. L. Dimesso, C. Spanheimer, W. Jaegermann, Influence of isovalent ions (Ca and Mg) on the properties of $LiCo_{0.9}M_{0.1}PO_4$ powders. *Journal of Power Sources* **2013**, *243*, 668-675.
129. L. Dimesso, C. Spanheimer, W. Jaegermann, Investigation of the $LiCo_{1-x}Mg_xPO_4$ ($0 \leqslant x \leqslant 0.1$) system. *Journal of Alloys and Compounds* **2014**, *582*, 69-74.
130. L. Dimesso, C. Spanheimer, M. M. Mueller, H.-J. Kleebe, W. Jaegermann, Properties of Ca-containing $LiCoPO_4$-graphitic carbon foam composites. *Ionics* **2015**, *21* (8), 2101-2107.
131. J. Wolfenstine, Electrical conductivity of doped $LiCoPO_4$. *Journal of Power Sources* **2006**, *158* (2) 1431-1435.
132. K. J. Kreder, G. Assat, Manthiram, A., Aliovalent substitution of $V^{3+}$ for $Co^{2+}$ in $LiCoPO_4$ by a low-temperature microwave-assisted solvothermal process. *Chemistry of Materials* **2016**, *28*, 1847-1853.
133. F. Wang, J. Yang, Y. NuLi, J. Wang, Highly promoted electrochemical performance of 5 V $LiCoPO_4$ cathode material by addition of vanadium. *Journal of Power Sources* **2010**, *195*, 6884-6887.
134. H. Li, Y. Wang, X. Yang, L. Liu, L. Chen, J. Wei, Improved electrochemical performance of 5 V $LiCoPO_4$ cathode materials via yttrium doping. *Solid State Ionics* **2014**, *255*, 84-88.
135. A. Örnek, M. Can, A. Yeşildağ, Improving the cycle stability of $LiCoPO_4$ nanocomposites as 4.8 V cathode: Stepwise or synchronous surface coating and Mn substitution. *Materials Characterization* **2016**, *116*, 76-83.
136. W. Zhang, Y. Hu, X. Tao, H. Huang, Y. Gan, C. Wang, Synthesis of spherical $LiFePO_4$/C via Ni doping. *Journal of Physics and Chemistry of Solids* **2010**, *71* (9), 1196-1200.
137. N. Okita, K. Kisu, E. Iwama, Y. Sakai, Y. Lim, Y. Takami, M. T. Sougrati, T. Brousse, P. Rozier, P. Simon, W. Naoi, K. Naoi, Stabilizing the structure of $LiCoPO_4$ nanocrystals via addition of $Fe^{3+}$: Formation of $Fe^{3+}$ surface layer, creation of diffusion-enhancing vacancies, and enabling high-voltage battery operation. *Chemistry of Materials* **2018**, *30* (19), 6675-6683.
138. Y. Wang, J. Chen, J. Qiu, Z. Yu, H. Ming, M. Li, S. Zhang, Y. Yang, Cr-substituted $LiCoPO_4$ core with a conductive carbon layer towards high-voltage lithium-ion batteries. *Journal of Solid State Chemistry* **2018**, *258*, 32-41.
139. L. Fang, H. Zhang, Y. Zhang, L. Liu, Y. Wang, Design and synthesis of two-dimensional porous Fe-doped $LiCoPO_4$ nano-plates as improved cathode for lithium ion batteries. *Journal of Power Sources* **2016**, *312*, 101-108.

140. J. F. Ni, Y. Han, J. Liu, H. Wang, L. Gao, Improving electrochemical properties of $LiCoPO_4$ by Mn substitution: A case research on $LiCo_{0.5}Mn_{0.5}PO_4$. *ECS Electrochemistry Letters* **2013**, *2* (1), A3-A5.
141. L. Dimesso, C. Spanheimer, W. Jaegermann, Influence of isovalent ions (Ca and Mg) on the properties of $LiCo_{0.9}M_{0.1}PO_4$ powders. *Journal of Power Sources* **2013**, *243*, 668-675.
142. L. Dimesso, C. Spanheimer, M. M. Mueller, H.-J. Kleebe, W. Jaegermann, Properties of Ca-containing $LiCoPO_4$-graphitic carbon foam composites. *Ionics* **2015**, *21*, 2101-2107.
143. D. Zhang, J. Zhou, J. Chen, B. Xu, W. Qin, C. Chang, Rapid synthesis of $LiCo_{1-x}Fe_xPO_4$/C cathodes via microwave solvothermal method for Li-ion batteries. *International Journal of Electrochemical Science* **2018**, *13* (3), 2544-2555.
144. J. Wu, C.-J. Tsai, Discovered intermediate phase and improved electrochemical performance of Zn-Doped $LiCoPO_4$ for high-energy Li-ion batteries. *ACS Applied Energy Materials* **2021**, *4* (7), 6408-6413.
145. K. K. Surthi, K. K. Kar, Spherical shaped $LiCo_{0.5}Mn_{0.5}PO_4$-carbon composite as high voltage cathode material for conventional and flexible Li-ion batteries. *Carbon* **2022**, *193*, 140-150.
146. H. Li, S.-C. Huang, S.-Y. Chen, J. Wu, H.-Y. Chen, C.-J. Tsai, Effect of Fe and Zn co-doping on $LiCoPO_4$ cathode materials for high-voltage lithium-ion batteries. *Journal of Colloid and Interface Science* **2024**, *669*, 117-125.
147. B. Jin, H.-B. Gu, K.-W. Kim, Effect of different conductive additives on charge/discharge properties of $LiCoPO_4$/Li batteries. *Journal of Solid-State Electrochemistry* **2008**, *12*, 105-111.
148. J. Ludwig, C. Marino, D. Haering, C. Stinner, D. Nordlund, M. M. Doeff, H. A. Gasteiger, T. Nilges, Facile, ethylene glycol-promoted microwave-assisted solvothermal synthesis of high-performance $LiCoPO_4$ as a high-voltage cathode material for lithium-ion batteries. *RSC Advances* **2016**, *6*, 82984-82994.
149. J. Ludwig, C. Marino, D. Haering, C. Stinner, H. A. Gasteiger, T. Nilges, Morphology-controlled microwave-assisted solvothermal synthesis of high-performance $LiCoPO_4$ as a high-voltage cathode material for Li-ion batteries. *Journal of Power Sources* **2017**, *342*, 214-223.
150. X. Wu, M. Meledina, H. Tempel, H. Kungl, J. Mayer, R.-A. Eichel, Morphology-controllable synthesis of $LiCoPO_4$ and its influence on electrochemical performance for high-voltage lithium ion batteries. *Journal of Power Sources* **2020**, *450*, 227726.
151. G. Xie, H.-J. Zhu, X.-M. Liu, H. Yang, A core–shell $LiFePO_4$/C nanocomposite prepared via a sol–gel method assisted by citric acid. *Journal of Alloys and Compounds* **2013**, *574*, 155-160.
152. N. Priyadharsini, P. R. Kasturi, A. Shanmugavani, S. Surendran, S. Shanmugapriya, R. K. Selvan, Effect of chelating agent on the sol-gel thermolysis synthesis of $LiNiPO_4$ and its electrochemical properties for hybrid capacitors. *Journal of Physics and Chemistry of Solids* **2018**, *119*, 183-192.
153. S. H. Feng, G. H. Li, Chapter 4 – Hydrothermal and solvothermal syntheses. *Modern Inorganic Synthetic Chemistry*, **2017**, 73-104.
154. J. Li, Q. Wu, J. Wu, Synthesis of nanoparticles via solvothermal and hydrothermal methods. *Handbook of Nanoparticles*, **2015**, 1-28.
155. K. Byrappa, T. Adschiri, Hydrothermal technology for nanotechnology. *Progress in Crystal Growth and Characterization of Materials* **2007**, *53* (2), 117-166.
156. Z. L. Wang, New developments in transmission electron microscopy for nanotechnology. *Advanced Materials* **2003**, *15* (18), 1497-1514.
157. H. C. Helgeson, D. H. Kirkham, Theoretical prediction of the thermodynamic behavior of aqueous electrolytes at high pressures and temperatures; I, Summary of the thermodynamic/electrostatic properties of the solvent. *American Journal of Science* **1974**, *274* (10), 1089.

158. E. L. Shock, E. H. Oelkers, J. W. Johnson, D. A. Sverjensky, H. C. Helgeson, Calculation of the thermodynamic properties of aqueous species at high pressures and temperatures. Effective electrostatic radii, dissociation constants and standard partial molal properties to 1000 °C and 5 kbar. *Journal of the Chemical Society, Faraday Transactions* **1992**, *88*, 803-826.
159. Parr Instrument Company, Stirred reactors and pressure Vessels. **2015**, *15*, 24-66.
160. G. P. Demopoulos, Aqueous precipitation and crystallization for the production of particulate solids with desired properties. *Hydrometallurgy* **2009**, *96* (3), 199-214.
161. J. M. Mullin, 5 - Nucleation. in crystallization (Fourth Edition), *Butterworth-Heinemann: Oxford*, **2001**, 181-215.
162. K. Victor, LaMer, R. H. D., Theory, production and mechanism of formation of monodispersed hydrosols. *Journal of the American Chemical Society* **1950**, *72* (11), 4847-4854.
163. M. L. Whittaker, P. M. Dove, D. Joester, Nucleation on surfaces and in confinement. *MRS Bulletin* **2016**, *41*, 388-392.
164. J. J. D. Yoreo, P. U. P. A. Gilbert, N. A. J. M. Sommerdijk, R. L. Penn, S. Whitelam, D. Joester, H. Zhang, J. D. Rimer, A. Navrotsky, J. F. Banfield, A. F. Wallace, F. M. Michel, F. C. Meldrum, H. Cölfen, P. M. Dove, Crystallization by particle attachment in synthetic, biogenic, and geologic environments. *Science* **2015**, *349* (6247), aaa6760.

# Chapter 3: Surface and bulk defect formation during hydrothermal synthesis of $LiCoPO_4$ crystals and their electrochemical implications

This chapter addresses the 1st objective of thesis. Specifically, in-depth and fundamental characterizations of hydrothermal HT-LCP lead to identification of two types of defects one in the form of $Co(OH)_2$ surface layer induced by surface hydrolysis due to the alkaline environment in LCP synthesis and the other in the form of anti-site defects that severely hinder the electrochemically-driven intercalation process. The Chapter is published as peer reviewed manuscript:

Moohyun Woo, Jinhyuk Lee and George P. Demopoulos, 2023, "Surface and bulk defect formation during hydrothermal synthesis of $LiCoPO_4$ crystals and their electrochemical implications", *Mater. Adv.*, *2023, 4, 4823-4834*.


**Abstract**

Lithium cobalt phosphate ($LiCoPO_4$, LCP) is a high-voltage cathode material with a lot of promise in delivering high energy density in comparison to the established $LiFePO_4$ counterpart. However, the road to developing LCP is hampered not only by electrolyte interfacial reaction due to high voltage but also by the lack of critical knowledge regarding material crystal properties linked to synthesis that limit the attainment of full discharge capacity. Herein, we study in-depth the synthesis of LCP by the hydrothermal method and its post-synthesis modifications by high-energy planetary-milling and conductive carbon coating in order to shed light on the crystal chemistry affecting its electrochemical performance. Via adjusting the Li/Co molar ratio and pH of precursor solution, the supersaturation is controlled to achieve high-purity and well-crystalline LCP particles with sub-micron size. After carefully characterizing the hydrothermally synthesized LCP crystalline material, we discovered the presence of two types of defects, surface composition inhomogeneities and bulk cation mixing, which adversely affect the Li-ion intercalation kinetics and storage capacity. More specifically, we identified i) the formation of undesired nano-scale $Co(OH)_2$ passivation layer on the LCP surface and ii) abundant anti-site defects blocking one-dimensional (1-D) Li-ion diffusion channels. These crystal defects impose critical limitations to hydrothermally produced LCP materials in delivering near theoretical discharge capacities; hence on the basis of these new insights, alternative crystal engineering approaches need to be developed in pursuit of high-performance LCP cathodes.

### 3.1. Introductoion

Rechargeable Li-ion batteries bring a wide spectrum of applications in modern society, from mobile electronic devices to large-scale energy storage for electromobility and the smart grid.[1-5] With this trend, the ever-growing demand for state-of-the-art rechargeable Li-ion batteries with greater energy density has triggered intensive research on high-voltage cathode materials.[6-11]

Lithium transition metal phosphates ($LiMPO_4$: M = Fe, Mn, Co, and Ni) represent a large class of Li-ion cathode materials. Out of all members of this family, $LiFePO_4$ (LFP) has been the most successful cathode so far for its high safety, low cost, excellent cyclability, and high power capability.[12-18] The LFP cathode has been heavily investigated and optimized but cannot provide high-energy density as demanded by the electromobility sector due to its low voltage. As a result, there has been a strong interest in developing the rest of $LiMPO_4$ cathode materials. In particular, $LiCoPO_4$ (LCP) has received much attention for its very high voltage of 4.8 V vs. $Li/Li^+$ (as compared to 3.5 V vs. $Li/Li^+$ for the commercially available LFP).[7, 10, 19-22] Having the same specific capacity as LFP (~167 mAh $g^{-1}$), the LCP cathode with a much higher operating voltage than LFP has a significantly increased theoretical energy density of 800 Wh $kg^{-1}$ vs. 590 Wh $kg^{-1}$ of LFP.[23-25] Also, similarly to LFP, the strong P–O bonds guarantee a robust host framework for Li-ion storage, resulting in excellent thermal safety.[26-28]

Hence, considerable work has been undertaken on developing LCP cathodes from various synthesis routes (*e.g.*, solid-state, sol-gel, or hydrothermal and solvothermal synthesis)[29-39] to crystal modification via doping[23, 24, 31, 33, 40, 41] and/or coating[29, 34, 37, 42, 43] approaches. Among the synthesis methods, the hydrothermal process has been suggested as the most cost-effective and energy-efficient one, as it employs water as a green solvent rather than organic solvents and chemicals.[44, 45] However, it has been found the hydrothermally synthesized LCP (HT-LCP) is characterized by poor electrochemical performance, as evidenced by low reversible discharge capacity compared to LCP made with a different method such as the solid-state method (SS-LCP).[34-37] Several arguments have been made in previous research to explain the poor electrochemical response of HT-LCP, ranging from electrolyte decomposition owing to the relatively higher potential of $Co^{2+}/Co^{3+}$ redox couple[34, 46, 47] to cation exchange (anti-site defects) developed during Li-ion intercalation process[32, 48, 49]. However, both issues, *i.e.*, the electrolyte decomposition and the cycling-induced cation exchange[50], are not observed only with HT-LCP but also with other LCP materials but not to the same extent[22]. Hence, there is a gap in understanding the origin of this poor electrochemical capacity problem exhibited by HT-LCP from a material chemistry standpoint.

Given the importance of the scalable and green process of hydrothermal (HT) synthesis in the development of functional high-voltage LCP cathodes, in this work, we have investigated the impact of key HT-synthesis parameters (Li molar ratio & pH value of precursor solutions) but also post-synthesis modifications (nanosizing by planetary-milling (PM) and carbon coating (C-coating)) on LCP crystal structure/morphology/purity and electrochemical storage properties. Upon monitoring the evolution of surface and bulk structure during material fabrication, the formation of defects was characterized, and its impact on Li-ion intercalation responsible for the low discharge capacity was determined. During the study, our particular attention was paid to differentiating the effect of electrolyte decomposition from the effects of LCP material defects. These findings open new avenues toward developing LCP cathodes with fully unlocked high-voltage capacity.

## 3.2. Experimental section

### 3.2.1. Material preparation

#### 3.2.1.1. Hydrothermal synthesis (HT-LCP)

HT-LCP was prepared with lithium hydroxide monohydrate (98 % $LiOH{\cdot}H_2O$, Sigma-Aldrich), cobalt (II) sulfate heptahydrate (99 % $CoSO_4{\cdot}7H_2O$, Sigma-Aldrich), phosphoric acid (85 % aqueous solution, $H_3PO_4$, Fisher Scientific), ammonium hydroxide solution (28.0-30.0 % $NH_3$ basis, $NH_4OH$, Sigma-Aldrich), and L-Ascorbic acid (99 % $C_6H_8O_6$, Sigma-Aldrich) as a reducing agent. All the chemicals were utilized without purification.

In typical experiments, solutions with different concentrations (0.4, 0.6, 0.8, 1.0, and 1.2 M) of $LiOH{\cdot}H_2O$ along 0.4 M of $CoSO_4{\cdot}7H_2O$, 0.4 M of $H_3PO_4$, and 0.0095 M of $C_6H_8O_6$ were prepared in 200 mL of deoxygenated and deionized water to give a different molar ratio of Li to cobalt (Co) namely 1:1, 1.5:1, 2:1, 2.5:1, and 3:1. The pH of the precursor solutions was controlled at 8, 9, and 10 with $NH_4OH$ added dropwise. The pH variations before and after HT-synthesis is measured and summarized in Table A.2.1. The prepared precursor solution was transferred afterward to a 450 mL stainless steel autoclave reactor (Parr Instruments, Moline, IL) equipped with a glass liner. The whole solution preparation procedure was carried out in a nitrogen ($N_2$)-filled glovebox to prevent possible Co oxidation from $Co^{2+}$ to $Co^{3+}$. Preliminary HT-synthesis done at different temperatures (data shown in Figure A.2.1) determined 220 ºC for 6 hours and 300 rpm impeller agitation to achieve uniform mixing of reactants and produced particles and was used throughout this study. Additionally, the exact temperature and pressure (psi) were monitored and controlled with Parr 4848 reactor controller during

the synthesis. After HT-reaction, the reactor vessel was quenched down to room temperature within 30 minutes through internal tube cooling water flowing. The synthesized solids were separated from the solution via centrifugation and then rinsed with deoxygenated and deionized water twice and with ethanol once, followed by evaporating the remained ethanol in a vacuum oven at 80 $^{o}$C overnight after several times purging with $N_2$ gas.

#### 3.2.1.2. Solid-state reaction (SS-LCP)

SS-LCP was prepared by mixing first stoichiometric amounts of 98 % of $LiOH \cdot H_2O$, cobalt (II, III) oxide ($Co_3O_4$, Sigma-Aldrich), and ammonium dihydrogen phosphate (99.999 % $NH_4H_2PO_4$, Sigma-Aldrich). After that, the mixture was subjected to wet grinding in PM with isopropanol ($(CH_3)_2CHOH$, Fisher Scientific) (Powder:Solvent = 1:2 volume ratio) at 300 rpm for 6 hours and subsequently dried in an oven at 50 $^{o}$C overnight. After chemical mixing and drying, two times of calcination processes with a ramping rate of 5 $^{o}$C $min^{-1}$ were accomplished at 400 $^{o}$C for 10 hours in air first to remove the crystal water and at 800 $^{o}$C for 10 hours in argon (Ar) atmosphere to obtain pure LCP phase.[29, 30]

#### 3.2.1.3. Post-synthesis treatment

To reduce the particle size of HT-LCP and SS-LCP, the Planetary Micro Mill PULVERISETTE 7 premium line (Fritsch) was utilized. Specifically, wet milling was conducted involving 7.5 mL of LCP sample (Tapped density: 0.87 g $mL^{-1}$) in 15 mL of isopropanol with 100 g of zirconium oxide ($ZrO_2$) grinding media (1 mm sized balls) loaded in 80 mL milling jars. The jar assembly was carried out in a $N_2$-filled glovebox to avoid oxidation of $Co^{2+}$. The sealed jars were transferred to the loading stations, and pulverization was done in cycles consisting of 3-minute milling and a 7-minute pause at 500 rpm. After pulverization, ground LCP samples were collected by centrifugation and followed by drying in vacuum oven at 80 $^{o}$C overnight after several times of purging with $N_2$ gas.

For the C-coating process, lactose anhydrous ($C_{12}H_{22}O_{11}$, Sigma-Aldrich) as a carbon source was dissolved and stirred in deoxygenated and deionized water with a concentration of 22.4 g $L^{-1}$ for 30 minutes.[51] Then, 5 mL of the lactose solution was applied to 1 g of pulverized LCP powder in a graphite crucible. The slurry was dried in a vacuum oven at 80 $^{o}$C and transferred to MTI mini tube furnace (model OTF-1200X), and heated consecutively at three different intervals (120 $^{o}$C-1 h, 400 $^{o}$C-1 h, and 700 $^{o}$C-3 h) for lactose decomposition and carbonization on the surface of pulverized LCP particles.

### 3.2.2. Materials characterization

Laboratory XRD was employed for phase analysis with Bruker D8 Discovery X-ray diffractometer using Co K-alpha source with wavelength (λ) of 1.78892 Å from 2θ = 10 to 80 °. The diffraction patterns were collected by using Gadd software. Defect concentration was fitted and estimated with XRD Rietveld refinement by using the TOPAS Academic V5 program. The morphology characterization was done with a Hitachi cold-field emission SU-8000 scanning electron microscope (CFE-SEM). Inductively coupled plasma optical emission spectroscopy (ICP-OES, Thermo Scientific iCAP 6500 ICP spectrometer) was applied to determine the concentration of remaining elements in solution after HT-synthesis but also to determine the exact elemental ratio of Co/Li in different LCP samples. Prior to ICP-OES measurements, LCP samples were digested by using 50 vol.% concentrated hydrochloric acid (HCl, Fisher Scientific) followed by dilution with 4 vol.% nitric acid (TraceMetal Grade, $HNO_3$, Fisher Scientific). Brunauer-Emmett-Teller (BET) specific surface area measurements were made by using the TriStar 3000 analyzer (Micromeritics) in $N_2$ (-196 °C). The size-distribution analysis of LCP particles was achieved with Zetasizer Nano ZS using the dynamic light scattering analysis. Raman Spectroscopy (Witec Alpha 3000) with 514 nm wavelength was applied to confirm the existence of carbon layers on the surface of pulverized LCP particles and its quality with a D/G ratio. Transmission electron microscope (TEM) and high-resolution TEM (HR-TEM) images were achieved through Thermo Scientific Talos F200X G2 STEM. X-ray Photoelectron Spectroscopy (XPS) measurements were carried out with Thermo-Scientific K-Alpha using aluminum (Al) K-alpha micro-focused monochromator. The applied X-ray spot size was 400 μm, and an electron flood gun was used for the charge compensation. The spectrometer energy scale was calibrated using C 1s characteristic peak at 284.8 eV (C-C) as a reference. XPS data processing was performed with the Avantage data analysis system for peak fitting of C 1s, Li 1s, Co 2p, P 2p, and O 1s spectra with single or multiple peaks. Fourier Transform Infrared (FT-IR) spectroscopy (Perkin Elmer Spectrum II FT-IR Spectrometer) was employed in the wavenumber range of 4000 to 400 $cm^{-1}$ with a resolution of 0.5 $cm^{-1}$.

### 3.2.3. Electrochemistry

Free-standing working electrodes without Al current collector were prepared with dry-method as follows: 70 wt.% of LCP active material was gently mixed with 20 wt.% of acetylene black (Alfa Aesar) with an average particle size of 60 nm and an area of 75 $m^2$ $g^{-1}$ via mild PM at 300 rpm for 1 h using 20 e.a. of 10 mm $ZrO_2$ grinding balls. After mixing, the jar was transferred and disassembled

in the glovebox filled with high-purity Ar gas. 10 wt.% of Polytetrafluoroethylene (PTFE, $(C_2F_4)_n$, DuPont, Teflon 8 A) binder was added to the mixed powder and subsequently spread with sufficient pressure through the hand-pressing process using stainless steel bar until a film with 0.16 $cm^2$ area and ~ 2.5 mg weight was obtained. A polypropylene film (Celgard 2200) was used as the separator. A custom-made electrolyte with stabilizing additive for high-voltage cathode operation was produced with 1.2 M of Lithium hexafluorophosphate (99.99 % Trace metals basis $LiPF_6$, Sigma-Aldrich) dissolved in a 3:7 (wt.%) mixture of ethylene carbonate (EC, 99 % $(CH_2O)_2CO$, Sigma-Aldrich) and ethyl methyl carbonate (EMC, 99 % $CH_3CH_2OCOOCH_3$, Sigma-Aldrich) plus 2 wt.% tris(trimethylsilyl) phosphite (95 % $[(CH_3)_3SiO]_3P$, Sigma-Aldrich).[41] The galvanostatic charge-discharge data was collected on an Arbin cycler. The battery cycling was carried out at a C/20 rate (1 C = 167 mAh $g^{-1}$) in the voltage range of 3.5–5.2 V vs. $Li/Li^+$ at room temperature. Cyclic voltammetry (CV) was performed by using an electrochemical workstation (Bio-Logic) at the specific conditions between 3.5-5.2 V with a scan rate of 0.1 mV $s^{-1}$. Electrochemical Impedance Spectroscopy (EIS) measurements of the pristine working electrodes were made after 6-hour relaxation in the equilibrium state in the potentiostat mode between 1 MHz and 10 mHz at open circuit voltage (OCV). The charge-transfer resistance was determined by fitting the Nyquist plot with the equivalent electric circuit by the Z-fit method provided by ZView® 4.0 software.

### 3.3. Results and discussion

#### 3.3.1. Hydrothermal synthesis parameter effects on crystal formation

To identify the conditions to synthesize high-purity HT-LCP at 220 ºC, we first investigated the effects of Li molar ratio (0.4. 0.6, 0.8, 1, and 1.2 M) and pH (8, 9, and 10) on LCP properties. The Li molar ratio was found to influence the crystallization of LCP, leading to cube-like shape crystals when added in 50 % Li excess (1.5:1:1) over the stoichiometry (1:1:1) (Figures 3.1a-d). Cubic shape crystal formation was completed with 100 % Li excess (2:1:1). It is postulated the cubic crystals grow via oriented attachment of the initially nucleating crystallites.[52-56] Further crystal growth was not observed if the Li excess was raised to 150 % excess (2.5:1:1), but instead, there was particle size reduction from 5 μm to less than 1 μm.

Figure 3.1e shows XRD patterns of HT-LCP materials made with different Li molar ratios at 220 ºC for 6 hours. The patterns of the HT-LCP materials prepared up to a 2.5:1:1 molar ratio can be clearly indexed to the orthorhombic phase with the space group, *pnma* (JCPDS 89-6192). Further, from the sharpening of the XRD peaks, we can see the crystallinity of LCP improves as the over-

stoichiometric Li ratio increases, consistent with the SEM image observations. However, if the Li ratio increases beyond 2.5:1:1, extra peaks appear, corresponding most likely to the formation of $Li_3PO_4$ (JCPDS 07-2815) and $Co_3O_4$ (JCPDS 78-1969). In addition, according to the residual element composition in the solution shown in Figure 3.1f, it can be seen the concentration of Co and P ($PO_4$) decreases with increasing Li concentration, implying the excess Li drives the reaction to a higher yield.

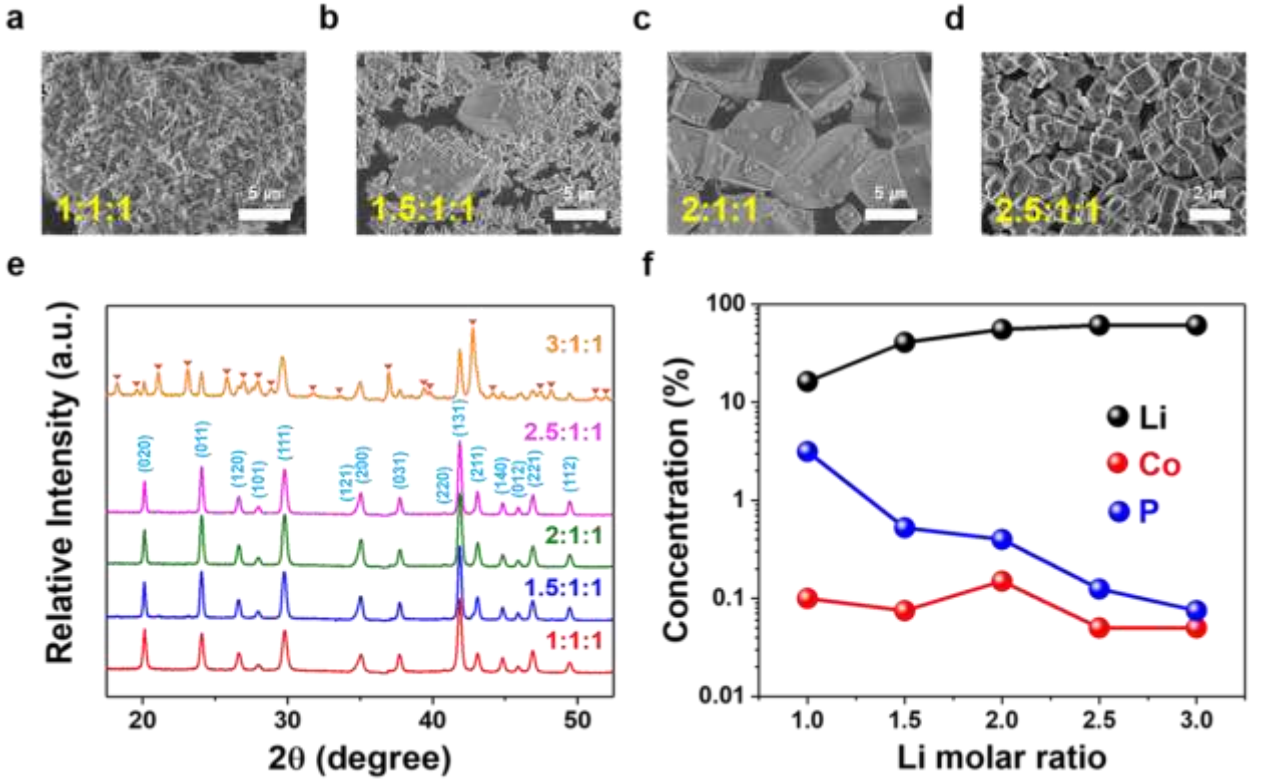


**Figure 3.1.** Morphology, phase, and residual solution composition of LCP materials obtained with different Li/Co/P molar ratios at pH 9 and 220 ºC via (a-d) SEM, (e) XRD, and (f) ICP-OES.

Other than pH 9, additional tests were performed with various Li molar ratios at pH 8 and 10, the results of which are shown in Figure A.2.2. In this case, all samples produced at pH 8 were found to contain impurities. Nanosized and pure LCP phase was produced (at a lower yield of 83 %), on the other hand, at pH 10, but this time, only when the precursor solution was prepared with the stoichiometric ratio of 1:1:1 (Figure A.2.3). Interestingly, in this case, as the Li ratio was increased above 1, the XRD patterns revealed the formation of amorphous LCP nanocrystals. Therefore, based on the above findings, we conclude that the optimal conditions for producing high-purity sub-micron size LCP crystals are with a 2.5:1:1 molar ratio and pH 9, denoted as "HT-LCP".

The formation of high-crystalline sub-micron-sized LCP cube-shaped particles using a 2.5:1:1 molar ratio at pH 9 and 220 ºC can be understood on the basis of governing nucleation & growth

kinetics.[57-59] The nucleation rate ($J$) as a function of supersaturation, $S$, is given by equation (1) described below,

$$J = A\ exp\left(-\frac{16\pi\gamma^3 v^2}{3{k_B}^3 T^3 (ln\ S)^2}\right) \quad (1)$$

where $J$ is nucleation rate, $A$ is the pre-exponential factor, $\gamma$ is the surface free energy per unit area, $v$ is molecular volume, $k_B$ is Boltzmann constant, $T$ is temperature, and $S$ is supersaturation (defined by equation (2)).

$$S = \alpha/\alpha_{eq} \quad (2)$$

where $a$ is the activity of solid species in solution ($= \alpha_{Li^+}.\alpha_{Co^{2+}}.\alpha_{{PO_4}^{3-}}$), $a_{eq}$ is the activity of the solid compound in saturated solution, *i.e.,* at equilibrium state represented by the solubility product: $K_{sp} = \alpha_{Li^+}.\alpha_{Co^{2+}}.\alpha_{{PO_4}^{3-}}$. The activity of $PO_4^{3-}$ anions ($\alpha_{{PO_4}^{3-}}$) meanwhile depends on pH value and temperature[60-62]:

$$H_3PO_4 = H_2PO_4^- + H^+ \quad K_1 = 7.52 \times 10^{-3}$$
$$H_2PO_4^- = HPO_4^{2-} + H^+ \quad K_2 = 6.23 \times 10^{-8}$$
$$HPO_4^{2-} = PO_4^{3-} + H^+ \quad K_3 = 4.80 \times 10^{-13}$$

It is postulated that at 220 °C and pH 9, $HPO_4^{2-}$ to dominate and thus maintain low $\alpha_{{PO_4}^{3-}}$,[62] hence the necessity of excess $\alpha_{Li^+}$ to modulate supersaturation which in turn controls the nucleation rate. This is a delicate equilibrium state as at pH 8, the appearance of impurity formation implies $\alpha_{{PO_4}^{3-}}$ to be too low, leading to parasitic reactions involving dihydrogen phosphate, while at pH 10 is too high; hence only stoichiometric amount of Li produced LCP. Excess Li apparently was counter-productive in the case of pH 10 solution as the high supersaturation regime resulted in the formation of amorphous LCP nanoparticles.

### 3.3.2. Post-synthesis LCP crystals modifications

Since the intrinsic ionic and electronic conductivities of LCP are low, it was decided to consider nanosizing (to boost ion conductivity) and carbon coating (to boost electron conductivity). Nanosizing of HT-LCP was induced by high energy planetary-milling (PM) at different times from 1 to 4 hours. The related size distribution, BET surface area, SEM, and XRD results are summarized in Figure 3.2a-c. According to size-distribution analysis (shown in Figure 3.2a), their mean size was reduced after 2 h of PM to around 200 nm (from 800 nm), and the corresponding specific surface area (Figure 3.2b) increased from 1.59 $m^2\ g^{-1}$ to 28.29 $m^2\ g^{-1}$. In addition, inset SEM images in Figure 3.2b show the morphology of the obtained particles after milling.

Meanwhile, as per XRD patterns (Figure 3.2c), nanosizing caused progressive crystal disordering with increasing milling time, as evidenced by the peak broadening, an observation that is in agreement with previous reports.[63] Of the different nanosized LCP materials, the one obtained after 2 h of PM (hereafter referred to as "HT-PM-LCP") was retained for subsequent electrochemical performance evaluation as it provided a short diffusion length without major loss of crystallinity. Finally, the nanosized HT-PM-LCP was subjected to C-coating by mixing the powder with lactose solution and annealing under an inert Ar atmosphere.[59] The planetary-milled/carbon-coated material was labeled "HT-PM-C-LCP".

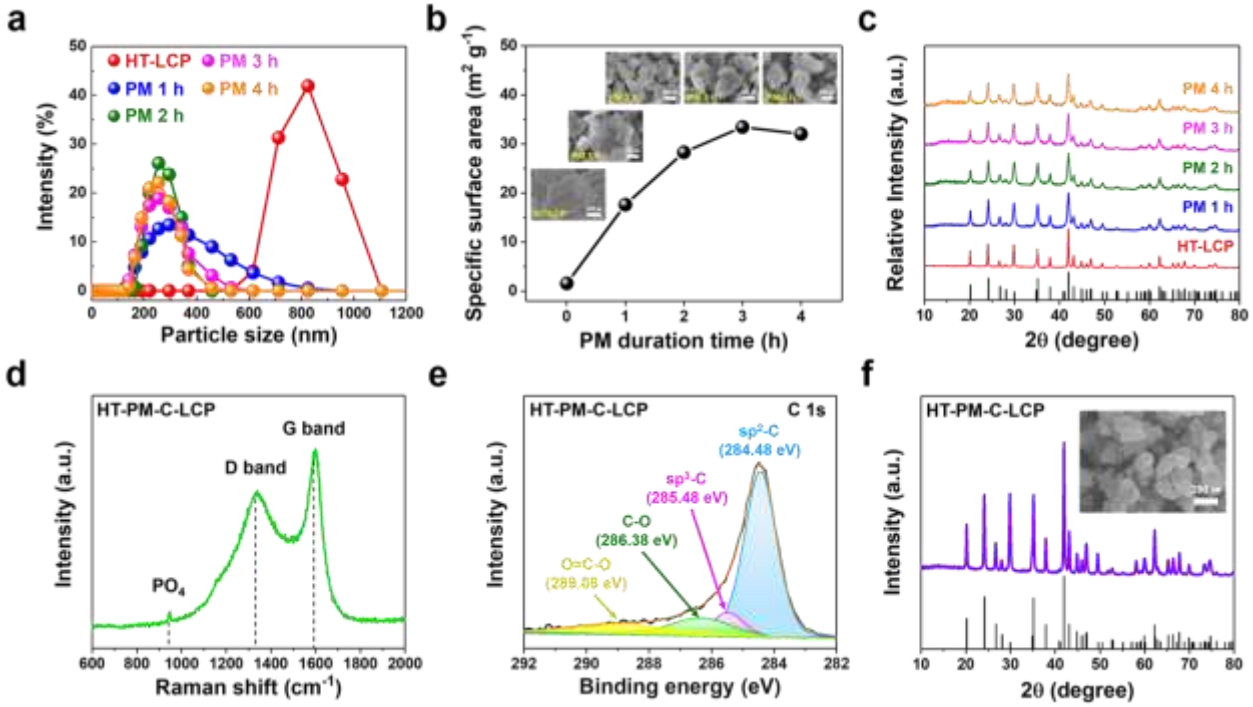


**Figure 3.2.** Characterization of HT-LCP crystals after post-synthesis modifications (High-energy PM and conductive C-coating) via (a) Size-distribution, (b) BET analysis, and (c) XRD with different milling duration time; (d) Raman, and (e) XPS C 1s spectra, (f) XRD.

Figure 3.2d shows the Raman spectra for HT-PM-C-LCP material recorded at the laser excitation wavelength of 514 nm. Three peaks with high intensity were clearly detected at 947.09, 1340.65, and 1590.10 $cm^{-1}$. The first peak in the 600-1100 $cm^{-1}$ region corresponds to the intramolecular stretching modes of the $PO_4$ group in LCP structure;[64] and the other two peaks indicate the presence of a carbon layer on the surface of HT-PM-LCP particles. These peaks are referred to as the "D" (1340 $cm^{-1}$) and "G" (1590 $cm^{-1}$) bands, respectively.[20, 65, 66] Hence, the carbon layer was favorably developed on the surface of HT-PM-LCP particles. The intensity ratio ($I_D/I_G$) from the deposited carbon layer was 0.77, indicating that the carbon layer mainly consists of disordered

carbon.[67] In order to further verify the nature of carbon, we performed XPS measurement on HT-PM-C-LCP. The C 1s spectrum (Figure 3.2e) was fitted with multiple peaks at different binding energies: $sp^2$ C-C at 284.48 eV, $sp^3$ C-C at 285.48 eV, C-O group at 286.38 eV, and O=C-O group at 289.08 eV, respectively.[68-70] By comparing the relative atomic ratios of $sp^2$ (88.92 %) and $sp^3$ (11.02 %), $sp^2$ representing C-C bonding is found to be dominant in the carbon layer on HT-PM-C-LCP over $sp^3$, which indicates C-H bonding. The XPS result is consistent with the $I_D/I_G$ in Raman analysis.

Moreover, as shown in Figure 3.2f, the phase and morphology of HT-PM-C-LCP were successfully preserved after C-coating without suffering agglomeration. In addition, the crystallinity was markedly restored due to the high-temperature treatment required for lactose decomposition and carbonization.[71]

In order to evaluate the impact of HT-synthesis on LCP crystal properties and electrochemistry, LCP material was also synthesized via conventional solid-state reaction.[29, 30] Again, three samples were prepared (summarized in Figure A.2.4), a pristine one (SS-LCP) and two after post-synthesis treatments (SS-PM-LCP and SS-PM-C-LCP).

### 3.3.3. Electrochemistry

After the satisfactory synthesis and post-synthesis modifications, we investigated the electrochemical properties of the differently prepared LCP materials either via HT-method or solid-state reaction so to probe synthesis-impacted LCP functionality. Galvanostatic charge-discharge tests were carried out at a C/20 rate within the voltage range of 3.5-5.2 V vs. $Li/Li^+$ at ambient (~22 ºC) temperature. The initial charge-discharge curves are summarized in Figure 3.3a-b. Despite the high purity and well-developed crystallinity of HT-LCP material, it exhibited a poor discharge capacity of only 33 mAh $g^{-1}$ (vis-a-vis the theoretical capacity of 167 mAh $g^{-1}$). The 1$^{st}$ discharge capacity was marginally increased to 53 mAh $g^{-1}$ after PM because of nanosizing (HT-PM-LCP), whereas the capacity was dropped to 25 mAh $g^{-1}$ after the subsequent C-coating process (HT-PM-C-LCP). In comparison, even with the agglomerated and larger particle size (shown in Figure A.2.4a), SS-LCP could deliver 53.3 mAh $g^{-1}$, while after the PM treatment (SS-PM-LCP), its discharge capacity was improved to 76.2 mAh $g^{-1}$ and after C-coating, registered a slightly dropped discharge capacity at 62 mAh $g^{-1}$. The unexpected drop in discharge capacity after carbon coating of the planetary-milled LCP obtained by both synthesis methods (HT and SS) is discussed later.

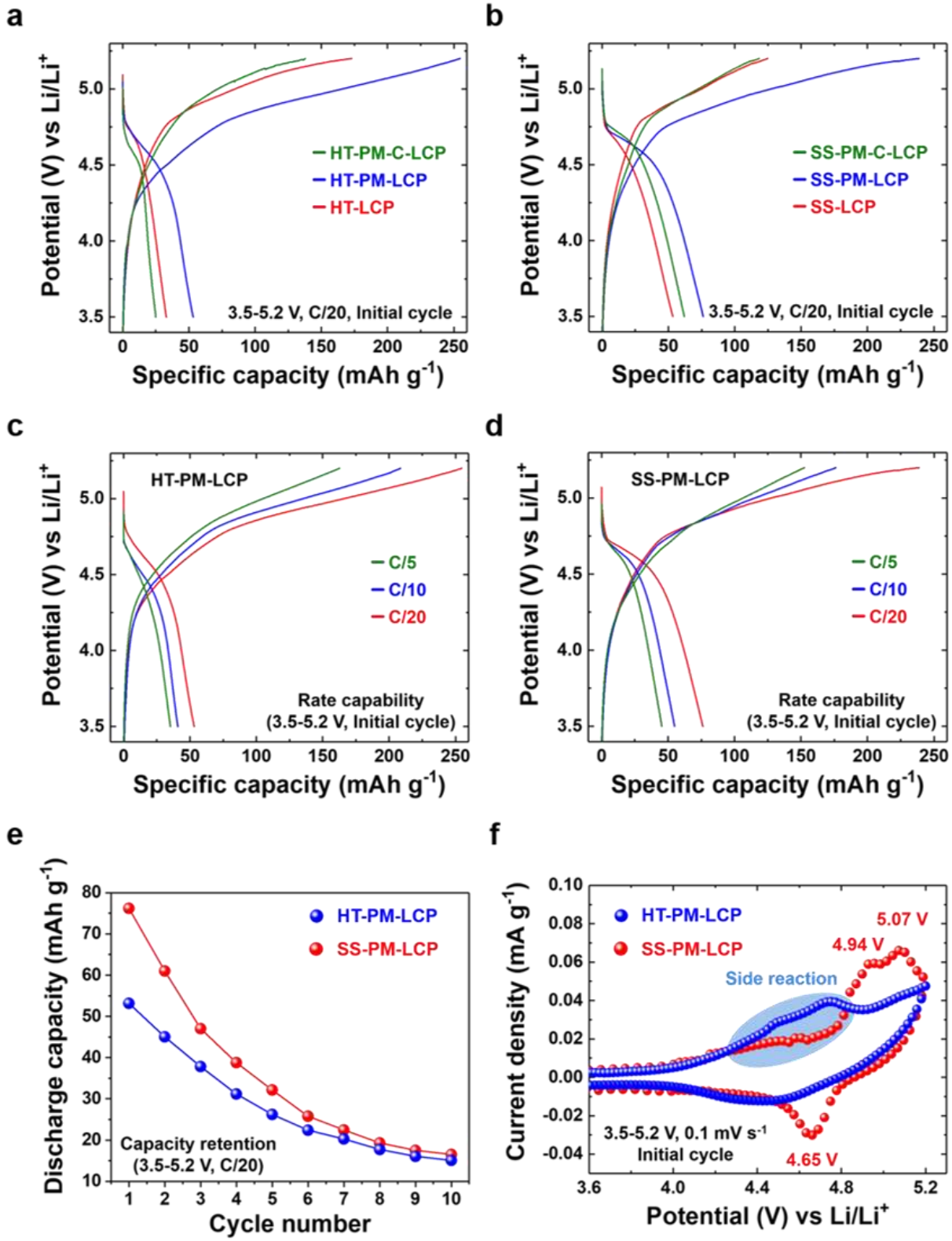


**Figure 3.3.** Comparison of the electrochemical properties of LCP materials obtained by hydrothermal (HT) and solid-state (SS) synthesis: (a-b) Galvanostatic charge-discharge, (c-d) Rate capability, (e) Capacity retention, and (f) Cyclic voltammetry (CV).

Figure 3.3c-d display the rate capability of HT-PM-LCP and SS-PM-LCP, which were found to deliver respectively the highest initial charge-discharge capacity among the different samples. As the C-rate is gradually increased, both milled LCP samples reveal significantly reduced initial discharge capacity of 53, 40.8, and 35.3 mAh $g^{-1}$ at C/20, C/10, and C/5 for HT-PM-LCP and 76, 54.9, and 45.3 mAh $g^{-1}$ for SS-PM-LCP. In addition, Figure 3.3e shows the capacity retention of HT-PM-LCP and SS-PM-LCP over 10 cycles. There is a severe capacity loss after 10 cycles, which at least in part is due to accelerated electrolyte decomposition at high voltage on the exposed surface of the nanosized LCP particles, as also observed by other researchers.[50, 72-74]

In order to probe further the origin of the observed poor discharge capacity and retention, cyclic voltammetry (Figure 3.3f) was performed over the 3.5-5.2 V range at a scan rate of 0.1 mV $s^{-1}$. During the anodic sweep, SS-PM-LCP exhibits two distinct oxidation peaks at 4.94 and 5.07 V vs. $Li/Li^+$. This two-step delithiation process is consistent with the formation of the previously identified intermediate phase with the stoichiometry $Li_{2/3}(Co^{2+})_{2/3}(Co^{3+})_{1/3}PO_4$.[25, 75, 76] However, during the cathodic sweep, only one reduction peak is observed (corresponding to $Co^{2+/3+}$) at 4.65 V vs. $Li/Li^+$ and a rather high polarization of 0.42 V. By comparison, the current linked to the redox couple of $Co^{2+/3+}$ is substantially depressed for HT-PM-LCP. In addition, there is no clear peak during both oxidation and reduction processes. This broad curve feature obviously reflects a rather hampered Li-ion intercalation. Moreover, we noticed the magnitude of electrolyte decomposition to be more prominent in HT-PM-LCP than in SS-PM-LCP above 4.3 V vs. $Li/Li^+$ (marked with blue-colored area in Figure 3.3f) despite the use of stabilizing additive tris(trimethylsilyl) phosphite suggested by Allen et al.[42]. Although side reactions with electrolyte due to the LCP nanosizing are expected[40, 72, 77], the contrasting redox activity difference between the HT and SS samples points to other possible causes.

Hence, overall, we find poor cycling performance in the HT-synthesized LCP samples regardless of post-synthesis treatment, which is worse than that of the SS-synthesized LCP sample. Thus, elucidating the intrinsic material chemistry factors responsible for the poor charge-transfer kinetics and Li-ion storage of LCP is critical to unlocking its full theoretical capacity.

### 3.3.4. Nanoscale $Co(OH)_2$ layer on the surface of HT-LCP

To investigate the factors that limit the performance of HT-LCP, we first performed TEM and HRTEM on a HT-LCP particle to see if there were any structural defects. As per Figure A.2.5a, HT-LCP crystal *d*-spacing is 1.02 nm, which corresponds to the (100) plane of the LCP *pnma* space group. In addition, the SAED pattern shown in Figure A.2.5b indicates that HT-LCP consists of a single-

crystal motif.[72] However, we discovered the existence of a nearly 3.8 nm thick surface layer covering the whole HT-LCP particle, as shown in Figure 3.4a-b, which might be interfering with the electrochemical performance of HT-LCP by increasing charge-transfer resistance.

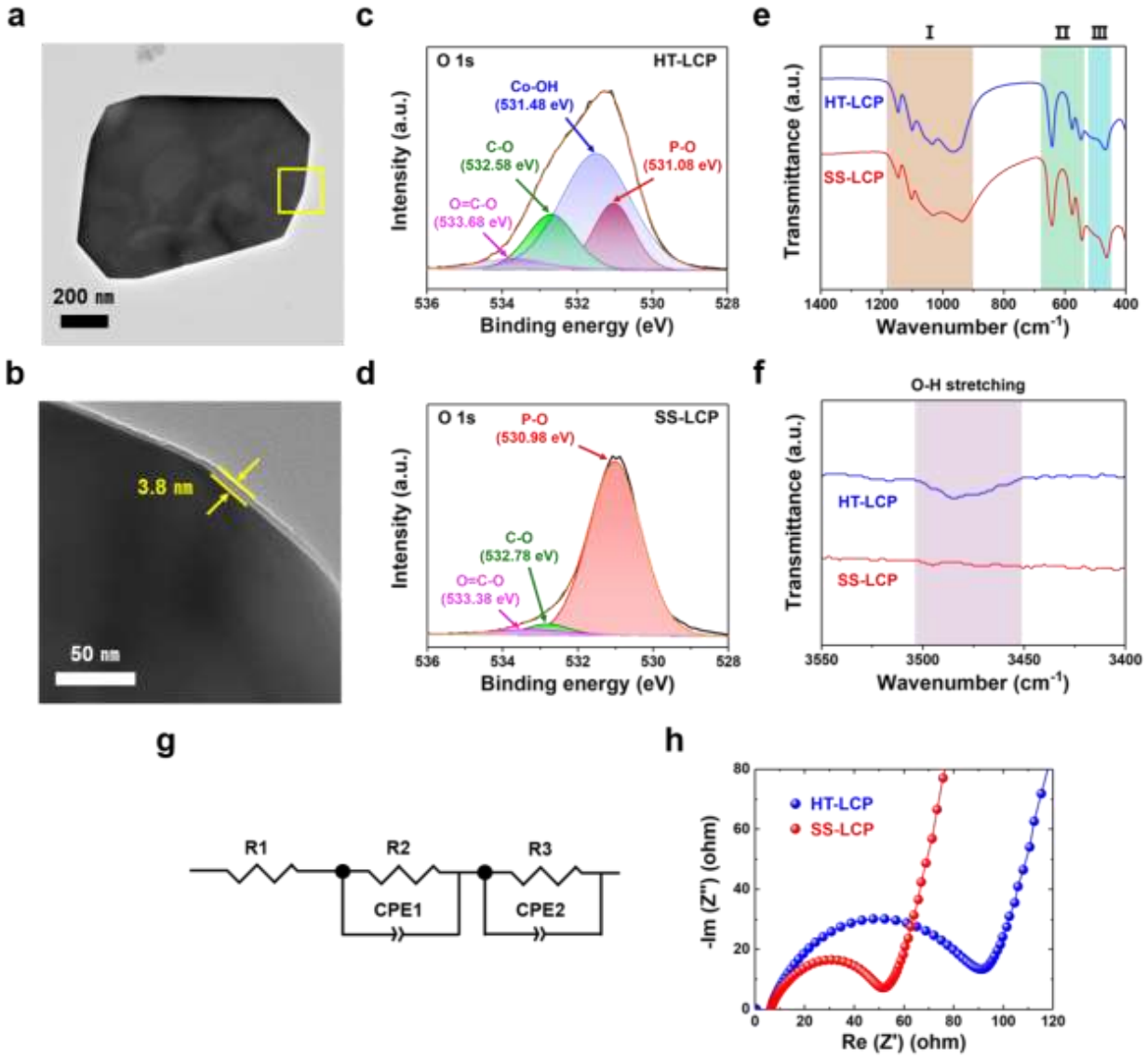


**Figure 3.4.** Characterization of nano-scale $Co(OH)_2$ layer on the surface of HT-LCP. (a-b) TEM and HRTEM images of HT-LCP; (c-d) XPS O 1s and (e-f) FTIR spectra of HT-LCP and SS-LCP; (g-h) Nyquist plots of pristine HT-LCP and SS-LCP electrodes with equivalent circuit used to fit the EIS model.

To understand the nature of the surface layer, we performed XPS on HT-LCP and SS-LCP (Figures A.2.6 and A.2.7). The chemical composition of the surface area is clearly comprising Li, Co, P, and oxygen (O) in both LCP samples, and the corresponding peaks can be associated with the binding energies of Li 1s, Co 2p, P 2p, O 1s, and C 1s. The high-resolution spectra of Co 2p, O 1s, and C 1s were fitted with the Gaussian method. The Co 2p spectrum is resolved into Co $2p_{3/2}$ and Co

$2p_{1/2}$ contributions centered at 780.88 and 797.28 eV for HT-LCP and 781.18 and 797.58 eV for SS-LCP, which can be ascribed to the $Co^{2+}$ in LCP crystal structure.[78-80] However, Figure 3.4c-d reveals different chemical environments for O in the surface of HT-LCP and SS-LCP in regard to the high-resolution spectrum and curve fitting of O 1s. SS-LCP shows three deconvoluted O 1s peaks from the polyanion phosphate group ($PO_4^{3-}$) group (530.98 eV), the C-O bonding (532.78 eV), and the O=C-O bonding (533.38 eV) from surface contaminations. Yet, there is another O discernible peak in HT-LCP with binding energy of 531.48 eV indicative cobalt hydroxide (Co-OH) group.[81-84] This result clearly thus identifies the thin surface layer on HT-LCP particles (as seen in TEM images) to be made up of $Co(OH)_2$.

In addition, HT-LCP was subjected to XPS depth profile analysis with the integration of mild beam energy (200 eV) and Ar ion etching every 20 seconds, shown in Figure A.2.8. The profile result shows that the area under the fitting curve indicating nano-scale $Co(OH)_2$ progressively decreases and entirely disappears after 80-second etching. We propose that the nano-scale $Co(OH)_2$ layer forms via a side reaction after hydrothermal synthesis favored by the alkaline solution pH.

We also performed FT-IR to verify the presence of nano-scale $Co(OH)_2$ layer on HT-LCP particles. Figure 3.4e-f shows the FT-IR spectra of HT-LCP in comparison to those of SS-LCP. The spectra for both HT-LCP and SS-LCP samples in the lower wavenumber region are mainly dominated by the vibrations from the stretching and bending modes of $PO_4^{3-}$ guaranteeing the stable framework and the translational vibrations of Li-ion[20, 85, 86]: I) The broad band between 900–1100 $cm^{-1}$ and 1050–1150 $cm^{-1}$ corresponding to the symmetric and asymmetric stretching of $PO_4^{3-}$, respectively. II) The peaks around 500–700 $cm^{-1}$ are attributed to the bending vibration mode of $PO_4^{3-}$. III). And the two peaks at 499 and 463 are derived from the translational vibrations of Li-ion adjacent to the oxygen atoms in the orthorhombic structure. However, we note that only HT-LCP shows the weakened O-H stretching band at 3484 $cm^{-1}$ originating from the surface $Co(OH)_2$ layer in the higher wavenumber region. These findings are further consistent with our XPS results (Figure 3.4c-d), proving the existence of nano-scale $Co(OH)_2$ layer on the HT-LCP surface.

To study the impact of nano-scale $Co(OH)_2$ layer on the electrochemical functionality of HT-LCP, as-made HT-LCP, and SS-LCP electrodes were subjected to EIS analysis. A direct comparison between the two electrodes is made with the Nyquist plots in Figure 3.4g-h, where the EIS results are plotted together with the equivalent circuit model. Notably, HT-LCP displays a higher charge-transfer resistance (90.96 Ω) compared to SS-LCP (51.84 Ω), as can be inferred from the relative size of the semicircle in the high-frequency region.[87] This result shows that the nano-scale $Co(OH)_2$ layer on the

HT-LCP acts as a passivation layer hampering charge transfer at the cathode/electrolyte interface and, as a consequence, resulting in poorer cycling performance compared to SS-LCP without the surface layer.

We note that the alkaline precursor solution with a high pH value above 8 creates an environment for $Co(OH)_2$ formation, as indicated in the Pourbaix diagram of cobalt at 298.15 K (Figure A.2.9)[88, 89] explaining why our HT-LCP has the $Co(OH)_2$ surface layer. It is hypothesized residual $Co^{2+}$ ions in hydrothermal solution adsorb on the surface of the precipitated LCP crystals and following surface hydrolysis due to high pH to form the *in-situ* nano-scale $Co(OH)_2$ layer. The $Co(OH)_2$ layer would not have been a problem if $Co(OH)_2$ were a fast Li-ion conductor. However, it is known that $Co(OH)_2$ works as an anode material that goes through a sluggish conversion reaction at the lower voltage window (0.0 – 3.0 V vs. $Li/Li^+$)[90-92], which is below the operating potential of LCP. Therefore, this nano-scale $Co(OH)_2$ layer would serve as an insulating layer during the cycling of LCP, consistent with the observed increased charge-transfer resistance for the HT-LCP compared to SS-LCP.

Meanwhile, since PM of the as-made HT-LCP particles should damage and at least partially remove the surface $Co(OH)_2$ layer (Figure A.2.10), it explains, other than nanosizing, why HT-PM-LCP delivers a higher capacity. However, still, the capacity of HT-PM-LCP is significantly below the theoretical one, implying that there must be other factors than the surface layer that further limit its cycling performance.

### 3.3.5. Anti-site defect evolution in HT-LCP

To probe other factors that may limit the cycling performance of HT-LCP, we tracked the defect concentrations in the bulk LCP crystal structure by applying XRD and ICP-OES techniques.[32, 48, 49, 93, 94] Figure 3.5 shows the abundance of the anti-site defects (*i.e.*, Co in Li site) and excess Co (*i.e.*, excess amount of Co compared to the desired Li:Co = 1:1 ratio) in our LCP materials, extracted via XRD Rietveld refinement (also shown in Figure A.2.11) and ICP-OES analysis, respectively. Noticeably, pristine HT-LCP (9.14 %) has a high anti-site defect concentration nearly six times higher than that of pristine SS-LCP (1.73 %). Such a significant amount of anti-site defects (9.14 %) greatly limits 1-D Li-ion diffusion in the olivine structure, which constitutes another limiting factor explaining the small capacity in pristine HT-LCP samples.

In terms of anti-site defect evolution induced by PM and C-coating treatment steps, HT-LCP exhibits a modest increase from 9.63 to 10.52 %. By comparison, anti-site defects in SS-LCP increased

from 1.73 % to 7.29 and 7.46 % after the post-synthesis treatments. As mentioned earlier, PM causes a degree of disordering mobilizing the movement of ions hence introducing defects that seem to persist even after the C-coating at elevated temperature. Thus, it is reasonable to suspect that anti-site defects obtained during synthesis remained critical obstacles impeding Li-ion diffusion, and other than conventional annealing strategies need to be explored.

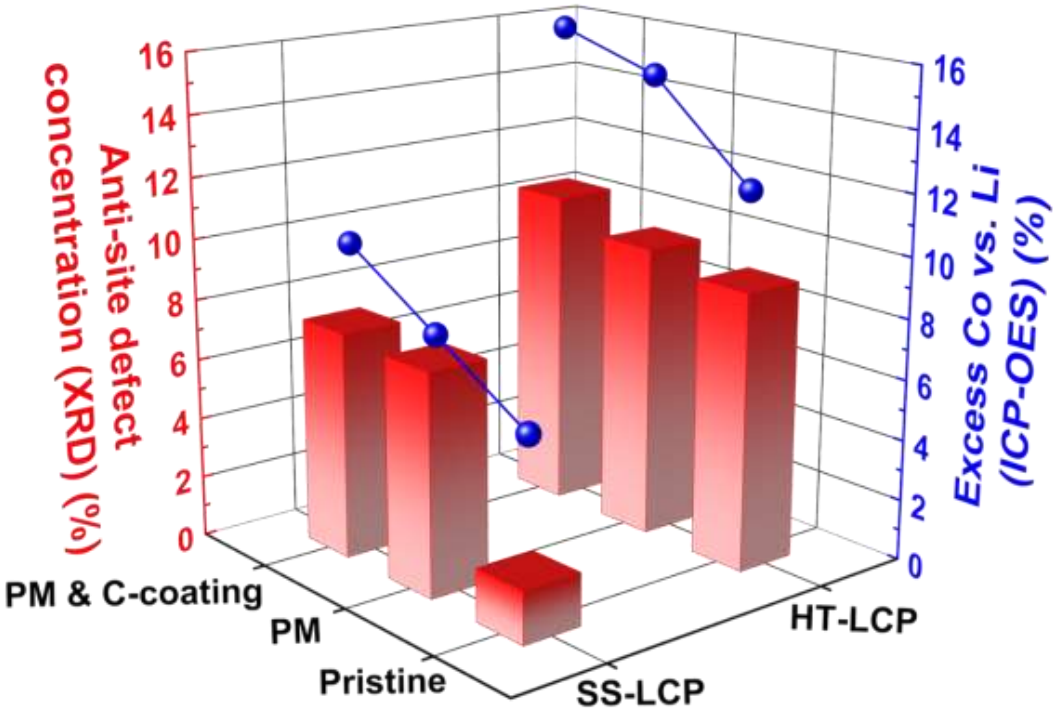


**Figure 3.5.** Anti-site defect concentration (Red bar) and excess Co (Blue sphere) calculated with XRD Rietveld refinement and ICP-OES analysis**.**

The ICP-OES results show that hydrothermal synthesis resulted in significant excess of Co (vs. Li) in HT-LCP composition (12.47 %) compared to SS-LCP (6.4 %). Since excess Co ions would occupy other cation sites than the original Co sites (thus Li sites), the greater excess Co found from HT-LCP than SS-LCP is consistent with the XRD Rietveld refinement results showing more anti-site defects (Co in Li sites) in HT-LCP. It must be noted that we used 150 % excess Li (Li:Co:P = 2.5:1:1) in the precursor solution. Thus, it is surprising to observe Co excess instead of Li excess in HT-LCP, implying that this issue does not simply arise from the precursor ratio in the HT solution. Instead, this problem might be related to the nucleation and growth mechanism during the HT-synthesis, which limits full Li-ion incorporation to the Co-P-O intermediate species needed to form stoichiometric LCP. Finally, we note that the excess Co values increased after the post-synthesis treatments (HT-PM-LCP: 14.78 %, HT-PM-C-LCP: 15.72 %, and SS-PM-LCP: 7.90 %, SS-PM-C-LCP: 10.16 %) following a similar trend with anti-site defect concentration. This increasing excess Co after post-synthesis

treatments may be due to the loss of Li-ion to the isopropanol solvent used during PM or Li-ion evaporation upon the C-coating process at a high temperature.

Note that as LCP is a 1-D Li-ion diffusion material[26, 95-97], keeping its stoichiometry would be critical to achieving high capacity because off-stoichiometry can either (i) block Li-ion diffusion in the crystal structure (found in Co-rich LCP such as $Li_{0.8}Co_{1.1}PO_4$, excess Co in Li sites would block Li-ion diffusion) or (ii) limit the transition metal redox capacity (found in Li-rich LCP, *e.g.*, $Li_{1.1}[Co^{2+}_{0.8}Co^{3+}_{0.1}]PO_4$, excess Li in Co sites which would increase the average Co oxidation state and decrease the Co-redox capacity). Our experiments suggest that off-stoichiometry from excess Co is another critical problem to overcome if HT-synthesis is to be used.

Overall, our experiments reveal two critical limitations of using the HT-synthesis of LCP. Although HT-synthesis can be green and has some important advantages (*e.g.*, relatively easy control of particle size and morphology) over other synthesis methods, we reveal that a high pH value (pH 9) during the HT-synthesis (which is needed to form a high-purity and well crystalline LCP powder) also creates an environment that favors the nano-scale $Co(OH)_2$ formation on the LCP particle surface introducing severe charge-transfer resistance. Moreover, even with the use of "excess Li" in the precursor solution, we reveal that HT-synthesis leads to the formation of LCP with "excess Co", which introduces a large occurrence of anti-site defects in the bulk LCP crystal structure, significantly limiting the 1-D Li-ion diffusion. Avoidance of these stumbling blocks via modifications to the hydrothermal synthesis process or adoption of water-free synthesis routes should be pursued.

### 3.4. Conclusion

In conclusion, we successfully synthesized high-purity and single-crystal $LiCoPO_4$ material (HT-LCP) with sub-micron particle size via HT-method by controlling the degree of supersaturation with over-stoichiometric Li contents (Li:Co:P = 2.5:1:1) and pH value of precursor solution 9 at 220 ºC. Also, we applied nanosizing by planetary-milling and C-coating on the HT-LCP to enhance its discharge capacity via shortening its diffusion length and increasing electron conductivity but with only partial success. Via a suite of surface and bulk crystal characterizations coupled with electrochemical analysis, we discovered hydrothermal synthesis to lead to (i) the formation of resistive nano-scale $Co(OH)_2$ surface passivation layer and (ii) abundant anti-site defects arising from excess Co in HT-LCP samples compared to SS-LCP samples. These findings should allow for new routes to be explored so we ultimately design processes for achieving the full high-voltage capacity of $LiCoPO_4$ and other types of polyanionic cathode materials.

### 3.5. References


1. G. E. Blomgren, The development and future of lithium-ion batteries. *Journal of The Electrochemical Society* **2016**, *164* (1), A5019-A5025.
2. V. Sivaram, J. O. Dabiri, D. M. Hart, The need for continued innovation in solar, wind, and energy storage. *Joule* **2018**, *2* (9), 1639-1642.
3. Y. Miao, P. Hynan, A. von Jouanne, A. Yokochi, Current Li-ion battery technologies in electric vehicles and opportunities for advancements. *Energies* **2019**, *12* (6), 1074.
4. C. Xu, Q. Dai, L. Gaines, M. Hu, A. Tukker, B. Steubing, Future material demand for automotive lithium-based batteries. *Communications Materials* **2020**, *1* (99), 1-10.
5. A. Masias, J. Marcicki, W. A. Paxton, Opportunities and challenges of lithium-ion batteries in automotive applications. *ACS Energy Letters* **2021**, *6* (2), 621-630.
6. D. Andre, S.-J. Kim, P. Lamp, S. F. Lux, F. Maglia, O. Paschos, B. Stiaszny, Future generations of cathode materials: an automotive industry perspective. *Journal of Materials Chemistry A* **2015**, *3* (13), 6709-6732.
7. W. Li, B. Song, A. Manthiram, High-voltage positive electrode materials for lithium-ion batteries. *Chemical Society Reviews* **2017**, *46* (10), 3006-3059.
8. S. Zhang, J. Ma, Z. Hu, G. Cui, L. Chen, Identifying and addressing critical challenges of high-voltage layered ternary oxide cathode materials. *Chemistry of Materials* **2019**, *31* (16), 6033-6065.
9. E. M. Erickson, W. Li, A. Dolocan, A. Manthiram, Insights into the cathode-tlectrolyte interphases of high-energy-density cathodes in lithium-ion batteries. *ACS Applied Materials & Interfaces* **2020**, *12* (14), 16451-16461.
10. J. Ling, C. Karuppiah, S. G. Krishnan, M. V. Reddy, I. I. Misnon, M. H. Ab Rahim, C.-C. Yang, R. Jose, Phosphate polyanion materials as high-voltage lithium-ion battery cathode: A review. *Energy & Fuels* **2021**, *35* (13), 10428-10450.
11. S. Zhao, Z. Guo, K. Yan, S. Wan, F. He, B. Sun, G. Wang, Towards high-energy-density lithium-ion batteries: Strategies for developing high-capacity lithium-rich cathode materials. *Energy Storage Materials* **2021**, *34*, 716-734.
12. K. Striebel, J. Shim, A. Sierra, H. Yang, X. Song, R. Kostecki, K. McCarthy, The development of low cost $LiFePO_4$-based high power lithium-ion batteries. *Journal of Power Sources* **2005**, *146* (1-2), 33-38.
13. K. Zaghib, J. Dubé, A. Dallaire, K. Galoustov, A. Guerfi, M. Ramanathan, A. Benmayza, J. Prakash, A. Mauger, C. M. Julien, Enhanced thermal safety and high-power performance of carbon-coated $LiFePO_4$ olivine cathode for Li-ion batteries. *Journal of Power Sources* **2012**, *219*, 36-44.
14. C. Sun, S. Rajasekhara, J. B. Goodenough, F. Zhou, Monodisperse porous $LiFePO_4$ microspheres for a high-power Li-ion battery cathode. *Journal of the American Chemical Society* **2011**, *133* (7), 2132-5.
15. S. Wang, L. Lu, X. Liu, A simulation on safety of $LiFePO_4$/C cell using electrochemical–thermal coupling model. *Journal of Power Sources* **2013**, *244*, 101-108.
16. H. Huang, S. C. Yin, L. F. Nazar, Approaching theoretical capacity of $LiFePO_4$ at room temperature at high rates. *Electrochemical and Solid-State Letters* **2001**, *4* (10) A170.
17. S. Lim, C. S. Yoon, J. Cho, Synthesis of nanowire and hollow $LiFePO_4$ cathodes for high-performance lithium batteries. *Chemistry of Materials* **2008**, *20*, 4560-4564.
18. K. Zaghib, A. Guerfi, P. Hovington, A. Vijh, M. Trudeau, A. Mauger, J. B. Goodenough, C. M. Julien, Review and analysis of nanostructured olivine-based lithium recheargeable batteries: Status and trends. *Journal of Power Sources* **2013**, *232*, 357-369.

19. G. Hautier, A. Jain, S. P. Ong, B. Kang, C. Moore, R. Doe, G. Ceder, Phosphates as lithium-ion battery cathodes: An evaluation based on high-throughput *ab initio* calculations. *Chemistry of Materials* **2011**, *23* (15), 3495-3508.
20. Q. D. Truong, M. K. Devaraju, Y. Ganbe, T. Tomai, I. Honma, Controlling the shape of $LiCoPO_4$ nanocrystals by supercritical fluid process for enhanced energy storage properties. *Scientific Reports* **2014**, *4*, 3975.
21. K. Amine, H. Yasuda, M. Yamachi, Olivine $LiCoPO_4$ as 4.8 V electrode material for lithium batteries. *Electrochemical and Solid-State Letters* **2000**, *3*, 178.
22. M. Zhang, N. Garcia-Araez, A. L. Hector, Understanding and development of olivine $LiCoPO_4$ cathode materials for lithium-ion batteries. *Journal of Materials Chemistry A* **2018**, *6* (30), 14483-14517.
23. D. Liu, W. Zhu, C. Kim, M. Cho, A. Guerfi, S. A. Delp, J. L. Allen, T. R. Jow, K. Zaghib, High-energy lithium-ion battery using substituted $LiCoPO_4$: From coin type to 1 Ah cell. *Journal of Power Sources* **2018**, *388*, 52-56.
24. D.-W. Han, Y.-M. Kang, R.-Z. Yin, M.-S. Song, H.-S. Kwon, Effects of Fe doping on the electrochemical performance of $LiCoPO_4$/C composites for high power-density cathode materials. *Electrochemistry Communications* **2009**, *11* (1), 137-140.
25. F. C. Strobridge, R. J. Clement, M. Leskes, D. S. Middlemiss, O. J. Borkiewicz, K. M. Wiaderek, K. W. Chapman, P. J. Chupas, C. P. Grey, Identifying the structure of the intermediate, $Li_{2/3}CoPO_4$, formed during electrochemical cycling of $LiCoPO_4$. *Chemistry of Materials* **2014**, *26* (21), 6193-6205.
26. C. A. J. Fisher, V. M. H. Prieto, M. S. Islam, Lithium battery materials $LiMPO_4$ (M = Mn, Fe, Co, and Ni): Insights into defect association, transport mechanisms, and doping behavior. *Chemistry of Materials* **2008**, *20*, 5907-5915.
27. N. N. Bramnik, K. Nikolowski, D. M. Trots, H. Ehrenberg, Thermal stability of $LiCoPO_4$ cathodes. *Electrochemical and Solid-State Letters* **2008**, *11* (6), A89.
28. S. Theil, M. Fleischhammer, P. Axmann, M. Wohlfahrt-Mehrens, Experimental investigations on the electrochemical and thermal behaviour of $LiCoPO_4$-based cathode. *Journal of Power Sources* **2013**, *222*, 72-78.
29. I. C. Jang, H. H. Lim, S. B. Lee, K. Karthikeyan, V. Aravindan, K. S. Kang, W. S. Yoon, W. I. Cho, Y. S. Lee, Preparation of $LiCoPO_4$ and $LiFePO_4$ coated $LiCoPO_4$ materials with improved battery performance. *Journal of Alloys and Compounds* **2010**, *497* (1-2), 321-324.
30. A. Freiberg, M. Metzger, D. Haering, S. Bretzke, S. Puravankara, T. Nilges, C. Stinner, C. Marino, H. A. Gasteiger, Anodic decomposition of trimethylboroxine as additive for high voltage Li-ion batteries. *Journal of The Electrochemical Society* **2014**, *161* (14), A2255-A2261.
31. S. M. G. Yang, V. Aravindan, W. I. Cho, D. R. Chang, H. S. Kim, Y. S. Lee, Realizing the performance of $LiCoPO_4$ cathodes by Fe substitution with off-Stoichiometry. *Journal of The Electrochemical Society* **2012**, *159* (7), A1013-A1018.
32. Q. D. Truong, M. K. Devaraju, T. Tomai, I. Honma, Direct observation of antisite defects in $LiCoPO_4$ cathode materials by annular dark- and bright-field electron microscopy. *ACS Applied Materials & Interfaces* **2013**, *5* (20), 9926-32.
33. R. Hanafusa, Y. Oka, T. Nakamura, Electrochemical and magnetic studies of Li-deficient $Li_{1-x}Co_{1-x}Fe_xPO_4$ olivine cathode compounds. *Journal of The Electrochemical Society* **2015**, *162* (2), A3045-A3051.
34. A. V. Murugan, T. Muraliganth, A. Manthiram, One-pot microwave-hydrothermal synthesis and characterization of carbon-coated $LiMPO_4$ (M = Mn, Fe, and Co) cathodes. *Journal of The Electrochemical Society* **2009**, *156* (2), A79.

35. Y. Zhao, S. Wang, C. Zhao, D. Xia, Synthesis and electrochemical performance of $LiCoPO_4$ micron-rods by dispersant-aided hydrothermal method for lithium-ion batteries. *Rare Metals* **2009**, *28* (2), 117-121.
36. C. Neef, H.-P. Meyer, R. Klingeler, Morphology-controlled two-step synthesis and electrochemical studies on hierarchically structured $LiCoPO_4$. *Solid State Sciences* **2015**, *48*, 270-277.
37. Y. Maeyoshi, S. Miyamoto, Y. Noda, H. Munakata, K. Kanamura, Effect of organic additives on characteristics of carbon-coated $LiCoPO_4$ synthesized by hydrothermal method. *Journal of Power Sources* **2017**, *337*, 92-99.
38. J. Ludwig, C. Marino, D. Haering, C. Stinner, D. Nordlund, M. M. Doeff, H. A. Gasteiger, T. Nilges, Facile, ethylene glycol-promoted microwave-assisted solvothermal synthesis of high-performance $LiCoPO_4$ as a high-voltage cathode material for lithium-ion batteries. *RSC Advances* **2016**, *6* (86), 82984-82994.
39. X. Wu, M. Meledina, H. Tempel, H. Kungl, J. Mayer, R.-A. Eichel, Morphology-controllable synthesis of $LiCoPO_4$ and its influence on electrochemical performance for high-voltage lithium-ion batteries. *Journal of Power Sources* **2020**, *450*, 227726.
40. D. Liu, C. Kim, A. Perea, D. Joel, W. Zhu, S. Collin-Martin, A. Forand, M. Dontigny, C. Gagnon, H. Demers, S. Delp, J. Allen, R. Jow, K. Zaghib, High-voltage lithium-ion battery using substituted $LiCoPO_4$: Electrochemical and safety performance of 1.2 Ah Pouch Cell. *Materials* **2020**, *13* (19), 4450.
41. J. L. Allen, J. L. Allen, T. Thompson, S. A. Delp, J. Wolfenstine, T. R. Jow, Cr and Si substituted-$LiCo_{0.9}Fe_{0.1}PO_4$: Structure, full and half Li-ion cell performance. *Journal of Power Sources* **2016**, *327*, 229-234.
42. K. J. Kreder, A. Manthiram, Vanadium-substituted $LiCoPO_4$ core with a monolithic $LiFePO_4$ shell for high-voltage lithium-ion batteries. *ACS Energy Letters* **2016**, *2* (1), 64-69.
43. Y. Wang, J. Chen, J. Qiu, Z. Yu, H. Ming, M. Li, S. Zhang, Y. Yang, Cr-substituted $LiCoPO_4$ core with a conductive carbon layer towards high-voltage lithium-ion batteries. *Journal of Solid-State Chemistry* **2018**, *258*, 32-41.
44. J. A. Darr, J. Zhang, N. M. Makwana, X. Weng, Continuous hydrothermal synthesis of inorganic nanoparticles: Applications and future directions. *Chemical Reviews* **2017**, *117* (17), 11125-11238.
45. M. K. Devaraju, I. Honma, Hydrothermal and solvothermal process towards development of $LiMPO_4$ (M = Fe, Mn) nanomaterials for lithium-ion batteries. *Advanced Energy Materials* **2012**, *2* (3), 284-297.
46. N. N. Bramnik, K. Nikolowski, C. Baehtz, K. G. Bramnik, H. Ehrenberg, Phase transitions occurring upon lithium insertion-extraction of $LiCoPO_4$. *Chemistry of Materials* **2007**, *19*, 908-915.
47. Y. Wang, H. Ming, J. Qiu, Z. Yu, M. Li, S. Zhang, Y. Yang, Improving cycling performance of $LiCoPO_4$ cathode material by adding tris(trimethylsilyl) borate as electrolyte additive. *Journal of Electroanalytical Chemistry* **2017**, *802*, 8-14.
48. M. K. Devaraju, Q. D. Truong, T. Tomai, H. Hyodo, Y. Sasaki, I. Honma, Antisite defects in $LiCoPO_4$ nanocrystals synthesized via a supercritical fluid process. *RSC Advances* **2014**, *4* (94), 52410-52414.
49. A. Boulineau, T. Gutel, Revealing electrochemically induced antisite defects in $LiCoPO_4$: Evolution upon cycling. *Chemistry of Materials* **2015**, *27* (3), 802-807.
50. X. Wu, M. Meledina, J. Barthel, Z. Liu, H. Tempel, H. Kungl, J. Mayer, R.-A. Eichel, Investigation of the Li–Co antisite exchange in Fe-substituted $LiCoPO_4$ cathode for high-voltage lithium-ion batteries. *Energy Storage Materials* **2019**, *22*, 138-146.

51. M. Uceda, H. C. Chiu, J. Zhou, R. Gauvin, K. Zaghib, G. P. Demopoulos, Nanoscale assembling of graphene oxide with electrophoretic deposition leads to superior percolation network in Li-ion electrodes: $TiNb_2O_7$/rGO composite anodes. *Nanoscale* **2020**, *12* (45), 23092-23104.
52. S. Ferrari, R. L. Lavall, D. Capsoni, E. Quartarone, A. Magistris, P. Mustarelli, P. Canton, Influence of particle size and crystal orientation on the electrochemical behavior of carbon-coated $LiFePO_4$. *Journal of physical chemistry C* **2010**, *114*, 12598-12603.
53. B. Ellis, W. H. Kan, W. R. M. Makahnouk, L. F. Nazar, Synthesis of nanocrystals and morphology control of hydrothermally prepared $LiFePO_4$. *Journal of Materials Chemistry* **2007**, *17* (30), 3248-3254.
54. K. Dokko, S. Koizumi, H. Nakano, K. Kanamura, Particle morphology, crystal orientation, and electrochemical reactivity of $LiFePO_4$ synthesized by the hydrothermal method at 443 K. *Journal of Materials Chemistry* **2007**, *17* (45), 4803-4810.
55. X.-L. Pan, C.-Y. Xu, L. Zhen, Synthesis of $LiMnPO_4$ microspheres assembled by plates, wedges and prisms with different crystallographic orientations and their electrochemical performance. *CrystEngComm* **2012**, *14* (20), 6412-6418.
56. Z. Li, K. Zhu, J. Li, X. Wang, Morphological and orientational diversity of $LiFePO_4$ crystallites: Remarkable reaction path dependence in hydrothermal/solvothermal syntheses. *CrystEngComm* **2014**, *16* (43), 10112-10122.
57. J. M. García-Ruiz, Nucleation of protein crystals. *Journal of Structural Biology* **2003**, *142* (1), 22-31.
58. G. P. Demopoulos, Aqueous precipitation and crystallization for the production of particulate solids with desired properties. *Hydrometallurgy* **2009**, *96* (3), 199-214.
59. L.-D. Shiau, Determination of the nucleation and growth kinetics for aqueous L-glycine solutions from the turbidity induction time data. *Crystals* **2018**, *8* (11), 403.
60. R. Zeitoun, A. Biswas, Review—Potentiometric determination of phosphate using cobalt: A review. *Journal of The Electrochemical Society* **2020**, *167* (12), 127507.
61. J. Conrad, P. R. Tremaine, Third dissociation constant of phosphoric acid in $H_2O$ and $D_2O$ from 75 to 300 $^oC$ at p = 20.4 MPa using raman spectroscopy and a titanium-sapphire flow cell. *Physical Chemistry Chemical Physics* **2021**, *23* (17), 10670-10685.
62. D. R. Kester, R. M. Pytkowicx, Determination of the apparent dissociation constants of phosphoric acid in seawater. *Limnology and Oceanography* **1967**, *12* (2), 243-252.
63. K. T. Lee, J. Cho, Roles of nanosize in lithium reactive nanomaterials for lithium ion batteries. *Nano Today* **2011**, *6* (1), 28-41.
64. K. J. Kreder, G. Assat, A. Manthiram, Microwave-assisted solvothermal synthesis of three polymorphs of $LiCoPO_4$ and their electrochemical properties. *Chemistry of Materials* **2015**, *27* (16), 5543-5549.
65. E. Markevich, R. Sharabi, O. Haik, V. Borgel, G. Salitra, D. Aurbach, G. Semrau, M. A. Schmidt, N. Schall, C. Stinner, Raman spectroscopy of carbon-coated $LiCoPO_4$ and $LiFePO_4$ olivines. *Journal of Power Sources* **2011**, *196* (15), 6433-6439.
66. R. Sharabi, E. Markevich, V. Borgel, G. Salitra, G. Gershinsky, D. Aurbach, G. Semrau, M. A. Schmidt, N. Schall, C. Stinner, Raman study of structural stability of $LiCoPO_4$ cathodes in $LiPF_6$ containing electrolytes. *Journal of Power Sources* **2012**, *203*, 109-114.
67. P. Puech, M. Kandara, G. Paredes, L. Moulin, E. Weiss-Hortala, A. Kundu, N. Ratel-Ramond, J.-M. Plewa, R. Pellenq, M. Monthioux, Analyzing the raman spectra of graphenic carbon materials from kerogens to nanotubes: What type of information can be extracted from defect bands? *C-Journal of Carbon Research* **2019**, *5* (4), 69.

68. D. Y. Kang, C. Kim, G. Park, J. H. Moon, Liquid immersion thermal crosslinking of 3D polymer nanopatterns for direct carbonisation with high structural integrity. *Scientific Reports* **2015**, *5*, 18185.
69. E. Sviridova, A. Barras, A. Addad, E. Plotnikov, A. D. Martino, D. Deresmes, K. Nikiforova, M. Trusova, S. Szunerits, O. Guselnikova, P. Postnikov, R. Boukherroub, Surface modification of carbon dots with tetraalkylammonium moieties for fine tuning their antibacterial activity. *Biomaterials Advances* **2022**, *134*, 112697.
70. S. Sawalha, M. Assali, M. Raddad, T. Ghneem, T. Sawalhi, M. Almasri, A. Zarour, G. Misia, M. Prato, A. Silvestri, Broad-spectrum antibacterial activity of synthesized carbon nanodots from d-Glucose. *ACS Applied Bio Materials* **2022**, *5* (10), 4860-4872.
71. M. Uceda, J. Zhou, J. Wang, R. Gauvin, K. Zaghib, G. P. Demopoulos, Highly conductive NMP-free carbon-coated nano-lithium titanate/carbon composite electrodes via SBR-assisted electrophoretic deposition. *Electrochimica Acta* **2019**, *299*, 107-115.
72. M. Devaraju, Q. Truong, H. Hyodo, T. Tomai, I. Honma, Supercritical fluid synthesis of $LiCoPO_4$ nanoparticles and their application to lithium ion battery. *Inorganics* **2014**, *2* (2), 233-247.
73. Y. Li, I. Taniguchi, Facile synthesis of spherical nanostructured $LiCoPO_4$ particles and its electrochemical characterization for lithium batteries. *Advanced Powder Technology* **2019**, *30* (8), 1434-1441.
74. S. Sreedeep, S. Natarajan, V. Aravindan, Recent advancements in $LiCoPO_4$ cathodes using electrolyte additives. *Current Opinion in Electrochemistry* **2022**, *31*, 100868.
75. M. Kaus, I. Issac, R. Heinzmann, S. Doyle, S. Mangold, H. Hahn, V. S. K. Chakravadhanula, C. Kübel, H. Ehrenberg, S. Indris, Electrochemical delithiation/relithiation of $LiCoPO_4$: A two-step reaction mechanism investigated by *in situ* X-ray diffraction, *in situ* X-ray absorption spectroscopy, and *ex situ* $^{7}Li/^{31}P$ NMR spectroscopy. *The Journal of Physical Chemistry C* **2014**, *118* (31), 17279-17290.
76. M. G. Palmer, J. T. Frith, A. L. Hector, A. W. Lodge, J. R. Owen, C. Nicklin, J. Rawle, *In situ* phase behaviour of a high capacity $LiCoPO_4$ electrode during constant or pulsed charge of a lithium cell. *Chemical Communications* **2016**, *52* (98), 14169-14172.
77. T. Kozawa, K. Fukuyama, A. Kondo, M. Naito, Wet milling synthesis of $NH_4CoPO_4 \cdot H_2O$ platelets: Formation reaction, growth mechanism, and conversion into high-voltage $LiCoPO_4$ cathode for Li-ion batteries. *Materials Research Bulletin* **2021**, *135*, 111149.
78. J. Su, B.-Q. Wei, J.-P. Rong, W.-Y. Yin, Z.-X. Ye, X.-Q. Tian, L. Ren, M.-H. Cao, C.-W. Hu, A general solution-chemistry route to the synthesis $LiMPO_4$ (M = Mn, Fe, and Co) nanocrystals with [010] orientation for lithium-ion batteries. *Journal of Solid-State Chemistry* **2011**, *184* (11), 2909-2919.
79. B. Wu, H. Xu, D. Mu, L. Shi, B. Jiang, L. Gai, L. Wang, Q. Liu, L. Ben, F. Wu, Controlled solvothermal synthesis and electrochemical performance of $LiCoPO_4$ submicron single crystals as a cathode material for lithium-ion batteries. *Journal of Power Sources* **2016**, *304*, 181-188.
80. Y. Maeyoshi, S. Miyamoto, H. Munakata, K. Kanamura, Effect of conductive carbon additives on electrochemical performance of $LiCoPO_4$. *Journal of Power Sources* **2018**, *376*, 18-25.
81. Y. Ge, K. Kan, Y. Yang, L. Zhou, L. Jing, P. Shen, L. Li, K. Shi, Highly mesoporous hierarchical nickel and cobalt double hydroxide composite: fabrication, characterization and ultrafast $NO_x$ gas sensors at room temperature. *Journal of Materials Chemistry A* **2014**, *2* (14), 4961-4969.
82. Y. Xu, Z. Liu, D. Chen, Y. Song, R. Wang, Synthesis and electrochemical properties of porous $\alpha$-$Co(OH)_2$ and $Co_3O_4$ microspheres. *Progress in Natural Science: Materials International* **2017**, *27* (2), 197-202.
83. H. Liu, D. Guo, W. Zhang, R. Cao, $Co(OH)_2$ hollow nanoflowers as highly efficient electrocatalysts for oxygen evolution reaction. *Journal of Materials Research* **2017**, *33* (5), 568-580.

84. A. Roy, H. S. Jadhav, G. M. Thorat, J. G. Seo, Electrochemical growth of $Co(OH)_2$ nanoflakes on Ni foam for methanol electro-oxidation. *New Journal of Chemistry* **2017**, *41* (17), 9546-9553.
85. A. Rajalakshmi, V. D. Nithya, K. Karthikeyan, C. Sanjeeviraja, Y. S. Lee, R. K. Selvan, Physicochemical properties of $V^{5+}$ doped $LiCoPO_4$ as cathode materials for Li-ion batteries. *Journal of Sol-Gel Science and Technology* **2013**, *65* (3), 399-410.
86. W. Li, J. Hwang, W. Chang, H. Setiadi, K. Y. Chung, J. Kim, Ultrathin and uniform carbon-layer-coated hierarchically porous $LiFePO_4$ microspheres and their electrochemical performance. *The Journal of Supercritical Fluids* **2016**, *116*, 164-171.
87. E. J. Kim, X. Yue, J. T. S. Irvine, A. R. Armstrong, Improved electrochemical performance of $LiCoPO_4$ using eco-friendly aqueous binders. *Journal of Power Sources* **2018**, *403*, 11-19.
88. J. Chivot, L. Mendoza, C. Mansour, T. Pauporté, M. Cassir, New insight in the behaviour of Co–$H_2O$ system at 25–150 °C, based on revised Pourbaix diagrams. *Corrosion Science* **2008**, *50* (1), 62-69.
89. P. Meshram, U. Prakash, L. Bhagat, Abhilash, H. Zhao, E. D. V. Hullebusch, Processing of waste copper converter slag using organic acids for extraction of copper, nickel, and cobalt. *Minerals* **2020**, *10* (3), 290.
90. Y.-S. He, D.-W. Bai, X. Yang, J. Chen, X.-Z. Liao, Z.-F. Ma, A $Co(OH)_2$−graphene nanosheets composite as a high performance anode material for rechargeable lithium batteries. *Electrochemistry Communications* **2010**, *12* (4), 570-573.
91. J. Wu, W.-M. Lau, D.-S. Geng, Recent progress in cobalt-based compounds as high-performance anode materials for lithium-ion batteries. *Rare Metals* **2017**, *36* (5), 307-320.
92. S. H. Lim, G. D. Park, Y. C. Kang, Investigation of cobalt hydroxysulfide as a new anode material for Li-ion batteries and its conversion reaction mechanism with Li-ions. *Chemical Engineering Journal* **2020**, *401*, 126121.
93. M. K. Devaraju, Q. D. Truong, H. Hyodo, Y. Sasaki, I. Honma, Synthesis, characterization and observation of antisite defects in $LiNiPO_4$ nanomaterials. *Scientific Reports* **2015**, *5*, 11041.
94. A. Paolella, S. Turner, G. Bertoni, P. Hovington, R. Flacau, C. Boyer, Z. Feng, M. Colombo, S. Marras, M. Prato, L. Manna, A. Guerfi, G. P. Demopoulos, M. Armand, K. Zaghib, Accelerated removal of Fe-antisite defects while nanosizing hydrothermal $LiFePO_4$ with $Ca^{2+}$. *Nano Letters* **2016**, *16* (4), 2692-2697.
95. D. Morgan, A. V. D. Ven, G. Ceder, Li Conductivity in $Li_xMPO_4$ (M = Mn, Fe, Co, Ni) olivine materials. *Electrochemical and Solid-State Letters* **2004**, *7*, A30-A32.
96. M. S. Islam, D. J. Driscoll, C. A. J. Fisher, P. R. Slater, Atomic-scale investigation of defects, dopants, and lithium transport in the $LiFePO_4$ olivine-type battery material. *Chemistry of Materials* **2005**, *17*, 5085-5092.
97. G. K. P. Dathar, D. Sheppard, K. J. Stevenson, G. Henkelman, Calculations of Li-ion diffusion in olivine phosphates. *Chemistry of Materials* **2011**, *23* (17), 4032-4037.

# Chapter 4: Attaining full Li-ion storage capacity in nearly defect-free and preferential orientation grown $LiCoPO_4$ via *ab initio* solvothermal crystallization control

**Bridge:** In Chapter 3, comprehensive analysis of surface and bulk crystal properties, combined with extensive electrochemical studies, has shed light on the intricate challenges associated with the hydrothermally (HT) synthesized $LiCoPO_4$ (LCP). This research revealed two critical defects that significantly impact the material's performance: firstly, the formation of a resistive nano-scale $Co(OH)_2$ surface passivation layer, and secondly, the presence of abundant anti-site defects during the synthesis and post-synthesis treatments. The $Co(OH)_2$ surface layer, induced by surface hydrolysis in the alkaline synthesis environment, acts as a barrier to efficient Li-ion and electron transfer. This passivation layer effectively increases the overall resistance of the material, hindering its electrochemical performance. Concurrently, the abundance of anti-site defects, where cobalt ions occupy lithium sites in the crystal structure, is notably higher in HT-LCP samples compared to the solid-state (SS-LCP) counterparts. These structural imperfections severely impede the electrochemically driven intercalation process, which is crucial for the material's functionality as a cathode in Li-ion batteries. The combined effect of these defects explains the poor discharge capacity observed in HT-LCP materials. This realization underscores the need for alternative synthesis methods that can mitigate these issues and unlock the full potential of LCP as a high-V cathode material.

In response to these findings, Chapter 4 of this thesis focuses on developing a novel LCP crystal variety. This is pursued via ethylene glycol (EG)-based solvothermal (ST) synthesis followed by Argon (Ar)-annealing, specifically designed to address the fundamental limitations identified in the HT synthesis method. In conjunction with experimental validation, computational modeling using first-principles methods was employed to elucidate the mechanism of preferential orientation growth. These simulations revealed that ethylene glycol (EG) molecules play a critical role in modulating the interfacial energies of LCP crystal facets, facilitating this preferential growth. This novel design of LCP crystals results in shortened Li-ion diffusion pathways within the crystal structure, leading to superior electrochemical performance that achieves nearly theoretical full discharge capacity and superior rate capability—a milestone previously unattained. By addressing core issues at the crystal structure level, this research opens new avenues for the practical application of LCP in next-generation high-V Li-ion batteries.

This chapter is replication of a manuscript to be submitted in a peer-reviewed journal, with the following citation:

Moohyun Woo, Sang-Wook Park, Jinhyuk Lee, Dong-Hwa Seo and George P. Demopoulos, 2024, "Attaining full Li-ion storage capacity in nearly defect-free and preferential orientation grown $LiCoPO_4$ via *ab initio* solvothermal crystallization control", *Adv. Energy Mater.*, *2024, 2404404*.

**Abstract**

Boosting energy density beyond the current status of Li-ion batteries is actively sought after yet it remains very challenging. One promising pathway towards this goal is the development of defect-free high-voltage cathode materials via novel crystal engineered approaches. In response to this demand, the present study focuses on synthesizing $LiCoPO_4$, which is a high-voltage polyanionic compound, into nearly defect-free structure and preferential orientation grown crystals via solvothermal method using ethylene glycol (EG) as surface energy control medium. Notably, *ab initio* molecular dynamics simulations and density functional theory calculations elucidate the role of interfacial energy variations induced by EG molecule interaction with particular crystal facets of $LiCoPO_4$ giving rise to the desired growth direction in comparison with hydrothermal method. In addition to solvent regulated crystal growth, Argon-annealing alleviates the undesired charge transfer resistance on the crystal surface by eliminating EG residue and further reduces the anti-site defect concentration, thereby engineering essentially highly ordered crystal structure. The novel $LiCoPO_4$ crystals are shown to possess nearly theoretical full discharge capacity (163.0 mAh $g^{-1}$ and 774.7 Wh $kg^{-1}$ at C/10) and superior rate capability (151.6 mAh $g^{-1}$ and 716.9 Wh $kg^{-1}$ at 1 C), a truly unmatched functionality offering new high-voltage cathode design possibilities.

## 4.1. Introduction

Rechargeable Li-ion batteries (LIBs) first introduced by Whittingham in 1976, have become an indispensable power source for portable electronic devices and electric vehicle transportation.[1, 2] LIBs consist of three main components, the two electrodes (Cathode-Anode) and the electrolyte. Among these components, the cathode active materials determine largely the total mass, cost, and performance of LIBs.[3] With the expanding application of LIBs in electric vehicles, there exists an enormous demand for higher energy density, not delivered by conventional cathode materials such as $LiNi_xCo_yMn_{1-x-y}O_2$ (NCM) and $LiFePO_4$ (LFP).[2, 4, 5] Consequently, there is a strong interest in developing high-voltage (high-V) cathode materials with robust structure.[6]

Lithium cobalt phosphate ($LiCoPO_4$, LCP) with olivine-type crystal structure, has been recognized as a promising high-V cathode material owing to its superior theoretical energy density and excellent thermal stability by the virtue of relatively higher operating voltage (4.8 V × 167 mAh $g^{-1} \approx 800$ Wh $kg^{-1}$) and particular crystal structure.[7] However, the practical application of LCP is still restricted by several limitations such as intrinsically low ionic and electronic conductivity and anti-site defects (Co in Li site) that limit the attainment of its optimal capacity and compromise its cyclability.[8-10] To unlock the full potential of LCP, it is imperative to control its crystal structure and morphology towards nearly zero-defects with shortened Li-ion diffusion length that can lead to enhanced kinetics.[11, 12]

To enhance LCP kinetics, various methods such as pulverization and doping strategies have been intensively utilized. While pulverization offers the possibility of achieving high charge-discharge capacity for a few initial cycles, it imparts abundant anti-site defects in bulk crystal structure and induces severe side reactions with electrolyte at the interface.[7, 13] The above-mentioned drawbacks are notably fatal in LCP but also in other high-V cathode materials.[14] It is well understood that anti-site defects interrupt the one-dimensional (1-D) Li-ion diffusion pathway, which combined with enlarged surface area and high operating voltage creates a notorious ensemble further accelerating electrolyte decomposition, negatively affecting cycling.[15, 16] Additionally, the pulverization method leads to a nano-size distribution of the resulting powder yielding poor tap density and low volumetric energy density desirable in large-scale applications.[17, 18]

Alternatively, through employing doping strategies, improved structural features can be realized that are able to suppress anti-site defect formation upon cycling tests and enhance the kinetics by creating Li and/or Co vacancies via aliovalent dopants.[19, 20] While some LCP doping advances were experimentally verified, charge compensation with increasing dopant concentration and narrow cut-off voltage (4.3-5.0 V vs. $Li/Li^+$) results in a decline from the theoretical capacity value.[21] Besides, existing research on LCP reveals a significant imbalance, with most studies focusing on cation substitution rather than fundamental investigations of the material itself. This lack of comprehensive crystal studies on pure LCP indicates a critical gap in understanding of its intrinsic properties hindering the development of more effective strategies for improving the electrochemical performance of LCP as a cathode material.

In this work, we designed micron-scale and preferentially grown LCP particles incorporating the defect-free olivine crystal structure as a practical cathode material delivering nearly full discharge capacity and energy density in addition to the enhanced rate capability. The synthesis of this new LCP

crystal variety is accomplished solvothermally using ethylene glycol (EG) guided by *ab initio* computational crystal modeling. The morphological and structural advantages of utilizing EG as a solvent were confirmed by both experimental characterizations (XRD, Rietveld refinement, SEM, and TEM) and computational approaches including *ab initio* molecular dynamics (AIMD) simulation and density functional theory (DFT) calculation. Additionally, particular attention was paid to characterizing the electrochemical properties of our LCP samples–hydrothermal (HT-LCP), solvothermal (ST-LCP), and solvothermal-annealed (ST-A-LCP)–to correlate their functionality in terms of Li-ion diffusivity and storage capacity to their crystal structure properties. Our work offers new insight into the EG-regulated crystal formation mechanism and the elimination of surface and bulk anti-site defects that have limited so far, the Li-ion intercalation kinetics and storage capacity of LCP as high-V cathode model

## 4.2. Experimental section

### 4.2.1. Material preparation

Hydrothermally and solvothermally synthesized lithium cobalt phosphate (HT-LCP and ST-LCP) were fabricated using lithium hydroxide monohydrate (98 % $LiOH{\cdot}H_2O$, Sigma-Aldrich), cobalt (II) sulfate heptahydrate (99 % $CoSO_4{\cdot}7H_2O$, Sigma-Aldrich), phosphoric acid (85 % aqueous solution, $H_3PO_4$, Fisher Scientific), ethylene glycol (EG, 99 % $C_2H_6O_2$, Sigma-Aldrich) as a solvent, ammonium hydroxide solution ($NH_4OH$, 28.0-30.0 % $NH_3$ basis, Sigma-Aldrich) for pH control, and L-Ascorbic acid (99 % $C_6H_8O_6$, Sigma-Aldrich) as a reducing agent. For HT-LCP synthesis, the detailed procedures can be found in our previous work.[7] For ST-LCP, $LiOH{\cdot}H_2O$, $CoSO_4{\cdot}7H_2O$, and $H_3PO_4$ were dissolved and blended in 200 mL of EG solvent (more details in the Supporting Information) on three different molar ratios of $Li/Co/PO_4 = x/1/1$ (x = 1, 1.5, and 2), while maintaining the concentration of $CoSO_4$ and $H_3PO_4$ is fixed at 0.4 M. Afterwards, the pH of the precursor solutions was adjusted at 9 with $NH_4OH$ added dropwise. To investigate the evolution of precipitation reactions during ST synthesis, slurry samples were collected from the autoclave (Parr 4888 model) via a dip tube under pressure at various temperatures (25-100-150-200-260 $^oC$) and reaction times (0-2-4-6 hours). For the subsequent Ar-annealing treatment, the as-synthesized ST-LCP was transferred to an MTI mini tube furnace (model OTF-1200X) and heated at 700 $^oC$ for 1 h with continuous Ar gas flow. The samples after Ar-annealing treatment are denoted as 'ST-A-LCP'.

### 4.2.2. Material characterizations

Powder X-ray diffraction (PXRD) patterns were collected with Bruker D8 Discovery X-ray diffractometer using Co Kα radiation with the wavelength (λ) of 1.78892 Å from 2θ = 10 to 80 °. Crystal structure information for lattice parameters, grain size, and anti-site defect concentration was fitted and estimated by XRD Rietveld refinement using TOPAS Academic V5 software. The morphology of LCP samples was evaluated with Hitachi cold-field emission SU-8000 scanning electron microscope (CFE-SEM). The Thermo Scientific Talos F200X G2 STEM was used with an accelerating voltage of 200 kV for transmission electron microscope observation (TEM), high-resolution TEM (HR-TEM), energy dispersive spectroscopy (EDS) mapping and line spectrum results. X-ray Photoelectron Spectroscopy (XPS) measurements were carried out with Thermo Scientific K-Alpha using an aluminum (Al) Kα micro-focused monochromator. XPS data processing was performed with the Avantage data system for peak fitting.

### 4.2.3. Computational methodology

#### 4.2.3.1. Surface energy calculation

The surface energy of clean surface ($\gamma$) is calculated using following equation:

$$\gamma = \frac{1}{2A}(E_{slab} - nE_{bulk}) \quad [1]$$

where $A$ denotes the area of the surface unit cell, $E_{slab}$ is the energy of the slab supercell, $n$ is the number of atoms in the slab supercell, and $E_{bulk}$ is the energy of the bulk structure per atom. The *1/2* factor accounts for two surfaces of a slab supercell.

The surface energy after molecule adsorption ($\gamma'$) is evaluated using following equation:

$$\gamma' = \gamma - \frac{1}{2A}(n'E_d) \quad [2]$$

where $\gamma$ denotes the surface energy before adsorption, $n'$ is the number of adsorbed water ($H_2O$) or EG molecules on the slab supercell, and $E_d$ is the adsorption energy of $H_2O$ or EG molecules.

The surface energy change ($\Delta\gamma$) is straightforwardly described as the difference between surface energy after adsorption ($\gamma'$) and before adsorption ($\gamma$) using following equation:

$$\Delta\gamma = \gamma - \gamma' \quad [3]$$

where a lower $\Delta\gamma$ value indicates the surface after adsorption is thermodynamically more stabilized.

However, the $\Delta\gamma$ changes based on diverse adsorption configurations involving different atoms and orientations of solvent molecules on LCP facets in response to variation of local surface composition and molecular solvent groups. Therefore, AIMD simulations were conducted to generate

unbiased absorption configurations for six distinct systems consisting of three primary crystal facets ((100), (010), and (001)) and two types of solvent molecules ($H_2O$ or EG). Ten adsorption configurations for each system were created with surface dangling bonds minimized and fully relaxed in these configurations using DFT.

#### 4.2.3.2. AIMD simulation and DFT calculation

AIMD simulations and DFT calculations were performed using the Vienna *ab initio* Simulation Package, employing the Perdew–Burke–Ernzerhof functional for generalized gradient approximation (GGA) exchange-correlation.[22, 23] A Hubbard U correction (GGA + U) was applied to Co, using a U value of 3.32 eV.[24, 25] To accommodate van der Waals forces, all our calculations employed Grimme's zero damping DFT-D3 method, setting IVDW = 11.[26] In the DFT calculations, plane-wave cut-off energies of 520 eV for bulk and 600 eV for slab LCP structures were utilized. The relaxation of structures continued until forces on each atom were below 0.02 eV. An 8 × 8 × 8 k-point mesh was employed for bulk calculations, and a 2 × 2 × 1 k-point mesh was used for slab calculations. For the generated (100), (010), and (001) slab structures ($Li_{16}Co_{16}P_{16}O_{64}$), half of the structures ($Li_8Co_8P_8O_{32}$) from the vacuum layer were considered as the surface layers, while the remaining ($Li_8Co_8P_8O_{32}$) were assumed to be bulk layers. Each slab system was taken to have vacuum layers of approximately 10 Å.

AIMD simulations were conducted under the canonical ensemble (NVT) using a Nosé-Hoover thermostat with an 80 fs period. Starting at 100 K, temperatures were ramped up to 1,000 K over 300 time steps and held constant for 4,000 time steps (4 ps). To minimize computational cost, plane-wave energy cutoff of 400 eV and gamma-centered 1 × 1 × 1 k-point mesh were utilized. Atomic configurations were sampled at 1,000 K during AIMD simulations and fully relaxed using DFT. The initial 1,000 time steps were disregarded due to the equilibration process, and one configuration was constrained to 300 time steps to ensure variation in configurations.

### 4.2.4. Electrochemical characterization

To fabricate the cathode electrode slurry, the active material (HT-LCP, ST-LCP, and ST-A-LCP), acetylene black (Alfa Aesar) as conductive carbon, and polyvinylidene fluoride (PVDF, $(C_2H_2F_2)_n$, Sigma-Aldrich) binder were mixed in 1-methyl-2-pyrrolidone (NMP, 99.5 % $C_5H_9NO$, Sigma-Aldrich) solvent with a weight ratio of 7:2:1 corresponding to 140, 40, and 20 mg respectively. The slurry was pasted on a high-purity Al foil current collector, and then dried overnight at 80 °C in a vacuum oven. The mass loading of cathode electrodes is an average 2.0-2.5 mg $cm^{-2}$. Lithium metal

chips (MSE Supplies) and polypropylene film (Celgard 2200) were used as anodes and separators. The customized electrolyte solution (5 mL) was prepared with 1 M of lithium hexafluorophosphate (> 97 % $LiPF_6$, TCI Chemicals) solution in a 1:1:3 (vol.%) mixture of ethylene carbonate (EC, 99 % $(CH_2O)_2CO$, Sigma-Aldrich), propylene carbonate (PC, 99.7 % $CH_3C_2H_3O_2CO$, Sigma-Aldrich), and dimethyl carbonate (DMC, 99 % $H_3COCOOCH_3$, Sigma-Aldrich) electrolyte and 2 wt. % tris(trimethylsilyl) phosphite (95 % $[(CH_3)_3SiO]_3P$, Sigma-Aldrich) as high-V stabilizing additive.[20] All electrochemical measurements were performed on Swagelok cells assembled in an Ar-filled glovebox. The galvanostatic charge-discharge profile was measured on Arbin cycler (BT2403). The battery cycling test was carried out at different C-rates (1 C = 167 mAh $g^{-1}$) in the voltage range of 3.5–5.0 V vs. $Li/Li^+$. Galvanostatic intermittent titration technique (GITT) measurements were conducted during 5$^{th}$ cycle at C/2 (10 min pulse and 30 min rest) in the same voltage range with the galvanostatic charge-discharge profile. Cyclic voltammetry (CV) measurements were made by using an electrochemical workstation (Bio-Logic) at the specific conditions between 3.5-5.0 V vs. $Li/Li^+$ with various scan rates 0.1, 0.25, and 0.5 mV $s^{-1}$. The stability of electrolyte at high-V was investigated via Linear sweep voltammetry (LSV) at 3.5-5.5 V vs. $Li/Li^+$ and 2 mV $s^{-1}$ scan rate. Electrochemical Impedance Spectroscopy (EIS) analysis of the pristine working electrodes was conducted using Bio-Logic in potentiostatic mode between 1 MHz and 10 mHz. Nyquist plots were fitted using ZView® software.

### 4.3. Results and discussion

#### 4.3.1. Impact of Li content on ST-LCP crystal structure

As the first step, stoichiometric and over-stoichiometric Li concentrations were introduced into the cobalt phosphate base composition using molar ratios of Li/Co/P = x/1/1 (x = 1, 1.5, and 2). Tailoring the Li molar ratio can be a key factor to not only modulate the preferred crystallographic orientation but also reduce anti-site defect occurrence during ST synthesis. Previous work by Paolella et al. has established that a $Li^+/Fe^{2+}$ ratio of 2:1 near the surface of forming LFP crystals during HT synthesis is critical in eliminating anti-site defects via cation exchange.[27] This is corroborated by the XRD patterns (Figure 4.1a), indicating that (200) and (020) facets were subject to considerable changes with the excess Li content while the intensity of other peaks remained relatively similar. Consequently, ST synthesis utilizing Li over-stoichiometry can readily reduce the length of the (200) crystal plane in parallel to the *b* direction, which is the actual Li-ion diffusion pathway.[8, 28] As we will

discuss in the following sections 4.3.3, this shortened Li-ion diffusion length can critically enhance kinetics and result in improved rate capability.

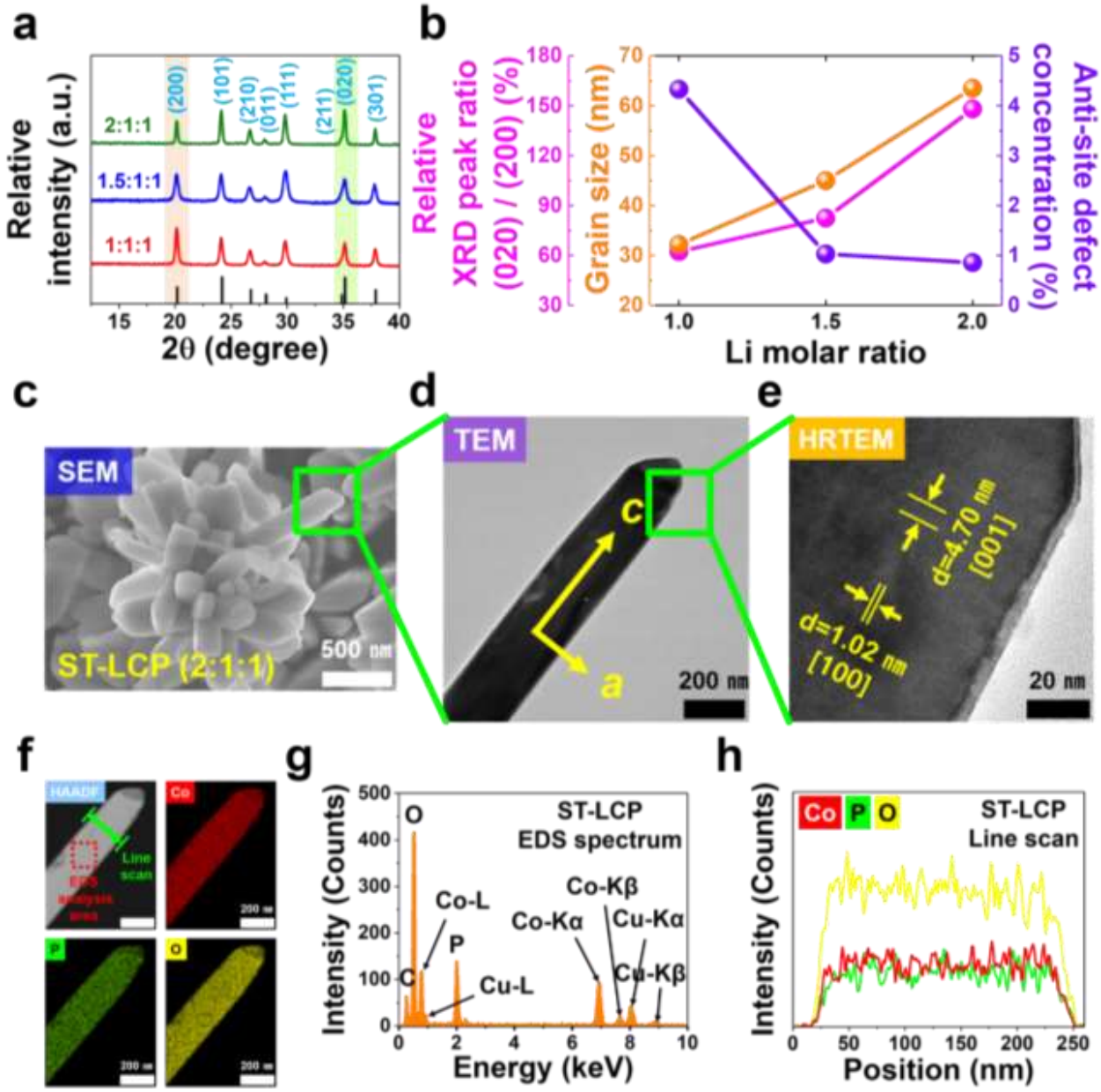


**Figure 4.1.** (a) XRD patterns (b) crystallographic information including relative XRD peak ratio of (020) / (200), grain size, and anti-site defect concentration of LCP samples via ST synthesis with different Li molar ratios; morphology and crystal orientation of ST-LCP via (c) SEM, (d) TEM, and (e) HRTEM; atomic arrangement investigations of ST-LCP with (f) TEM elemental mapping, (g) EDS spectrum, and (h) Line scan.

In addition, Figure 4.1b integrates the crystal structure information including the relative peak ratio of (020) / (200), grain size, and anti-site defect concentration using Rietveld refinement of the corresponding XRD patterns exhibited in Figure A.3.1 and Table A.3.1. With increased Li

concentration, one would expect oversaturation in precursor solution leading to increased nuclei density and consequently smaller grains.[29, 30] However, from the result of Rietveld refinement in Figure 4.1b, it can be seen that increasing Li molar ratio leads to enlarged grain size. This observation can be attributed to using EG as a polar and surface active solvent.[31, 32] We believe that increasing the over-stoichiometric Li concentration can lead to increased nuclei density. However, EG is able to modulate the complex interplay between nucleation and growth favouring formation of larger-sized grains. Indeed, it can be confirmed by SEM images shown in Figure A.3.2 that the grain size was enlarged as the Li molar ratio increased, supporting our argument. Thus far, we have shown that growth-dominated LCP synthesis, using the ST method and EG as solvent, offers a promising pathway for reducing anti-site defect concentration (< 1 %). Since the specific molar ratio of Li:Co:P = 2:1:1 produced the most suitable structural properties (as shown in Figure 4.1a-b), further characterizations including morphology and elemental distribution were performed on this structure which will be denoted as 'ST-LCP'.

To further monitor the evolution of precipitation products during ST synthesis, slurry samples were systematically collected at various temperatures, ranging from room temperature to the target temperature for ST synthesis (260 ºC). The collected samples were subsequently dried, and characterized via XRD analysis. As shown by the XRD results in Figure A.3.3a, the precipitate initially produced at room temperature primarily consists of $Co_5(PO_4)_2(OH)_4$, $Li(NH_4)SO_4$, and $LiPO_3$. As the temperature increases to 200 ºC, most of these precipitated compounds have transformed to the intermediate LCP phase with the *Pna2₁* space group. Upon reaching the target temperature of 260 ºC, the final LCP phase (space group: *Pnma*) is seen to have crystalized, with only a small amount of intermediate LCP (space group: *Pna2₁*) remaining. With prolonged ST holding time at 260 ºC (Figure A.3.3b), the LCP (space group: *Pna2₁*) phase finally and fully evolves into pure *Pnma* LCP phase with high crystallinity. In other words, as also has been established in the case of LFP crystallization,[27] it is assumed the early-forming cobalt phosphate hydroxylate, $Co_5(PO_4)_2(OH)_4$ via cation exchange with Li-ions transforms to LCP, first as the kinetically favorable *Pna2₁* LCP phase, which ultimately rearranges into the stable *Pnma* LCP phase. The role of excess Li, as per the LFP formation model,[27] is to build a Li-ion dominating layer near the surface of the precursor $Co_5(PO_4)_2(OH)_4$ to drive the cation exchange transformation into LCP with concomitant elimination of anti-site defects. It is further hypothesized that such Li-ion surface accumulation is better accomodated in the EG solvent than in $H_2O$ due to difference in viscocity between the two solvents (EG: 18.38 cP vs. $H_2O$: 1 cP at 20 ºC).[33, 34]

To verify the morphological evolution and crystal orientation of ST-LCP, SEM and TEM techniques were applied and the obtained images are displayed in Figure 4.1c-e. Unlike the other two LCP samples with the stoichiometric composition (1:1:1) and 50 % excess of Li (1.5:1:1) shown in Figure A.3.2, ST-LCP demonstrates a preferential orientation growth extending from the core section. The micron sized ST-LCP particles have a width of about 200 nm, resulting in very thin rod-shaped microstructure as shown in Figure 4.1c. Furthermore, crystal orientations of ST-LCP were defined based on the lattice parameters, obtained from TEM and HRTEM shown in Figure 4.1d-e. The *d*-spacing value in the horizontal direction is 1.02 nm, which is consistent with *a* direction. Likewise, the *d*-spacing value in the longitudinal direction is 4.70 nm with 10 atomic layers, which coincides with the *c* direction. Therefore, the *b* direction along which Li-ion diffusion takes place is not the longitudinal direction of ST-LCP. Overall, these findings are corroborating the progressively shortened Li-ion diffusion pathway along *b* direction with increasing over-stoichiometric Li contents. Moreover, the elemental homogeneity of ST-LCP particle was probed via TEM mapping, EDS spectrum, and line scan displayed in Figure 4.1f-h. These results clearly indicate that the as-synthesized ST-LCP particles possess high purity as well as uniform distribution of Co, P, and O throughout the entire crystal structure at the nanoscale level.

### 4.3.2. Anisotropic growth mechanism of ST-LCP through computational modeling

We attribute the preferential anisotropic growth mechanism of ST-LCP along the *c* direction to the beneficial role of EG during ST synthesis in comparison with $H_2O$ solvent in HT synthesis. To validate our hypothesis, in-depth computational studies were undertaken with the incorporation of AIMD simulation and DFT calculation. Considering the progressively increasing grain size, the growth-favouring environment was effectively induced in both HT and ST synthesis by regulating the degree of supersaturation with over-stoichiometric Li contents. However, ST-LCP using EG as a solvent demonstrates the anisotropic growth unlike HT-LCP which grows isotropically (as shown in Figure A.3.4). In terms of thermodynamics, we postulate that this difference may originate from the relative surface energy differences due to solvent molecule adsorption on separate LCP facets. Thus, our intention is narrowed down to understand the growth mechanism of LCP crystals accompanying the adsorption process of a single molecule of two solvents ($H_2O$ and EG) on each of LCP crystal facets and their surface energy changes ($\Delta\gamma$) accordingly.

Prior to the adsorption of solvent molecules, it is necessary to construct the model of each LCP facet to obtain the intrinsic surface energy before adsorption as a baseline. Based on previous research,

the slab structure of $Li_{16}Co_{16}P_{16}O_{64}$ was generated from the optimized bulk LCP structure (space group: *pnma*), incorporating the lowest Miller indices, (100), (010), and (001).[35] Details on the surface termination of each LCP facet are provided in Figure A.3.5.

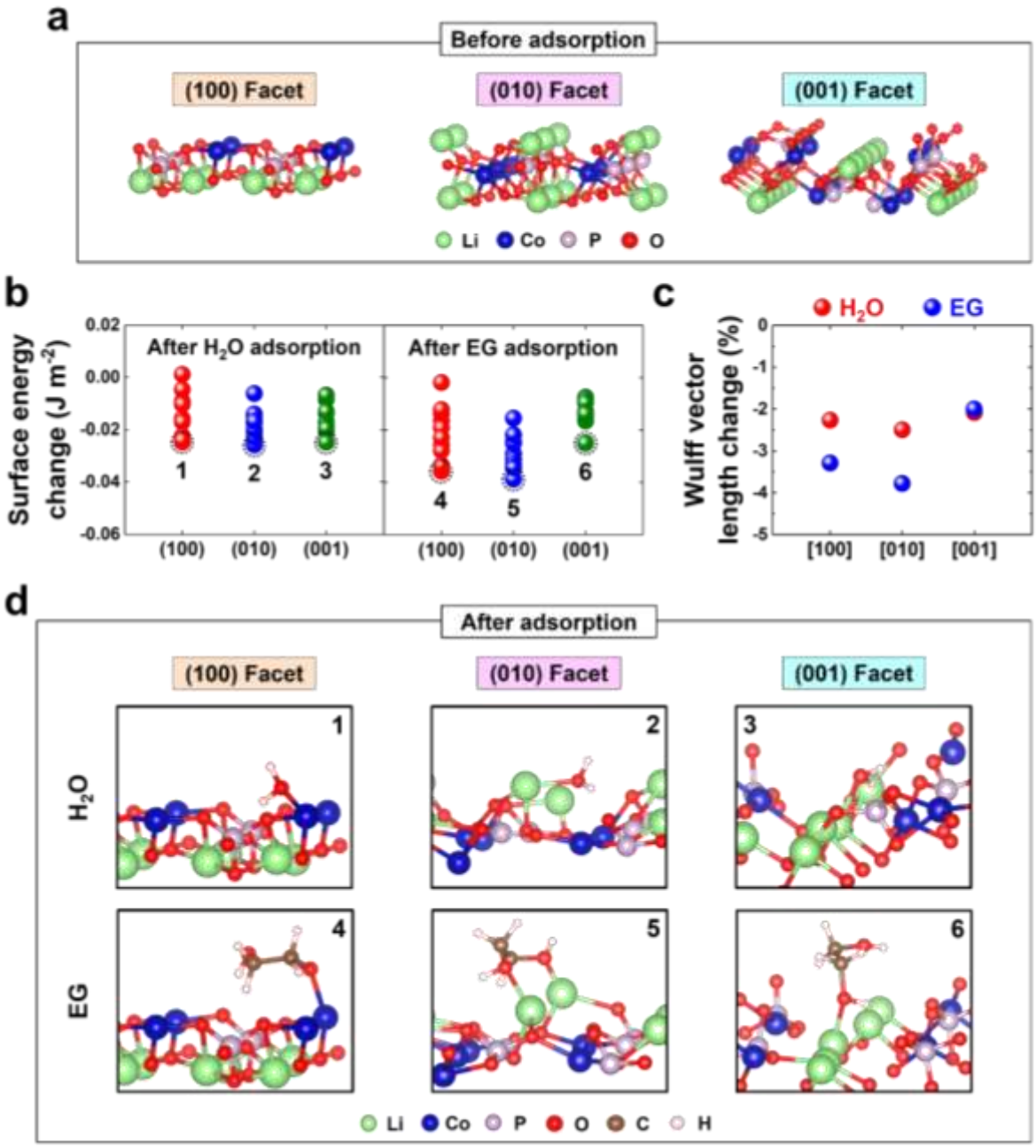


**Figure 4.2.** (a) Optimized outermost three atomic layer models of LCP facets; (b) surface energy and (c) Wulff vector length changes after mono-solvent molecule ($H_2O$ and EG) adsorption via AIMD/DFT; (d) atomic-scale adsorption configurations of $H_2O$ and EG on LCP facets.

Figure 4.2a depicts the slab structure of the (100), (010), and (001) facets, with surface energies of 1.130, 1.070, and 1.253 J $m^{-2}$, respectively, showing a trend of (010) < (100) < (001) that aligns well with the reference. We note that the entire number of atoms in our model ($Li_{16}Co_{16}P_{16}O_{64}$)

is downgraded compared to the reference ($Li_{36}Co_{36}P_{36}O_{144}$) to reduce the computational cost of AIMD calculations; however, despite the reduced model size, the overall trends agree well with those reported in the literature.

Afterwards, we observed how a single $H_2O$/EG solvent molecule is adsorbed with AIMD simulations and how much the surface energy is thermodynamically stabilized on different LCP facets via DFT calculation to examine the preferential growth mechanism of ST-LCP. Figure 4.2b exhibits the surface energy changes after the single-molecule adsorption of $H_2O$ and EG on each LCP facet obtained from AIMD/DFT. Ten representative adsorption configurations of a single solvent molecule on each LCP (100), (010), and (001) facets were generated, and the lowest $\Delta\gamma$ for individual cases was selected for comparison. For $H_2O$ adsorption, the lowest $\Delta\gamma$ of (100), (010), and (001) LCP facets were calculated to be -0.025, -0.026, and -0.025 J $m^{-2}$ indicating marginal surface stabilization. Yet, for EG adsorption, the lowest $\Delta\gamma$ of (100), (010), and (001) LCP facets are -0.036, -0.039, -0.025 J $m^{-2}$ demonstrating the magnitude of surface energy changes after the adsorption is more significant for ST-LCP in comparison to HT-LCP. These computational findings, based on unbiased adsorption configurations from AIMD simulations, provide more accurate insights into our experimental results by comparison to sole reliance on DFT calculations–as evidenced by Figure A.3.6–only.

Moreover, it must be noted that the morphology of final products is determined by the relative surface energy among three crystal facets upon growth process.[36-38] With pre-calculated surface energies ($\gamma$ and $\gamma'$ for both solvents) as input values, the equilibrium shape of the LCP crystal after the adsorption of $H_2O$ and EG can be determined using the Wulff construction. In this method, the surface energy influences the relative shape and proportions of the crystal by determining the relative sizes of its facets in the crystal model. The energy of each specific surface is represented by the length of a vector extending perpendicularly from the crystal core to that surface. This Wulff vector length is proportional to the surface energy, and the equilibrium shape of the crystal is determined by the inner envelope formed by these vectors. In Figure 4.2c, the Wulff vector lengths along the [100] and [010] axes decreased by -2.26 and -2.49 % after $H_2O$ adsorption, respectively. For comparison, the length decreases were -3.29 and -3.78 % after the EG adsorption along these same axes. The results show that the length changes along the [100] and [010] axes with EG are at least 45 % greater compared to those observed with $H_2O$. On the other hand, the Wulff vector length along [001] axis decreased by -2.02 and -2.04 % after the adsorption of EG and $H_2O$, correspondingly.

We further confirmed that as the number of adsorbed molecules (EG or $H_2O$) increases from one to two, EG shows a stronger preference for anisotropic growth compared to $H_2O$ (Figure A.3.7).

However, in multi-molecule systems, intermolecular interactions arise, significantly impacting the surface energy, particularly for EG due to its larger size and more complex structure compared to $H_2O$. To account for this, we restricted our calculations to systems with a maximum of two adsorbed molecules per surface. It is challenging to accurately quantify surface energy changes to describe the experimental observations in crystal morphology via single- or two-molecule adsorption simulation. Nevertheless, this computational modeling analysis based on AIMD/DFT demonstrates its feasibility in predicting the observed anisotropic growth trend along the *c* direction, highlighting the significance of this approach in crystal engineering.

In order to probe the adsorption mechanisms further, we analyzed the most stable configurations in six systems, assigning case numbers from 1 to 6 for each system shown in Figure 4.2d. In all configurations, phosphorus (P) in LCP already formed strong covalent bonds with four surrounding oxygen (O) atoms. Thus, no interaction is observed between P and solvent molecules. Instead, each lithium (Li) or cobalt (Co) atom in LCP formed bonds with the O atoms in either $H_2O$ or EG molecule. It is noted that each Li or Co atom bonds with six surrounding O atoms in a bulk LCP structure, whereas they bond with one to six neighboring O atoms at the outermost layers (including up to the second layer from the vacuum layer) in pristine slab structures.

On the (100) facet (Case: 1 and 4), Co atoms in the first layer have three dangling bonds; in contrast, Li atoms in the second layer do not have a dangling bond. Thus, the (100) facet is stabilized by reducing the dangling bond of Co by forming a Co (in LCP) – O (in $H_2O$ or EG) bond. Likewise, on the (010) facet (Case: 2 and 5), Li atoms in the first layer have three dangling bonds. However, Co atoms in the second layer have solely one dangling bond. Therefore, the (010) facet is stabilized by reducing the larger number of dangling bonds of Li by forming the Li (in LCP) – O (in $H_2O$ or EG) bond. Notably, two O atoms in the EG molecule bond with two Li atoms in LCP (Case: 5), indicating the lowest $\Delta\gamma$ in all configurations. Comparing two other facets, each Li and Co atom is positioned in the second layer of (001) facet with three dangling bonds. Although the Li-O bond is stronger than the Co-O bond, the O atom of EG preferentially bonds with the Li atom rather than Co atoms during adsorption.[39] This suggests another compensating factor, likely the electrostatic repulsion between the O atoms in LCP and EG when EG bonds with a Co atom. In the second layer, each Co atom bonds with an O atom diagonally above it, increasing the possibility of O (in LCP) – O (in EG) electrostatic repulsion, while each Li atom bonds with the O atoms directly below it, reducing the likelihood of this repulsion (see Figure 4.2a).

To investigate the superior stabilizing effect of EG on the (100) and (010) facet compared to the (001) facets, we examined the interaction of the O-H bond in EG solvent with LCP surfaces. Previous research on the adsorption configuration of EG on platinum (Pt) surfaces has emphasized the significance of how the two O-H bonds in EG interact with a Pt surface.[40] For example, configurations, where both O-H bonds in EG are positioned close to and interact with the Pt surface, show more stable energy compared to configurations where only one O-H bond is positioned near the Pt surface (with the other O-H bond placed further away from the surface). In this regard, the LCP (100) and (010) facets, where both O-H bonds in EG are closely positioned to the outermost atomic layer, would contribute more to surface stabilization compared to the LCP (001) facet, where only one O-H bond is positioned near the surface, with the other O-H placed away from LCP. We anticipate that the atomic arrangement of the LCP (100) and (010) facets enhances the interaction with the O atoms in EG, resulting in lower $\Delta\gamma$ values compared to the (001) facet. Conversely, in the case of $H_2O$ adsorption, since one O-H bond of $H_2O$ molecule bonds with each LCP facet, comparable $\Delta\gamma$ values are observed in all cases.

Thus far, numerous studies have attempted to achieve the anisotropic growth of LCP crystals by applying diverse organic solvents and additives to control the Li-ion diffusion length without a definitive answer for the growth mechanism.[12, 41] Herein, we report that the preferential growth along *c* direction can be manipulated by adjusting the surface energy of each facet, facilitated by switching the solvent from $H_2O$ to EG. With the newly discovered knowledge through our computational modeling work, we will probe next the positive implications in terms of the shortened diffusion length of ST-LCP on Li-ion diffusivity.

### 4.3.3. Enhanced Li-ion diffusion coefficient in ST-LCP crystal structure

To obtain insights into the Li-ion diffusion kinetics in preferentially grown ST-LCP crystals with the shortened diffusion pathway, we implemented a galvanostatic intermittent titration technique (GITT) analysis on both HT-LCP and ST-LCP. Basically, Li-ion diffusivity is one of crucial kinetic parameters governing the electrochemical properties of cathode materials, especially for 1-D polyanionic Li-ion diffusor such as LCP. Hence, the current study aims to investigate Li-ion diffusivity of our LCP samples during the charge and discharge process. Note that our GITT results were collected from the 5$^{th}$ cycle with the relatively accelerated C-rate for the shortened periods (C/2, 10 min pulse and 30 min rest) to focus on the substantive Li-ion diffusivity by avoiding the considerable initial charge capacity caused by severe side reactions.[42]

Figure 4.3a-b exhibit the magnified GITT profiles as a function of the measurement time. This profile reveals that ST-LCP exhibits a notable reduction of overpotential compared to HT-LCP regarding the potential where plateaus are located. In addition, the inset image shows the whole profile indicating the number of relaxation steps was obviously enlarged from 2 to 9 upon charge and from 1 to 8 upon discharge, respectively. In our previous study, we verified the fundamental limitations of $H_2O$-based synthesized HT-LCP and determined to be suffering from formation of $Co(OH)_2$ surface insulating layer and abundant bulk structure defects.[7] And we now note in comparison to the performance of ST-LCP, how these critical factors affect Li-ion intercalation dynamics unfavorably during charge and discharge steps resulting in imperfect voltage profile and capacity.

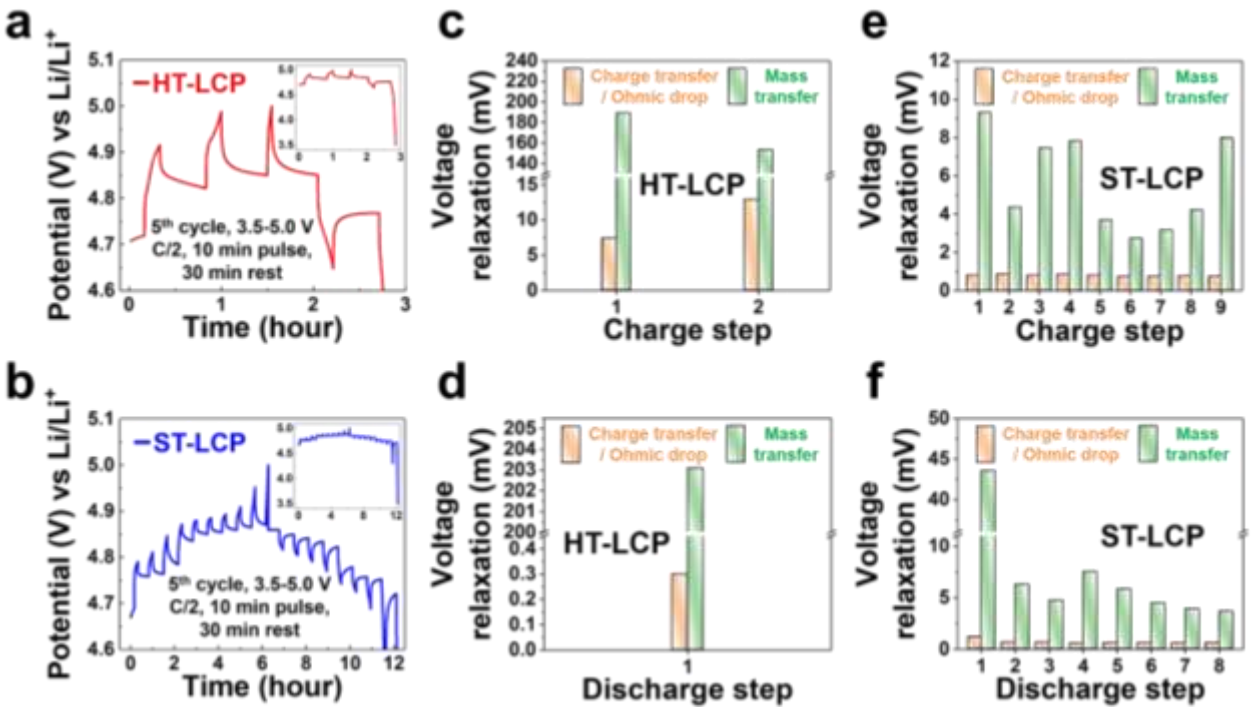


**Figure 4.3.** Galvanostatic intermittent titration technique (GITT) analysis of HT-LCP and ST-LCP during the 5th cycle in the voltage range of 3.5-5.0 V vs $Li/Li^+$ at C/2. (a-b) GITT profiles as a function of the measurement time (The inset image shows the whole GITT profile); (c-f) voltage relaxation upon charge and discharge.

In more detail, surface composition homogeneity and improved elemental distribution were achieved by switching the solvent to EG, as evidenced by the XPS O 1s spectra (Figure A.3.8a) that confirm the absence of Co-OH bonds, unlike HT-LCP. Besides, the anti-site defect concentration based on Rietveld refinement (Figure A.3.8b) is significantly reduced (from 9.14 to 0.86 %). These two changes kinetically promote Li-ion transport inside the crystal structure and at cathode-electrolyte interface. Previous studies have systematically shown, using DFT calculations, that anti-site defects

significantly hinder Li-ion diffusion in olivine materials like $LiMPO_4$ (M = Fe, Mn, Co, and Ni), which have a 1-D Li-ion diffusion channel.[43] Thus, the elimination of these defects results in remarkable performance improvement of ST-LCP in terms of enhanced Li-ion storage capacity as shown in Figure A.3.9 presenting the GITT profiles as a function of capacity.

Also, the voltage relaxation in the GITT curves is determined by two intrinsic components: (i) prompt relaxation (Charge-transfer resistance at the electrode-electrolyte interface and Ohmic drop, CT/IR), which is manifested by linear drop instantly after the current is cut-off, and (ii) time-reliant relaxation (Mass-transfer resistance relating to bulk Li-ion diffusion in crystal structure, MT) which is manifested by non-linear curve during each of rest periods.[44] As summarized in Figure 4.3c-f, ST-LCP exhibits tremendously mitigated CT/IR and MT resistances compared to HT-LCP. Except for the CT/IR in the discharge step, we observed a significant decrease in CT/IR resistance (about 12.8 times smaller) upon charge and MT resistance (30.4 and 20.3 times smaller) upon charge and discharge respectively. We attribute the decreased voltage relaxation to not only the elimination of defects from which HT-LCP suffers (Removal of $Co(OH)_2$ insulating surface layer and abundant anti-site defects) but also to preferential crystal orientation benefits (Shortened Li-ion diffusion pathway) endowed by the specific crystal plane surface energy action of EG during ST synthesis. Furthermore, Figure A.3.10 provides the overall trend of Li-ion diffusivity values for both HT-LCP and ST-LCP, as determined from the voltage relaxation results.

As mentioned previously, contrary to ST synthesis, other methods such as mechanochemical nanosizing and cation substitution result in detrimental side reactions with electrolyte that limit the accessible capacity due to the charge compensation deficit.[13, 21] Hence, we further narrowed our focus on optimizing the outcome from ST method. In one strategy to address this goal and following previous works in the literature, Ar-annealing was performed post ST synthesis (which will be referred to as ST-A-LCP).[12, 21, 45] As corroborated by comparing the C 1s spectra in XPS measurement (Figure A.3.11a-b), organic compound incorporating carbon and oxygen (O=C-O and C-O bonding) still persists on the surface of ST-LCP despite the washing steps and it is only alleviated after Ar-annealing treatment. This organic residue causes extra CT resistance at the interface with the electrolyte (Figure A.3.11c). Moreover, while the morphology (Figure A.3.12a-b) and XRD peaks (Figure A.3.12c) are not modulated, Ar-annealing further reduces the defect concentration approaching to nearly defect-free crystal structure from 0.86 to 0.01 % (Figure A.3.12d) based on the Rietveld refinement results (Figure A.3.12e and Table A.3.2). Accordingly, the synthesized HT-LCP, ST-LCP, and ST-A-LCP were fabricated into cathodes and tested next to investigate how the enhanced Li-ion diffusivity of the

highly ordered and preferentially oriented LCP crystals impacts the overall electrochemical performance.

### 4.3.4. Electrochemical characterization of HT-LCP, ST-LCP, and ST-A-LCP

In order to investigate the electrochemical behavior of HT-LCP, ST-LCP, and ST-A-LCP, CV tests were run and the obtained results are plotted in Figure 4.4a-c. For the initial CV cycle with the voltage scan rate at 0.1 mV $s^{-1}$ rate, the potentials at which the current signals occur are similar for the two HT-LCP and ST- LCP samples. Meanwhile, the current density of ST-LCP is larger than that of HT-LCP, but as the cycle progresses, the current density of both LCP samples dramatically decreases, and the position of peaks is gradually polarized due to rising resistances. Furthermore, the two peaks corresponding to oxidation and reduction are combined into broad and flattened profiles. On the contrary, the current density of ST-A-LCP is obviously superior to that of HT-LCP and ST-LCP. The total current density and the two redox peaks are clearly consistent and well-maintained even after five CV cycles owing to the lower amount of overpotential in ST-A-LCP. Additionally, the ratio of the two oxidation/reduction peaks is very close to the ideal behavior predicted for LCP based on two-phase reactions with the intermediate phase ($Li_{2/3}(Co^{2+})_{2/3}(Co^{3+})_{1/3}PO_4$).[20, 42, 46] For additional insights, Figure A.3.13 presents extra CV results at different scan rates to evaluate redox peak currents, overpotentials, and calculate Li-ion diffusion coefficients through the Randles–Ševčík equation.

Likewise, the evolution of specific charge-discharge capacity for different C-rates is depicted in Figure 4.4d-f. HT-LCP exhibits progressively reduced initial discharge capacity of 45.8, 39.6, 31.6, and 24.9 mAh $g^{-1}$ at C/10, C/5, C/2, and 1 C. Despite the advantages regarding morphological and structural improvements via the ST method, ST-LCP exhibits progressively reduced initial discharge capacity of 127.1, 120.3, 112.5, and 107.7 mAh $g^{-1}$ at C/10, C/5, C/2, and 1 C accordingly. We believe that the unique morphology and reduced concentration of anti-site defect through ST synthesis would guarantee the relatively higher accessible initial discharge capacity at a slow C-rate, but the anti-site defects still prove to be fatal with respect to the kinetics (Li-ion diffusion in LCP crystal structure). On the other hand, ST-A-LCP delivers a relatively consistent initial discharge capacity of 163.0, 162.9, 159.6, and 151.6 mAh $g^{-1}$, approaching to the theoretical value (167 mAh $g^{-1}$), even at the gradually increasing C-rate from C/10 to 1 C.

To further identify the plateau positions and overpotential, the differential capacity (dQ/dV) based on the voltage profile of the 2nd charge-discharge cycle of HT-LCP, ST-LCP, and ST-A-LCP at 1 C is shown in Figure 4.4g. As mentioned earlier, the intercalation process of Li-ion in LCP crystal structure is carried out in two stages due to the intermediate phase. Thus, intuitively, one should be able to detect distinctive double peaks or plateaus in CV, dQ/dV, and voltage profiles to determine the target materials operating flawlessly. Above all, HT-LCP represents a relatively smaller differential capacity value and higher polarization compared to the other two LCP samples. In addition, HT-LCP displays a singular peak during the reduction indicating the discharge process.

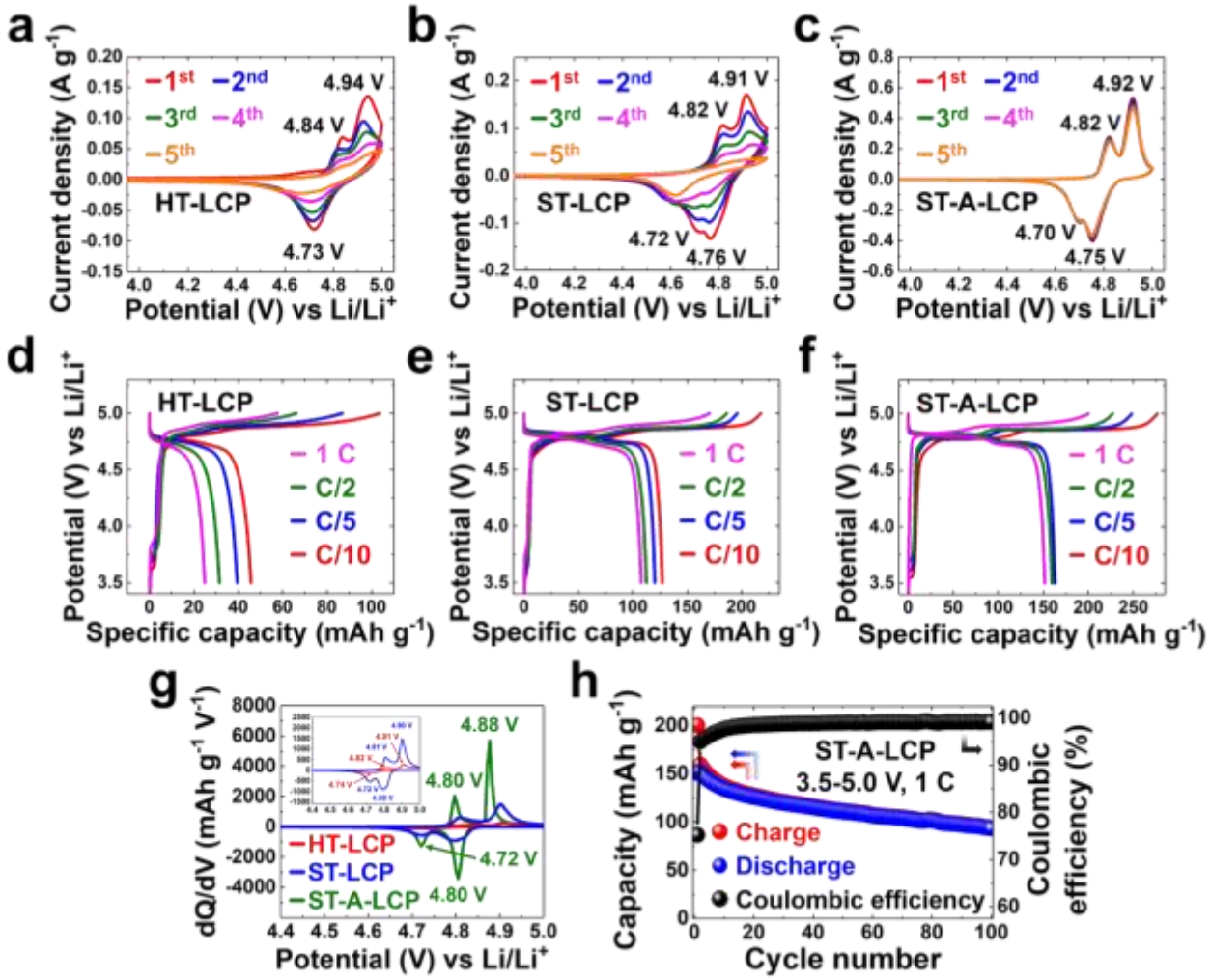


**Figure 4.4.** Electrochemical behavior of HT-LCP, ST-LCP, and ST-A-LCP verified through (a-c) CV within the voltage range 3.5-5.0 V vs. $Li/Li^+$ at a scan rate of 0.1 mV $s^{-1}$; (d-f) rate capability at various C-rates from C/10, C/5, and C/2, to 1 C; (g) differential capacity for the 2nd cycle at 1 C; (h) capacity retention and Coulombic efficiency of ST-A-LCP during cycling within the voltage range 3.5-5.0 V vs. $Li/Li^+$ at 1 C.

Again, we believe this electrochemically non-ideal behavior of HT-LCP results from the defect-prone HT synthesis method.[7] Meanwhile, for both ST-LCP and ST-A-LCP, two well-separated peaks are observed for each charge and discharge process, which correspond to the optimal Li-ion intercalation process. In particular, considering the peak intensity, it can be seen that the total capacity of ST-A-LCP is much higher than that of ST-LCP. Moreover, the peak positions of ST-LCP are shifted towards higher potentials, which reflects a larger overpotential associated with the redox-driven extraction and insertion of Li-ions. This trend can be explained by the benefits of ST synthesis and Ar-annealing treatment resulting in the shortening of the Li-ion diffusion pathway and mitigating the anti-site defect occurrence during synthesis. By taking advantage of EG to control the crystal growth during ST synthesis and Ar-annealing, we have successfully engineered the best performing yet LCP crystal variety regarding to Li-ion diffusion length and anti-site defect concentration. Thus, our engineered LCP crystals achieve nearly theoretically accessible discharge capacity and improved rate capability, unmatched in comparison to previously reported LCP materials fabricated via other synthesis methods.

In terms of prolonged cycling, Figure 4.4h exhibits the evolution of charge-discharge capacity and Coulombic efficiency of ST-A-LCP at 1 C. The discharge capacity at 1 C starts from the nearly theoretical value, 151.6 mAh $g^{-1}$ dropping to 93.4 mAh $g^{-1}$ after 100 cycles which corresponds to 61.65 % retention. Figure A.3.14 summarizes the capacity retention results of ST-LCP and ST-A-LCP at different C-rates. There we can see both samples to achieve higher initial discharge capacities at slower C-rates but to record higher capacity fade. It should be noted that the electrolyte was prepared with a stabilizing additive, TMSP with the LSV analysis (plotted in Figure A.3.15) slowing insignificant current density of 0.01 mA $cm^{-1}$ at 5.0 V vs. $Li/Li^{+}$. Notwithstanding the issue of complex dependency of capacity fade on C-rate, an issue for future study, the recorded capacity fade at 1 C rate (Figure 4.4h), is very promising as surpasses in a major way previous LCP cathode works opening an unexplored crystal engineering avenue to attain desired cycling stability via surface and composition-based modification strategies.

In principle, the reason behind capacity fade in LCP materials has been a topic of debate with the major culprits thought to relate to interfacial degradation and structural deformation due to high-V operation.[48-50] Given that a nearly defect-free LCP crystal structure was attained in this work, we may assume that the CEI layer dynamics at the interface relates predominantly with the capacity fade issue rather than bulk defects. Hence, further investigations will be followed aiming at elucidating and controlling the interfacial capacity fade mechanism.

## 4.4. Conclusion

In this study, we designed novel LCP crystals with improved Li-ion intercalation kinetics achieving near theoretical storage capacity at C-rate up to one. In a departure from the standard hydrothermal (HT) synthesis method that is prone to defects, we have employed solvothermal (ST) synthesis using ethylene glycol (EG) as a solvent followed by Ar-annealing treatment. Consequently, nearly defect-free and preferential orientation crystal structure was obtained, characterized by shortened Li-ion diffusion pathways. The origin of these crystal advantages was probed with the study of surface energy at various LCP crystal facets in different solvents ($H_2O$ and EG molecule adsorption) through *ab initio* molecular dynamics (AIMD) simulation and density functional theory (DFT) calculation. Each LCP facet has a different interfacial energy with EG, that is taken advantage in promoting growth along the preferential orientation. In the meantime, anti-site defect concentration was also curtailed via adjusting Li content and performing Ar-annealing leading to nearly defect-free LCP crystals. Thanks to these morphological and structural advantages, the new LCP crystal variety exhibits noticeably augmented Li-ion diffusivity, with nearly theoretical full capacity value (163.0 mAh $g^{-1}$ at C/10), improved rate capability (151.6 mAh $g^{-1}$ at 1 C), and relatively stabilized capacity retention (61.65 % after 100 cycles at 1 C). Nevertheless, the major issue for LCP's commercialization still remains unresolved in terms of capacity retention over prolonged cycling time. This is the subject of future work. Notwithstanding this issue, the present work provides a powerful example of how specific crystal plane surface energy modulation via EG adsorption can engineer favorable crystal properties to maximize the functionality of materials like LCP in terms of Li-ion storage capacity and kinetics that can be emulated in other cathode materials too.

## 4.5. References


1. M. S. Whittingham, Electrical energy storage and intercalation chemistry. *Science* **1976**, *192* (4244), 1126-1127.
2. Z. Yang, H. Huang, F. Lin, Sustainable electric vehicle batteries for a sustainable world: Perspectives on battery cathodes, environment, supply chain, manufacturing, life cycle, and policy. *Advanced Energy Materials* **2022**, *12* (26), 2200383.
3. H. Li, R. Fong, M. Woo, H. Ahmed, D.-H. Seo, R. Malik, J. Lee, Toward high-energy Mn-based disordered-rocksalt Li-ion cathodes. *Joule* **2022**, *6* (1), 53-91.
4. Y. Zhang, Y. Katayama, R. Tatara, L. Giordano, Y. Yu, D. Fraggedakis, J. G. Sun, F. Maglia, R. Jung, M. Z. Bazant, Y. Shao-Horn, Revealing electrolyte oxidation via carbonate dehydrogenation on Ni-based oxides in Li-ion batteries by *in situ* Fourier transform infrared spectroscopy. *Energy & Environmental Science* **2020**, *13* (1), 183-199.

5. W. Liu, P. Oh, X. Liu, M. J. Lee, W. Cho, S. Chae, Y. Kim, J. Cho, Nickel-rich layered lithium transition-metal oxide for high-energy lithium-ion batteries. *Angewandte Chemie International Edition* **2015**, *54* (15), 4440-4457.
6. W. Li, B. Song, A. Manthiram, High-voltage positive electrode materials for lithium-ion batteries. *Chemical Society Reviews* **2017**, *46* (10), 3006-3059.
7. M. Woo, J. Lee, G. P. Demopoulos, Surface and bulk defect formation during hydrothermal synthesis of $LiCoPO_4$ crystals and their electrochemical implications. *Materials Advances* **2023**, *4* (20), 4823-4834.
8. D. Morgan, A. Van der Van, G. Ceder, Li conductivity in $Li_xMPO_4$ (M = Mn, Fe, Co, Ni) olivine materials. *Electrochemical and Solid-State Letters* **2004**, *7* (2), A30-A32.
9. J. Wolfenstine, J. Read, J. L. Allen, Effect of carbon on the electronic conductivity and discharge capacity $LiCoPO_4$. *Journal of Power Sources* **2007**, *163* (2), 1070-1073.
10. A. Boulineau, T. Gutel, Revealing electrochemically induced antisite defects in $LiCoPO_4$: Evolution upon cycling. *Chemistry of Materials* **2015**, *27* (3), 802-807.
11. H. El-Shinawi, E. J. Cussen, S. A. Corr, Morphology-directed synthesis of $LiFePO_4$ and $LiCoPO_4$ from nanostructured $Li_{1+2x}PO_{3+x}$. *Inorganic Chemistry* **2019**, *58* (10), 6946-6949.
12. X. Wu, M. Meledina, H. Tempel, H. Kungl, J. Mayer, R.-A. Eichel, Morphology-controllable synthesis of $LiCoPO_4$ and its influence on electrochemical performance for high-voltage lithium ion batteries. *Journal of Power Sources* **2020**, *450*, 227726.
13. S. Sreedeep, S. Natarajan, V. Aravindan, Recent advancements in $LiCoPO_4$ cathodes using electrolyte additives. *Current Opinion in Electrochemistry* **2022**, *31*, 100868.
14. K. Guo, S. Qi, H. Wang, J. Huang, M. Wu, Y. Yang, X. Li, Y. Ren, J. Ma, High-voltage electrolyte chemistry for lithium batteries. *Small Science* **2022**, *2* (5), 2100107.
15. Q. D. Truong, M. K. Devaraju, Y. Ganbe, T. Tomai, I. Honma, Controlling the shape of $LiCoPO_4$ nanocrystals by supercritical fluid process for enhanced energy storage properties. *Scientific Reports* **2014**, *4*, 3975.
16. N. Boaretto, I. Garbayo, S. Valiyaveettil-SobhanRaj, A. Quintela, C. Li, M. Casas-Cabanas, F. Aguesse, Lithium solid-state batteries: State-of-the-art and challenges for materials, interfaces and processing. *Journal of Power Sources* **2021**, *502*, 229919.
17. R. Brow, A. Donakowski, A. Mesnier, D. J. Pereira, K. X. Steirer, S. Santhanagopalan, A. Manthiram, Mechanical pulverization of Co-Free nickel-rich cathodes for improved high-voltage cycling of lithium-ion batteries. *ACS Applied Energy Materials* **2022**, *5* (6), 6996-7005.
18. R. Zhu, G. Liu, G. Qu, X. Li, X. Chen, W. Wan, C. Wang, Y. Huang, Enhancing volumetric energy density of $LiFePO_4$ battery using liquid metal as conductive agent. *Advanced Functional Materials* **2024**, 2409230.
19. K. J. Kreder, G. Assat, A. Manthiram, Aliovalent substitution of $V^{3+}$ for $Co^{2+}$ in $LiCoPO_4$ by a low-temperature microwave-assisted solvothermal process. *Chemistry of Materials* **2016**, *28* (6), 1847-1853.
20. J. L. Allen, J. L. Allen, T. Thompson, S. A. Delp, J. Wolfenstine, T. R. Jow, Cr and Si substituted-$LiCo_{0.9}Fe_{0.1}PO_4$: Structure, full and half Li-ion cell performance. *Journal of Power Sources* **2016**, *327*, 229-234.
21. N. Okita, K. Kisu, E. Iwama, Y. Sakai, Y. Lim, Y. Takami, M. T. Sougrati, T. Brousse, P. Rozier, P. Simon, W. Naoi, K. Naoi, Stabilizing the structure of $LiCoPO_4$ nanocrystals via addition of $Fe^{3+}$: Formation of $Fe^{3+}$ surface layer, creation of diffusion-enhancing vacancies, and enabling high-voltage battery operation. *Chemistry of Materials* **2018**, *30* (19), 6675-6683.
22. G. Kresse, J. Furthmüller, Efficient iterative schemes for *ab initio* total-energy calculations using a plane-wave basis set. *Physical review B* **1996**, *54*, 11169.

23. J. P. Perdew, K. Burke, M. Ernzerhof, Generalized gradient approximation made simple. *Physical review letters* **1996**, *77*, 3865.
24. S. L. Dudarev, G. A. Botton, S. Y. Savrasov, C. J. Humphreys, A. P. Sutton, Electron-energy-loss spectra and the structural stability of nickel oxide: An LSDA+U study. *Physical Review B* **1998**, *57*, 1505.
25. A. Jain, S. P. Ong, G. Hautier, W. Chen, W. D. Richards, S. Dacek, S. Cholia, D. Gunter, D. Skinner, G. Ceder, K. A. Persson, Commentary: The materials project: A materials genome approach to accelerating materials innovation. *APL Materials* **2013**, *1*, 011002.
26. S. Grimme, J. Antony, S. Ehrlich, H. Krieg, A consistent and accurate *ab initio* parametrization of density functional dispersion correction (DFT-D) for the 94 elements H-Pu. *The Journal of chemical physics* **2010**, *132* (15), 154104.
27. A. Paolella, G. Bertoni, P. Hovington, Z. Feng, R. Flacau, M. Prato, M. Colombo, S. Marras, L. Manna, S. Turner, G. V. Tendeloo, A. Guerfi, G. P. Demopoulos, K. Zaghib, Cation exchange mediated elimination of the Fe-antisites in the hydrothermal synthesis of $LiFePO_4$, *Nano Energy* **2015**, *16*, 256-267.
28. G. K. P. Dathar, D. Sheppard, K. J. Stevenson, G. Henkelman, Calculations of Li-ion diffusion in olivine phosphates. *Chemistry of Materials* **2011**, *23* (17), 4032-4037.
29. X. Tang, Z. Wang, D. Wu, Z. Wu, Z. Ren, R. Li, P. Liu, G. Mei, J. Sun, J. Yu, F. Zheng, W. C. H. Choy, R. Chen, X. W. Sun, F. Yang, K. Wang, *In situ* growth mechanism for high-quality hybrid perovskite single-crystal thin films with high area to thickness ratio: Looking for the sweet spot. *Advanced Science* **2022**, *9* (13), 2104788.
30. W. Ke, T. M. Svrataas, D. Chen, A review of gas hydrate nucleation theories and growth models. *Journal of Natural Gas Science and Engineering* **2019**, *61*, 169-196.
31. T. Nazemi, R. Sadeghi, Effect of polar organic solvents on the surface adsorption and micelle formation of surface-active ionic liquid 1-dodecyl-3-methylimidazolium bromide in aqueous solutions and comparison with the traditional cationic surfactant dodecyltrimethylammonium bromide. *Colloids and Surfaces A: Physicochemical and Engineering Aspects* **2014**, *462*, 271-279.
32. L. Ren, H. Xu, Effect of ethylene glycol as solvent on the composition and morphology of nickel phosphide. *Micro & Nano Letters* **2018**, *13* (12), 1646-1648.
33. D. Bohne, S. Fischer, E. Obermeier, Thermal, conductivity, density, viscosity, and prandtl-numbers of ethylene glycol-water mixtures, *Ber. Bunsenges. Phys. Chem.* **1984**, *88*, 739-742.
34. K. Song, J. Y. Koo, H. C. Choi, Viscosity effect on the strategic kinetic overgrowth of molecular crystals in various morphologies: concave and octapod fullerene crystals, *RSC Adv.* **2021**, *11*, 20992-20996.
35. K.-C. Wu, C.-M. Hsieh, B. K. Chang, First principles calculations on lithium diffusion near the surface and in the bulk of Fe-doped $LiCoPO_4$. *Physical Chemistry Chemical Physics* **2022**, *24* (2), 1147-1155.
36. E. Pastor, L. Montanes, A. Gutierrez-Blanco, F. S. Hegner, C. A. Mesa, N. Lopez, S. Gimenez, The role of crystal facets and disorder on photo-electrosynthesis. *Nanoscale* **2022**, *14* (42), 15596-15606.
37. Y. Gao, W. Song, J. Yang, X. Ji, N. Wang, X. Huang, T. Wang, H. Hao, Crystal morphology prediction models and regulating methods. *Crystals* **2024**, *14* (6), 484.
38. C. Himawan, V. M. Starov, A. G. F. Stapley, Thermodynamic and kinetic aspects of fat crystallization. *Advances in Colloid and Interface Science* **2006**, *122* (1-3), 3-33.
39. Y.-R. Luo, Comprehensive handbook of chemical bond energies. *CRC Press* **2007**.
40. R. C. Bezerra, P. C. D. Mendes, R. R. Passos, J. L. F. D. Silva, *Ab initio* investigation of the role of transition-metal dopants in the adsorption properties of ethylene glycol on doped Pt(100) surfaces. *Physical Chemistry Chemical Physics* **2020**, *22* (31), 17646-17658.

41. J. Ludwig, C. Marino, D. Haering, C. Stinner, H. A. Gasteiger, T. Nilges, Morphology-controlled microwave-assisted solvothermal synthesis of high-performance $LiCoPO_4$ as a high-voltage cathode material for Li-ion batteries. *Journal of Power Sources* **2017**, *342*, 214-223.
42. M. G. Palmer, J. T. Frith, A. L. Hector, A. W. Lodge, J. R. Owen, C. Nicklin, J. Rawle, *In situ* phase behaviour of a high capacity $LiCoPO_4$ electrode during constant or pulsed charge of a lithium cell. *Chemical Communications* **2016**, *52* (98), 14169-14172.
43. C. A. J. Fisher, V. M. H. Prieto, M. S. Islam, Lithium battery materials $LiMPO_4$ (M = Mn, Fe, Co, and Ni): Insights into defect association, transport mechanisms, and doping behavior. *Chemistry of Materials* **2008,** *20* (18), 5907-5915.
44. J. Lee, D. Yu, Z. Zhu, X. Yao, C. Wang, Y. Dong, R. Malik, J. Li, Kinetic rejuvenation of Li-rich Li-ion battery cathodes upon oxygen redox. *ACS Applied Energy Materials* **2020,** *3* (8), 7931-7943.
45. S. Brutti, J. Manzi, D. Meggiolaro, F. M. Vitucci, F. Trequattrini, A. Paolone, O. Palumbo, Interplay between local structure and transport properties in iron-doped $LiCoPO_4$ olivines. *Journal of Materials Chemistry A* **2017**, *5* (27), 14020-14030.
46. F. C. Strobridge, R. J. Clément, M. Leskes, D. S. Middlemiss, O. J. Borkiewicz, K. M. Wiaderek, K. W. Chapman, P. J. Chupas, C. P. Grey, Identifying the structure of the intermediate, $Li_{2/3}CoPO_4$, formed during electrochemical cycling of $LiCoPO_4$. *Chemistry of Materials* **2014**, *26* (21), 6193-6205.
47. L. Yang, K. Yang, J. Zheng, K. Xu, K. Amine, F. Pan, Harnessing the surface structure to enable high-performance cathode materials for lithium-ion batteries. *Chemical Society Review* **2020**, *49* (14), 4667-4680.
48. M. Qi, L. Wang, X. Huang, M. Ma, X. He, Surface engineering of cathode materials: enhancing the high performance of lithium-ion batteries. *Small* **2024**, 2402443.
49. G. Kaur, B. D. Gates, Review—Surface coatings for cathodes in lithium-ion batteries: From crystal structures to electrochemical performance. *Journal of The Electrochemical Society* **2022**, *169*, 043504.

# Chapter 5: Interfacial capacity fade mechanism of high-voltage $LiCoPO_4$ cathode and its mitigation

**Bridge:** Chapter 4 introduced a novel designed $LiCoPO_4$ (LCP) crystal variant synthesized through a solvothermal (ST) process using ethylene glycol (EG), followed by Argon (Ar)-annealing. This method yielded a defect-free crystal structure with optimized Li-ion diffusion pathways. Computational techniques, including *ab initio* molecular dynamics (AIMD) and density functional theory (DFT), helped establish the crystal growth mechanism, revealing the role of EG in regulating interfacial energies of LCP crystal facets. This preferential orientation growth led to exceptional electrochemical performance, achieving nearly theoretical full capacity and superior rate capability. Despite this breakthrough, long-term cycling stability remains as a critical challenge. ST-A-LCP showed compromised cycle life due to inconsistent Coulombic efficiency (CE), originated from charge-discharge capacity disparities. This issue is attributed to electrolyte degradation under high-V conditions and intensive chemical-electrochemical reactions at the cathode-electrolyte interface. While the high cut-off voltage (5.0 V vs. $Li/Li^+$) enhances energy density, it also triggers parasitic side reactions, necessitating further investigation for the development of durable high-V cathodes.

In Chapter 5, the relationship between capacity fade mechanisms and irreversible interfacial reactions is investigated through comprehensive post-mortem analysis of cycled electrodes under various aging conditions. The study identified two main degradation mechanisms: increased charge-transfer resistance due to cathode-electrolyte interphase (CEI) layer formation and capacity loss from redox metal (RM) dissolution. To address these issues, a reduced graphene oxide (RGO) coating strategy was developed. This coating effectively mitigated interfacial side reactions by enhancing charge-transfer kinetics and suppressing RM dissolution. As a result, the RGO-coated LCP (ST-R-LCP) exhibited significantly improved cycle life compared to its uncoated counterpart. This research offers an integrated approach to optimizing LCP for high-V Li-ion batteries through crystal structure engineering and surface modification, paving the way for overcoming current limitations and advancing the practical application of LCP-based energy storage systems.

This chapter is replication of a manuscript to be submitted in a peer-reviewed journal, with the following citation:

Moohyun Woo and George P. Demopoulos, 2025, “Interfacial capacity fade mechanism of high-voltage $LiCoPO_4$ cathode and its mitigation” *(Submitted)*

**Abstract**

Lithium cobalt phosphate ($LiCoPO_4$, LCP) is a high-voltage (high-V) polyanionic compound, of critical application importance due to its potential on delivering high energy density compared to the commercialized lithium iron phosphate ($LiFePO_4$, LFP) counterpart. Despite this potential, LCP's application has been hampered by inferior Coulombic efficiency and capacity retention owing to cathode degradation triggered by the elevated cut-off voltage of up to 5.0 V vs. $Li/Li^+$. Namely, such high-V leads to severe parasitic side reactions at the cathode-electrolyte interface involving complex phenomena, the understanding of which holds the key to designing robust high-V cathodes. Herein, we have focused on post-mortem analysis of cycled LCP electrodes in different aging/cycling conditions to help establish the link of capacity fade on high-V interfacial side reactions. Through this analysis, it has been revealed that the detrimental surface degradation of LCP, caused by electrochemical and chemical reactions with liquid electrolyte components, proceeds via irreversible cathode-electrolyte interphase (CEI) layer evolution and redox metal (RM) dissolution. Specifically, the progressively evolving CEI layer and RM dissolution induce extra charge-transfer resistance and loss of RM-related capacity, the extent of which is directly dependent on applied C-rates. To combat this undesired phenomenon, a sucrose-derived reduced graphene oxide (RGO) surface coating strategy has been successfully engineered to develop a protective layer. This unique conductive layer enables accelerated charge-transfer kinetics through the cathode-electrolyte interface while suppressing RM dissolution via surface complexation control leading to significantly improved rate capability and cycling stability.

## 5.1. Introduction

As the energy storage industry expands exponentially through a wider scope of applications, notably the fast growing electric vehicle (EV) and upcoming electric aircraft (EA) markets, there is an ever-growing demand for next generation Li-ion batteries (LIBs) beyond the current energy density level.[1-4] To push the energy density level higher, it is essential to develop cathode materials based on several selection criteria including higher operating voltage, storage capacity, rate capability, and cycling stability.[5-7] Design and development of high-voltage (high-V) cathodes is identified as critical step in our pursuit for high energy density LIBs.[8] In the context, lithium cobalt phosphate ($LiCoPO_4$, LCP) is of great interest as a high-V polyanionic compound with high theoretical energy density of 800 Wh $kg^{-1}$ thanks to high redox voltage and capacity (4.8 V * 167 mAh $g^{-1}$) properties.[9] Additionally, LCP, like its commercial counterpart lithium iron phosphate ($LiFePO_4$, LFP), belongs to the olivine

crystal structure family, boasting very stable framework.[10, 11] These attributes, despite its cobalt content, have made LCP a strong candidate for niche applications where high energy density systems are critical.[12, 13]

Despite these promising benefits, the development of LCP cathodes has been hampered by certain compromising inherent material properties: (1) intrinsically low ionic and electronic conductivity causing sluggish kinetics, (2) abundant anti-site defects blocking one-dimensional (1-D) Li-ion diffusion pathway, and (3) capacity fade predominantly due to interphasial degradation at high-V—a relatively less explored yet critical contributor requiring further investigations..[14-16] Recently, we have developed a new crystal variety of LCP characterized by shortened Li-ion diffusion length thanks to preferential orientation grown morphology and defect-free crystal structure achieving for the first time nearly theoretical full discharge capacity and remarkable rate capability; this is achieved via specific solvent molecule-crystal plane regulation and subsequent argon (Ar)-annealing.[17] Nevertheless, capacity fade, although somewhat improved, has persisted upon prolonged cycling owing to the high operating voltage, which seemingly causes electrolyte decomposition despite the use of a stabilizing additive.

Parasitic side reactions at the cathode-electrolyte interface are known to be promoted with elevated operating voltage leading to the evolution of cathode-electrolyte interphase (CEI) layer via decomposition of lithium (Li) salts and organic carbonate solvents; as a consequence severe charge-transfer resistance develops resulting in rapid capacity decay and ultimately battery breakdown.[18-20] Accordingly, fundamental and comprehensive post-mortem investigations are required on the above-mentioned interfacial phenomena under various electrochemical environments with different aging/cycling conditions at the raised cut-off voltage, to provide insights as to the origin of LCP capacity fade. At the same time, research into surface engineering of the newly developed LCP crystals to mitigate destructive electrode-electrolyte interfacial reactions via proper functional surface coating is of great urgency to improve charge transport kinetics and prevent capacity fade via interface stabilization.

In this work, we have focused on scrutinizing the relationship between capacity fade and irreversible side reactions by conducting extensive post-mortem analysis including TEM, TGA, EIS, MP-AES and XPS. We have identified, surface degradation of LCP to involve thicker CEI layers formation and considerable RM dissolution under relatively long-term cycling operation. These side reactions lead to extra charge-transfer resistance and parasitic current manifested as an excess charge capacity—higher than the theoretical value—resulting in curtailed Coulombic efficiency. More

importantly, it is revealed that RM dissolution works as another contributor to severe capacity fade induced by a complex dissolution-migration-deposition mechanism carrying soluble metal species from the cathode to the separator and anode upon prolonged cycling. To tackle this, we developed a sucrose-derived reduced graphene oxide (RGO) coating strategy to boost the charge exchange mechanism while minimizing the undesired RM dissolution and exploiting the intrinsic electronic conductivity of RGO. Also, we unveiled how RGO coating significantly mitigates RM dissolution by serving as a barrier against complexation of surface RM cations with organic ligands produced by oxidation of electrolyte at high-V. Our coating strategy demonstrates remarkable rate capability, achieving nearly theoretical Li-ion storage capacity across all C-rates, ranging from C/10 to 1 C. The enhancement is particularly notable at 1 C, delivering both superior rate capability accompanied by outstanding discharge capacity of 163.0 mAh $g^{-1}$ (equal to 771.2 Wh $kg^{-1}$ in energy density) and relatively enhanced retention.

## 5.2. Experimental section

### 5.2.1. Material preparation

The LCP material was synthesized via a solvothermal (ST) process utilizing ethylene glycol (EG) as a reaction medium at 260 ºC for 6-hour duration with agitation at 300 rpm. This methodology, the details of which are described in our previous reports, facilitates the preferential anisotropic crystal growth.[17, 21] For sucrose-derived reduced graphene oxide (RGO) coating, the method involved dispersion and stirring of pristine ST-LCP in deoxygenated deionized water containing sucrose (99.5 %, $C_{12}H_{22}O_{11}$, Sigma-Aldrich) of different weight percent (0, 30, 40, 50 wt.%). The well-mixed suspension was transferred in an alumina crucible. The slurry was then dried in a vacuum oven at 80 ºC and transferred to an MTI mini tube furnace (model OTF-1200X) and heated at 700 ºC for 1 hour with continuous Ar gas flow to induce sucrose decomposition and subsequent carbonization. The samples after Ar-annealing are denoted as 'ST-A-LCP' (without sucrose) and 'ST-R-LCP' (with sucrose).

### 5.2.2. Material characterization

High-resolution transmission electron microscopy (HRTEM) with High-angle annular dark-field (HAADF) imaging and energy dispersive X-ray (EDS) analysis for elemental mapping was applied to monitor the evolved CEI and RGO layer using the Thermo Scientific Talos F200X G2 STEM with accelerating voltage 200 kV. The morphology of LCP samples was evaluated with a

Hitachi cold-field emission SU-8000 scanning electron microscope (CFE-SEM). Thermogravimetic analysis (TGA) was performed in air from room temperature to 700 °C with the heating rate at 10 °C $min^{-1}$ using a TGA 5500 thermal analyzer and platinum crucibles for quantitative analysis of CEI and RGO layer. For the surface layer composition analysis, X-ray photoelectron spectroscopy (XPS) measurements were made with the Thermo Scientific K-Alpha using aluminum (Al) Kα micro-focused monochromator. XPS data processing was performed with Avantage data system for peak fitting. Powder X-ray diffraction (PXRD) patterns were collected with Bruker D8 Discovery X-ray diffractometer using Co Kα radiation with the wavelength (λ) of 1.78892 Å from 2θ = 10 to 80 °. Crystal structure information for lattice parameters and anti-site defect concentration was fitted and estimated with XRD Rietveld refinement by using TOPAS Academic V5 software. The microwave plasma atomic emission spectrometer (MP-AES) from Agilent was used to determine the concentration ratio of remaining cobalt to phosphate (Co/P) in LCP electrodes after cycling tests. Prior to MP-AES measurements, cycled electrodes were soaked in ethanol and sonicated for three hours to separate LCP active material from carbon black and PVDF binder. Subsequently, they were digested by using 50 vol.% concentrated hydrochloric acid (HCl, Fisher Scientific) followed by dilution with 4 vol.% nitric acid (TraceMetal Grade, $HNO_3$, Fisher Scientific). Raman spectroscopy (DXR2 Raman Microscope, Thermo Scientific) with 532 nm wavelength and Fourier transform infrared (FT-IR) spectroscopy (Perkin Elmer Spectrum II FT-IR Spectrometer) were employed in the wavenumber range of 4000 to 400 $cm^{-1}$ with a resolution of 0.5 $cm^{-1}$ to confirm the existence of RGO layer and its oxygen-containing functional groups on the surface of ST-R-LCP sample.

### 5.2.3. Battery assembly and electrochemical protocols

In this study, we followed the detailed procedures for cell assembly as described in our previous work.[17] In brief summary, the active material, conductive carbon, and polyvinylidene fluoride (PVDF) binder were mixed in NMP solvent with a weight ratio of 7:2:1, and the slurry was pasted on Al and then dried overnight at 80 °C in a vacuum oven. Lithium metal was used as anode. The customized electrolyte solution was prepared with 1 M of $LiPF_6$ solution in a 1:1:3 (vol.%) mixture of EC:PC:DMC electrolyte and 2 wt.% tris(trimethylsilyl) phosphite (95 % $[(CH_3)_3SiO]_3P$) as high-V stabilizing additive. The galvanostatic charge-discharge profile was measured on an Arbin cycler. The battery cycling test was carried out at different C-rates (1 C = 167 mAh $g^{-1}$) in the voltage range of 3.5–5.0 V vs. $Li/Li^+$. For capacity retention, we continued the cycling tests until the discharge capacity declined to 50 mAh $g^{-1}$. Electrochemical impedance spectroscopy (EIS) measurements of the

pristine and cycled working electrodes were made using a BioLogic workstation in potentiostatic mode between 1 MHz and 10 mHz with various forward bias potentials (3.5-5.0 V vs. $Li/Li^+$). Nyquist plots were fitted using ZView® software.

### 5.2.4. Post-mortem analysis

After performing the above-described cycling tests, cycled electrodes and separators were harvested in an Ar-filled glovebox ($H_2O$ and $O_2$ < 0.5 ppm) and rinsed with DMC three times to remove the residual electrolyte and Li salt. Subsequently, the collected electrodes and separators were dried in the glovebox for 48 hours. Further characterizations for crystal structure, surface, and elemental composition were carried out with the same parameters outlined above.

## 5.3. Results and discussion

### 5.3.1. Irreversible interfacial aging of $LiCoPO_4$ upon cycling

To visualize the formed CEI layer upon cycling, post-mortem analyses with HRTEM, HAADF, and elemental mapping techniques were implemented and the obtained results are summarized in Figure 5.1a-f. Before high-V operation, LCP from the pristine electrode exhibits clear and smooth surface without signs of any foreign precipitates (Figure 5.1a). Unlike the pristine sample, HRTEM images of cycled LCP after 10 cycles at 1 C and C/10, as shown in Figure 5.1b-c, demonstrate the formation of CEI layer with incremental thickness at slower rate. It is evident that longer exposure at high-V operation upon charge-discharge process (Figure 5.1c) at C/10 leads to thicker layer. In addition, the topographic roughness becomes irregular and coarse as a result of irreversible side reactions with liquid electrolyte. As the undesired phenomenon continuously progresses, parasitic ingresses into the bulk of the crystals appear resulting in graded zoning in the sub-surface region as revealed by the HRTEM images. This kind of ingression could imply RM dissolution (leaching) simultaneously occurring with CEI layer evolution as further characterization will show.

Furthermore, HAADF and elemental mapping images exhibit a stark difference between pristine and cycled electrodes (Figure 5.1d-f) with the gradual augmentation of topographic roughness and the discovery of fluorine apparently as a result of electrolyte decomposition.[22-25] In the pristine electrode shown in Figure 5.1d, the original shape uniformity is completely preserved which is consistent with HRTEM result (Figure 5.1a). Besides the LCP constituent elements—cobalt (Co), phosphorus (P), and oxygen (O)—a faint presence of fluorine (F) can be seen in the pristine sample, due to the PVDF binder. Meanwhile, after cycling, the roughening of the surface becomes evident in

the HAADF images (Figure 5.1e-f) compared to the pristine electrode (Figure 5.1d), a clear sign of reaction-induced surface degradation. Likewise, the elemental mappings highlight the escalated F concentration presence (Figure 5.1e-f), pointing to electrolyte decomposition.

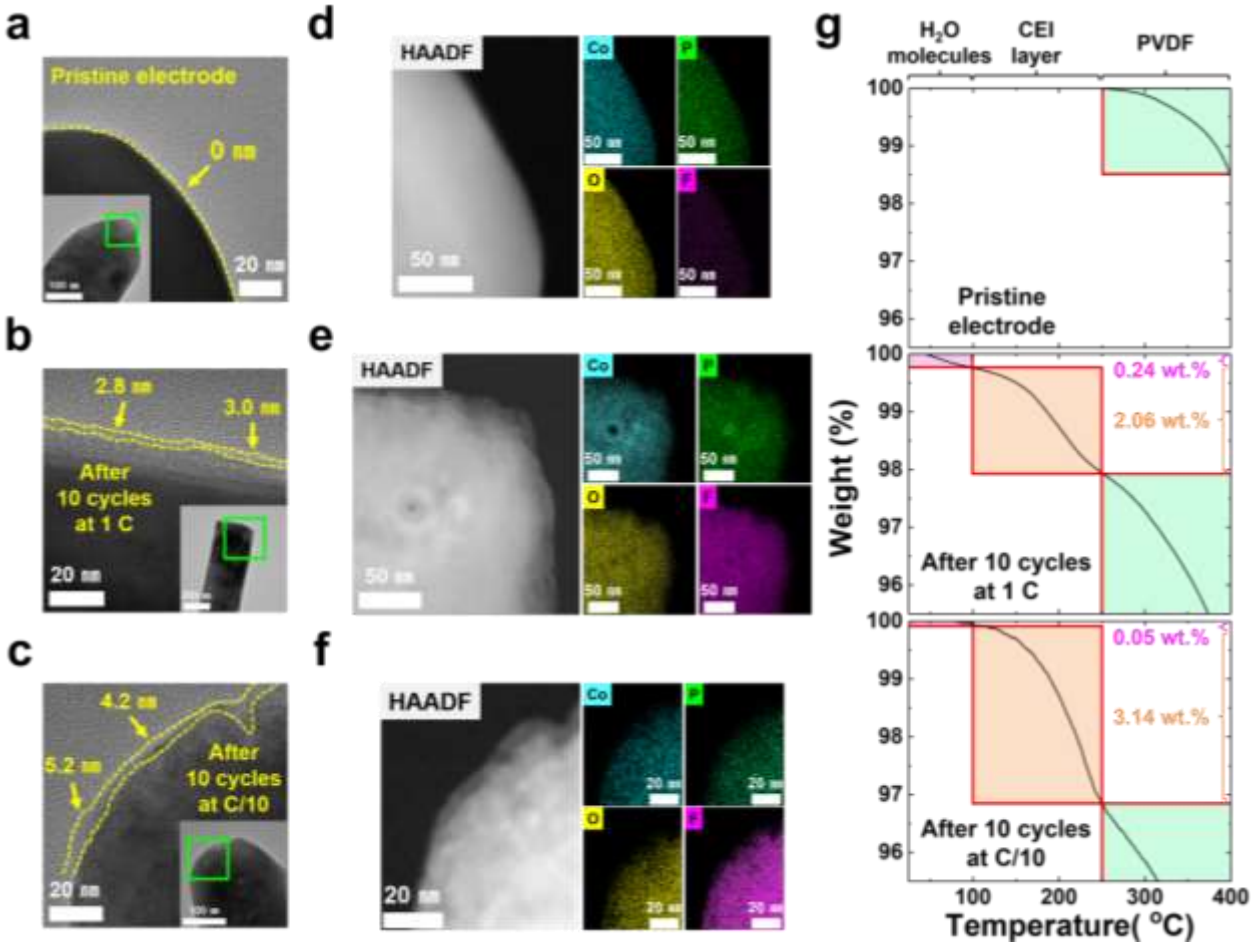


**Figure 5.1.** (a-c) HRTEM images displaying the CEI layer thickness evolution from pristine state, to after 10 cycles at 1 C and C/10; (d-f) the corresponding HAADF and elemental mapping (Co, P. O, and F) images; and (g) the respective TGA curves.

The above visual LCP surface and composition changes were corroborated by thermogravimetric analysis (TGA) as shown in Figure 5.1g. After cycling the LCP cathode registers a mass loss at the specific temperature range, 100-250 ºC, which may be attributed to volatilization of the CEI layer upon heating in air during TGA (25-700 ºC, 10 ºC $min^{-1}$, Air). Regarding TGA results in Figure 5.1g and Figure A.4.1, we firstly note that the overall weight loss for pristine and cycled electrodes is predominantly divided into the following four sections: i) evaporation of absorbed water ($H_2O$) molecules (25-100 ºC), which is negligible because of the storage in Ar-filled glovebox avoiding oxygen and moisture exposure; ii) dissociation of CEI layer (100-250 ºC); iii) decomposition of PVDF binder (250-500 ºC); and iv) combustion of carbon black (above 500 ºC).[26, 27] After the heat

treatment, the eventual mass remained is almost 70 wt.% accurately corresponding to the ratio of LCP active material in the electrode composition. The results below 400 ºC, as shown in Figure 5.1g, are further analyzed seeking to distinguish the CEI layer forming upon cycling from the other components. Considering the pristine electrode as the baseline, we can clearly see the weight loss involved with PVDF to occur above 250 ºC. On the other hand, there is another discernible weight loss occurring in the temperature range, 100-250 ºC for both cycled electrodes at 1 C (2.06 wt.%) and C/10 (3.14 wt.%) that must be assigned to the quantity of newly formed CEI layer. The TGA results (Figure A.4.1c) provide also indirect evidence of RM dissolution (signaled by parasitic ingress shown in Figure 5.1f) given that the mass of cycled LCP active material drops below 70 wt.% after the heat treatment. Additional evidence to these assertions is provided via XPS and electrochemical analysis in the following section.

### 5.3.2. Progressive CEI layer evolution on ST-A-LCP

To help establish the impact of cycling time on CEI layer formation, the dependency of Coulombic efficiency on C-rate is initially considered as shown in Figure 5.2a, and the corresponding numerical values are presented in Table A.4.1. We note that the average Coulombic efficiency is relatively low with the lowest observed at C/10. Evidently, at slow C-rate, the exposure of active material and electrolyte to high-V is longer and as such electrolyte decomposition resulting in extra charge capacity is more severe compared to relatively faster C-rates. Meanwhile, with increased C-rates, the average Coulumbic efficiency gradually increased, with the corresponding variability demonstrating an ever-narrower spread. For this reason, we are inclined to believe that the extent of irreversible side reactions at the interface are dictated by the exposure time at high-V.

To validate this hypothesis, post-mortem EIS and XPS measurements were made. Figure 5.2b displays the Nyquist plot obtained under the applied forward bias of 5.0 V $Li/Li^+$ on cycled cells as indicated on the plot. For all EIS patterns, there are two semi-circles, at high- and mid-frequency regions, observed in addition to a long tail at low frequency. An equivalent circuit, illustrated in the inset image of Figure 5.2b, is employed to model these features. For comparison, Figure A.4.2 displays the Nyquist plots of cycled ST-A-LCP electrodes measured at forward bias potentials corresponding to 3.5, 4.0, and 4.5 V vs. $Li/Li^+$ after 10 cycles at different C-rates. These plots consistently exhibit a characteristic pattern, featuring a single semi-circle followed by a long tail. Therefore, we attribute the high-frequency arc to the resistance imposed by the CEI layer ($R_{CEI}$ of the equivalent circuit). Correspondingly, the enlarged diameter of semi-circle in high-frequency region with lower C-rates

(or equivalently prolonged cycling time) can be attributed to increasing resistance due to the augmented thickness of the CEI layer. Throughout the cycling period, the second semi-circle in the mid-frequency region continuously expands, reflecting the augmented charge-transfer resistance ($R_{CT}$) attributed to progressive CEI layer development.[20]

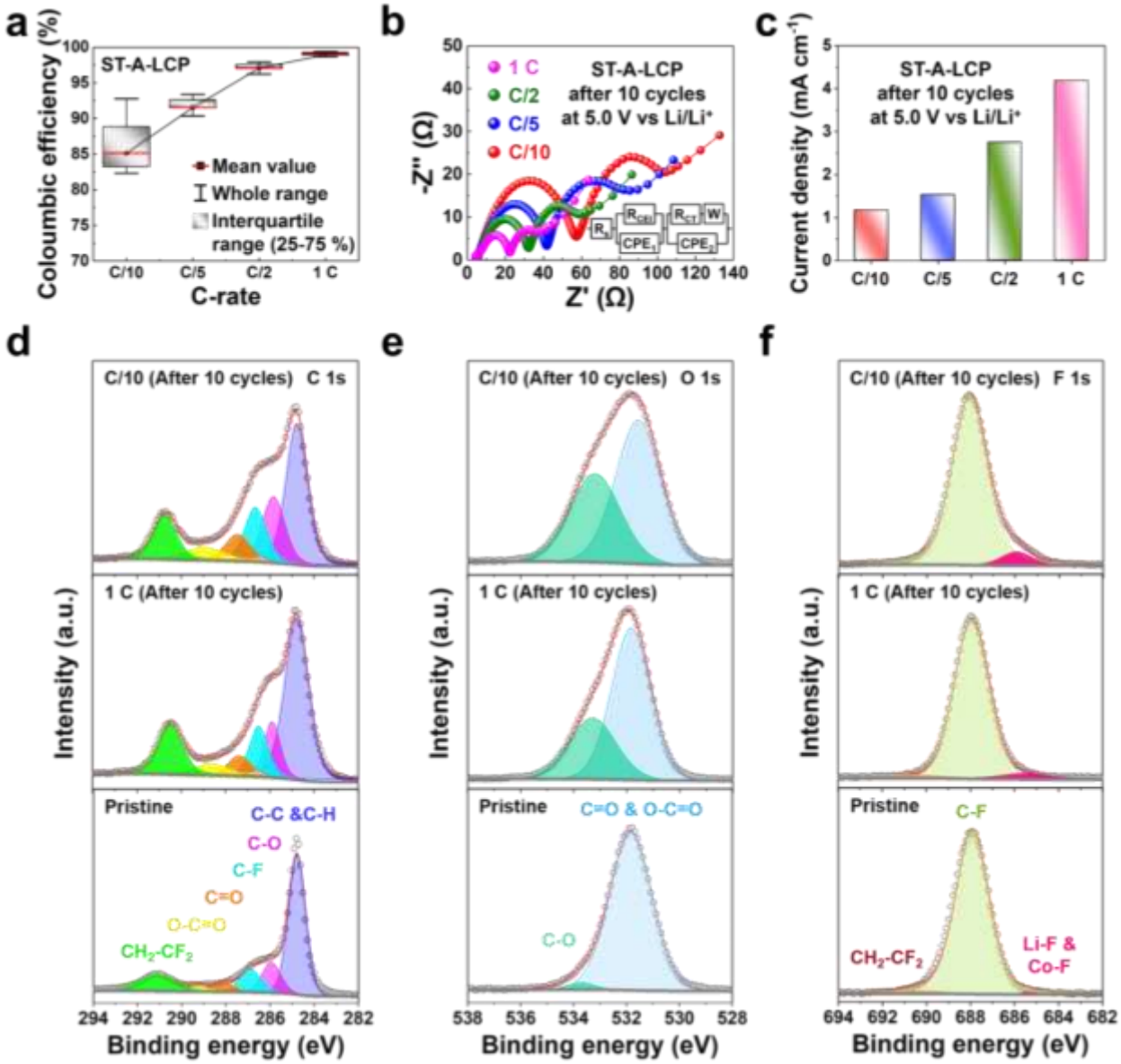


**Figure 5.2.** Post-mortem analysis of ST-A-LCP electrodes in different cycling states: (a) Coulombic efficiency as function of C-rate; (b) EIS analysis (the inset image shows the equivalent circuit model) and; (c) initial current density measurement from the Nyquist plot under the forward bias of 5.0 V vs. $Li/Li^+$; and XPS spectra of (d) C 1s, (e) F 1s, and (F) O 1s for pristine and cycled electrodes.

Moreover, the impact of this growing CEI layer resistance is demonstrated in Figure 2c through the initial current density measured from the Nyquist plot under the applied forward bias of 5.0 V vs. $Li/Li^+$ for the duration of EIS measurements (Figure A.4.3). As C-rate is reduced gradually,

cycled ST-A-LCP electrodes reveal significantly curtailed initial current density of 4.19, 2.75, 1.53, and 1.17 mA $cm^{-1}$ at 1 C, C/2, C/5 and C/10, respectively. Our findings validate the intimate correlation between progressive CEI layer evolution and C-rates, which determines the timeframe of high-V exposure. This relation is further corroborated with XPS analysis.

Post-mortem XPS analysis was performed and summarized in Figure 5.2d-f. It is presenting the data combination regarding the three most relevant elements of CEI layer composition (C 1s, O 1s, and F 1s) for three electrode films in different cycling states including pristine as a baseline and also cycled at 1 C and C/10. In Figure 5.2d, C 1s spectra display multiple peaks C-C, C-H, C-O, C=O and O-C=O originating from conductive acetylene black.[28] Additionally, C-F and $CH_2$-$CF_2$ peaks are attributed to another electrode component, PVDF binder.[29] All of the corresponding values for binding energy, full width at half maximum (FWHM), and atomic percentage of each peak are listed in Table A.4.2-4. Interestingly, compared with the pristine electrode, the cycled electrode at C/10 results in intensity increase of all peaks in the C1s spectra. This observation is indicative of the formation and growth of CEI layer derived from the decomposition of the carbonate solvents (EC, PC, and DMC) in the electrolyte but also the $LiPF_6$ salt aggravated by the high-V even after the small number of cycles involved.[30, 31] Furthermore, considering the peak intensity of the C 1s spectra peaks, we postulate that the CEI layer on the surface of cycled electrode at C/10 is relatively thicker than that of the 1 C electrode. Likewise, O 1s spectra shown in Figure 5.2e provide the most vivid dissimilarity concerning CEI layer thickness between the pristine and the two cycled electrodes. Most noticeably, the appearance of C-O peak becomes evident for both 1 C and C/10 compared to the pristine one as a consequence of the decomposition of EC, PC, and DMC.[32] As for the cycled electrodes at 1 C and C/10, it can be evidently observed that the peak intensity of C-O is strongly increased even after 10 cycles from 3.95 % (Pristine) to 32.34 % (1 C) and 40.49 % (C/10) for O 1s spectra. This change relates to the decomposition of carbonate solvents (comprising C, H, and O). Other than the elements presented above, F 1s spectra in Figure 5.2f, also exhibit similar trends related to the CEI layer evolution. Notably, the enlargement of Li-F & Co-F peaks demonstrates the undesired chemical reactions between surface atom of Li and Co from LCP crystals and F as a result of the $LiPF_6$ decomposition.[33, 34] In addition, it can be seen that the cycled electrode at C/10 exhibits more intense peaks than the 1 C electrode, a sign of more extensive side reactions due to the prolonged cycling time (C/10). Based on such observations, we ascribe the presence and evolution of the Li-F & Co-F peaks to the growing CEI layer with extended charge-discharge time. In Figure A.4.4, and Table A.4.5-6, the contrast in F 1s spectra between 1 C and C/10 becomes significantly accentuated with the atomic

percentage of combined Li-F & Co-F peaks amounting from 3.82 % (1 C) to 14.07 % (C/10) while the discharge capacity drops to 50 mAh $g^{-1}$ after 70 cycles for C/10 vs. 250 cycles for 1 C.

In our previous work, we reported the novel material fabrication of LCP via ST synthesis and subsequent Ar-annealing enabling enhanced Li-ion diffusivity and nearly theoretical discharge capacity aided by the shortened Li-ion diffusion pathway and defect-free olivine crystal structure.[17] However, limited rate capability and capacity retention were still persistent, hence the extensive electrochemical studies and post-mortem surface analysis of ST-A-LCP electrodes undertaken. Our results point to the irreversible side reaction at LCP-electrolyte interface as a result of high-V operation to be at the core of the observed capacity fade. Specifically, the initially demonstrated favourable kinetics of ST-A-LCP for Li-ion diffusion is disrupted by the adverse interfacial reactions and CEI layer evolution. Furthermore, long-term cycling accelerates the above-mentioned undesirable phenomena resulting in thicker layer translating into substantially augmented charge-transfer resistance and unwanted consumption of both LCP material itself and electrolyte. As a result, it is ultimately necessary to develop a coating strategy not only for boosting the interfacial charge-transfer kinetics but also to minimize the exposure of LCP to electrolyte at high-V thereby mitigating the parasitic surface degradation.

### 5.3.3. One-step facile RGO surface coating strategy

To mitigate the irreversible side reactions at the interface, we attempted at passivating the LCP-electrolyte interface. For this purpose, we simply used different amounts of sucrose (30, 40, and 50 wt.%) as a carbon source dissolved in D.I. water in which the ST-LCP powder was agitated. After drying and annealing in Ar atmosphere with the same condition as it was done with ST-A-LCP, the reduced graphene oxide coated LCP material was obtained (ST-R-LCP). In order to determine the optimal loading of sucrose, preliminary electrochemical evaluations shown in Figure A.4.5 were applied to LCP samples before and after coating. The sample with 40 wt.% of sucrose presents the most promising electrochemical results with respect to accessible initial discharge capacity at 1 C and retention after 100 cycles compared to the other concentrations. The SEM images in Figure 5.3a, reveal that our carbon coating process does not affect the elongated particle morphology that exhibits shortened Li-ion diffusion length.[17] TEM results shown in Figure 5.3b indicate the surface carbon layer on LCP crystal to be around 7-9 nm. Further characterizations including XPS, Raman, and FT-IR were carried out and displayed in Figure 5.3c-f to verify the nature of the surface carbon layer. Thus, the XPS results show the presence of carbon (C 1s) and oxygen (O 1s). The C 1s spectra shown

in Figure 5.3c were fitted with multiple carbon atom peaks corresponding to non-oxygenated and different oxygen-containing functional groups such as C=C, C-C, C-OH, C-O-C, C=O, COOH, and π-π delocalized π-electrons of the aromatic network.[35-38] In addition, Figure 5.3d reveals O 1s spectra consisting of phosphate group ($PO_4$) and functional groups including C=O, COOH, C-OH, and C-O-C.[39, 40] The corresponding values of binding energy for each peak are listed in Table A.4.7. Interestingly, the obtained results from XPS raise the possibility that the carbon layer on LCP surface is reduced graphene oxide, RGO.

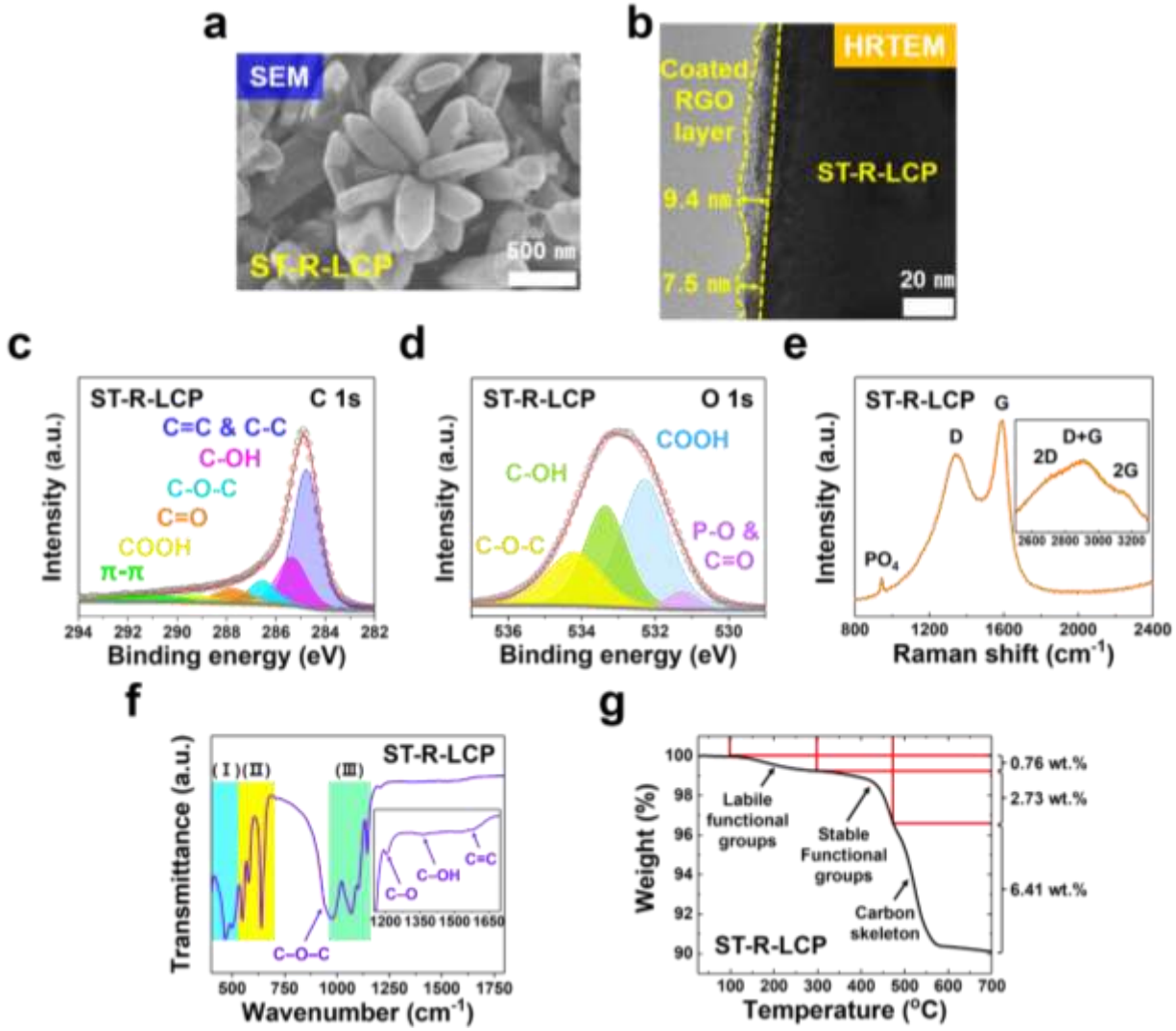


**Figure 5.3.** Characterizations of RGO coating layer on the surface of ST-R-LCP via (a) SEM, (b) HRTEM, XPS spectra of (c) C 1s and (d) O 1s, (e) Raman, (f) FT-IR, and (g) TG-DTA spectra.

To confirm our postulation, Raman and FT-IR spectra were collected. The Raman spectrum in Figure 5.3e displays the combined vibration modes at lower and higher Raman shift. At lower shift region, three main vibrations were detected at 944, 1349, and 1593 $cm^{-1}$ corresponding to $PO_4$, carbon

D and G bands, respectively. The second-order and combination bands in higher shift region were also observed and centered at 2714, 2910, and 3151 $cm^{-1}$ matched with 2D, D+G, and 2G peaks. These bands are attributed to the overtone of D and G bands.[41, 42] At the same time, FT-IR technique was also employed to prove the existence of RGO layer on ST-R-LCP crystals. In principal, both LCP samples pre- (Figure A.4.6) and post- (Figure 5.3f) coating are mainly dominated with three stretching and vibration modes of (I) Li-ion (450-550 $cm^{-1}$) and (II and III) $PO_4^{3-}$ group (500-700 and 900-1200 $cm^{-1}$).[21] However, we note that the post-coating sample solely incorporates extra features which are not strong but still persistent originated from the stretching vibration of functional groups in RGO such as C-O-C (942 $cm^{-1}$), C-O (1205 $cm^{-1}$), C-OH (1363 $cm^{-1}$), and C=C (1580 $cm^{-1}$) unlike the pre-coating sample.[43, 44] Thereafter, the coating is confirmed to be RGO and the coated LCP sample (with 40 wt.% of sucrose) denoted as ST-R-LCP is retained for further testing.

After the confirmation of RGO layer, we applied TGA analysis (Figure 5.3g) to accurately quantify RGO layer derived from sucrose as a source of carbon. The entire weight loss was recorded from room temperature to 700 ºC with the ramping rate being 10 ºC $min^{-1}$ in air. Three distinct sections of weight loss were observed at different temperature ranges: (i) 100-300 ºC for the decomposition of labile oxygen-containing functional groups (0.76 wt.%), (ii) 300-450 ºC for the removal of more stabilized oxygen-containing functional groups (2.73 wt.%), and (iii) 450-700 ºC for the pyrolysis of carbon skeleton (6.41 wt.%).[45, 46] On the other hand, TGA results of ST-A-LCP in Figure A.4.7 show the whole mass preserved without any weight loss up to 700 ºC. We note that, by simply utilizing 40 wt.% of sucrose, almost 10 wt.% of RGO coating has formed by the carbonization process conducted during Ar-annealing as in the case of ST-A-LCP preparation.

In sum, all above observations confirm the feasibility of coating LCP crystals with sucrose-derived RGO layer. It is worthy to note the anchoring effect of oxygen-containing functional groups in RGO layer ensuring remarkable adhesion on cathode surface.[47-49] In effect, these functional groups are favoured to be attached on LCP surface due to their polarity, resulting in rigid coordination interactions with Co in olivine structure, so that uniformly cover the entire LCP surface. Additionally, we should underline the favourable intrinsic RGO properties namely large specific surface area and superior electronic conductivity,[50, 51] which can enhance the electrochemical performance, as it is reported in the next section.

### 5.3.4. Enhanced electrochemical performance via RGO coating

Post-mortem EIS of ST-R-LCP analogous to the methodology used for ST-A-LCP is presented in Figure 5.4a-b. The smaller diameter of high-frequency semi-circle ($R_{CEI}$) and mid-frequency semi-circle ($R_{CT}$) in Figure 5.4a signifies the reduced thickness of CEI layer for ST-R-LCP under all C-rates compared to ST-A-LCP (Figure 5.2b). In addition, the initial current density obtained from the Nyquist plot under the applied forward bias of 5.0 V vs. $Li/Li^+$ demonstrates a significant rise for all C-rates vis-à-vis the corresponding values for ST-A-LCP (Figure 5.2c). At each C-rate, the initial current density of ST-R-LCP enhanced by 2.32, 3.4, 4.91, and 6.27 at C/10, C/5, C/2, and 1 C, respectively. In addition, Figure A.4.8 demonstrates a shortened current decay period of 200 seconds in ST-R-LCP, compared to 400 seconds observed for ST-A-LCP (Figure A.4.3).

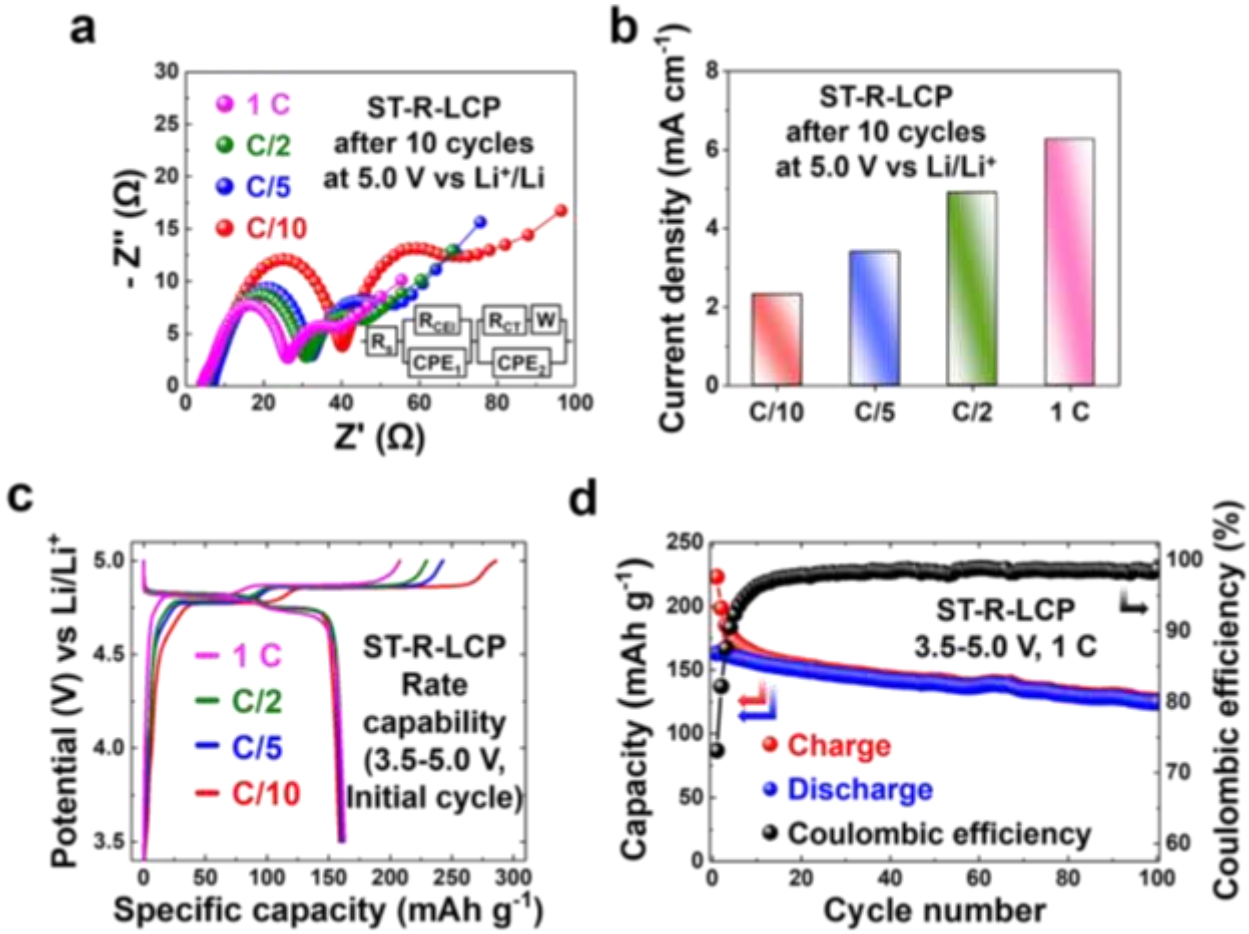


**Figure 5.4.** Electrochemical evaluation of ST-R-LCP cathode via (a) EIS analysis (the inset image shows the equivalent circuit model) and (b) initial current density measurement from the Nyquist plot under the applied forward bias of 5.0 V vs. $Li/Li^+$; (c) rate capability at various C-rates from C/10, C/5, C/2 and 1 C; and (d) capacity retention within the voltage range 3.5-5.0 V vs. $Li/Li^+$ at 1 C**.**

Aided by the RGO coating, improved electrochemical performance was achieved. Specifically, Figure 5.4c displays the excellent rate capability of ST-R-LCP, delivering discharge capacities of 158.8, 160.9, 162.6, and 163.0 mAh $g^{-1}$ across all tested C-rates from C/10 up to 1 C, values that

approach the nearly theoretical capacity. Thus, the anisotropically grown LCP crystals via ST synthesis can be effectively coated with conductive RGO successfully overcoming the sluggish kinetics by facilitating both Li-ion diffusion and electron transport.

Furthermore, an enhancement in capacity retention was observed in Figure 5.4d. The capacity retention of ST-R-LCP was boosted to 76.36 % compared to 61.65 % for the ST-A-LCP during the initial 100 cycles at 1 C. To emphasize the stark difference between ST-A-LCP and ST-R-LCP regarding capacity retention, Figure A.4.9 displays the discharge capacity retention data during the entire cycle periods for both samples. Our proposed coating strategy enhances the cell durability as evident by the number of cycles enabled until the discharge capacity drops to 50 mAh $g^{-1}$ (700 cycles for ST-R-LCP compared with 250 cycles for ST-A-LCP). In addition, unlike ST-A-LCP, ST-R-LCP exhibits improved capacity retention with prolonged cycle numbers at relatively faster C-rates (C/5, C/2, and 1 C) with the sole exception of C/10 as shown in Figure A.4.10.

### 5.3.5. Effect of RGO coating on electrolyte decomposition

After confirming the satisfactory rate capability with RGO surface coating, we implemented post-mortem analysis in the same manner with ST-A-LCP to further clarify how RGO layer contributes to the enhanced capacity retention. Figure 5.5a displays the standard deviation of Coulombic efficiency for ST-R-LCP at different C-rates C/10, C/5, C/2, and 1 C and the corresponding numerical values are compiled in Table A.4.8. In comparison to ST-A-LCP (Figure 5.2a), the distribution and average Coulombic efficiency exhibit negligible differences at escalated C-rates (C/2 and 1 C). However, these differences become significantly augmented as C-rate decreases (C/10 and C/5). This finding indicates that electrons generated from electrolyte oxidation at high-V are more readily transported to LCP electrode due to superior electronic conductivity and enlarged active surface area of RGO layer,[50, 51] resulting in undesired extra charge current. In other words, RGO serves as a “double-edged sword” as it does not only improve rate capability but also cause more oxidation of electrolyte at slower C-rates resulting in inferior and unevenly distributed Coulombic efficiency over extended cycling period. Indeed, as Figure 5.5b shows the Coulombic efficiency of ST-R-LCP is not markedly improved vis-à-vis that of ST-A-LCP but the number of cycles is substantially enlarged from 250 to 700.

To probe further the effect of RGO on interfacial reactivity, post-mortem XPS results were collected and summarized in Figure 5.5c-e and Table A.4.9-10 for ST-R-LCP electrodes including pristine and after their full cycling (700 cycles) at 1 C until the discharge capacity dropped to 50 mAh

$g^{-1}$. For C 1s and O 1s spectra of pristine ST-R-LCP electrode, the atomic percentage of each peak correlated to carbon skeleton (C-C) and oxygen-containing functional groups (C=O and O-C=O) is larger than the values from pristine ST-A-LCP electrode (refer to Figure 5.3d-e and Table A.4.2) due to RGO layer coated on LCP surface. Upon applying the RGO coating, we anticipated that the electronic conductive RGO layer would minimize CEI layer evolution and mitigating electrolyte oxidation. However, contrary to our expectation, this approach led to worse outcomes in long-term cycling. The final atomic percentage of each peak for C 1s and O 1s spectra reach similar values, whereas Li-F & Co-F peaks climb up from 3.82 to 18.94 % in comparison to fully cycled ST-A- LCP electrodes, due to apparent severe electrolyte oxidatiob (Table A.4.5 and A.4.10).

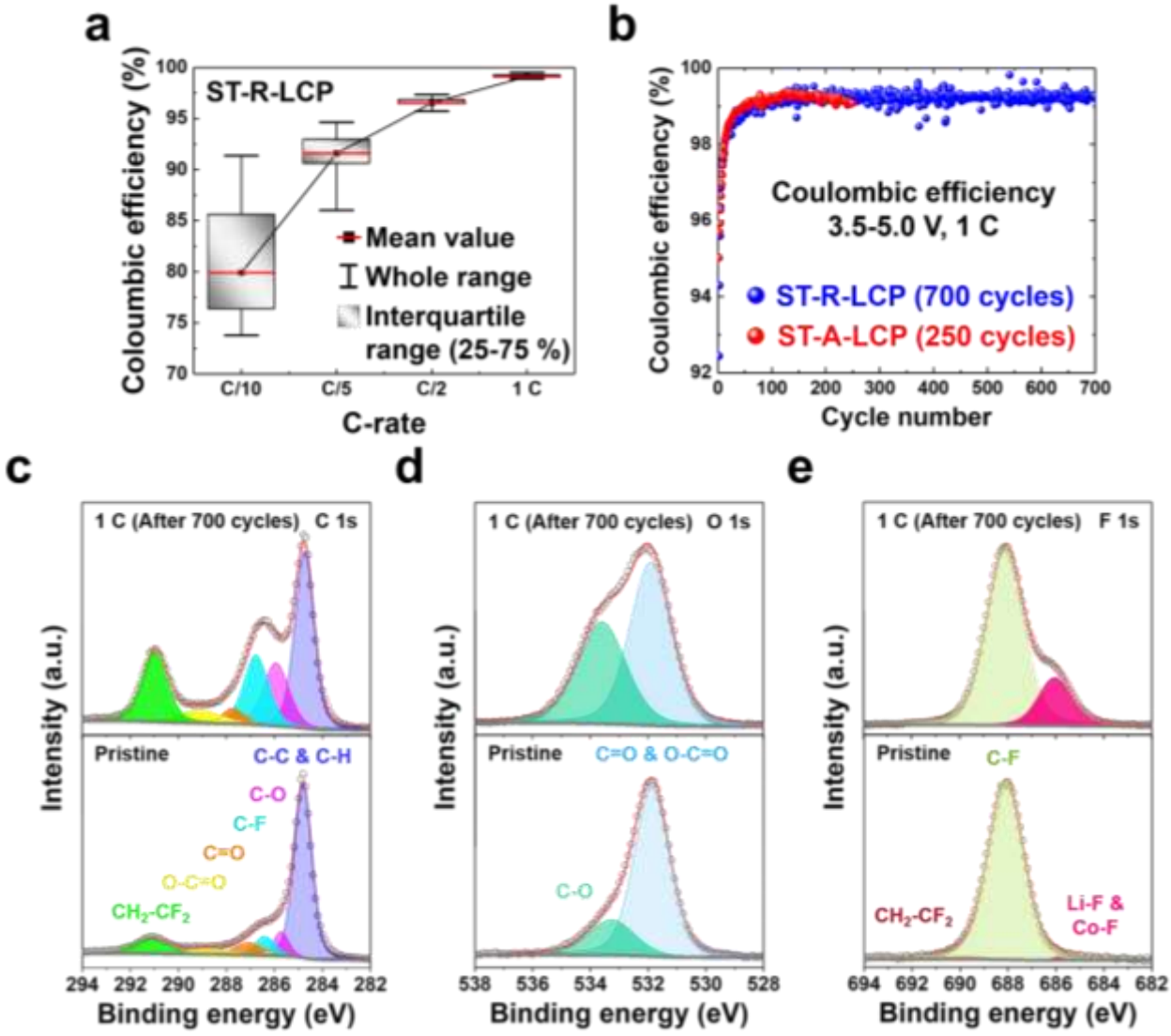


**Figure 5.5.** Analysis of CEI layer formation on ST-R-LCP cathode: (a) Coulombic efficiency as function of C-rate; (b) Coulombic efficiency comparison of ST-A-LCP and ST-R-LCP; and (c-e) XPS spectra of C 1s, O 1s, and F 1s for pristine and cycled ST-R-LCP electrodes after 700 cycles at 1 C.

Furthermore, XRD patters of ST-R-LCP powder, pristine and cycled ST-R-LCP electrodes after 700 cycles at 1 C were collected and analyzed (Figure A.4.11 and Table A.4.11). As observed, all ST-R-LCP peaks remain well-preserved even after 700 cycles with notable exceptions at 25.0 $^{o}$ and 27.8 $^{o}$, where intensified peaks and an associated hump appear. These changes indicate the presence of organic and poorly crystalline compounds intimately linked to CEI layer composition, including $CH_2$, $C_2H_4$, $C_6H_{10}O_2$, and $C_{15}H_{28}O_2$ and $Li_2CO_3$ etc. During cycling, we speculate that CEI layer develops an amorphous character on RGO layer due to the adsorption of degraded carbonate solvent species and possible nano-precipitates of metal (Li and Co) carbonate, fluoride, and/or phosphate salts.[52, 53]

Based on these results, RGO coating seems to promote electrolyte oxidation during prolonged cycling, which would typically result in accelerated capacity decay. Surprisingly, the opposite trend was observed, as capacity retention unexpectedly improved. This signifies that overall the RGO coating have played a beneficial role in enhancing capacity retention through alternative effects. Previous reports on LCP capacity fade have predominantly focused on bulk structural changes and electrochemical reactions, particularly the formation of anti-site defects and CEI layer evolution.[15, 54-58] However, another critical contributor to material degradation is the chemical reaction at the interface, as evidenced by the crystal ingress phenomenon illustrated in Figure 5.1. Therefore, our research shifted to investigate the role of RGO in mitigating RM dissolution, which serves as a crucial factor in cathode degradation not previously discussed in prior LCP studied.

### 5.3.6. Mitigating redox metal (RM) dissolution via RGO coating

First, we investigated RM dissolution via MP-AES technique to determine the relative molar ratio of Co/P for both pre- (ST-A-LCP) and post- (ST-R-LCP) coating cathode samples. Figure 5.6a presents Co/P values of pristine and cycled electrodes at different C-rates after 10 cycles. Note that Co/P ratio of fresh electrodes is close to the stoichiometry with 3 and 4 % of excess Co for ST-A-LCP and ST-R-LCP respectively. Considering Co/P values for the pristine electrodes as a baseline, Co/P ratio of ST-R-LCP is relatively well-preserved unlike ST-A-LCP indicating Co dissolution upon cycling. As a consequence, we postulate that RM dissolution also serves as another important contributor to severe capacity fade in the absence of RGO coating.

To probe deeper this phenomenon, we employed TEM techniques including HRTEM, HAADF, and line scanning to examine LCP particles retrieved from electrodes after 100 cycles at 1 C. Figure 5.6b and A.4.12a display HAADF and HRTEM images confirming the original shape uniformity of

ST-R-LCP without parasitic ingress owed to the protection by RGO coating. Notably, the inset line scan image in Figure 5.6b shows uniform elemental distributions of Co, P, and O in ST-R-LCP with the rectangular shape. In contrast, we observed the ST-A-LCP crystal to have "corrosion" signs and loss of metal composition near the surface. As shown in Figure 5.6c and A.4.12b, parasitic ingress occurred at the interface and gradually progressed toward LCP bulk structure. These results provide clear evidence that RGO coating largely prevents RM dissolution. In addition, these findings underline our postulation that RM dissolution occurring at the interface can be an important contributor to LCP capacity loss rather than alone the CEI layer inducing charge-transfer resistance.

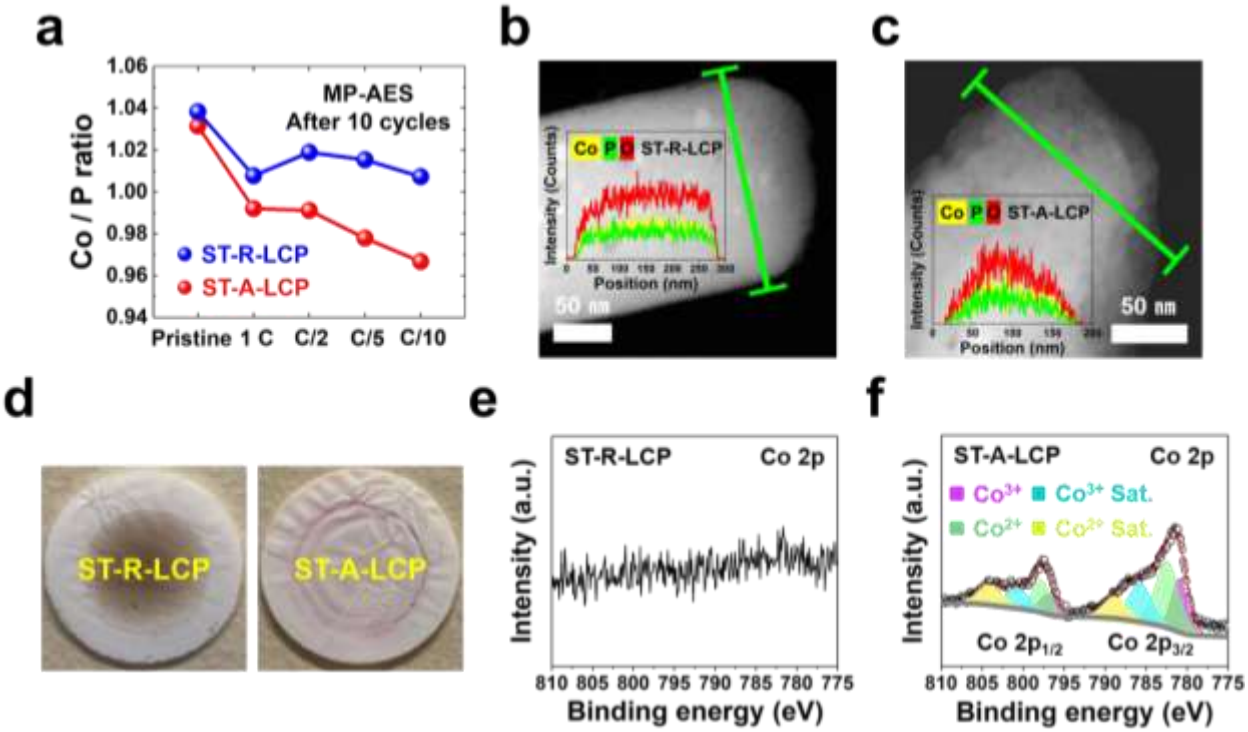


**Figure 5.6.** Investigation of redox metal (RM) dissolution upon cycling via (a) MP-AES analysis for the concentration ratio of cobalt to phosphorus (Co/P) for pristine and cycled ST-R-LCP and ST-A-LCP electrodes at different C-rates after 10 cycles; HAADF images (the inset image shows the line scan) of (b) ST-R-LCP and (c) ST-A-LCP particles extracted from the cycled electrodes after 100 cycles at 1 C; (d) photographs and Co 2p XPS spectra of separators extracted from (e) ST-R-LCP and (f) ST-A-LCP cells after 100 cycles at 1 C.

To observe the distinctive interfacial chemistry between pre- and post- coating LCP samples, extra post-mortem studies were undertaken focusing on the separators retrieved from the cycled cells after 100 cycles at 1 C. As shown in the photographs in Figure 5.6d, the separators collected from the cycled ST-R-LCP and ST-A-LCP cells display an apparent optical difference. In particular, the separator from the ST-A-LCP cell is seen to have a pinkish coloration apparently due to transfer and deposition on it of dissolved Co species. To substantiate this postulation, we further probe the surface

of separators via XPS characterization. As shown in Figure 5.6e and f, the XPS spectra clearly confirm the particular bonding associated with Co detected solely in the separator that was associated with the ST-A-LCP electrodes. Meanwhile, no signal for RM dissolution is identified in ST-R-LCP even after undergoing the same number of charge-discharge cycles. Furthermore, the separator from ST-A-LCP cells shows two different oxidation states of Co ($Co^{2+}$ and $Co^{3+}$) simultaneously. The relative atomic ratio of $Co^{2+}$ and $Co^{3+}$ following the deconvoluted Co 2p spectrum (Co $2p_{3/2}$ and Co $2p_{1/2}$) is about 64.6 and 35.4 % respectively (Table A.4.12). It should be noted that this value closely corresponds to the intermediate phase, $Li_{2/3}Co^{2+}{}_{2/3}Co^{3+}{}_{1/3}PO_4$ formed during the Li-ion intercalation process.[59-61] In addition, LCP undergoes phase transitions based on the shrinking core model, with the intermediate phase persisting at the interface with electrolyte for the longest duration upon Li-ion intercalation.[59] These findings clearly prove that parasitic ingress on the particle surface is the result of RM dissolution when LCP is exposed to high-V during Li-ion intercalation cycles regardless of charge and discharge steps, since the redox reactions of RM ($Co^{2+}\leftrightarrow Co^{3+}$) initiate at the interface at high-V.[62-64] Meanwhile, RM dissolution is not detected in ST-R-LCP even with the same number of charge-discharge cycles.

In the previous section, we confirmed that RGO coating of LCP crystals helps accelerate the charge-transfer kinetics but induces aggravated electrolyte decomposition in long-term cycles. Nevertheless, overall ST-R-LCP achieved markedly improved cycling stability without RM dissolution. Hence, we postulate that RGO surface coating serves as an effective barrier against severe RM dissolution. Mechanistically, we hypothesize that the progressively emerging ingress at the interface is promoted via complexation of surface RM cations located in the lattice fringes of LCP with diketonate chelating agents derived from carbonate solvent oxidation.[65] However, the RGO coating apparently suppresses RM dissolution by blocking the approach of the organic ligands to the LCP surface. Moreover, oxygen-containing functional groups in RGO layer (Figure 5.3) help anchor dissolved RM cations strongly via covalent bonding, so that the entire dissolution, migration, and deposition of RM upon cycling at high-V is significantly mitigated.[66-68]

In summary, following the development of preferentially oriented and defect-free LCP crystals with nearly theoretical full capacity, we have further surface engineered via one-step facile RGO coating LCP achieving substantial boosting of rate capability and capacity retention unattainable previously. Furthermore, through our detailed post-mortem investigations, we have identified that RM dissolution occurring upon cycling is a key contributor to interfacial capacity fade of LCP other than undesired CEI layer evolution. This result suggests that more dedicated research efforts are still

required to fine tune the surface coating with respect to interfacial chemistry, electronic properties, and deposition strategy to pave the way toward stable high-V LCP as a cathode with high energy density and long cycle life.

### 5.4. Conclusion

In this work, we focused on post-mortem analysis of two high-V LCP cathode materials to (i) elucidate the interphasial phenomena responsible for capacity fade and (ii) advance an RGO coating strategy to mitigate the extent of its associated detrimental effects. The first LCP material, labeled ST-A-LCP is characterised by defect-free optimized crystal morphology and the second one, labeled ST-R-LCP was an RGO-coated version of the first one. High-V operation of the uncoated LCP triggered i) irreversible CEI layer evolution intimately linked with enlarged charge-transfer resistance and ii) RM dissolution from olivine lattice fringes. This understanding motivated us to develop the sucrose-derived RGO coated LCP in order to facilitate charge exchange while mitigating/blocking undesirable interfacial side reactions. Consequently, our coating strategy achieved nearly theoretical Li-ion storage capacity at 1 C and exhibited a dual functionality: while found to promote electrolyte oxidation, it successfully suppresses RM dissolution hence lowering the RM-related capacity loss. Notably, this study reveals RM dissolution as a critical interfacial mechanism for LCP capacity fade—an important extension to previously reported causes, such as CEI layer. This newly developed defect-free preferentially grown LCP crystals upon optimization of the interfacial coating process can be subsequently further developed via appropriate doping scenarios to achieve enhanced cycling stability at 5.0 V vs. $Li/Li^+$ operation as a practical high-V cathode model.

### 5.5. References


1. W. Li, E. M. Erickson, A. Manthiram, High-nickel layered oxide cathodes for lithium-based automotive batteries. *Nature Energy* **2020**, *5*, 26-34.
2. G. Cui, Reasonable Design of high-energy-density solid-state lithium-metal batteries. *Matter* **2020**, *2* (4), 805-815.
3. V. Viswanathan, A. H. Epstein, Y.-M. Chiang, E. Takeuchi, M. Bradley, J. Langford, M. Winter, The challenges and opportunities of battery-powered flight. *Nature* **2022**, *601*, 519-525.
4. S. Wolf, M. Lüken, Emerging battery technologies to boost the clean energy transition. *Springer* **2024**.
5. C. Liu, Z. G. Neale, G. Cao, Understanding electrochemical potentials of cathode materials in rechargeable batteries. *Materials Today* **2016**, *19* (2), 109-123.
6. A. Konarov, S.-T. Myung, Y.-K. Sun, Cathode materials for future electric vehicles and energy storage systems. *ACS Energy Letters* **2017**, *2* (3), 703-708.
7. A. M. Nolan, Y. Liu, Y. Mo, Solid-state chemistries stable with high-energy cathodes for lithium-ion batteries. *ACS Energy Letters* **2019**, *4* (10), 2444-2451.

8. W. Li, B. Song, A. Manthiram, High-voltage positive electrode materials for lithium-ion batteries. *Chemical Society Review* **2017**, *46* (10), 3006-3059.
9. A. K. Padhi, K. S. Nanjundaswamy, J. B. Goodenough, Phospho-olivines as positive-electrode materials for rechargeable lithium batteries. *Journal of The Electrochemical Society* **1997**, *144*, 1188.
10. C. Masquelier, L. Croguennec, Polyanionic (phosphates, silicates, sulfates) frameworks as electrode materials for rechargeable Li (or Na) batteries. *Chemical Reviews* **2013**, *113* (8), 6552-6591.
11. Y.-M. Kang, Y.-I. Kim, M.-W. Oh, R.-Z. Yin, Y. Lee, D.-W. Han, H.-S. Kwon, J. H. Kim, G. Ramanath, Structurally stabilized olivine lithium phosphate cathodes with enhanced electrochemical properties through Fe doping. *Energy & Environmental Science* **2011**, *4* (12), 4978-4983.
12. D. Liu, W. Zhu, C. Kim, M. Cho, A. Guerfi, S. A. Delp, J. L. Allen, T. R. Jow, K. Zaghib, High-energy lithium-ion battery using substituted $LiCoPO_4$: From coin type to 1 Ah cell. *Journal of Power Sources* **2018**, *388*, 52-56.
13. J. Wu, C.-J. Tsai, Discovered intermediate phase and improved electrochemical performance of Zn-Doped $LiCoPO_4$ for high-energy Li-ion batteries. *ACS Applied Energy Materials* **2021**, *4* (7), 6408-6413.
14. Y. Maeyoshi, S. Miyamoto, Y. Noda, H. Munakata, K. Kanamura, Effect of organic additives on characteristics of carbon-coated $LiCoPO_4$ synthesized by hydrothermal method. *Journal of Power Sources* **2017**, *337*, 92-99.
15. X. Wu, M. Meledina, J. Barthel, Z. Liu, H. Tempel, H. Kungl, J. Mayer, R.-A. Eichel, Investigation of the Li–Co antisite exchange in Fe-substituted $LiCoPO_4$ cathode for high-voltage lithium ion batteries. *Energy Storage Materials* **2019**, *22*, 138-146.
16. J. G. Lapping, S. A. Delp, J. L. Allen, J. L. Allen, J. W. Freeland, M. D. Johannes, L. Hu, D. T. Tran, T. R. Jow, J. Cabana, Changes in electronic structure upon Li deintercalation from $LiCoPO_4$ derivatives. *Chemistry of Materials* **2018**, *30* (6), 1898-1906.
17. M. Woo, S.-W. Park, J. Lee, D.-H. Seo, G. P. Demopoulos, Attaining full Li-ion storage capacity in defect-free and preferential orientation grown $LiCoPO_4$ via *ab initio* solvothermal crystallization control. *Advanced Energy Materials* **2024,** 2404404.
18. A. Kotronia, H. D. Asfaw, C.-W. Tai, M. Hahlin, D. Brandell, K. Edström, Nature of the cathode–electrolyte interface in highly concentrated electrolytes used in graphite dual-ion batteries. *ACS Applied Materials & Interfaces* **2021**, *13* (3), 3867-3880.
19. C.-C. Su, M. He, R. Amine, Z. Chen, Z. Yu, T. Rojas, L. Cheng, A. T. Ngo, K. Amine, Unveiling decaying mechanism through quantitative structure-activity relationship in electrolytes for lithium-ion batteries. *Nano Energy* **2021**, *83*, 105843.
20. N. Zhang, B. Wang, F. Jin, Y. Chen, Y. Jiang, C. Bao, J. Tian, J. Wang, R. Xu, Y. Li, Q. Lv, H. Ren, D. Wang, H. Liu, S. Dou, X. Hong, Modified cathode-electrolyte interphase toward high-performance batteries. *Cell Reports Physical Science* **2022**, *3* (12), 101197.
21. M. Woo, J. Lee, G. P. Demopoulos, Surface and bulk defect formation during hydrothermal synthesis of $LiCoPO_4$ crystals and their electrochemical implications. *Materials Advances* **2023**, *4* (20), 4823-4834.
22. A. Tornheim, S. Sharifi-Asl, J. C. Garcia, J. Bareño, H. Iddir, R. Shahbazian-Yassar, Z. Zhang, Effect of electrolyte composition on rock salt surface degradation in NMC cathodes during high-voltage potentiostatic holds. *Nano Energy* **2019**, *55*, 216-225.
23. N. R. Park, Y. Li, W. Yao, M. Zhang, B. Han, C. Mejia, B. Sayahpour, R. Shimizu, B. Bhamwala, B. Dang, S. Kumakura, W. Li, Y. S. Meng, Understanding the role of lithium borate as the surface coating on high voltage single crystal $LiNi_{0.5}Mn_{1.5}O_4$. *Advanced Functional Materials* **2023**, *34* (13), 2312091.

24. M. Uitz, M. Sternad, S. Breuer, C. Täubert, T. Traußnig, V. Hennige, I. Hanzu, M. Wilkening, Aging of tesla's 18650 lithium-ion cells: Correlating solid-electrolyte-interphase evolution with fading in capacity and power. *Journal of The Electrochemical Society* **2017**, *164*, A3503.
25. W. M. Dose, W. Li, I. Temprano, C. A. O'Keefe, B. L. Mehdi, M. F. L. D. Volder, C. P. Grey, Onset potential for electrolyte oxidation and Ni-rich cathode degradation in lithium-ion Batteries. *ACS Energy Letters* **2022**, *7* (10), 3524-3530.
26. T. He, R. Jia, X. Lang, X. Wu, Y. Wang, Preparation and electrochemical performance of PVdF ultrafine porous fiber separator-cum-electrolyte for supercapacitor. *Journal of The Electrochemical Society* **2017**, *164*, E379.
27. W. Tang, Preparation of anatase-type $TiO_2$nanocrystal/acetylene black composites by a dry process, and their electrochemical lithium insertion. *Journal of Materials Chemistry* **2004**, *14* (23), 3457-3461.
28. R. Tatara, P. Karayaylali, Y. Yu, Y. Zhang, L. Giordano, F. Maglia, R. Jung, J. P. Schmidt, I. Lund, Y. Shao-Horn, The effect of electrode-electrolyte interface on the electrochemical impedance spectra for positive electrode in Li-ion battery. *Journal of The Electrochemical Society* **2019**, *166*, A5090.
29. J.-B. Gieu, V. Winkler, C. Courrèges, L. E. Ouatani, C. Tessier, H. Martinez, New insights into the characterization of the electrode/electrolyte interfaces within $LiMn_2O_4$/$Li_4Ti_5O_{12}$ cells, by X-ray photoelectron spectroscopy, scanning auger microscopy and time-of-flight secondary ion mass spectrometry. *Journal of Materials Chemistry A* **2017**, *5* (29), 15315-15325.
30. Z. Arthur, H.-C., Chiu, X. Lu, N. Chen, V. Emond, K. Zaghib, D.-T. Jiang, G. P. Demopoulos, Spontaneous reaction between an uncharged lithium iron silicate cathode and a $LiPF_6$-based electrolyte. *Chemical Communications* **2016,** *52*, 190-193.
31. Q. Li, Y. Wang, X. Wang, X. Sun, J.-N. Zhang, X. Yu, H. Li, Investigations on the fundamental process of cathode electrolyte interphase formation and evolution of high-voltage cathodes. *ACS Applied Materials & Interfaces* **2019**, *12* (2), 2319-2326.
32. E. Björklund, D. Brandell, M. Hahlin, K. Edström, R. Younesi, How the negative electrode influences interfacial and electrochemical properties of $LiNi_{1/3}Co_{1/3}Mn_{1/3}O_2$ cathodes in Li-ion batteries. *Journal of The Electrochemical Society* **2017**, *164*, A3054.
33. J. L. Tebbe, A. M. Holder, C. B. Musgrave, Mechanisms of $LiCoO_2$ cathode degradation by reaction with HF and protection by thin oxide coatings. *ACS Applied Materials & Interfaces* **2015**, *7* (43), 24265-24278.
34. Y. Ma, Y. Zhou, C. Du, P. Zuo, X. Cheng, L. Han, D. Nordlund, Y. Gao, G. Yin, H. L. Xin, M. M. Doeff, F. Lin, G. Chen, A new anion receptor for improving the interface between lithium- and manganese-rich layered oxide cathode and the electrolyte. *Chemistry of Materials* **2017**, *29* (5), 2141-2149.
35. R. Wang, Y. Wang, C. Xu, J. Sun, L. Gao, Facile one-step hydrazine-assisted solvothermal synthesis of nitrogen-doped reduced graphene oxide: reduction effect and mechanisms. *RSC Advances* **2013**, *3* (4), 1194-1200.
36. A. Kovtun, D. Jones, S. Dell'Elce, E. Treossi, A. Liscio, V. Palermo, Accurate chemical analysis of oxygenated graphene-based materials using X-ray photoelectron spectroscopy. *Carbon* **2019**, *143*, 268-275.
37. F. J. Sonia, H. Kalita, M. Aslam, A. Mukhopadhyay, Correlations between preparation methods, structural features and electrochemical Li-storage behavior of reduced graphene oxide. *Nanoscale* **2017**, *9* (31), 11303-11317.
38. B. D. Ossonona, D. Bélanger, Synthesis and characterization of sulfophenyl-functionalized reduced graphene oxide sheets. *RSC Advances* **2017**, *7* (44), 27224-27234.

39. Y. C. G. Kwan, G. M. Ng, C. H. A. Huan, Identification of functional groups and determination of carboxyl formation temperature in graphene oxide using the XPS O 1s spectrum. *Thin Solid Films* **2015**, *590*, 40-48.
40. R. Vinoth, S. G. Babu, V. Bharti, V. Gupta, M. Navaneethan, S. V. Bhat, C. Muthamizhchelvan, P. C. Ramamurthy, C. Sharma, D. K. Aswal, Y. Hayakawa, B. Neppolian, Ruthenium based metallopolymer grafted reduced graphene oxide as a new hybrid solar light harvester in polymer solar cells. *Scientific Reports* **2017**, *7*, 43133.
41. B. Ma, R. D. Rodriguez, A. Ruban, S. Pavlov, E. Sheremet, The correlation between electrical conductivity and second-order raman modes of laser-reduced graphene oxide. *Physical Chemistry Chemical Physics* **2019**, *21* (19), 10125-10134.
42. K. K. H. D. Silva, P. Viswanath, V. K. Rao, S. Suzuki, M. Yoshimura, New insight into the characterization of graphene oxide and reduced graphene oxide monolayer flakes on Si-based substrates by optical microscopy and raman spectroscopy. *The Journal of Physical Chemistry C* **2021**, *125* (14), 7791-7798.
43. C. R. Minitha, V. S. Anithaa, V. Subramaniam, R. T. R. Kumar, Impact of oxygen functional groups on reduced graphene oxide-based sensors for ammonia and toluene detection at room temperature. *ACS Omega* **2018**, *3* (4), 4105-4112.
44. E. Mahmud, M. R. Islam, Improved electrochemical performance of bio-derived plasticized starch/reduced graphene oxide/molybdenum disulfide ternary nanocomposite for flexible energy storage applications. *Scientific Reports* **2023**, *13*, 20967.
45. J. Shen, Y. Hu, M. Shi, X. Lu, C. Qin, C. Li, M. Ye, Fast and facile preparation of graphene oxide and reduced graphene oxide nanoplatelets. *Chemistry of Materials* **2009**, *21* (15), 3514-3520.
46. D. C. Marcano, D. V. Kosynkin, J. M. Berlin, A. Sinitskii, Z. Sun, A. Slesarev, L. B. Alemany, W. Lu, J. M. Tour, Improved synthesis of graphene oxide. *ACS Nano* **2010**, *4* (8), 4806-4814.
47. W. Liu, G. Speranza, Tuning the oxygen content of reduced graphene oxide and effects on its properties. *ACS Omega* **2021**, *6* (9), 6195-6205.
48. Y. Li, J. Liu, X. Wang, X. Zhang, N. Chen, L. Qian, Y. Zhang, X. Wang, Z. Chen, $CoFe_2O_4$@rGO as a separator coating for advanced lithium–sulfur batteries. *Small Sccience* **2023**, *3* (8), 2300045.
49. D. Xiong, X. Li, H. Shan, Y. Zhao, L. Dong, H. Xu, X. Zhang, D. Li, X. Sun, Oxygen-containing functional groups enhancing electrochemical performance of porous reduced graphene oxide cathode in lithium-ion batteries. *Electrochimica Acta* **2015**, *174*, 762-769.
50. A. Capezza, R. L. Andersson, V. Ström, Q. Wu, B. Sacchi, S. Farris, M. S. Hedenqvist, R. T. Olsson, Preparation and comparison of reduced graphene oxide and carbon nanotubes as fillers in conductive natural rubber for flexible electronics. *ACS Omega* **2019**, *4* (2), 3458-3468.
51. E. A. Ryan, Z. D. Seibers, J. R. Reynolds, M. L. Shofner, Surface-localized chemically modified reduced graphene oxide nanocomposites as flexible conductive surfaces for space applications. *ACS Applied Polymer Materials* **2023**, *5* (7), 5092-5102.
52. J.-N. Zhang, Q. Li, Y. Wang, J. Zheng, X. Yu, H. Li, Dynamic evolution of cathode electrolyte interphase (CEI) on high voltage $LiCoO_2$ cathode and its interaction with Li anode. *Energy Storage Materials* **2018,** *14*, 1-7.
53. G. Kang, G. Zhong, K. Cai, J. Ma, J. Biao, Y. Cao, S. Lu, K. Yu, F. Kang, Y. Cao, Dimethyl Sulfide Electrolyte Additive Enabled High-Voltage Lithium-Ion Battery. *ACS Energy Letters* **2024,** *9* (6), 2572-2581.
54. J.L. Allen, T.R. Jow, J. Wolfenstine, Improved cycle life of Fe-substituted $LiCoPO_4$. *Journal of Power Sources* **2011**, *196* (20), 8656-8661.

55. E. Markevich, R. Sharabi, H. Gottlieb, V. Borgel, K. Fridman, G. Salitra, D. Aurbach, G. Semrau, M. A. Schmidt, N. Schall, C. Bruenig, Reasons for capacity fading of $LiCoPO_4$ cathodes in $LiPF_6$ containing electrolyte solutions. *Electrochemistry Communications* **2012**, *15* (1), 22-25.
56. Q. D. Truong, M. K. Devaraju, T. Tomai, I. Honma, Direct observation of antisite defects in $LiCoPO_4$ cathode materials by annular dark- and bright-field electron microscopy. *ACS Applied Materials & Interfaces* **2013**, *5* (20), 9926-9932.
57. E. Markevich, G. Salitra, K. Fridman, R. Sharabi, G. Gershinsky, A. Garsuch, G. Semrau, M. A. Schmidt, D. Aurbach, Fluoroethylene carbonate as an important component in electrolyte solutions for high-voltage lithium batteries: Role of surface chemistry on the cathode. *Langmuir* **2014**, *30* (25), 7414-7424.
58. Y. H. Ikuhara, X. Gao, C. A. J. Fisher, A. Kuwabara, H. Moriwake, K. Kohama, H. Iba, Y. Ikuhara, Atomic level changes during capacity fade in highly oriented thin films of cathode material $LiCoPO_4$. *Journal of Materials Chemistry A* **2017**, *5* (19), 9329-9338.
59. M. G. Palmer, J. T. Frith, A. L. Hector, A. W. Lodge, J. R. Owen, C. Nicklin, J. Rawle, *In situ* phase behaviour of a high capacity $LiCoPO_4$ electrode during constant or pulsed charge of a lithium cell. *Chemical Communications* **2016**, *52* (98), 14169-14172.
60. J. L. Allen, J. L. Allen, T. Thompson, S. A. Delp, J. Wolfenstine, T. R. Jow, Cr and Si substituted-$LiCo_{0.9}Fe_{0.1}PO_4$: Structure, full and half Li-ion cell performance. *Journal of Power Sources* **2016**, *327*, 229-234.
61. R. J. C. Fiona, C. Strobridge, M. Leskes, D. S. Middlemiss, O. J. Borkiewicz, K. M. Wiaderek, K. W. Chapman, P. J. Chupas, C. P. Grey, Identifying the structure of the intermediate, $Li_{2/3}CoPO_4$, formed during electrochemical cycling of $LiCoPO_4$. *Chemistry of Materials* **2014**, *26* (21), 6193-6205.
62. S. Sreedeep, S. Natarajan, V. Aravindan, Recent advancements in $LiCoPO_4$ cathodes using electrolyte additives. *Current Opinion in Electrochemistry* **2022**, *31*, 100868.
63. W. M. Dose, I. Temprano, J. P. Allen, E. Björklund, C. A. O'Keefe, W. Li, B. L. Mehdi, R. S. Weatherup, M. F. L. D. Volder, C. P. Grey, Electrolyte reactivity at the charged Ni-rich cathode interface and degradation in Li-ion batteries. *ACS Applied Materials & Interfaces* **2022**, *14* (11), 13206-13222.
64. M. Gauthier, T. J. Carney, A. Grimaud, L. Giordano, N. Pour, H.-H. Chang, D. P. Fenning, S. F. Lux, O. Paschos, C. Bauer, F. Maglia, S. Lupart, P. Lamp, Y. Shao-Horn, Electrode–electrolyte interface in Li-ion batteries: Current understanding and new insights. *The Journal of Physical Chemistry Letters* **2015**, *6* (22), 4653-4672.
65. A. Jarry, S. Gottis, Y.-S. Yu, J. Roque-Rosell, C. Kim, J. Cabana, J. Kerr, R. Kostecki, The formation mechanism of fluorescent metal complexes at the $Li_xNi_{0.5}Mn_{1.5}O_{4-\delta}$/carbonate ester electrolyte interface. *Journal of the American Chemical Society* **2015**, *137* (10), 3533-3539.
66. S. Wolf, M. Roschger, B. Genorio, D. Garstenauer, V. Hacker, Mixed transition-metal oxides on reduced graphene oxide as a selective catalyst for alkaline oxygen reduction. *ACS Omega* **2023**, *8* (12), 11536-11543.
67. P. V. Kamat, Graphene-based nanoarchitectures. Anchoring semiconductor and metal nanoparticles on a two-dimensional carbon support. *The Journal of Physical Chemistry Letters* **2009**, *1* (2), 520-527.
68. L. Liu, X. Zhao, G. Ding, C. Han, J. Liu, $Fe_3N$ sites anchored reduced graphene oxide activate peroxymonosulfate via singlet oxygen dominated process: Performance and mechanisms. *Chemical Engineering Journal* **2023**, *470*, 143820.

# Chapter 6: Global Discussion

## 6.1. Thesis Overview

As discussed in Chapter 1 and Chapter 2, the importance of high energy Li-ion batteries (LIBs) is increasingly evident across a wide range of applications. LIBs have established themselves as essential energy storage solution from portable electronic devices to large-scale applications such as electric vehicles (EVs) and renewable energy storage systems.[1-3] This growing demand has sparked significant interest in researching next-generation cathode materials to surpass the current energy levels of the five major cathode materials developed and commercialized so far, including $LiCoO_2$ (LCO), $LiNi_xCo_yMn_zO_2$ (NCM, where x+y+z = 1), $LiNi_xCo_yAl_zO_2$ (NCA, where x+y+z = 1), $LiMn_2O_4$ (LMO), and $LiFePO_4$ (LFP).[4-6] Each of these cathode materials has various advantages and disadvantages. LCO offers high energy density but suffers from poor thermal stability and high cost.[7] NCM and NCA aim to reduce costs and improve electrochemical performance by partially replacing cobalt with nickel, manganese, or aluminum.[8, 9] LMO with spinel structure offers a significant cost advantage over LCO, but its lower energy density and shorter cycle life limit its widespread use.[10] LFP, while providing excellent thermal stability and safety, has lower energy density.[11]

After the development and commercialization of the cathode materials above, lithium cobalt phosphate ($LiCoPO_4$, LCP) has emerged as a promising candidate for next-generation cathode materials. LCP aims to build upon the success of LFP, which gained attention for its superior thermal stability despite lower energy density compared to LCO.[12-14] LCP offers a high operating voltage of 4.8 V vs. $Li/Li^+$ and a potential energy density of 800 Wh $kg^{-1}$, significantly higher than its predecessors. However, LCP cathodes face significant obstacles limiting their practical application in LIBs. Notably, they suffer from poor Li-ion mobility and inefficient electron transfer but also crystal structure defects and interfacial stability at high-voltage (high-V).[15, 16] These issues originate from the fundamental properties of olivine materials, primarily their restricted ability to conduct ions and electrons and the high potential of the $Co^{3+}/Co^{2+}$ redox couple. To address these challenges, strategies such as nanosizing, surface coating, and cation substitution have been adopted.

Reducing particle size can shorten the length of Li-ion diffusion pathways, enhance initial discharge capacity and rate capability but cause severe side reactions with electrolytes due to the increased interfacial area resulting in lower volumetric energy density.[17, 18] Surface coating with conductive carbon-based materials ensures enhanced electronic conductivity, and non-carbon layers

help mitigate the volumetric stresses and strains typically associated with Li-ion intercalation.[19-21] However, the preparation of these non-carbon coatings necessitates multiple synthesis techniques. Applying cation substitution has been demonstrated to improve structural features, effectively suppressing anti-site defect formation upon cycling tests, and improving overall kinetics.[22, 23] While some LCP doping advances have been experimentally verified, challenges still persist. In detail, charge compensation with increasing dopant concentration and a narrow cut-off voltage (4.3-5.0 V vs. $Li/Li^+$) maintaining the dopant in a non-redox state leads to a reduction in capacity from the theoretical capacity value.[24] Moreover, the body of research addressing the fundamental aspects of LCP prior to cation doping is markedly insufficient. Thus, the necessity for more intensive research on the material itself is emphasized to gain a complete understanding and maximize the utilization of LCP in high energy density LIBs.

In response to the deficiencies of the aforementioned approaches, crystallographic orientation control has been recognized to be an effective strategy to address the challenges associated with conventional nanosizing techniques.[25-28] This strategy prioritizes optimizing the length of the Li-ion diffusion pathway of LCP along [010] while preserving particle size at the micron scale, rather than reducing the overall particle size. For morphology tailoring, solution synthesis methods such as hydrothermal and solvothermal techniques are the most suitable for controlling particle shape through various experimental parameters.

While significant progress has been made in optimizing morphology, there remains a critical need for further research to address knowledge gaps in two key areas of LCP as a cathode material: the relationship between material synthesis and crystal properties that hinder achieving the theoretical full discharge capacity, and the role of interface chemistry in capacity fade upon cycling tests. Therefore, this thesis describes comprehensive investigations, focusing on multiple aspects of the target LCP material. It encompasses solution synthesis including hydrothermal (HT) and solvothermal (ST) methods, thorough characterization, electrochemical performance evaluation, and post-mortem analysis. This integrated study aimed at elucidating the fundamental limitations of LCP and propose potential solutions. The research findings provide new insights into solution synthesis techniques that can lead to production of defect-free crystal structures with optimized Li-ion diffusion pathways. Additionally, the study clarifies the interfacial chemistry intimately associated with capacity fade mechanism that occurs due to high-V operation. Ultimately, this comprehensive investigation contributes to bringing LCP closer to its theoretical full capacity and enhancing its cycling stability,

addressing key challenges in the development of high-performance cathode materials for next-generation LIBs.

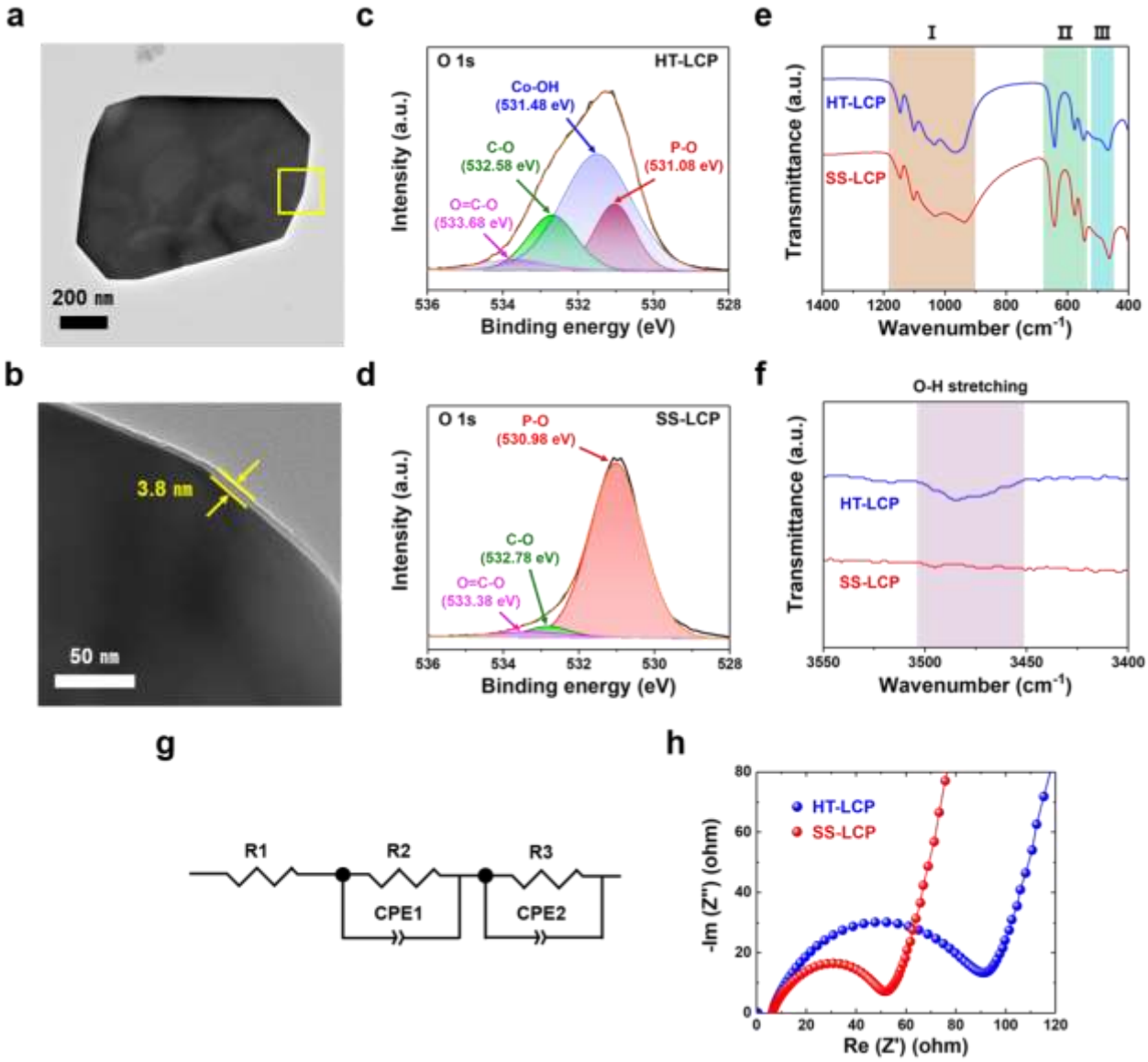


**Figure 6.1.** Characterization of nano-scale $Co(OH)_2$ layer on the surface of HT-LCP. (a-b) TEM and HRTEM images of HT-LCP; (c-d) XPS O 1s and (e-f) FTIR spectra of HT-LCP and SS-LCP; (g-h) Nyquist plots of pristine HT-LCP and SS-LCP electrodes with equivalent circuit used to fit the EIS model.

In Chapter 3, HT synthesis of LCP was performed by adjusting Li molar ratio and pH value of the precursor solution to control the degree of supersaturation. This approach produced high-purity, well-crystalline LCP particles with the 150 % excess of Li (2.5:1:1) at pH 9. Subsequent to HT synthesis, the material was subjected to high-energy planetary-milling (PM) and conductive carbon coating (C-coating) labeled as HT-PM-LCP and HT-PM-C-LCP respectively. These post-synthesis treatments aimed to improve electrochemical properties by reducing particle size and enhancing

electronic conductivity. To provide a comparative baseline, LCP was also synthesized using the conventional solid-state reaction (SS) method, which does not involve solution-based processes. This approach fabricated three sample analogues to HT method: pristine material (SS-LCP) and two post-processed versions (SS-PM-LCP and SS-PM-C-LCP).

In-depth characterizations of HT-LCP identified two major types of defects: surface composition inhomogeneity-not previously reported (Figure 6.1) and bulk cation mixing (Figure 6.2). Specifically, during this study we noted the formation of undesired nano-scale $Co(OH)_2$ passivation layer on the LCP surface and a significant presence of anti-site defects, where cobalt occupies lithium sites, blocking the one-dimensional (1-D) Li-ion diffusion channels.[29-34] The $Co(OH)_2$ layer forms on the LCP surface due to *in-situ* hydrolytic reactions favored by the alkaline environment, increasing charge-transfer resistance and adversely affecting the electrochemical performance. Moreover, abundant anti-site defects were detected, significantly higher in HT-LCP (9.14 %) compared to SS-LCP (1.73 %). These defects obstruct Li-ion diffusion channels thereby limiting Li-ion intercalation during charge-discharge cycling. The initial galvanostatic charge-discharge tests at C/20 within the voltage range of 3.5-5.2 V vs. $Li/Li^+$ demonstrated poor discharge capacities for pristine HT-LCP (33 mA h $g^{-1}$) and only marginal improvements following the post-synthesis treatment (53 mA h $g^{-1}$ for HT-PM-LCP). Despite the agglomeration and larger particle size, SS-LCP achieved a discharge capacity of 53.3 mAh $g^{-1}$. This capacity was improved to 76.2 mAh $g^{-1}$ after PM treatment (SS-PM-LCP). Although PM and C-coating were intended to escalate the electrochemical performance by reducing Li-ion diffusion lengths and enhancing electronic conductivity, these improvements were still insufficient to overcome the limitations imposed by the inherent defects.

While PM eliminates $Co(OH)_2$ layer on LCP surface and improves the initial discharge capacity, nano-sizing, as previously mentioned, leads to severe side reactions with the electrolyte and introduces difficulties for practical large-scale applications due to volumetric energy density concerns. The ICP-OES analysis revealed that the excess cobalt increased following the post-synthesis treatments, with HT-PM-LCP at 14.78 %, HT-PM-C-LCP at 15.72 %, SS-PM-LCP at 7.90 %, and SS-PM-C-LCP at 10.16 %. This trend aligns with the rise in anti-site defect concentration. The increase in excess cobalt after the post-synthesis treatments might be attributed to the loss of Li-ions to the isopropanol solvent used during PM or the evaporation of Li-ions during the high-temperature C-coating process. Furthermore, the high-temperature heat treatment required for C-coating does not reduce the anti-site defects formed during HT synthesis stage. This indicates that HT synthesis method

significantly impacts on the crystal structure and surface of LCP, which in turn affects the electrochemical performance.

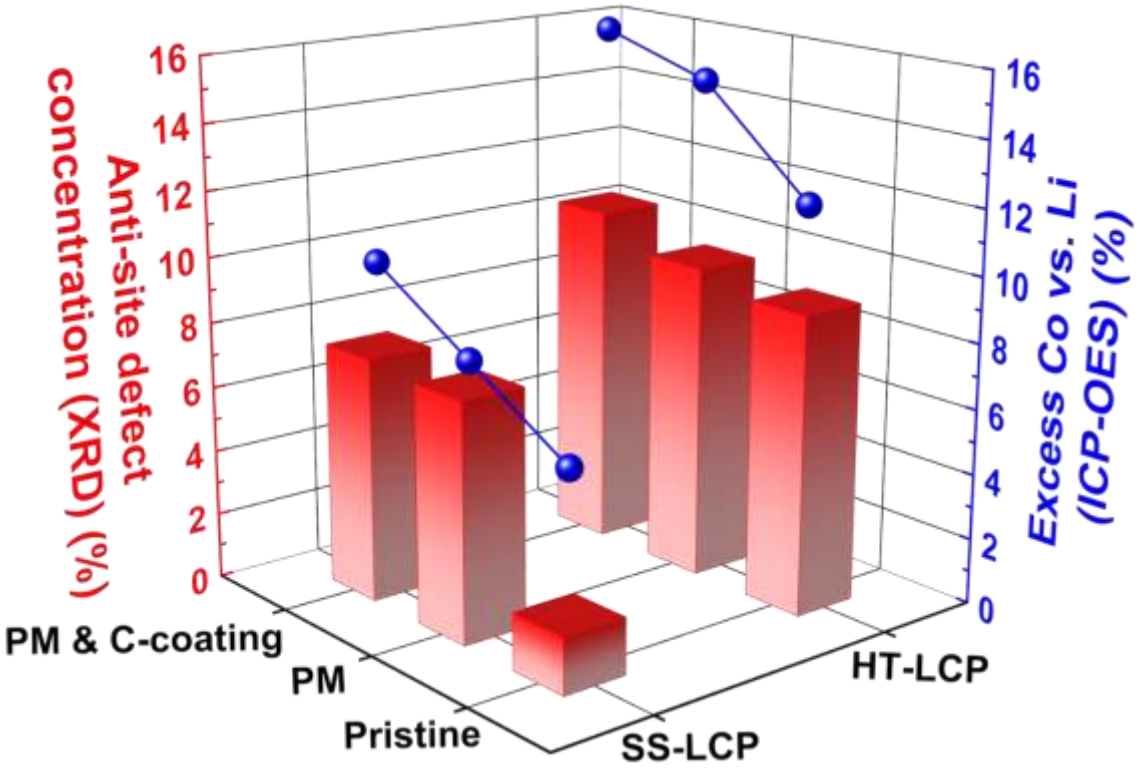


**Figure 6.2.** Anti-site defect concentration (Red bar) and excess Co (Blue sphere) calculated with XRD Rietveld refinement and ICP-OES analysis.

Therefore, this study concludes that HT synthesis, while advantageous for producing high-purity and well-crystalline LCP particles, inherently results in significant surface and bulk defects that curtail the electrochemical performance. The formation of nano-scale $Co(OH)_2$ surface layer and high concentration of anti-site defects are dominant factors limiting the functionality of LCP cathode. To fully obtain the theoretical capacity value of LCP, alternative crystal engineering approaches with water-free solvent are necessary to prevent the formation of $Co(OH)_2$ and minimize anti-site defects, making LCP viable for the application of high-energy LIBs.

In Chapter 4, to address the surface and bulk defects originated from water-based HT synthesis, the research aim was shifted to synthesize defect-free, preferentially oriented LCP crystals using a solvothermal method with ethylene glycol (EG) serving as the surface energy control medium (Figure 6.3). The experimental results indicated that adjusting the Li molar ratio in precursor solutions (1:1:1, 1.5:1:1, 2:1:1) modulates the preferred crystallographic orientation and reduces anti-site defect

concentration. XRD patterns showed that 100 % excess Li source (2:1:1) reduced the Li-ion diffusion length along [010] direction, enhancing Li-ion diffusion kinetics. SEM and TEM analyses revealed the preferential growth of ST-LCP particles, confirming the effectiveness of EG in tailoring crystal growth. To elucidate the preferential growth of LCP, the role of interfacial energy variations induced by EG molecule interaction with LCP crystal facets were analyzed through *ab initio* molecular dynamics (AIMD) and density functional theory (DFT) calculations to study adsorption configurations and surface energy. These computational modeling provided insights into the role of EG in significantly reducing interfacial energy and promoting desired crystal growth by stabilizing LCP facets with EG compared to water, explaining the observed anisotropic growth in ST-LCP.

To demonstrate the effect of solvent modification from water to EG, a comparative galvanostatic intermittent titration technique (GITT) analysis between LCP samples synthesized via ST and HT methods was conducted, with a particular emphasis on improving Li-ion diffusion kinetics. Compared to HT-LCP, ST-LCP exhibited significantly reduced overpotential, potentially indicative of enhanced electrochemical performance. Moreover, ST-LCP exhibited a superior number of redox peaks compared to HT-LCP, attributable to elimination of surface and bulk defects but also preferential crystal growth orientation, leading to enhanced Li-ion storage and rate capability. These improvements translated into substantially decreased charge-transfer and mass-transfer resistances in ST-LCP. Notably, ST-LCP showed the escalated Li-ion diffusion coefficients (ranging from $10^{-18}$ to $10^{-16}$ $cm^2$ $s^{-1}$) compared to HT-LCP, indicating expedited Li-ion transport within the crystal structure.

Nevertheless, the solvent modification introduced residual organic contaminants on the pristine ST-LCP surface, increasing charge-transfer resistance. In an effort to further optimize the material, ST-LCP was subjected to Ar-annealing process (700 ºC for 1 hour), and the obtained product is labeled ST-A-LCP. This additional treatment successfully removed residual EG from the ST-LCP surface and further reduced anti-site defect concentration, approaching near defect-free crystal structure. Cyclic voltammetry (CV), differential capacity (dQ/dV) and galvanostatic charge-discharge measurements revealed that ST-A-LCP exhibited superior electrochemical performance surpassing all previous works, achieving nearly theoretical discharge capacity (163.0 mAh $g^{-1}$ at C/10) and improved rate capability (151.6 mAh $g^{-1}$ at 1 C). Prolonged cycling tests demonstrated improved capacity retention vis-à-vis other reports, with ST-A-LCP maintaining 61.65 % of its initial discharge capacity after 100 cycles at 1 C rate, but still below the desired level. This research provides valuable insights into the synthesis-structure-property relationships in LCP cathode materials. By demonstrating the

benefits of ST method with EG and subsequent Ar-annealing, defect-free, preferentially oriented LCP crystals were successfully synthesized providing enhanced electrochemical performance.

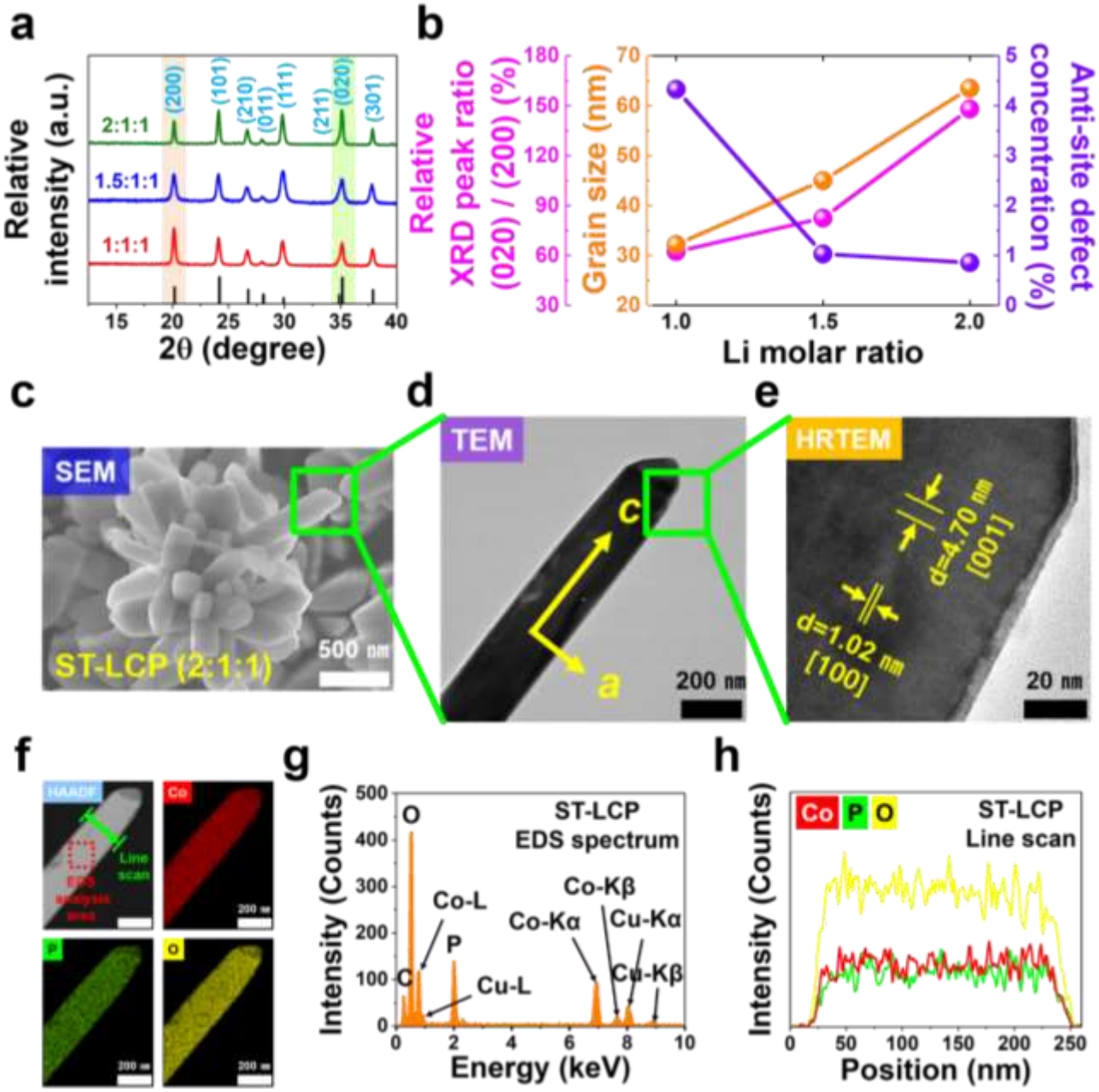


**Figure 6.3.** (a) XRD patterns (b) crystallographic information including relative XRD peak ratio of (020) / (200), grain size, and anti-site defect concentration of LCP samples via ST synthesis with different Li molar ratios; morphology and crystal orientation of ST-LCP via (c) SEM, (d) TEM, and (e) HRTEM; atomic arrangement investigations of ST-LCP with (f) TEM elemental mapping, (g) EDS spectrum, and (h) Line scan.

Despite the attainment of nearly theoretical discharge capacity, the cycling stability has not been satisfactory. Notably, the cycle life of ST-A-LCP was compromised by inconsistent Coulombic efficiency (CE) induced from the imbalance between charge and discharge capacities. This gap is

attributed to the electrolyte decomposition under high-V of LCP, exacerbated by severe interfacial reactions. The elevated cut-off voltage of 5.0 V vs. $Li/Li^+$, while beneficial from the standpoint of energy density, leads to parasitic side reactions at the cathode-electrolyte interface. These reactions are complex and multifaceted, involving intricate chemical and electrochemical processes that are not yet fully understood. Thus, obtaining a comprehensive understanding of these phenomena is crucial for the design and development of robust high-V cathodes capable of maintaining optimal performance over extended cycling periods.

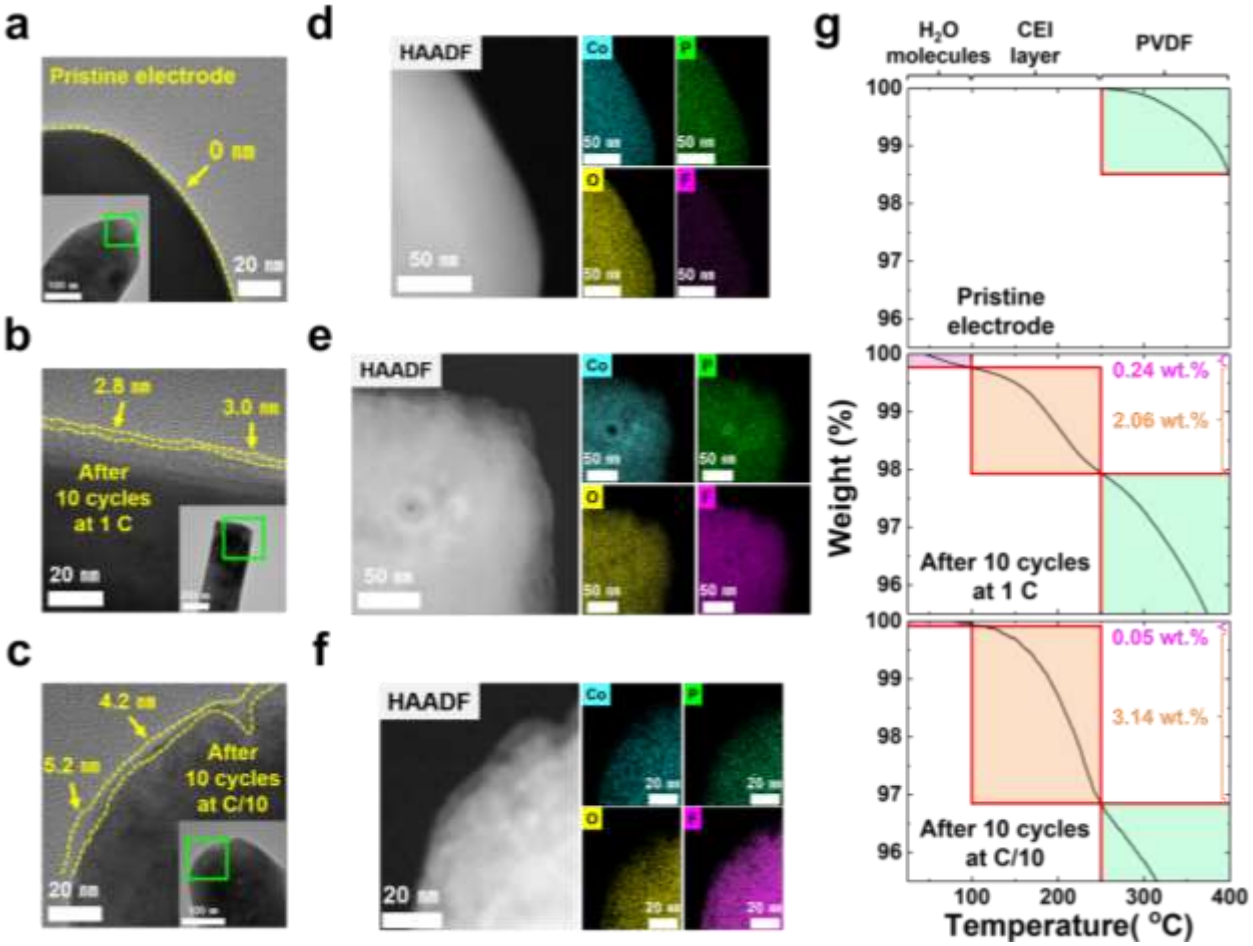


**Figure 6.4.** (a-c) HRTEM images displaying the CEI layer thickness evolution from pristine state, to after 10 cycles at 1 C and C/10; (d-f) the corresponding HAADF and elemental mapping (Co, P. O, and F) images; and (g) the respective TGA curves.

In Chapter 5, the research focus indeed shifted towards better understanding the capacity fade mechanisms of LCP via post-mortem analysis investigating cycled LCP electrodes under various aging conditions (Figure 6.4). The primary objective was to elucidate the correlation between interfacial chemistry and capacity loss during high-V operation and develop a novel coating strategy to mitigate these issues. In-depth post-mortem analysis employing a range of advanced techniques,

including TEM, TGA, EIS, MP-AES and XPS unveiled the intricate nature of LCP surface degradation. This deterioration, originating from parasitic reactions at the cathode-electrolyte interface, predominantly occurs through two interconnected processes: the progressive and irreversible evolution of the cathode-electrolyte interphase (CEI) layer and the gradual dissolution of redox metal (RM) primarily cobalt, a poorly understood phenomenon.

Specifically, the analysis revealed that the CEI layer on LCP particles thickened progressively with cycling, particularly at slower C-rates, indicating that prolonged exposure to high-V accelerates irreversible side reactions. The formation of the CEI layer, while initially beneficial as a protective film, can evolve into a performance-limiting factor with repeated charge-discharge cycles.[35] As the layer grows, it impedes Li-ion transport, increasing charge-transfer resistance and reducing the overall efficiency of LIBs. The formation of this layer also necessitates the consumption of electrolyte components, potentially leading to electrolyte depletion.[36] Simultaneously, the dissolution of RM species from the cathode surface not only results in a loss of RM-related capacity but also can lead to the migration and deposition of these species elsewhere in other battery components such as separator or anode, potentially causing further degradation or short-circuiting (refer to Figure 6.5).[37] Additionally, the dissolution process creates surface defects on the cathode, exacerbating degradation.[38] Importantly, it is observed that the extent of these degradation processes is directly dependent on the applied C-rate during cycling, providing valuable insights into optimizing operational parameters for LCP-based batteries.

To combat these undesired phenomena and improve the overall performance of LCP cathodes, an innovative surface engineering technique utilizing sucrose-derived reduced graphene oxide (RGO) has been successfully applied. This novel approach creates a protective layer on LCP particles (referred to as ST-R-LCP), serving multiple critical functions. The conductive RGO layer facilitates accelerated charge-transfer kinetics at the cathode-electrolyte interface, thereby reducing the increased resistance caused by CEI layer formation. Furthermore, this coating inhibits RM dissolution via prevention of aggressive surface complexation, effectively preserving the active material and minimizing capacity loss during prolonged cycling. The application of this RGO coating strategy has resulted in remarkable improvements in the electrochemical performance of LCP cathodes, particularly in terms of rate capability and cycling stability. Notably, ST-R-LCP exhibited significantly enhanced rate capability with the values of 158.8, 160.9, 162.6, and 163.0 mAh $g^{-1}$ corresponding to the increased C-rate from C/10 up to 1 C, demonstrating the ability to preserve relatively high capacity

even at faster charge and discharge rates allowing for quick charge and discharge without compromising capacity. Moreover, the cycling stability of ST-R-LCP during the initial 100 cycles at 1 C has shown substantial improvement, retaining higher capacity retention over numerous cycles compared to the uncoated counterparts (76.36 % compared to 61.65 % for the ST-A-LCP).

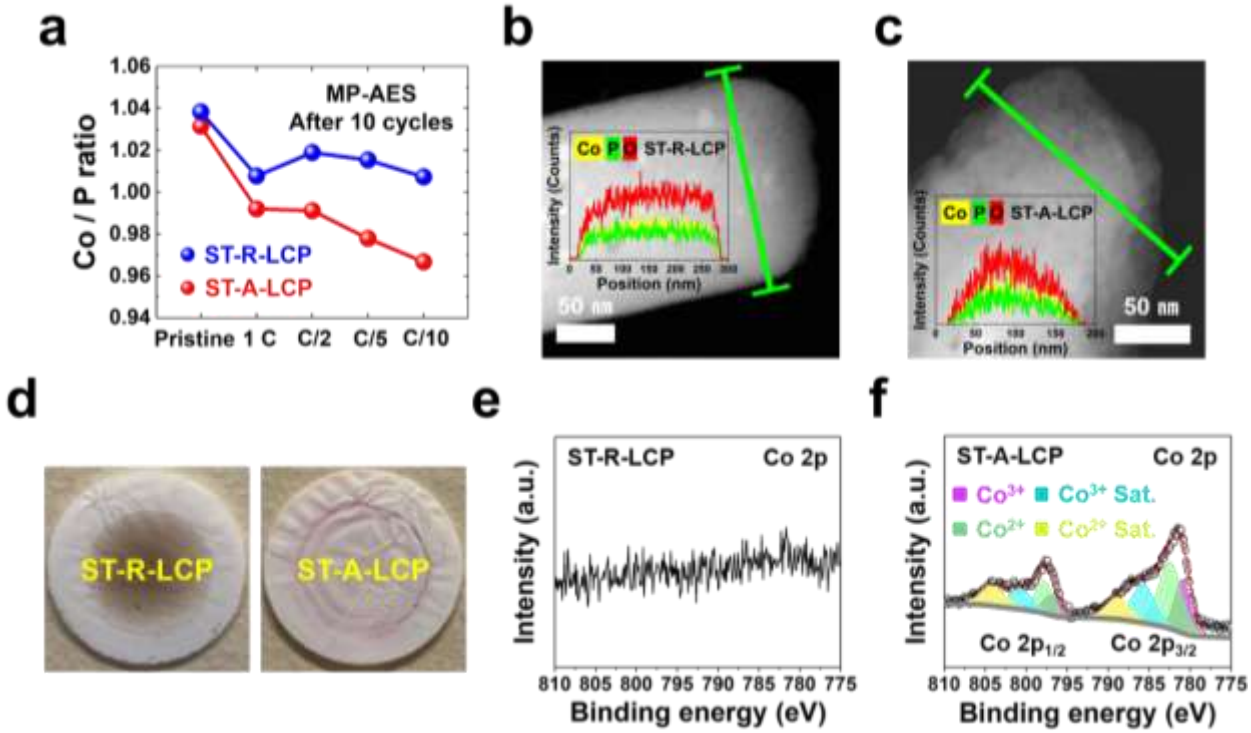


**Figure 6.5.** Investigation of redox metal (RM) dissolution upon cycling via (a) MP-AES analysis for the concentration ratio of cobalt to phosphorus (Co/P) for pristine and cycled ST-R-LCP and ST-A-LCP electrodes at different C-rates after 10 cycles; HAADF images (the inset image shows the line scan) of (b) ST-R-LCP and (c) ST-A-LCP particles extracted from the cycled electrodes after 100 cycles at 1 C; (d) photographs and Co 2p XPS spectra of separators extracted from (e) ST-R-LCP and (f) ST-A-LCP cells after 100 cycles at 1 C.

While RGO coating enhances charge transfer kinetics, it also accelerates initial electrolyte decomposition. However, the overall cycling stability of ST-R-LCP is significantly improved compared to ST-A-LCP due to the suppression of RM dissolution. This suggests that the RGO layer acts as a protective barrier against RM migration. The dissolution mechanism involves the interaction between surface RM cations and diketonate chelating agents derived from the oxidation of carbonate solvent including ethylene carbonate (EC), propylene carbonate (PC), and dimethyl carbonate (DMC), which is interrupted by the RGO coating.[39] The oxygen-containing functional groups in RGO further contribute to RM retention by forming strong coordination bonds with RM ions.

MP-AES analysis demonstrated that the relative molar ratio of Co/P at different C-rates after 10 cycles for both pre- and post-coating cathode samples. ST-R-LCP possesses a relatively well-

preserved Co/P ratio rather than ST-A-LCP, suggesting mitigated RM dissolution via RGO coating. In addition, TEM examination of LCP particles extracted from electrodes after 100 cycles at 1 C showed preservation of the original shape uniformity of ST-R-LCP without signs of parasitic ingress owed to protection by RGO coating. The inset line scan image reveals a significant contrast in elemental distribution between ST-R-LCP and ST-A-LCP particles. For ST-R-LCP, the image shows a uniform distribution of the three main elements–cobalt (yellow), phosphorus (green), and oxygen (red)–throughout the rectangular-shaped particle. This uniformity suggests that RGO coating has effectively maintained the structural integrity and composition of the LCP material. In contrast, ST-A-LCP particle exhibits noticeable loss of LCP composition, particularly near its surface. This compositional change at the lattice fringe suggests that the surface has undergone significant alteration, due to the irreversible side reactions with the electrolyte.

This comprehensive post-mortem analysis on LCP highlights that RM dissolution constitutes a critical factor contributing to capacity fade of LCP compared to the gradually evolving CEI layer. The protective nature of RGO coating in ST-R-LCP is evident, as it effectively preserves the elemental composition and structure. In contrast, the uncoated ST-A-LCP exhibits clear indications of surface degradation. This stark difference emphasizes the crucial role of surface protection in maintaining the stability and performance of high-V battery applications like LCP. Moving forward, further in-depth investigations into the correlation between capacity fade and interfacial chemistry are necessary to elucidate specific mechanisms of electrolyte decomposition, CEI layer formation, and RM dissolution under high-V condition. Such research will enable the development of targeted strategies to overcome these challenges, paving the way for high-energy LIBs with improved cycle life and stability.

### 6.2. References


1. D. Larcher, J. M. Tarascon, Towards greener and more sustainable batteries for electrical energy storage. *Nature Chemistry* **2015**, *7* (1), 19-29.
2. B. Dunn, H. Kamath, J. M. Tarascon, Electrical energy storage for the grid: A battery of choices. *Science* **2011**, *334* (6058), 928-935.
3. J. B. Goodenough, Y. Kim, Challenges for rechargeable Li batteries. *Chemistry of Materials* **2010**, *22* (3), 587-603.
4. K. Ozawa, Lithium-ion rechargeable batteries with $LiCoO_2$ and carbon electrodes: The $LiCoO_2$/C system. *Solid State Ionics* **1994**, *69*, 212-221.
5. N. Nitta, F. Wu, J. T. Lee, Yushin, G., Li-ion battery materials: Present and future. *Materials Today* **2015**, *18* (5), 252-264.
6. Q. Zhao, S. Stalin, C. Z. Zhao, L. A. Archer, Designing solid-state electrolytes for safe, energy-dense batteries. *Nature Reviews Materials* **2020**, *5* (3), 229-252.

7. Y. Furushima, C. Yanagisawa, T. Nakagawa, Y. Aoki, N. Muraki, Thermal stability and kinetics of delithiated $LiCoO_2$. *Journal of Power Sources* **2011**, *196* (4), 2260-2263.
8. W. Li, E. M. Erickson, A. Manthiram, High-nickel layered oxide cathodes for lithium-based automotive batteries. *Nature Energy* **2020**, *5* (1), 26-34.
9. W. Li, B. Song, A. Manthiram, High-voltage positive electrode materials for lithium-ion batteries. *Chemical Society Reviews* **2017**, *46* (10), 3006-3059.
10. Y. Huang, Y. Dong, S. Li, J. Lee, C. Wang, Z. Zhu, W. Xue, Y. Li, J. Li, Lithium manganese spinel cathodes for lithium-ion batteries. *Advanced Energy Materials* **2021**, *11* (2), 2000997.
11. A. Yamada, S. C. Chung, K. Hinokuma, Optimized $LiFePO_4$ for lithium battery cathodes. *Journal of The Electrochemical Society* **2001**, *148* (3), A224-A229.
12. D. Liu, W. Zhu, C. Kim, M. Cho, A. Guerfi, S. A. Delp, J. L. Allen, T. R. Jow, K. Zaghib, High-energy lithium-ion battery using substituted $LiCoPO_4$: From coin type to 1 Ah cell. *Journal of Power Sources* **2018**, *388*, 52-56.
13. D.-W. Han, Y.-M. Kang, R.-Z. Yin, M.-S. Song, H.-S. Kwon, Effects of Fe doping on the electrochemical performance of $LiCoPO_4$/C composites for high power-density cathode materials. *Electrochemistry Communications* **2009**, *11* (1), 137-140.
14. F. C. Strobridge, R. J. Clement, M. Leskes, D. S. Middlemiss, O. J. Borkiewicz, K. M. Wiaderek, K. W. Chapman, P. J. Chupas, C. P. Grey, Identifying the structure of the intermediate, $Li_{2/3}CoPO_4$, formed during electrochemical cycling of $LiCoPO_4$. *Chemistry of Materials* **2014**, *26* (21), 6193-6205.
15. C. Wang, J. Hong, Ionic/electronic conducting characteristics of $LiFePO_4$ cathode materials: The determining factors for high-rate performance. *Electrochemical and Solid-State Letters* **2007**, *10*, A65.
16. B. L. Ellis, K. T. Lee, L. F. Nazar, Positive electrode materials for Li-ion and Li-batteries. *Chemistry of Materials* **2010**, *22* (3), 691-714.
17. T. N. L. Doan, I. Taniguchi, Preparation of $LiCoPO_4$/C nanocomposite cathode of lithium batteries with high rate performance. *Journal of Power Sources* **2011**, *196* (13), 5679-5684.
18. B. Jin, H.-B. Gu, K.-W. Kim, Effect of different conductive additives on charge/discharge properties of $LiCoPO_4$/Li batteries. *Journal of Solid-State Electrochemistry* **2008**, *12*, 105-111.
19. A. Örnek, An impressive approach to solving the ongoing stability problems of $LiCoPO_4$ cathode: Nickel oxide surface modification with excellent core–shell principle. *Journal of Power Sources* **2017**, *356*, 1-11.
20. Y. Wang, J. Qiu, Z. Yu, H. Ming, M. Li, S. Zhang, Y. Yang, $AlF_3$-modified $LiCoPO_4$ for an advanced cathode towards high energy lithium-ion battery. *Ceramics International* **2018**, *44* (2), 1312-1320.
21. N. Laszczynski, A. Birrozzi, K. Maranski, M. Copley, M. E. Schuster, S. Passerini, Effect of coatings on the green electrode processing and cycling behaviour of $LiCoPO_4$. *Journal of Materials Chemistry A* **2016**, *4*, 17121-17128.
22. M. D. Johannes, K. Hoang, J. L. Allen, K. Gaskell, Hole polaron formation and migration in olivine phosphate materials. *Physical Review B* **2012**, *85*, 115106.
23. D. D. Lecce, J. Manzi, F. M. Vitucci, A. D. Bonis, S. Panero, S. Brutti, Effect of the iron doping in $LiCoPO_4$ cathode materials for lithium cells. *Electrochimica Acta* **2015**, *185*, 17-27.
24. N. Okita, K. Kisu, E. Iwama, Y. Sakai, Y. Lim, Y. Takami, M. T. Sougrati, T. Brousse, P. Rozier, P. Simon, W. Naoi, K. Naoi, Stabilizing the structure of $LiCoPO_4$ nanocrystals via addition of $Fe^{3+}$: Formation of $Fe^{3+}$ surface layer, creation of diffusion-enhancing vacancies, and enabling high-voltage battery operation. *Chemistry of Materials* **2018**, *30* (19), 6675-6683.

25. B. Wu, H. Xu, D. Mu, L. Shi, B. Jiang, L. Gai, L. Wang, Q. Liu, L. Ben, F. Wu, Controlled solvothermal synthesis and electrochemical performance of $LiCoPO_4$ submicron single crystals as a cathode material for lithium-ion batteries. *Journal of Power Sources* **2016**, *304*, 181-188.
26. J. Ludwig, C. Marino, D. Haering, C. Stinner, D. Nordlund, M. M. Doeff, H. A. Gasteiger, T. Nilges, Facile, ethylene glycol-promoted microwave-assisted solvothermal synthesis of high-performance $LiCoPO_4$ as a high-voltage cathode material for lithium-ion batteries. *RSC Advances* **2016**, *6*, 82984-82994.
27. J. Ludwig, C. Marino, D. Haering, C. Stinner, H. A. Gasteiger, T. Nilges, Morphology-controlled microwave-assisted solvothermal synthesis of high-performance $LiCoPO_4$ as a high-voltage cathode material for Li-ion batteries. *Journal of Power Sources* **2017**, *342*, 214-223.
28. X. Wu, M. Meledina, H. Tempel, H. Kungl, J. Mayer, R.-A. Eichel, Morphology-controllable synthesis of $LiCoPO_4$ and its influence on electrochemical performance for high-voltage lithium-ion batteries. *Journal of Power Sources* **2020**, *450*, 227726.
29. X. Wu, F. Rohman, M. Meledina, H. Tempel, R. Schierholz, H. Kungl, J. Mayer, R.-A. Eichel, Analysis of the effects of different carbon coating strategies on structure and electrochemical behavior of $LiCoPO_4$ material as a high-voltage cathode electrode for lithium-ion batteries. *Electrochimica Acta* **2018**, *279*, 108-117.
30. S. Y. Chung, J. T. Bloking, Y. M. Chiang, Electronically conductive phospho-olivines as lithium storage electrodes. *Nature Materials* **2002**, *1* (2), 123-128.
31. A. K. Padhi, K. S. Nanjundaswamy, J. B. Goodenough, Phospho-olivines as positive-electrode materials for rechargeable lithium batteries. *Journal of the Electrochemical Society* **1997**, *144* (4), 1188-1194.
32. A. Boulineau, T. Gutel, Revealing electrochemically induced antisite defects in $LiCoPO_4$: Evolution upon cycling. *Chemistry of Materials* **2015**, *27* (3), 802-807.
33. M. K. Devaraju, Q. D. Truong, T. Tomai, H. Hyodo, Y. Sasaki, I. Honma, Antisite defects in $LiCoPO_4$ nanocrystals synthesized via a supercritical fluid process. *RSC Advances* **2014**, *4* (94), 52410-52414.
34. Q. D. Truong, M. K. Devaraju, T. Tomai, I. Honma, Direct observation of antisite defects in $LiCoPO_4$ cathode materials by annular dark- and bright-field electron microscopy. *ACS Applied Materials & Interfaces* **2013**, *5* (20), 9926-9932.
35. N. Zhang, B. Wang, F. Jin, Y. Chen, Y. Jiang, C. Bao, J. Tian, J. Wang, R. Xu, Y. Li, Q. Lv, H. Ren, D. Wang, H. Liu, S. Dou, X. Hong, Modified cathode-electrolyte interphase toward high-performance batteries. *Cell Reports Physical Science* **2022**, *3* (12), 101197.
36. H. Wang, X. Li, F. Li, X. Liu, S. Yang, J. Ma, Formation and modification of cathode electrolyte interphase: A mini review. *Electrochemistry Communications* **2021**, *122*, 106870.
37. B. J. Jeong, J. Y. Sung, F. Jiang, S. P. Jung, C. W. Lee, Providing high stability to suppress metal dissolution in $LiMn_{0.5}Fe_{0.5}PO_4$ cathode materials by Zn doping. *Journal of Energy Storage* **2024**, *96*, 112552.
38. J. M. Kim, X. Zhang, J.-G. Zhang, A. Manthiram, Y. S. Meng, W. Xu, A review on the stability and surface modification of layered transition-metal oxide cathodes. *Materials Today* **2021**, *46*, 155-182.
39. A. Jarry, S. Gottis, Y. S. Yu, J. Roque-Rosell, C. Kim, J. Cabana, J. Kerr, R. Kostecki, The formation mechanism of fluorescent metal complexes at the $Li_xNi_{0.5}Mn_{1.5}O_{4-\delta}$/carbonate ester electrolyte interface. *Journal of the American Chemical Society* **2015**, *137* (10), 3533-3539.

# Chapter 7: Synopsis

## 7.1. Global Conclusions

The research described in Chapters 3, 4, and 5 presents significant advances on the development and optimization of lithium cobalt phosphate ($LiCoPO_4$, LCP) as a high-performance cathode material for lithium-ion batteries (LIBs). The study progressed through several key stages, each addressing specific challenges and yielding important insights.

Initially, the target material, LCP was synthesized using both hydrothermal (HT) and conventional solid-state (SS) methods, followed by post-synthesis treatments including high-energy planetary-milling (PM) and carbon coating (C-coating) to enhance the intrinsically sluggish kinetics of LCP. In-depth material characterization revealed that HT synthesis brings two performance compromizing issues: the formation of a resistive nano-scale $Co(OH)_2$ layer on LCP surface causing extra charge-transfer resistance and an abundance of anti-site defects blocking one-dimensional (1-D) Li-ion diffusion channels compared to SS-LCP.

After revealing the fundamental limitation of HT synthesis, a novel LCP crystal variety with enhanced kinetics was designed. The new LCP material characterized by a defect-free crystal structure and shortened Li-ion diffusion pathways was produced through solvothermal (ST) synthesis using ethylene glycol (EG) as a water-free solvent and subsequent Argon (Ar)-annealing treatment. Computational modeling with the combination of *ab initio* molecular dynamics (AIMD) and density functional theory (DFT) calculations determined the surface-active role of EG in promoting anisotropic crystal growth by exhibiting interfacial energy variation upon molecular interaction with each LCP crystal facet. The resulting LCP (ST-A-LCP) exhibited superior Li-ion diffusivity, leading to near-theoretical capacity (163.0 mAh $g^{-1}$ at C/10) and excellent rate capability (151.6 mAh $g^{-1}$ at 1 C) but not the desired level of cycling stability (61.7 % capacity retention after 100 cycles at 1 C).

Subsequent to the achievement of nearly theoretical discharge capacity, post-mortem analysis of cycled LCP electrodes with different aging conditions was conducted to understand the relationship between capacity fade mechanism and irreversible interfacial chemistry between cathode and electrolyte. High-V operation of LCP triggered two main side-reactions: undesired cathode-electrolyte interhphase (CEI) layer evolution intimately linked with enlarged charge-transfer overpotential and redox metal (RM) dissolution causing unwanted RM-related capacity loss. To address these irreversible side reactions at cathode-electrolyte interface, one-step facile sucrose-derived RGO

coating was developed to expedite the charge-transfer kinetics and effectively mitigate RM dissolution. The RGO coated LCP sample (ST-R-LCP) delivered both superior accessible discharge capacity up to 163.0 mAh $g^{-1}$ (equal to 771.2 Wh $kg^{-1}$ as energy density) and significantly enhanced retention of 76.4 % after 100 cycles at 1 C, never achieved before without stabilizing dopants.

This comprehensive post-mortem analysis on LCP revealed that RM dissolution plays a major role in capacity fade of LCP compared to the gradually evolving CEI layer. These findings not only advance the understanding of LCP as a high-voltage (high-V) cathode material but also provide valuable insights into strategies for improving the performance and longevity of advanced LIBs.

### 7.2. Original Contributions to Knowledge

This thesis made significant contributions to original scientific knowledge of LCP research through comprehensive studies of solution synthesis methods, post-mortem analysis, and electrochemical evaluation. The research focused on elucidating the intricate relationships between material synthesis, crystal structure, electrochemical performance, and capacity fade mechanisms in LCP cathodes.

Firstly, via a suite of detailed surface and bulk crystal characterizations coupled with electrochemical analysis, the candidate discovered hydrothermal (HT) synthesis of $LiCoPO_4$ to lead to (i) the formation of resistive nano-scale $Co(OH)_2$ surface passivation layer and (ii) abundant anti-site defects arising from excess Co in HT-LCP samples compared to SS-LCP samples, thus explaining the poor discharge capacity of the HT-LCP material.

Secondly, the candidate developed a novel LCP crystal variety characterized by defect-free crystal structure and shortened Li-ion diffusion pathway via solvothermal (ST) synthesis using ethylene glycol (EG) as the crystal plane specific solvent and subsequent Argon (Ar)-annealing. The origin of crystal growth control that enabled the production of defect-free LCP was elucidated with the calculation of surface energy of different LCP crystal facets in different solvents ($H_2O$ and EG) after solvent molecule adsorption through AIMD simulation and DFT calculation. Owed to the morphological and structural advantages of the ST-A-LCP material, noticeably augmented Li-ion diffusivity is obtained, and nearly theoretical full capacity value (163.0 mAh $g^{-1}$ at C/10), and improved rate capability (151.6 mAh $g^{-1}$ at 1 C).

Thirdly, through post-mortem analysis, the relationship between capacity fade mechanism and irreversible interfacial chemistry between cathode and electrolyte was elucidated. Specifically, high-

V operation of LCP triggers two main side-reactions: i) undesired cathode-electrolyte interphase (CEI) layer evolution intimately linked with enlarged charge-transfer overpotential and ii) Redox metal (RM) dissolution causing unwanted consumption of RM from olivine structure. This understanding motivated us to develop a sucrose-derived RGO coating to promote charge exchange while mitigating irreversible side reactions at cathode-electrolyte interface and RM dissolution. With RGO coating strategy, the candidate achieved both superior accessible discharge capacity up to 163.0 mAh $g^{-1}$ (equal to 771.2 Wh $kg^{-1}$ as energy density) and significantly improved capacity retention of 76.4 % after 100 cycles at 1 C vs. 61.7 % without RGO coating.

### 7.3. Future Research Direction

The findings in this thesis highlight the importance of further in-depth investigations into the correlation between capacity fade and interfacial chemistry in LCP-based systems. Such research should aim to elucidate the specific mechanisms of electrolyte decomposition, CEI layer formation, and RM dissolution under the conditions of raised cut-off voltage. Understanding these processes at a molecular level could provide crucial insights for developing targeted strategies to mitigate these issues that can be advantageously combined with doping studies as stabilizing approach.

Potential avenues for future research may include:

1. Advanced *in-situ* and *operando* characterization techniques to observe interfacial reactions in real-time upon cycling.
2. Computational modeling of the cathode-electrolyte interface to predict and understand degradation mechanisms.
3. Development of novel electrolyte specifically designed to withstand at high-V.
4. Investigation of electrolyte additives that could form more stable and conductive CEI layers, minimizing capacity loss over extended cycling.
5. Exploration of advanced surface coating or modification techniques to create stable interfaces between cathode and electrolyte.

By addressing these challenges and gaining a deeper understanding of the interfacial chemistry in high-V cathode systems (in addition to appropriate doping strategies), it may be possible to unlock the full potential of this promising cathode material. Overcoming these hurdles could pave the way for the development of high-energy LIBs with significantly improved cycle life and stability.

# Appendixes

## A.1. Methodology and Characterization

This section has been prepared to provide comprehensive details on the methodology and characterization techniques employed in this thesis. It offers supplementary explanations and elaborations to help fully understand sample preparation and analyses outlined in the Experimental sections of Chapters 3, 4, and 5.

### A.1.1. Material preparation

#### A.1.1.1. Precursor solution preparation and hydrothermal synthesis (HT-LCP)


**Figure A.1.1.** (a) $N_2$-filled glovebox and (b) degassing process of deionized water in $N_2$-filled glovebox.

The experimental procedure begins with the preparation of deionized and deoxygenated water to prevent cobalt oxidation. This step involves transferring 1 L of deionized water into a nitrogen ($N_2$)-filled glovebox, as illustrated in Figure A.1.1a. To effectively degas the water, a bubble column connected to a rubber hose is submerged into the water. The degassing process continues for three hours, during which time the water is continuously stirred while maintaining a steady flow of $N_2$ gas, as depicted in Figure A.1.1b.

Once the deionized and deoxygenated water is ready, carefully transfer all the essential chemicals, along with the glass liner, autoclave head, and container, into $N_2$-filled glovebox. Within the glovebox, use a magnetic stirrer to thoroughly dissolve all the required chemicals in 200 mL of deionized and deoxygenated water. This includes varying amounts of lithium content to achieve different molar ratios (1:1:1, 1.5:1:1, 2:1:1, 2.5:1:1, and 3:1:1) relative to the cobalt and phosphate

sources. It is crucial to confirm that the stirring process continues until a completely homogeneous precursor solution is obtained, with no visible undissolved particles remaining in the mixture. Once the solution has reached a uniform consistency, cautiously transfer it into the glass liner, paying attention to avoid any spills or contamination that could compromise the integrity of the experiment.

Afterwards, the next step is to assemble the autoclave. This involves placing the glass liner with the precursor solution into the autoclave container, securely attaching the autoclave head, and ensuring that all components are correctly aligned. Once the assembly is complete, attentively remove the whole autoclave from $N_2$-filled glovebox. To mitigate the risk of any potential explosions during the experiment, take extra precautions by tightening all the screws on the autoclave assembly (Figure A.1.2a). This step is crucial to confirm that the autoclave is properly sealed and can withstand the elevated pressure and temperature it will be subjected to during the experiment. Finally, place the securely assembled autoclave on the loading station, assuring that it is correctly positioned and stable before proceeding with the following experimental procedures (Figure A.1.2b). For safety purposes, the autoclave station must be positioned behind a wall to reduce the risk of damage to other laboratory facilities. Additionally, it is important to regularly inspect the rupture disc to allow that it can release internal pressure above a certain level of pressure to prevent any potential explosions.

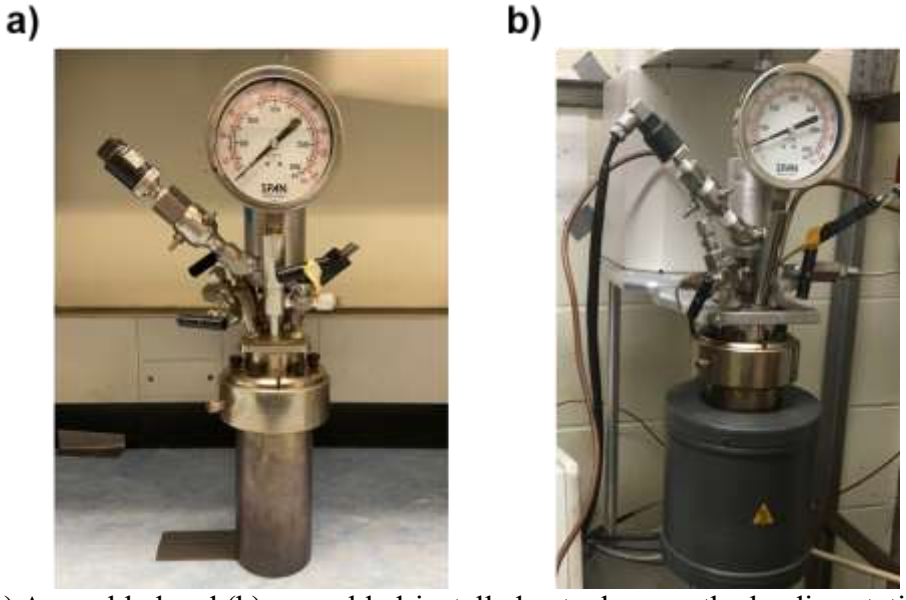


**Figure A.1.2.** (a) Assembled and (b) assembled-installed autoclave on the loading station.

### A.1.1.2. Planetary milling (HT-PM-LCP)

The process involves transferring 7.5 mL of HT-LCP powder, measured by tap density, along with PM jars and lids (Figure A.1.3a), 100 g of 1 mm zirconia ($ZrO_2$) balls (Figure A.1.3b), and 15

mL of isopropanol into $N_2$-filled glovebox. In the prepared PM jar, add the materials in the following order: HT-LCP powder, $ZrO_2$ balls, and isopropanol. Then, securely seal the jar with the lid. Once the jar is assembled, carefully remove it from $N_2$-filled glovebox and transport it to the PM machine, Planetary Micro Mill PULVERISETTE 7 premium line (Fritsch) as shown in Figure A.1.3c. Before installing the jar into the machine, confirm that the total weight of each jar should be balanced as possible. Set the milling machine by selecting the milling conditions including the duration time, pauses, and number of cycles determining the entire milling time. Finally, start the milling machine to begin the process.

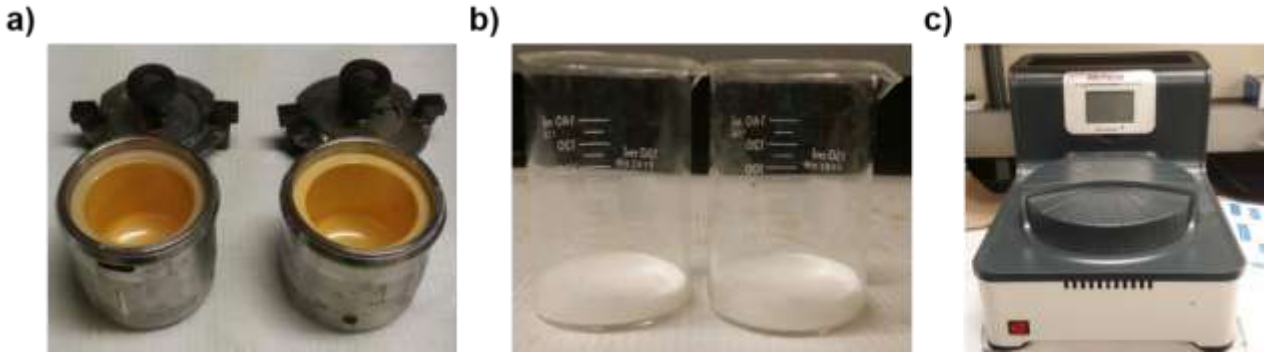


**Figure A.1.3.** (a) Grinding jar and lid, (b) 100 g of $ZrO_2$ ball with the diameter 1 mm, and (c) Planetary Micro Mill PULVERISETTE 7 premium line.

### A.1.1.3. Carbon coating (HT-PM-LCP)

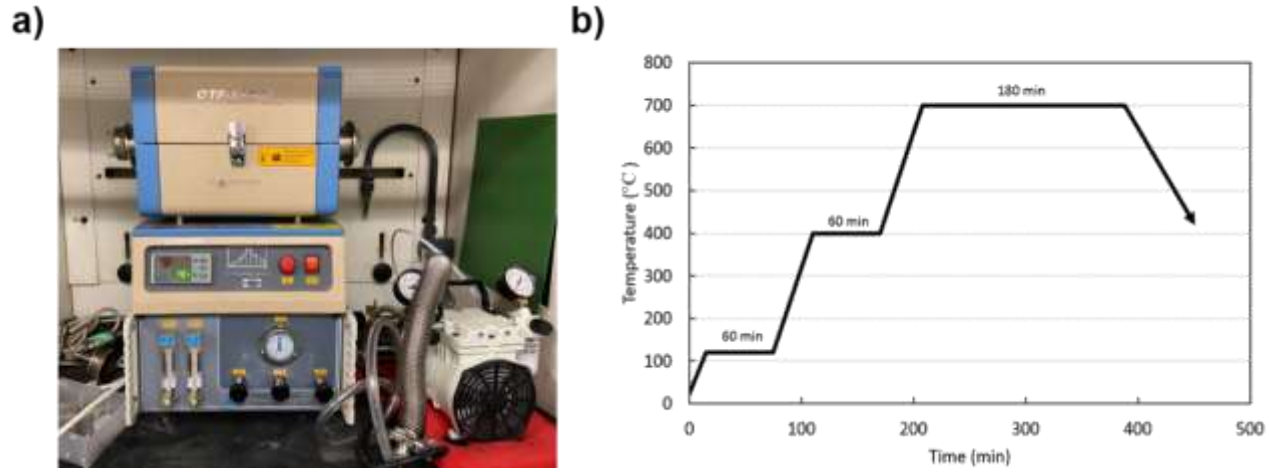


**Figure A.1.4.** (a) MTI mini tube furnace, and (b) heating schedule for carbon coating.

A lactose solution was prepared by dissolving lactose in deionized and deoxygenated water with the concentration, 22.4 g $L^{-1}$ and stirring for half an hour. Subsequently, 10 mL of this solution was combined with 2 g of HT-PM-LCP powder in a graphite crucible, resulting in a mixture ratio of 0.112 g lactose per gram of LCP sample. After oven-drying the resulting slurry, it was placed in an

MTI mini tube furnace (model OTF-1200X, Figure A.1.4a). The heating process then followed the schedule illustrated in Figure A.1.4b.

### A.1.1.4 Solid-state reaction synthesis (SS-LCP, SS-PM-LCP, and SS-PM-C-LCP)

The stoichiometric amounts of chemicals as a source of lithium, cobalt, and phosphate, along with PM jars and lids, 100 g of 1 mm $ZrO_2$ balls, and isopropanol with the two times larger volume of total chemicals were transferred into $N_2$-filled glovebox. Following the procedure described in section A.1.1.2, place the chemicals into the jar and proceed the wet grinding at 300 rpm for 6 hours. Afterward, dry the resulting material in an oven at 50 $^oC$ overnight. Following the chemical mixing and drying stages, the material underwent two separate calcination processes. Both processes used a heating rate of 5 $^oC\ min^{-1}$. The first calcination took place in air at 400 $^oC$ and lasted for 10 hours. This step was designed to eliminate crystal water from the mixture. The second calcination occurred in argon (Ar) atmosphere at 800 $^oC$, also for a duration of 10 hours. The purpose of this final step was to produce a pure LCP phase.

The procedures described in sections A.1.1.2 and A.1.1.3 were entirely replicated for the preparation of SS-PM-LCP and SS-PM-C-LCP samples. This replication was implemented to create a parallel set of samples to the HT-PM-LCP and HT-PM-C-LCP variants. The same methodologies were employed throughout this process to ensure consistency and comparability between the different sample sets.

### A.1.1.5 Solvothermal synthesis (ST-LCP)

The overall process closely resembles the HT synthesis outlined in section A.1.1.1, but with notable modifications. Instead of water, the organic solvent ethylene glycol (EG) is now used as the solvent. Additionally, the range of Li molar ratio options has been narrowed down to just three: 1:1:1, 1.5:1:1, and 2:1:1. These changes result in a more restricted set of synthesis conditions compared to the previous method. Despite these alterations, the fundamental approach remains consistent with the HT synthesis process described earlier.

### A.1.1.6. Argon annealing and RGO coating (ST-A-LCP and ST-R-LCP)

The process for Ar-annealing and coating with sucrose-derived reduced graphene oxide (RGO) began with dispersing pristine ST-LCP in deoxygenated and deionized water. This water contained varying amounts of sucrose (0 or 40 wt.%). After thorough mixing, the suspension was placed in an

alumina ($Al_2O$) crucible. The resulting slurry was then dried in a vacuum oven at 80 ºC. Following this, the dried material was transferred to the tube furnace previously mentioned in section A.1.1.3. There, it was heated to 700 ºC for one hour under a continuous flow of Ar gas. This step was designed to reduce the anti-site defect concentration further and cause sucrose decomposition and subsequent carbonization. The samples produced through this process were labeled differently based on the presence of sucrose: those annealed in Ar without sucrose were denoted as ST-A-LCP, while those processed with sucrose were designated as ST-R-LCP.

### A.1.7. Electrode preparation and cell assembly

For electrode preparation, two methods were employed: dry-method and wet-method. The dry-method was used to fabricate free-standing working electrodes without an Aluminum (Al) current collector. The process began in Ar-filled glovebox (Figure A.1.5) where a PM jar was assembled with 70 wt.% of LCP sample and 20 wt.% of acetylene black. These components underwent mild PM milling at 300 rpm for 1 hour without solvent by using twenty of $ZrO_2$ grinding balls (10 mm each) to ensure homogeneous blending. After mixing, the jar was carefully transferred back to Ar-filled glovebox and disassembled. The next step involved adding 10 wt.% of polytetrafluoroethylene (PTFE) binder into the mixed powder. This mixture was then spread and pressed using a stainless steel bar in a hand-pressing process. Sufficient pressure and cutting step were replicated until a film was formed with an area of 0.16 $cm^2$ and a weight of approximately 2.5 mg.

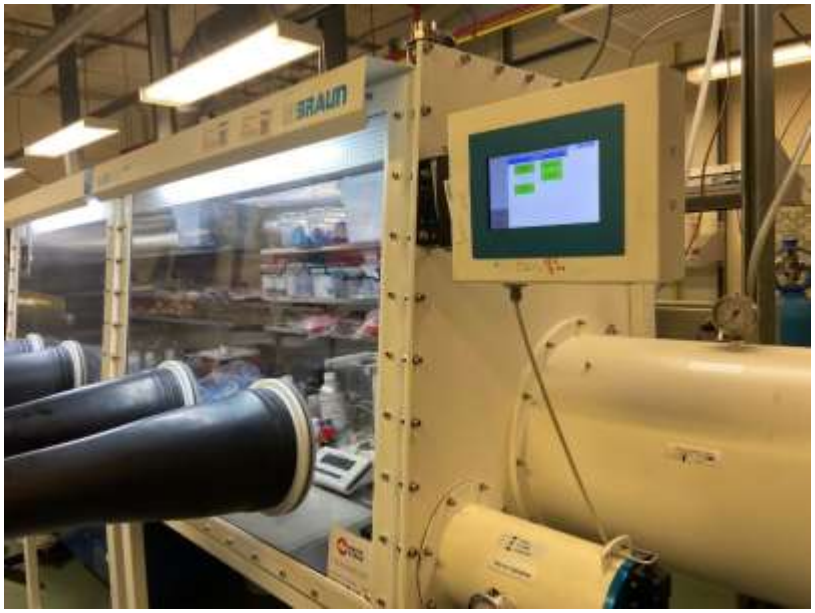


**Figure A.1.5.** Ar-filled glovebox for cell assembly and material preparation.

The wet-method for electrode preparation involved formulating a slurry by combining LCP samples, acetylene black, and polyvinylidene fluoride (PVDF, $(C_2H_2F_2)n$) binder in a 7:2:1 weight ratio. These components were mixed in 1-methyl-2-pyrrolidone (NMP) solvent. As illustrated in Figure A.1.6a, the resulting slurry was then placed on a high-purity Al foil, which served as the current collector. A doctor blade was used to ensure uniform spreading of the slurry across the foil surface. Subsequently, the coated foil was left to dry overnight in a vacuum oven at 80 $^oC$ to evaporate NMP solvent.

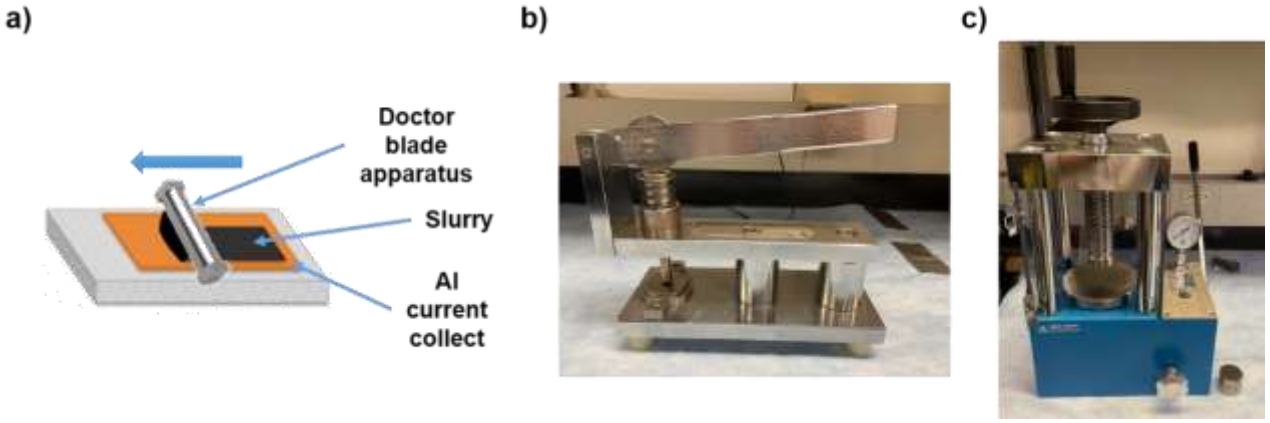


**Figure A.1.6.** (a) Schematic diagram of electrode paste on Al current collector, (b) electrode punch, and (c) press.

The dried electrode was punched into disks with a diameter of 10 mm and then pressed twice with 20 MPa (Figure A.1.6b-c). The final mass loading of the cathode electrodes produced by this wet-method averaged 2-2.5 mg $cm^{-2}$, which is comparable to the loading achieved with the dry-method described earlier. These manufactured electrodes were further dried in a vacuum oven at 80 $^oC$ for an additional day, then transferred to Ar-filled glovebox for cell assembly.

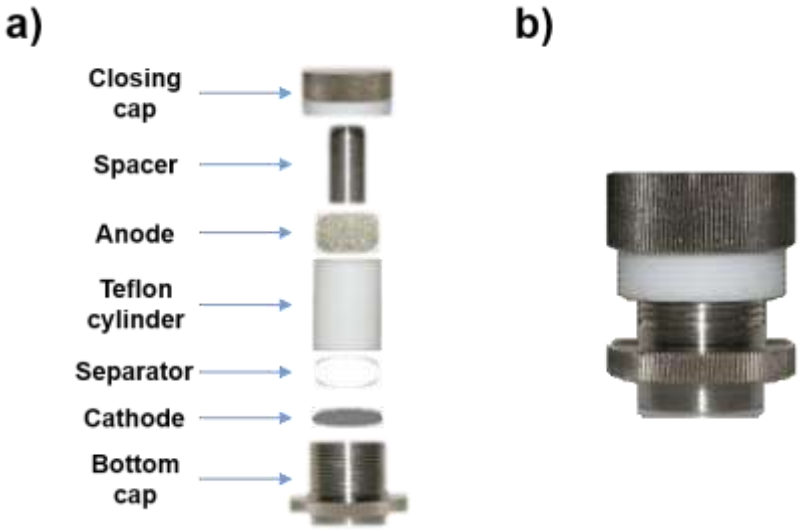


**Figure A.1.7.** (a) Swagelok cell components, and (b) assembled cell.

To evaluate electrochemical properties, the prepared electrodes were incorporated into a Swagelok-type cell. The assembly process, as illustrated in Figure A.1.7a, initiates by transferring all required components into Ar-filled glovebox. Within this controlled environment to avoid the exposure of oxygen and moisture, the cell is constructed by stacking the various parts in a specific order from bottom to top. Once all components are in place, the cell is sealed with a closing cap. During this assembly, it's crucial to maintain proper alignment of all components. A noteworthy detail is the use of 200 µL of electrolyte and two separators in the cell configuration. This careful assembly process ensures the integrity of the cell for subsequent electrochemical measurements.

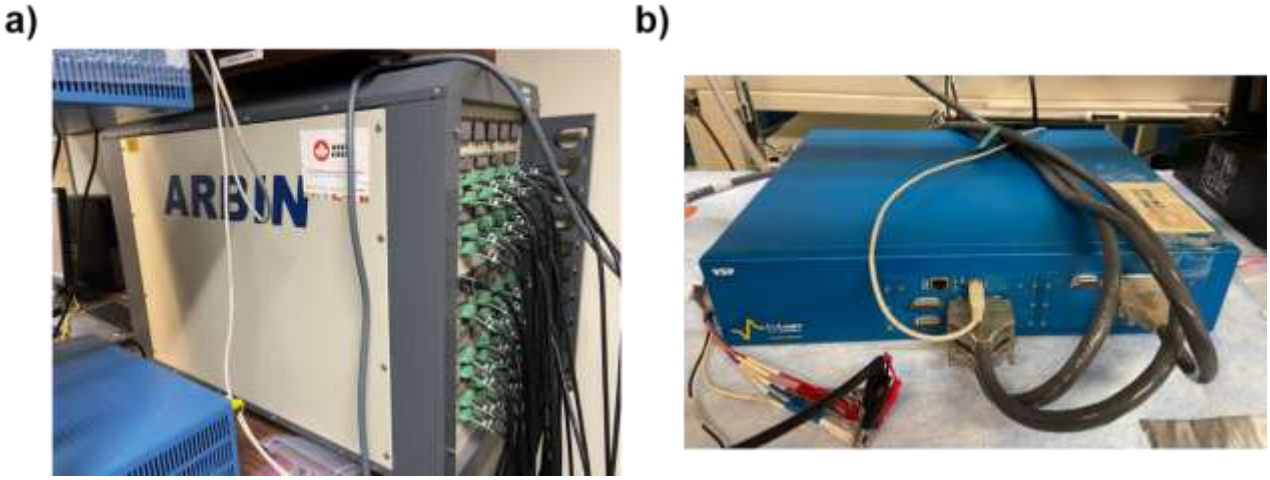


**Figure A.1.8.** (a) Arbin cycler (BT2403), and (b) Bio-Logic workstation.

After assembly, the Swagelok cells (Figure A.1.7b) were allowed to rest for 6 hours, providing sufficient time for the electrolyte to thoroughly wet LCP cathodes. Following this rest period, the cells were transferred to Arbin cycler (Figure A.1.8a) for various electrochemical tests. These tests included obtaining charge-discharge curves, capacity retention, and galvanostatic intermittent titration technique (GITT) analysis. For additional electrochemical characterizations, Bio-Logic workstation (Figure A.1.8b) was employed. This equipment was utilized to conduct electrochemical impedance spectroscopy (EIS) measurements, cyclic voltammetry (CV), and linear sweep voltammetry (LSV) analysis.

### A.1.2. Materials characterizations

#### A.1.2.1. Phase and crystal structure (XRD)

X-ray diffraction (XRD) analysis was performed using Bruker D8 Discovery X-ray diffractometer. The instrument employed a Co K-alpha source (Co-Kα) with a radiation wavelength

of 1.78892 Å. Operating conditions were set at 35 kV voltage and 45 mA current. The diffraction patterns were collected over a 2θ range from 10 to 80 º. For detailed structural analysis, Rietveld refinements of the crystal structure were conducted using TOPAS Academic V5 program software. This refinement process allowed for the determination of several key structural parameters, including lattice parameters, grain size, and defect concentration.

#### A.1.2.2. Electron microscopy (SEM and TEM)

Morphological characterization was conducted using Hitachi cold-field emission SU-8000 scanning electron microscope (CFE-SEM). The imaging parameters included an acceleration voltage of 5 kV and an emission current of 10 μA allowing for the acquisition of high-resolution images at various magnifications, including 10 k, 20 k, 50 k, and others.

For more advanced microscopy techniques, Thermo Scientific Talos F200X G2 STEM operating at 200 kV was utilized. This versatile instrument enabled the collection of multiple types of data, including transmission electron microscope (TEM), high-resolution TEM (HR-TEM), high-angle annular dark-field (HAADF) images, and selected area electron diffraction (SAED) patterns. Additionally, it allowed for energy dispersive X-ray (EDS) elemental mappings and line scans.

#### A.1.2.3. Size distribution (Zetasizer Nano ZS)

Sample preparation begins by mixing 0.05 g of LCP sample with 5 mL of deionized (DI) water in a 15 mL conical tube. The mixture is then subjected to at least 30 minutes of sonication to guarantee thorough dispersion. During the sonication, clean a 12 mL cuvette with isopropanol and use an air gun to evaporate the solvent. Following the sonication process, cautiously transfer the resulting solution into a 12 mL cuvette up to the marked line. Once the cuvette is filled with the solution, place it securely within the measurement device. With the sample properly positioned, the measurement procedure can be initiated.

#### A.1.2.4. Surface characterization (XPS)

X-ray photoelectron spectroscopy (XPS) analysis process began with an essential sample preparation step: Film- or powder- typed LCP samples were subjected to vacuum oven overnight for degassing to ensure optimal surface conditions. Afterwards, samples were carefully sealed into the sample holder within nitrogen-filled glovebox, preserving their pristine state. XPS spectra were then acquired using Nexsa G2 system from Thermo Scientific. The instrument utilized Al Kα radiation at

1486.6 eV with a focused X-ray spot size of 200 μm. To mitigate charging effects, a flood gun was employed during measurements. The acquisition parameters for all elemental spectra were standardized: 20 scans were performed, each with a 50 ms dwell time and a pass energy of 50 eV. To obtain accurate binding energy measurements, charge correction was implemented by referencing the C 1s peak to 284.8 eV. Additionally, an electron flood gun was used for charge neutralization during analysis.

### A.1.2.5. Vibrational spectroscopy (FT-IR and Raman)

To characterize the vibrational frequencies of LCP samples, two complementary spectroscopic techniques were employed: Fourier Transform Infrared (FT-IR) spectroscopy was conducted using Perkin Elmer Spectrum II FT-IR Spectrometer. The analysis covered a wavenumber range from 4000 to 400 $cm^{-1}$, with a high resolution of 0.5 $cm^{-1}$. This technique was specifically used to verify the presence of $Co(OH)_2$ passivation on HT-LCP samples and to identify oxygen-containing functional groups on the surface of ST-R-LCP.

Additionally, Raman spectroscopy was performed using Witec Alpha 3000 system with a laser wavelength of 514 nm. This method was employed to confirm the existence and nature of carbon layers on the surface of HT-PM-C-LCP and ST-R-LCP samples.

### A.1.2.6. Thermogravimetric analysis (TGA)

To investigate the cathode-electrolyte interphase (CEI) layer evolution of LCP electrodes during cycling and to perform a quantitative analysis of sucrose-derived reduced graphene oxide (RGO), TGA was carried out using Discovery 5500 instrument from TA Instruments. The analysis involved heating at a rate of 5 $^oC\ min^{-1}$, starting at 25 $^oC$ and increasing up to 700 $^oC$ in an air atmosphere. To achieve an adequate amount of sample, multiple cells were cycled under specific aging conditions. Following this, post-mortem analysis was conducted in Ar-filled glovebox to retrieve the LCP electrodes. These electrodes were then thoroughly cleaned by washing three times with dimethyl carbonate (DMC), dried within the glovebox, and subsequently collected for TGA analysis.

### A.1.2.7. Surface area (BET)

Sample preparation for Brunauer-Emmett-Teller (BET) analysis begins a day in advance for degassing. Initially, weigh between 0.5 to 1 g of LCP sample and transfer it into a glass container. The powder then undergoes an overnight degassing process, involving exposure to a continuous $N_2$ flow

at an elevated temperature of 120 ºC. Following the overnight degassing, measure the weight of the pure LCP sample, by subtracting the weight of the glass container. Next, carefully install the glass container including the degassed sample into the BET instrument. Once the measurement is complete, calculate the specific surface area ($m^2$ $g^{-1}$) by dividing the total surface area ($m^2$) obtained from the instrument with the weight of the pure LCP sample.

### A.1.2.8. Elemental concentration (ICP-OES and MP-AES)

Following the HT reaction, inductively coupled plasma optical emission spectrometry (ICP-OES) was utilized to quantify the concentration of remaining ions in the solution. The detailed experimental procedure is as follows: Initially, prepare a 4 % nitric acid solution in a fume hood. This involves combining 960 mL of DI water with 40 mL of nitric acid. Begin by pouring 400 mL of DI water into a container, then gradually add the 40 mL of nitric acid in multiple small portions. Use the remaining DI water to rinse the cylinder that contained the nitric acid, and add this rinse to the container. Seal the container and agitate thoroughly for further homogeneity.


**Figure A.1.9.** Volumetric flasks (10 and 25 mL) for dilution process.

For the dilution step, the goal is to reduce the ion concentration in the solution to a range of 10-1-0.1 ppm. Utilize 10 mL and 25 mL volumetric flasks (Figure A.1.9) for this process. First, add a small amount of the prepared 4 % nitric acid to each flask. Then, introduce 0.5 mL of the sample solution. Fill each flask to its calibration mark with the 4 % nitric acid solution. Seal the flasks with ParaFilm and shake vigorously to acquire homogeneous mixing.

To assess the Co/P ratio in electrodes subjected to various cycling-aging conditions, a thorough post-mortem analysis was conducted. The process began with collecting LCP electrodes from disassembled cells (Figure A.1.10a). These electrodes were immersed in ethanol and underwent a three-hour sonication treatment to separate the LCP material from other electrode components such as acetylene black and polyvinylidene fluoride (PVDF) binder (Figure A.1.10b). Following sonication, the LCP powder was isolated through centrifugation (Figure A.1.10c). The isolated LCP powder then underwent a digestion process using nitric acid, resulting in a solution. Subsequently, this digested solution was diluted following the previously described protocol for ICP-OES analysis.

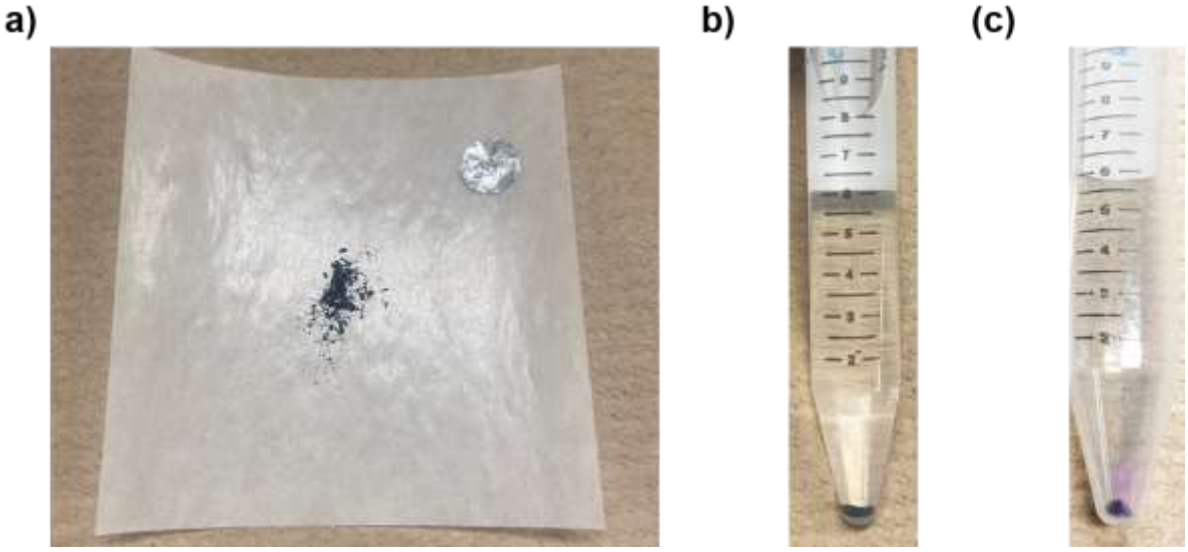


**Figure A.1.10.** (a) Collected electrode from Al current collector, (b) before and (c) after undergoing the separation process via sonication and centrifuge with ethanol.

## A.2. Supplementary Information – Chapter 3

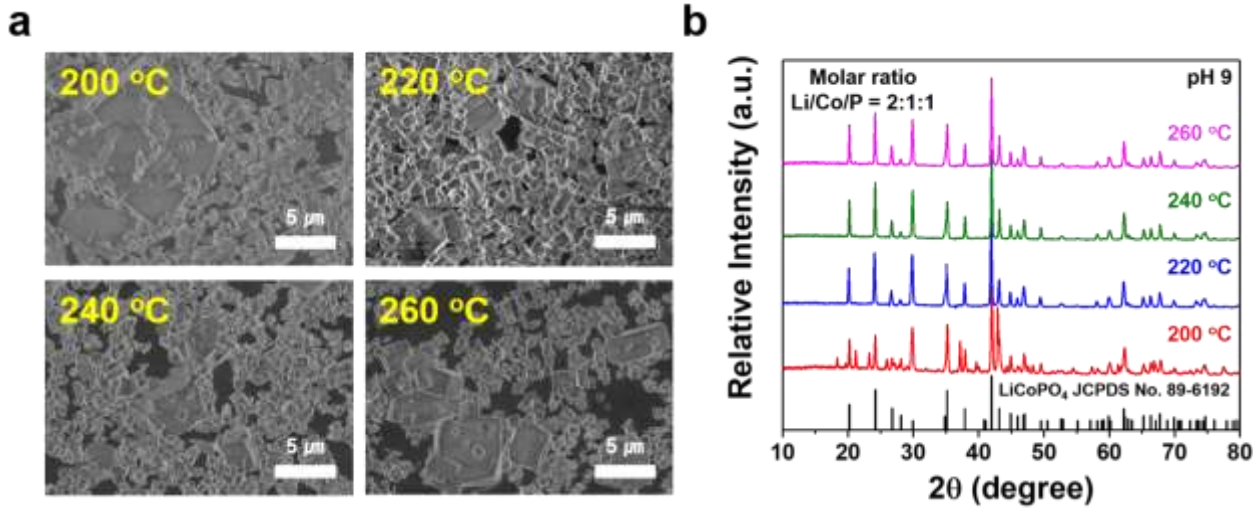


**Figure A.2.1.** Morphology and phase characterizations of hydrothermally synthesized LCP (HT-LCP) samples for 6 hours at different temperatures via (a) SEM and (b) XRD. (The concentration of $CoSO_4$ and $H_3PO_4$ is fixed at 0.4 M).

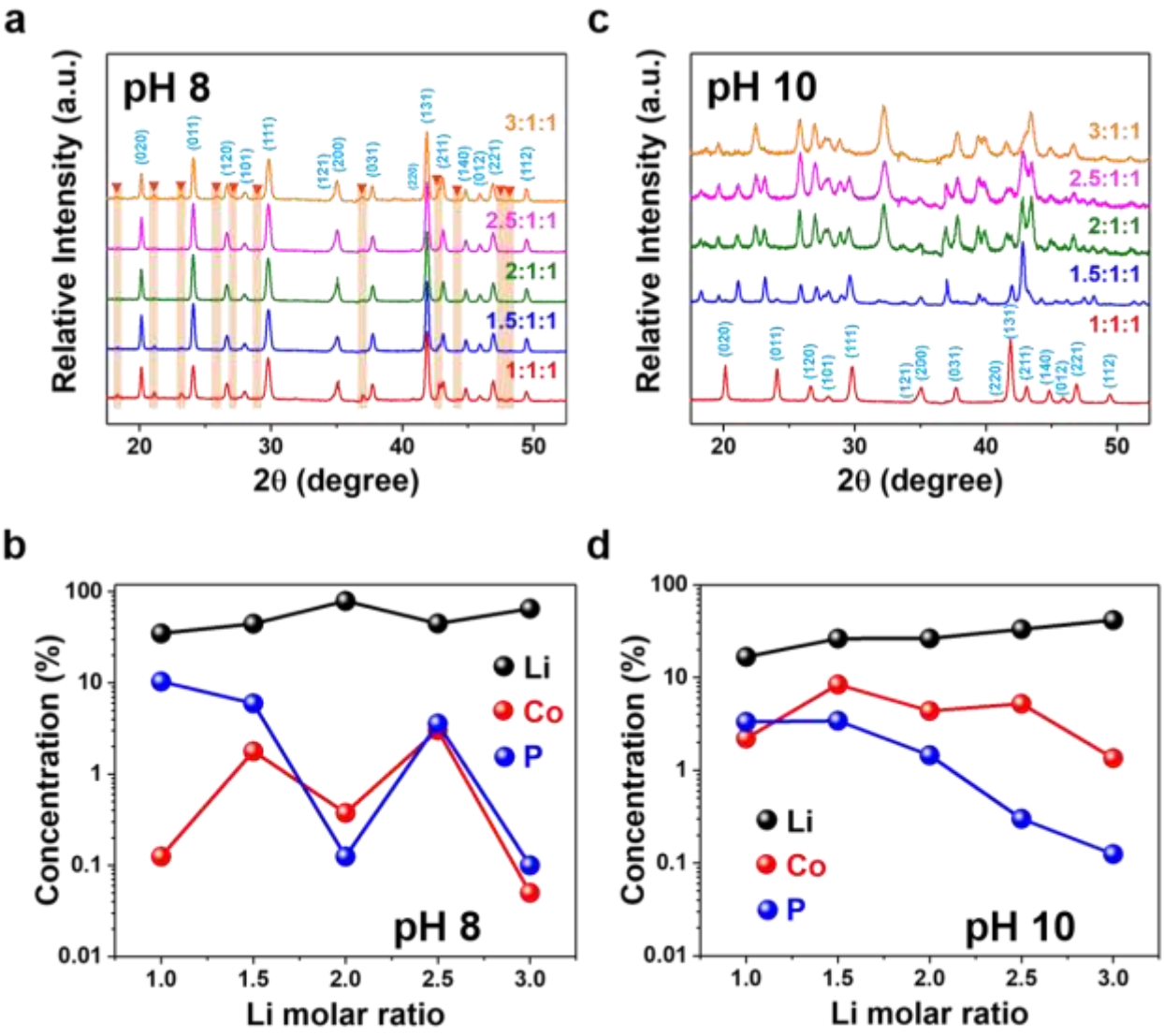


**Figure A.2.2.** Phase and elemental comparison of HT-LCP samples from the precursor solutions with different Li/Co/P molar ratio at (a-b) pH 8 and (c-d) 10 (The concentration of $CoSO_4$ and $H_3PO_4$ isfixed at 0.4 M).

**Table A.2.1** pH value variations before and after HT-synthesis.

| | pH 8 | | pH 9 | | pH 10 | |
|---|---|---|---|---|---|---|
| **Li/Co/P Molar ratio** | **Before** | **After** | **Before** | **After** | **Before** | **After** |
| 1:1:1 | 8 | 6.1 | 9 | 9.17 | 10 | 10 |
| 1.5:1:1 | 8 | 5.04 | 9 | 9.1 | 10 | 10.14 |
| 2:1:1 | 8 | 4.97 | 9 | 9.07 | 10 | 10.16 |
| 2.5:1:1 | 8 | 6.26 | 9 | 9.38 | 10 | 9.96 |
| 3:1:1 | 8 | 8.75 | 9 | 9.36 | 10 | 10 |

**(The concentration of $CoSO_4$ and $H_3PO_4$ is fixed at 0.4 M)**

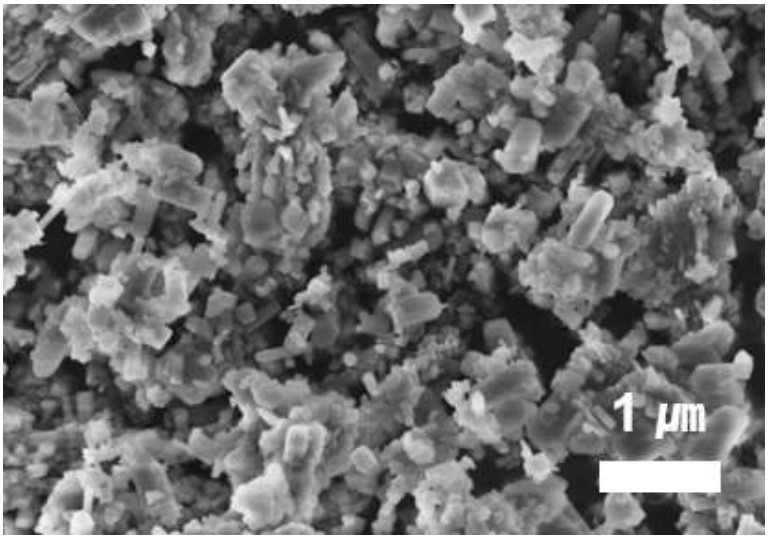


**Figure A.2.3.** Morphology of LCP nanocrystals from the precursor solutions with the stoichiometric ratio 1:1:1 (Li:Co:P) at pH 10.

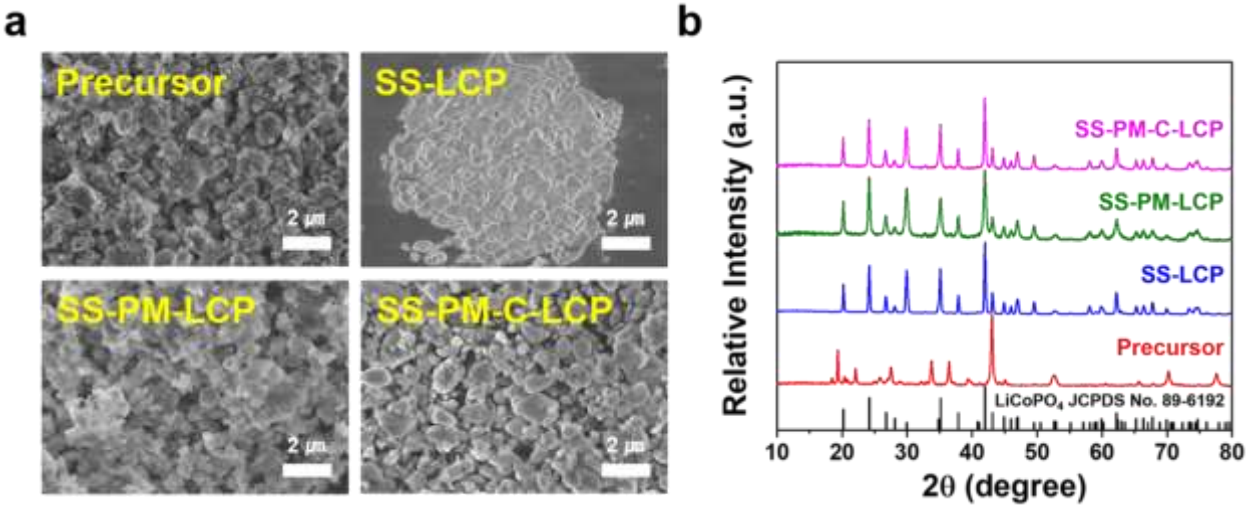


**Figure A.2.4.** Morphology and phase characterizations of LCP samples obtained by solid-state reaction (SS-LCP) and post-synthesis treatments (SS-PM-LCP and SS-PM-C-LCP) via (a) SEM and (b) XRD.

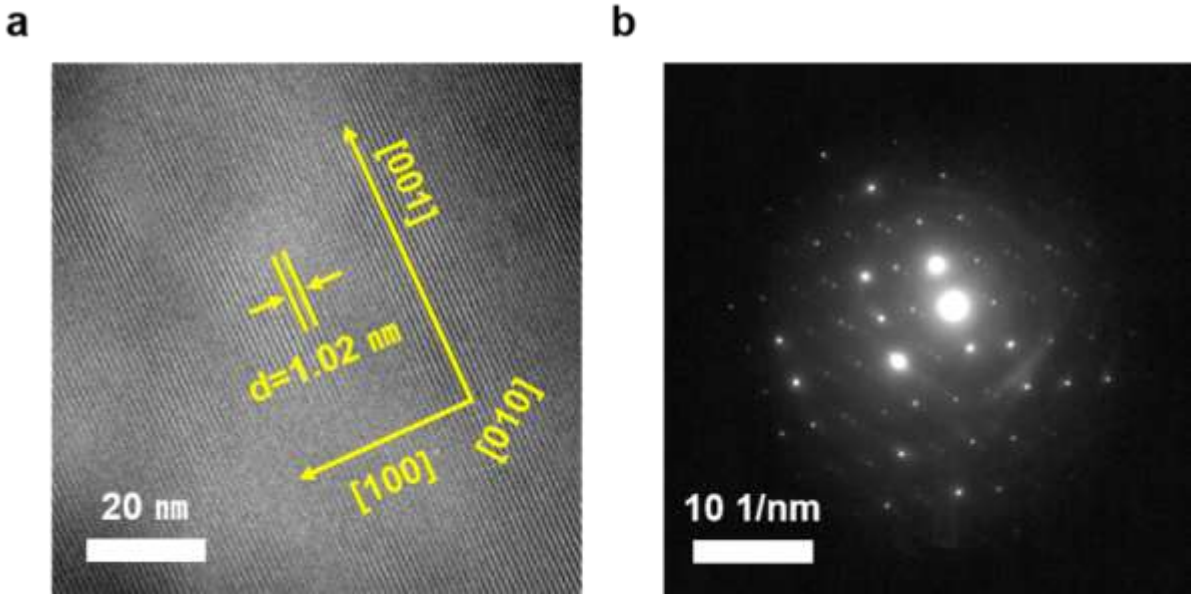


**Figure A.2.5.** (a) HRTEM and (b) SAED pattern of HT-LCP.

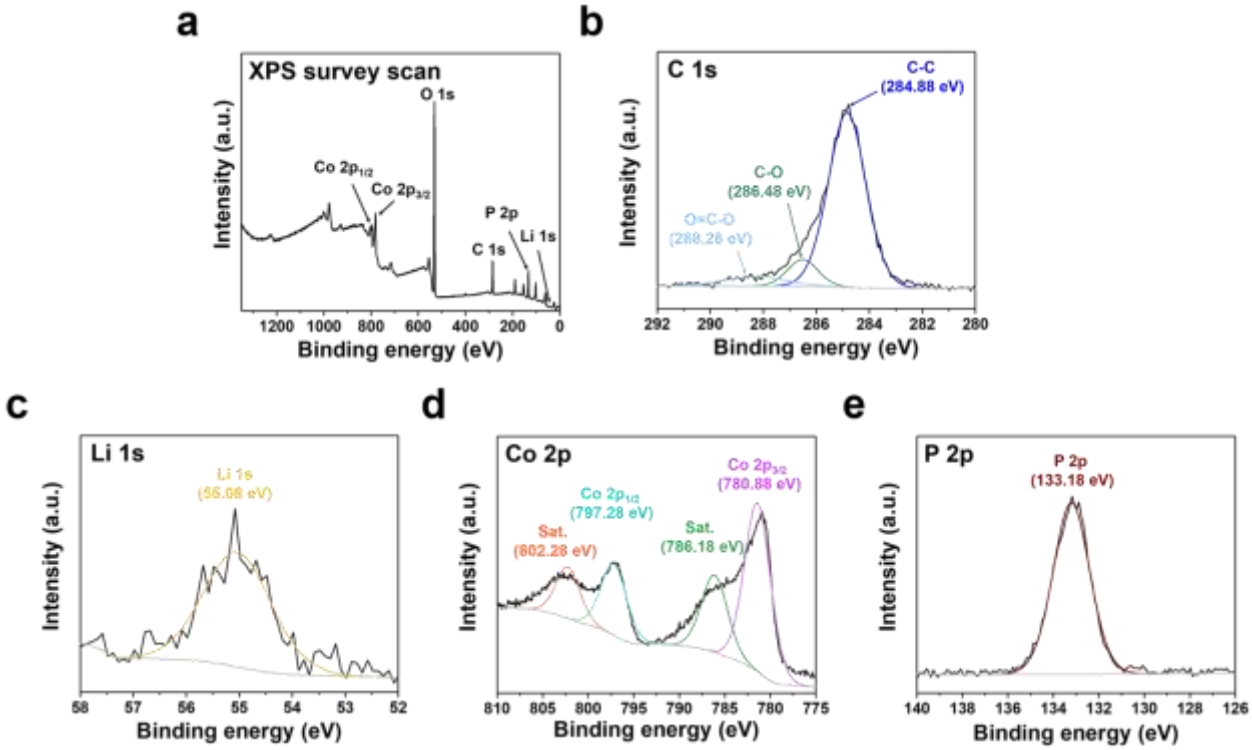


**Figure A.2.6.** XPS spectra of HT-LCP: (a) Survey scan, (b) C 1s spectrum, (c) Li 1s spectrum, (d) Co 2p spectrum, and (e) P 2p spectrum.

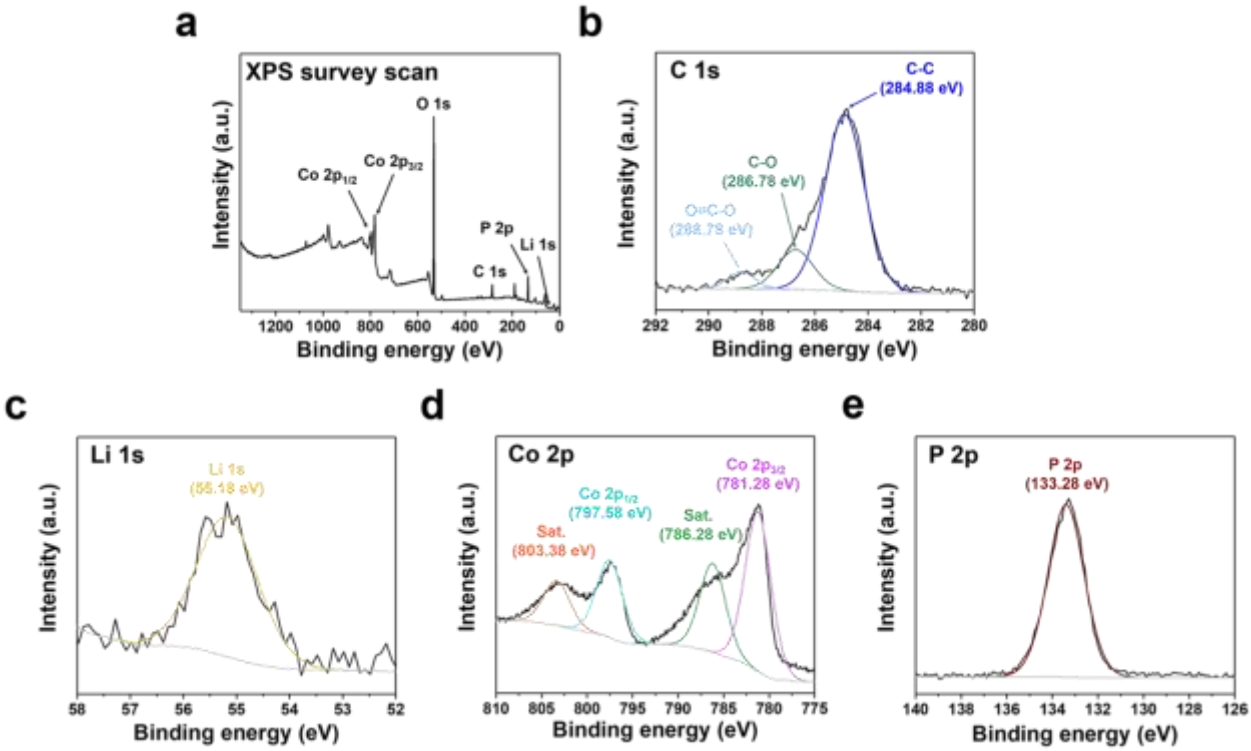


**Figure A.2.7.** XPS spectra of SS-LCP: (a) Survey scan, (b) C 1s spectrum, (c) Li 1s spectrum, (d) Co 2p spectrum, and (e) P 2p spectrum.

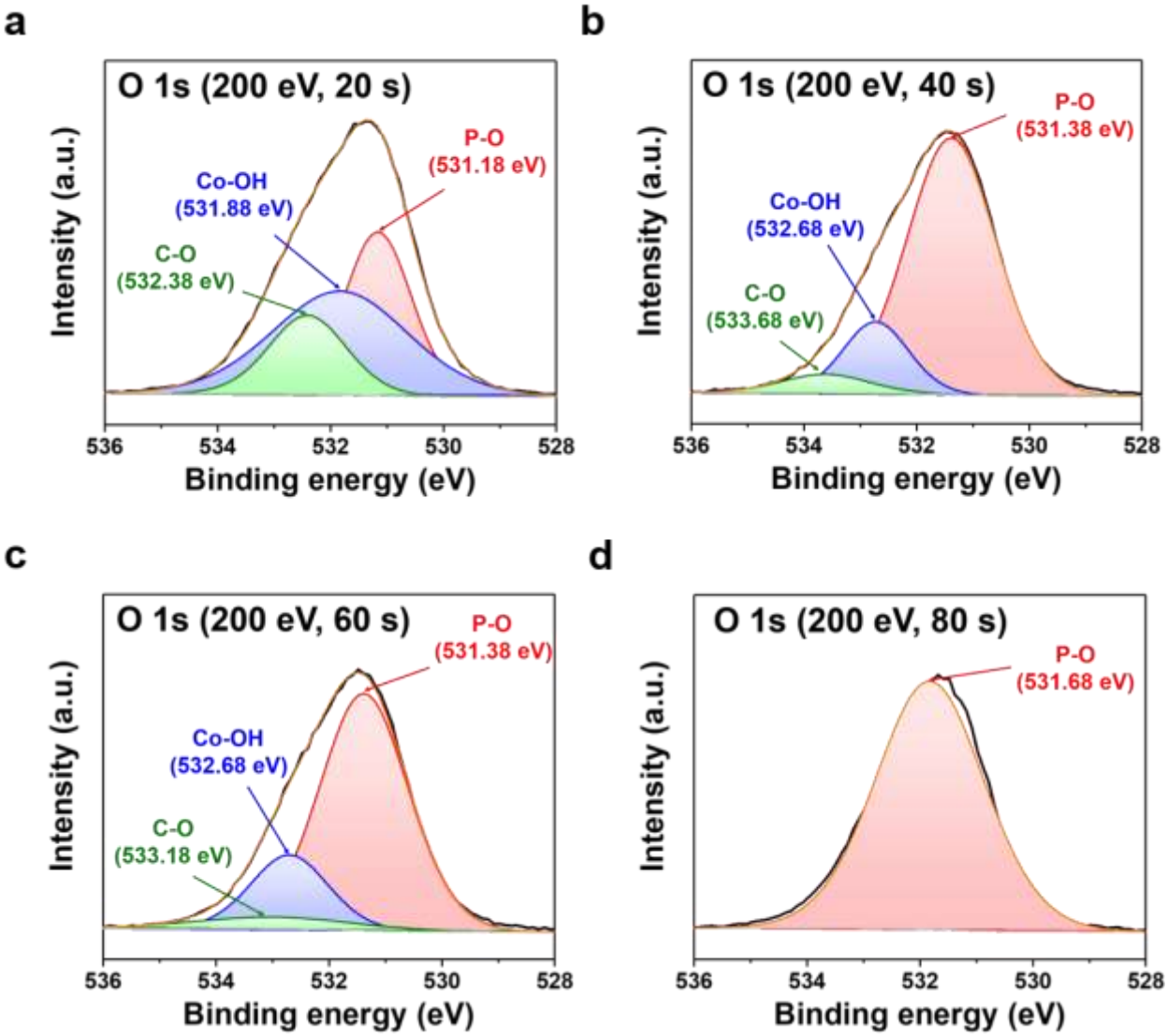


**Figure A.2.8.** XPS depth profile (O 1s) of HT-LCP with 200 eV laser for (a) 20 seconds, (b) 40 seconds, (c) 60 seconds and (d) 80 seconds.

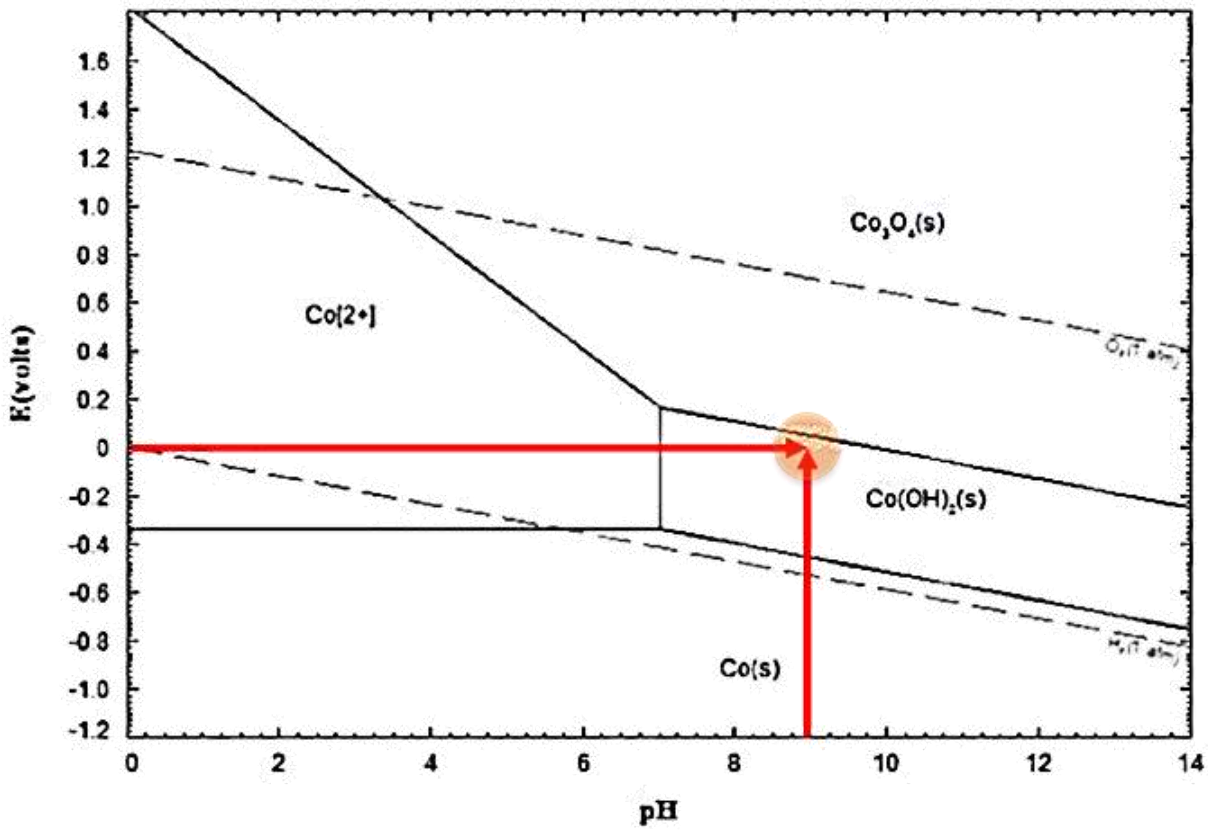


**Figure A.2.9.** Pourbaix diagram of cobalt (Co-$H_2O$ at 298.15 K, 0.01 M).[1]

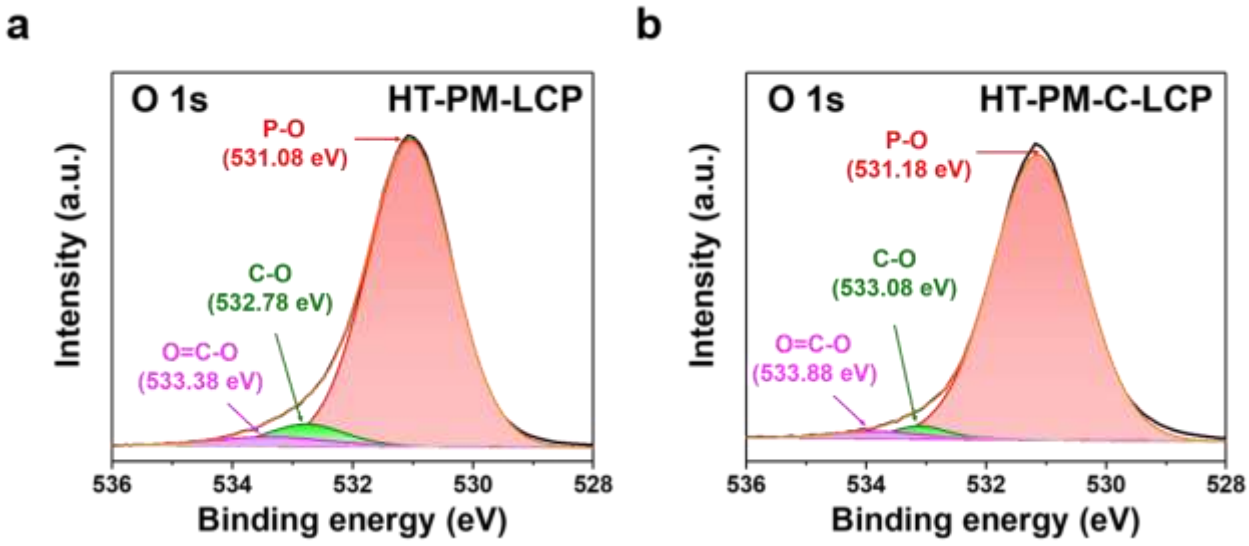


**Figure A.2.10.** XPS O 1s spectra of (a) HT-PM-LCP, and (b) HT-PM-C-LCP.

a

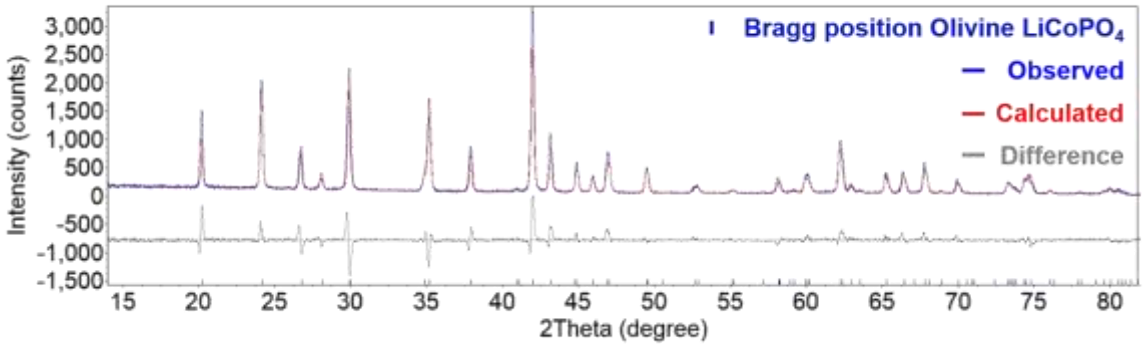
Bragg position Olivine LiCoPO4
Observed
Calculated
Difference
Intensity (counts)
2Theta (degree)

b

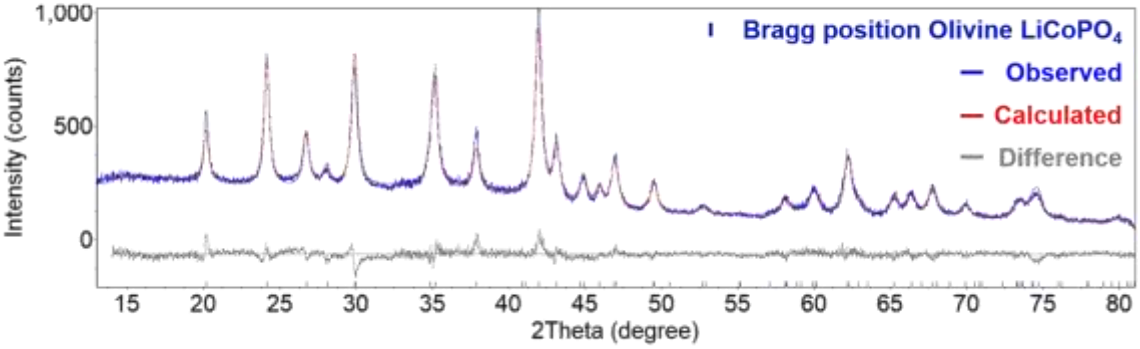
Bragg position Olivine LiCoPO4
Observed
Calculated
Difference
Intensity (counts)
2Theta (degree)

c

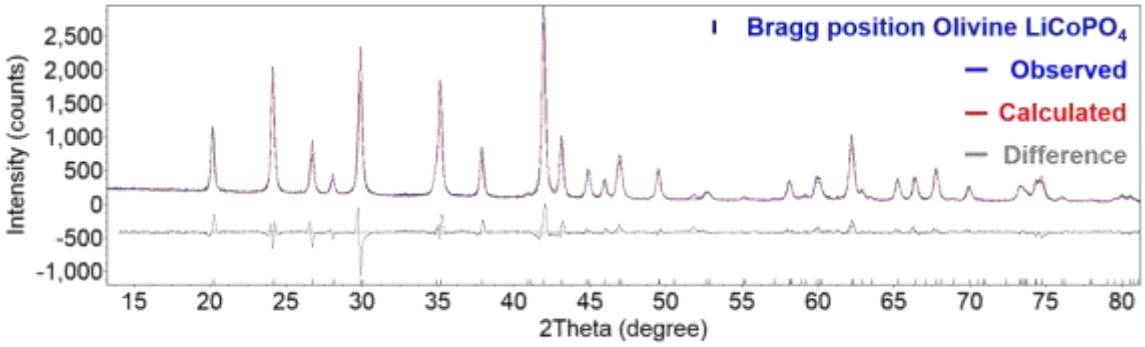
Bragg position Olivine LiCoPO4
Observed
Calculated
Difference
Intensity (counts)
2Theta (degree)

d

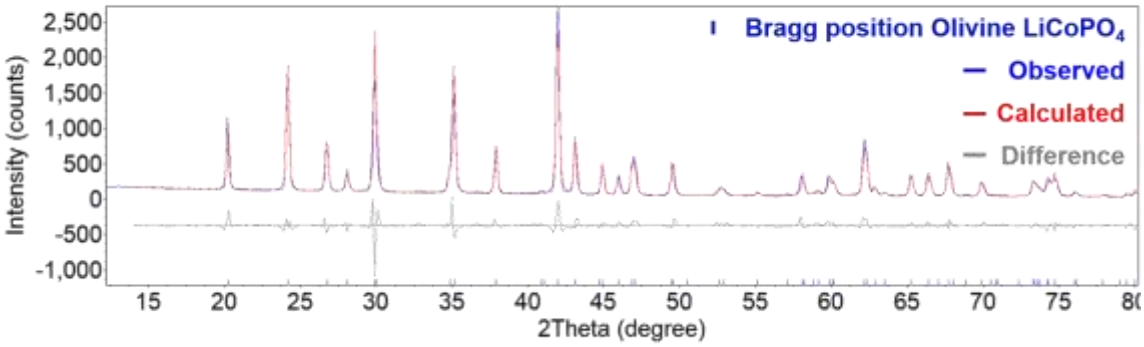
Bragg position Olivine LiCoPO4
Observed
Calculated
Difference
Intensity (counts)
2Theta (degree)

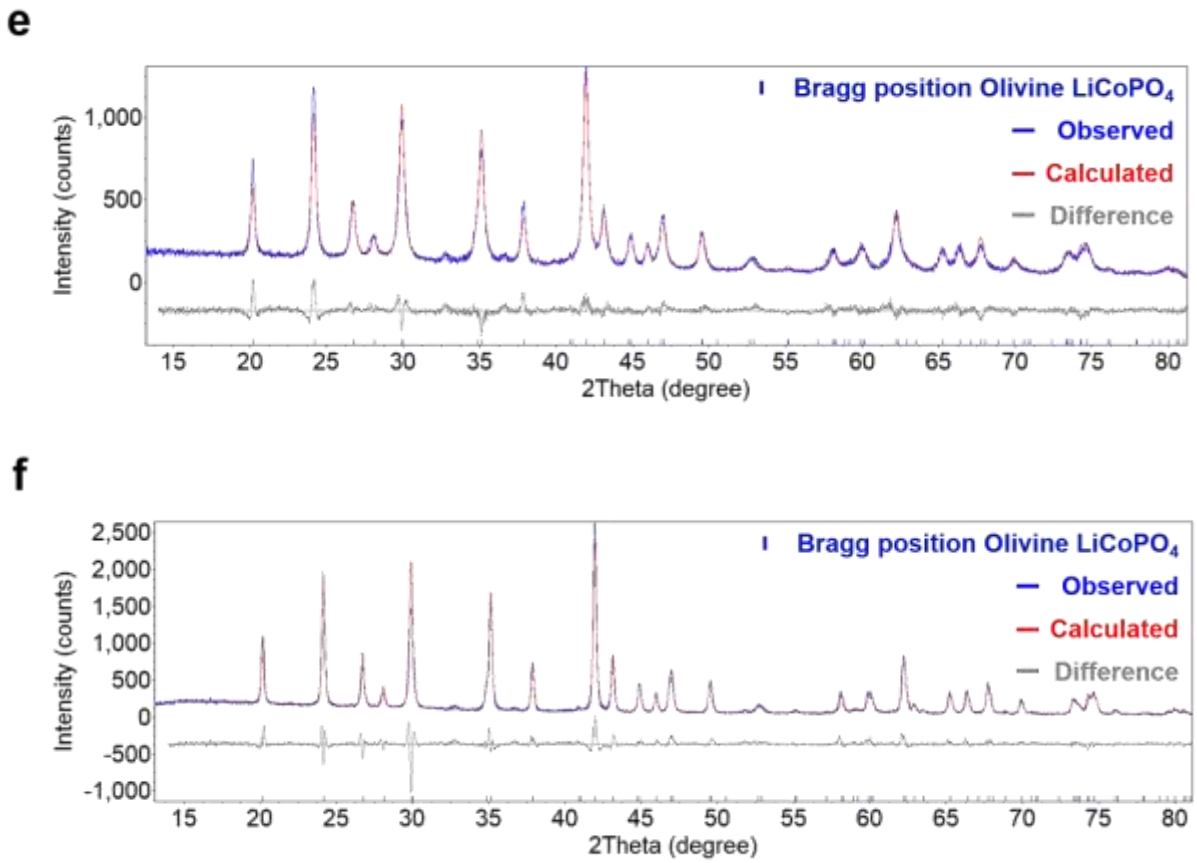


**Figure A.2.11.** XRD Rietveld refinement of HT-LCP and SS-LCP samples: (a) HT-LCP, (b) HT-PM-LCP, (c) HT-PM-C-LCP, (d) SS-LCP, (e) SS-PM-LCP, and (f) SS-PM-C-LCP.

**Reference A.2**

1. P. Meshram, U. Prakash, L. Bhagat, Abhilash, H. Zhao, E. D. V. Hullebusch, Processing of waste copper converter slag using organic acids for extraction of copper, nickel, and cobalt. *Minerals* **2020**, *10* (3), 290.

### A.3. Supplementary Information – Chapter 4

# Additional information on synthesis procedure

The detailed experimental procedure for the precursor solution preparation is as follows:

First, lithium hydroxide monohydrate, cobalt sulfate heptahydrate, and L-Ascorbic acid are initially added into a volumetric flask. Subsequently, 150 mL of ethylene glycol (EG) is poured into the flask as the solvent. After that, under continuous magnetic stirring, phosphoric acid in liquid form–serving as the phosphate source–is poured into the mixture, causing the pH to shift to acidic region. To restore the pH to an alkaline level, ammonium hydroxide solution is added in a controlled manner. Initially, a certain amount (e.g., 1 mL or 0.5 mL) is introduced, and sufficient time is allowed for the pH to stabilize. Additional increments of ammonium hydroxide solution are introduced only after observing the stabilization of the pH value. This step is repeated iteratively until the target pH value is reached. Once achieved, additional EG is poured into the flask to adjust the final volume to 200 mL.

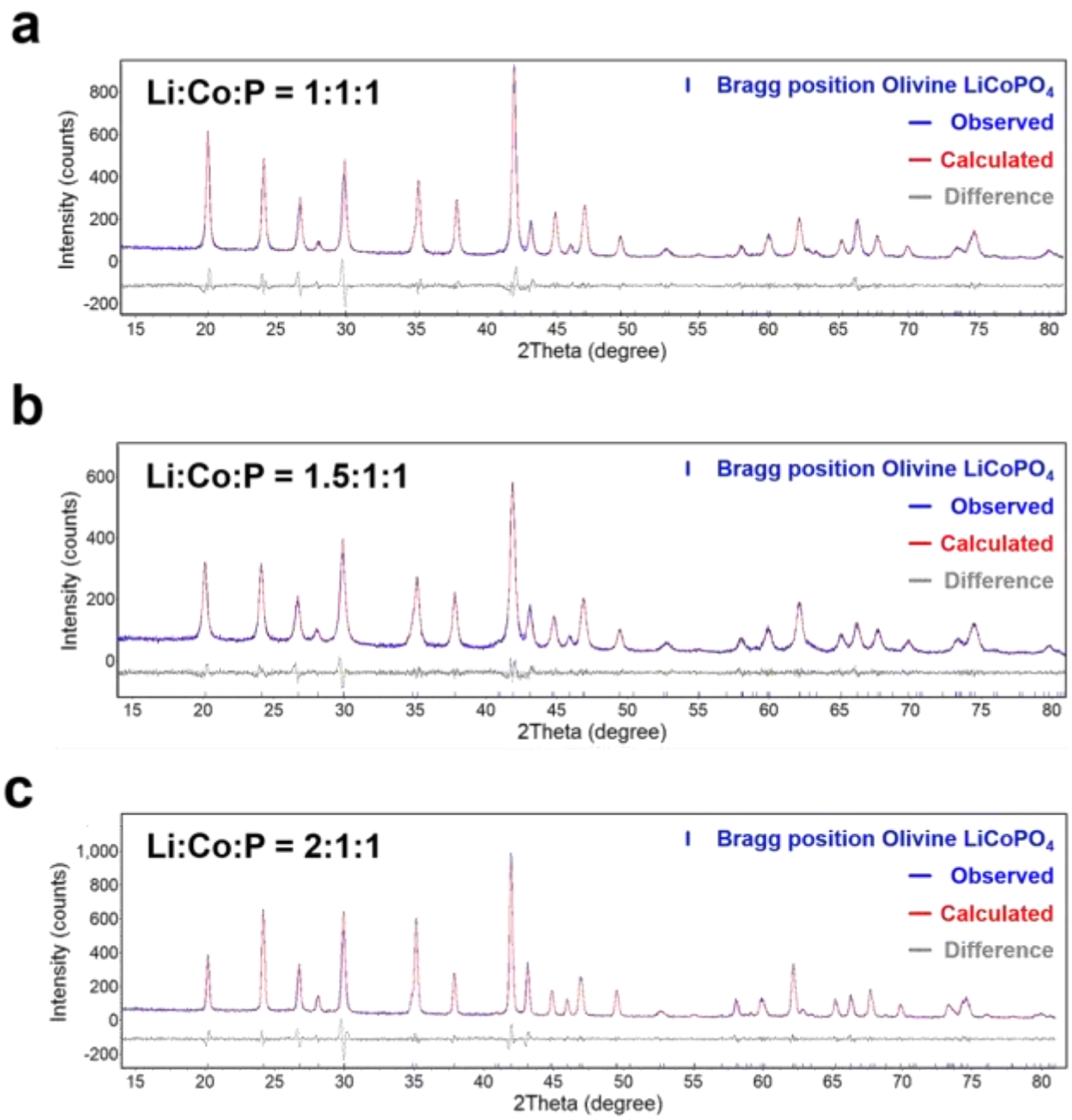


**Figure A.3.1.** Rietveld refinement results of LCP samples–obtained by ST synthesis at different Li contents–based on XRD patterns.

**Table A.3.1.** Refined XRD data for LCP samples via ST synthesis at different Li conent.

| **Li:Co:P Molar ratio** | **1:1:1** | **1.5:1:1** | **2:1:1** |
|---|---|---|---|
| *a* (Å) | 10.2217892 | 10.2001787 | 10.1955701 |
| *b* (Å) | 5.9254670 | 5.9209470 | 5.9184287 |
| *c* (Å) | 4.7084540 | 4.7033751 | 4.7017851 |
| Unit cell volume ($Å^3$) | 285.19 | 284.06 | 283.71 |
| Grain size (nm) | 32.3 | 45.3 | 63.5 |
| Anti-site defect concentration (%) | 4.329 | 1.029 | 0.8554 |
| $R_{wp}$ (%) | 7.117 | 10.511 | 11.986 |

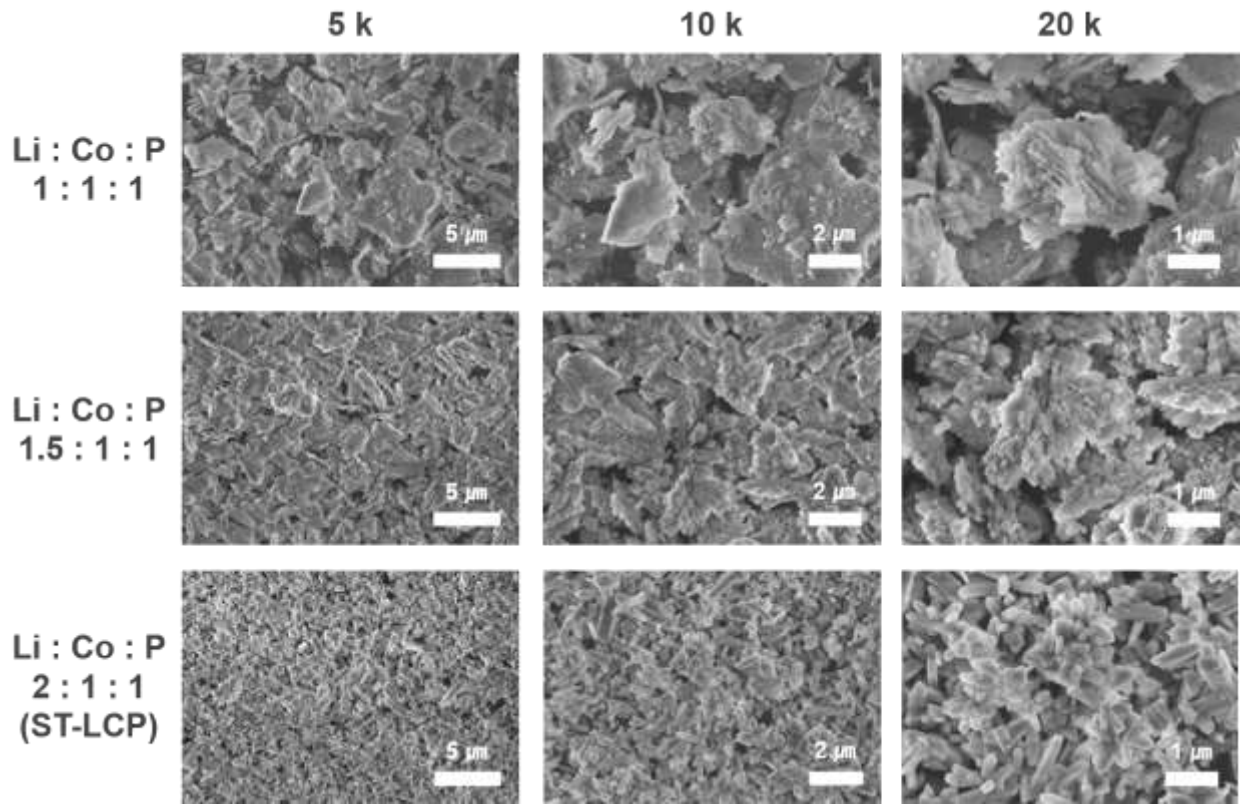


**Figure A.3.2.** Morphology of LCP samples via ST synthesis obtained with different Li molar ratio of 1:1:1, 1.5:1:1, and 2:1:1 (The concentration of $CoSO_4$ and $H_3PO_4$ is fixed at 0.4 M).

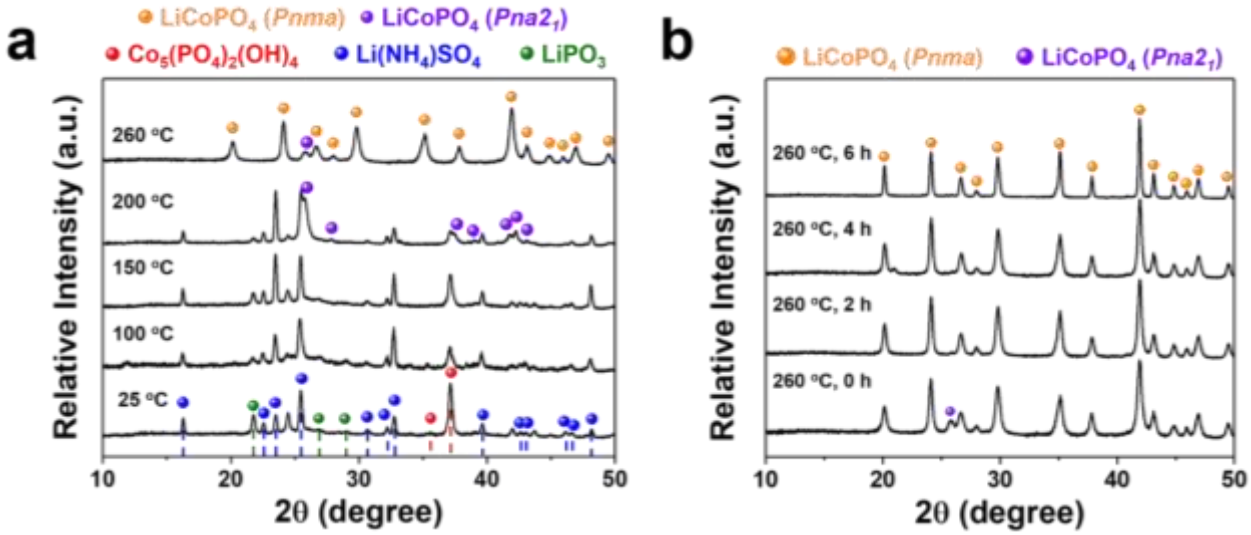


**Figure A.3.3.** XRD patterns of solvothermal precipitate collected under pressure at (a) increasing temperature and (b) reaction time.

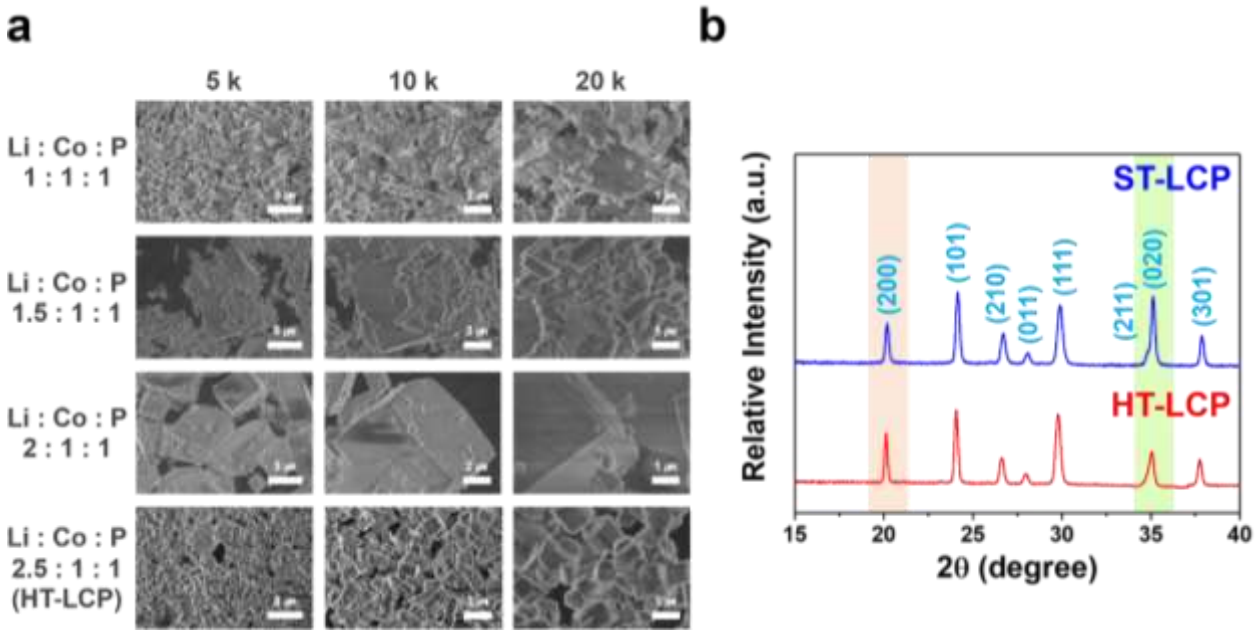


**Figure A.3.4.** (a) Morphology of LCP samples via HT synthesis obtained with different Li molar ratios of 1:1:1, 1.5:1:1, 2:1:1, and 2.5:1:1 (The concentration of $CoSO_4$ and $H_3PO_4$ is fixed at 0.4 M); (b) comparison of XRD patterns of isotropically grown HT-LCP and anisotropically grown ST-LCP.

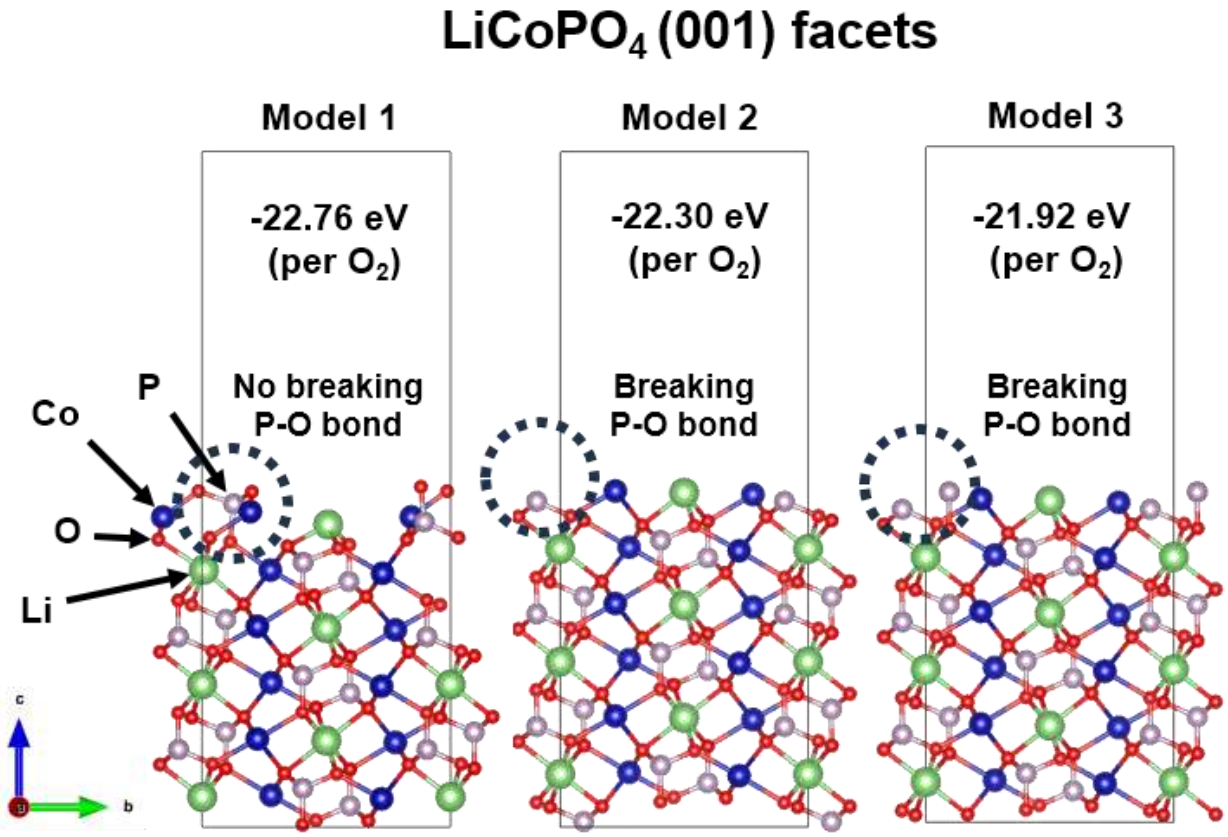


**Figure A.3.5.** Three different surface configurations of LCP (001) facets and their corresponding surface energies.

We have referred to the surface configurations of LCP (100), (010), and (001) proposed in a recent study by Wu et al., which identified the most energetically favorable terminations for these facets using DFT calculations.[1] The study highlights the importance of maintaining surface stoichiometry consistent with the bulk structure, i.e., avoiding the breaking of highly covalent P–O bonds in the $PO_4$ tetrahedra. This constraint significantly limits the range of viable surface termination candidates. As an example, we compared the surface energies of three slab models for the (001) facet of LCP with different surface configurations (refer to Figure A.3.5):

1. **Model 1**: P–O terminated surface (without breaking P–O bonds).
2. **Model 2**: Co–O and Li–O terminated surface (with P–O bonds broken).
3. **Model 3**: P–O terminated surface (with P–O bonds broken).

The calculated surface energies (per $O_2$) for models 1, 2, and 3 were -22.76 eV, -22.30 eV, and -21.92 eV, respectively. These results demonstrate that breaking P–O bonds significantly reduce surface stability, thereby limiting the range of viable surface termination candidates.

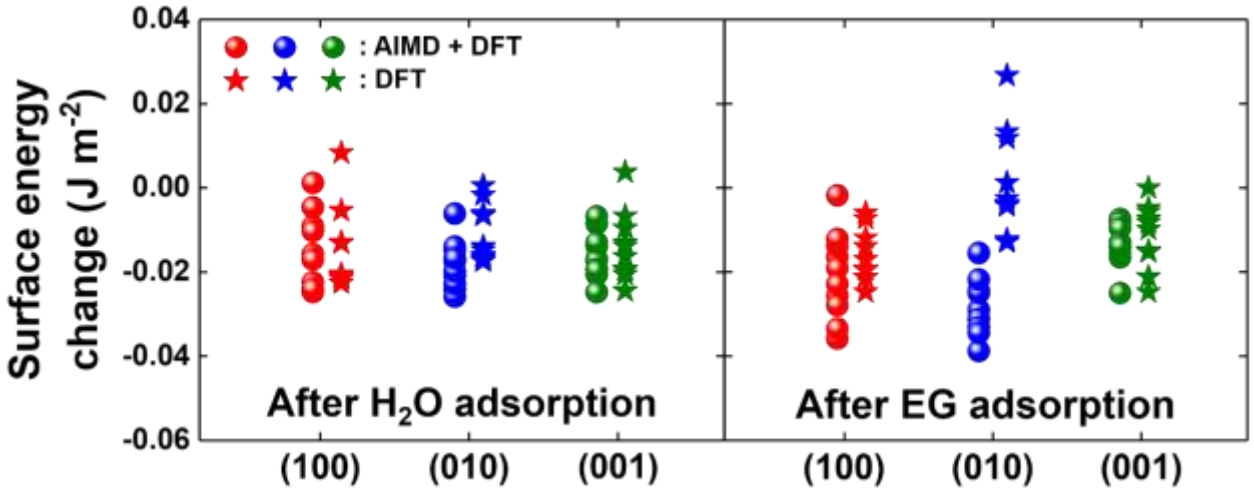


**Figure A.3.6.** Calculated surface energy change ($\Delta\gamma$) after the single-molecule adsorption of $H_2O$ and EG on the LCP (100), (010), and (001) facets.

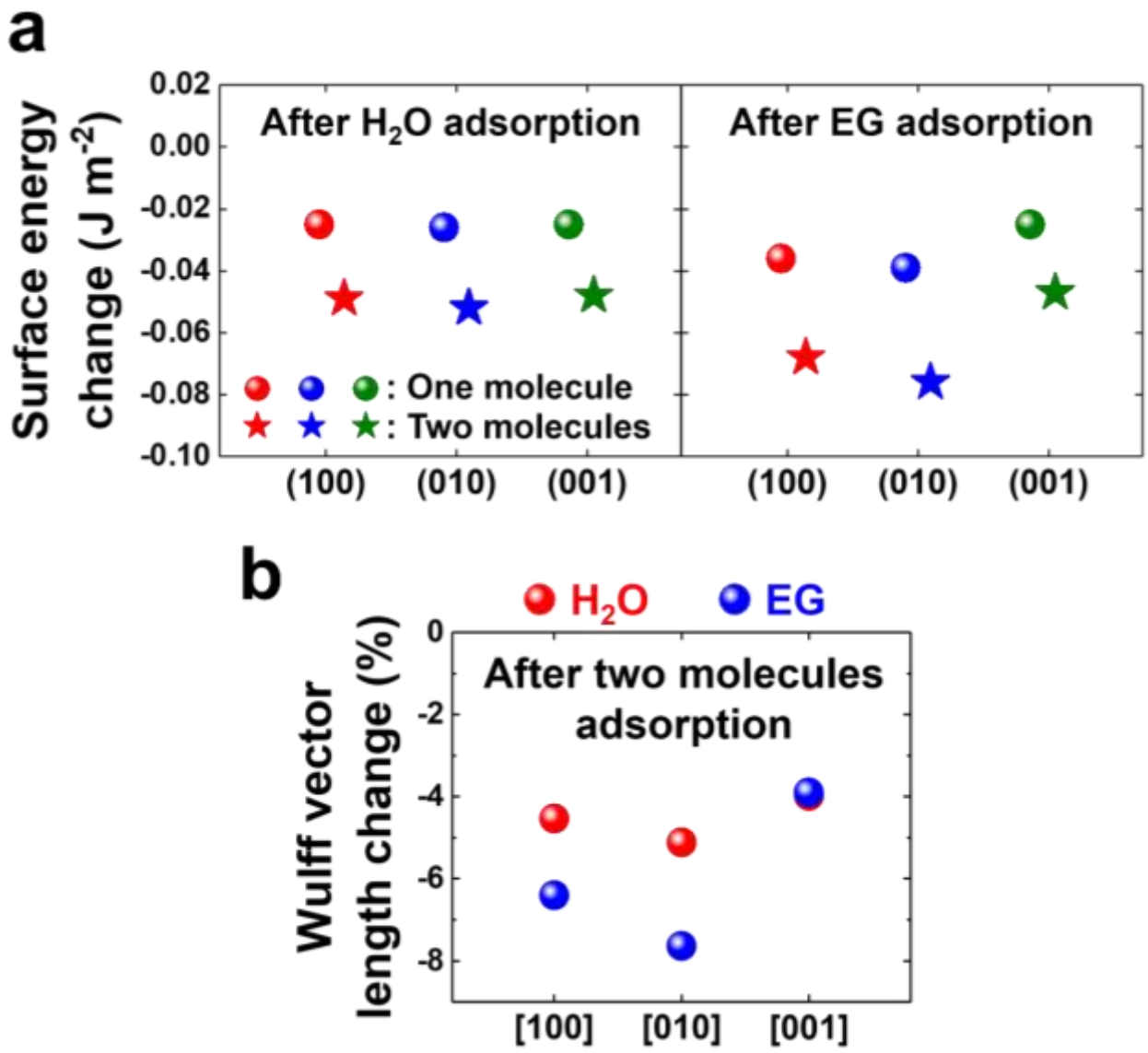


**Figure A.3.7.** (a) Calculated surface energy change ($\Delta\gamma$) of the LCP (100), (010), (001) facets after the adsorption of one or two molecules of $H_2O$ and EG; (b) Wulff vector length changes after the adsorption of two molecules of $H_2O$ and EG.

Additionally, we calculated both the surface energy change ($\Delta\gamma$) and the variation in Wulff vector lengths when two $H_2O$ or EG molecules adsorb on the (100), (010), and (001) facets of LCP (as shown in Figure A.3.7a). These results were systematically compared with those obtained for the adsorption of a single molecule. The configurations for two-molecule adsorption were carefully designed based on the most stable adsorption configuration of a single molecule on LCP (100), (010), and (001) facets. To minimize the influence of intermolecular interactions, particularly for EG due to its larger size and more complex structure than $H_2O$, our calculations were limited to two adsorbed molecules per facet.

When the number of $H_2O$ molecules increased from one to two, $\Delta\gamma$ increased from -0.025 J $m^{-2}$ to -0.049 J $m^{-2}$ on the (100) facet, from -0.026 J $m^{-2}$ to -0.052 J $m^{-2}$ on the (010) facet, and from -0.025 J $m^{-2}$ to -0.048 J $m^{-2}$ on the (001) facet. Similarly, for EG, $\Delta\gamma$ decreased from -0.036 J $m^{-2}$ to -0.068 J $m^{-2}$ on the (100) facet, from -0.039 J $m^{-2}$ to -0.076 J $m^{-2}$ on the (010) facet, and from -0.025 J $m^{-2}$ to -0.047 J $m^{-2}$ on the (001) facet. As a result, the difference in surface energy increases as the number of adsorbed molecules increases from one to two. For example, for EG system, the surface energy difference between the LCP (010) and (001) facets increased from 0.014 J $m^{-2}$ (-0.039 J $m^{-2}$ vs -0.025 J $m^{-2}$) for single-molecule system to 0.029 J $m^{-2}$ (-0.076 J $m^{-2}$ vs - 0.047 J $m^{-2}$) for two-molecule system.

When comparing Wulff vector length changes (displayed in Figure A.3.7b), the adsorption of two EG molecules resulted in reductions of -6.40 % and -7.65 % along the [100] and [010] axes, respectively. In contrast, the adsorption of two $H_2O$ molecules caused smaller reductions of -4.53 % and -5.11 % along the same axes. For single-molecule adsorption, EG caused decreases of -3.29 % and -3.78 % along the [100] and [010] axes, respectively, while $H_2O$ caused decreases of only -2.26 % and -2.49 %. On the other hand, the Wulff vector length along the [001] axis decreased by -3.90 and -3.98 % after the adsorption of EG and $H_2O$, correspondingly. Consequently, the difference for Wulff vector lengths increases with the adsorption of two molecules compared to the single-molecule system. For example, the Wulff vector lengths difference along [010] axe increased from 1.29 % (-3.78 % vs -2.49 %) for single-molecule system to 2.54 % (-7.65 % vs -5.11 %) for two-molecule system.

Although accurately replicating the experimentally observed changes in crystal shape through simple calculations of single- or two-molecule adsorption is challenging, our computational results still confirm the trend that EG promotes more anisotropic growth than $H_2O$ as more EG molecules adsorb on LCP facets compared to $H_2O$ molecules.

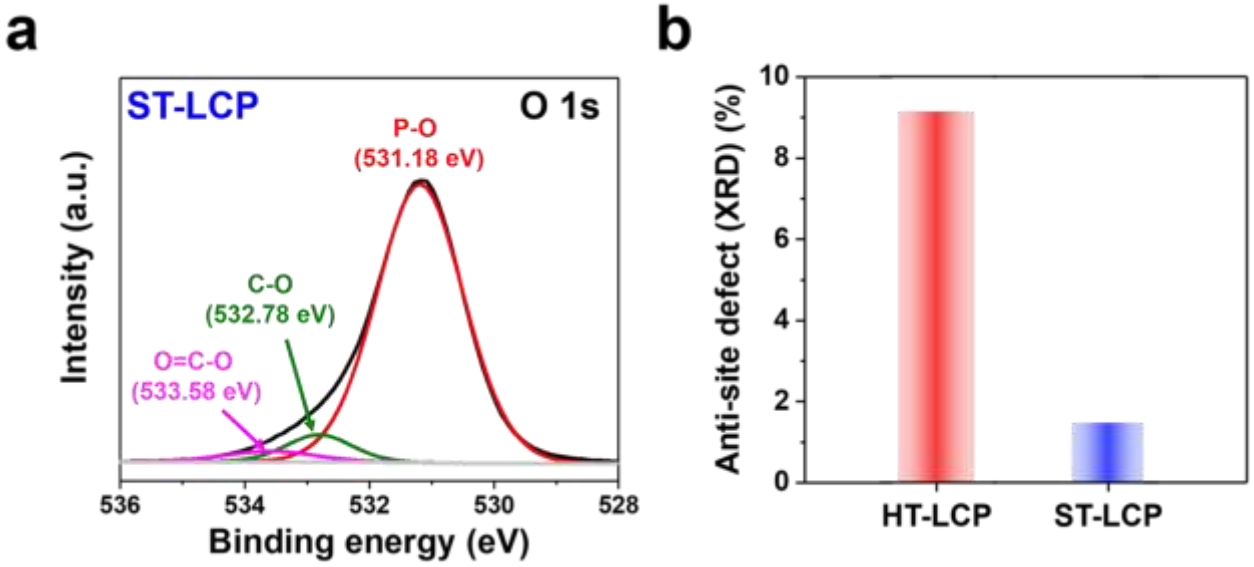


**Figure A.3.8.** (a) XPS O 1s spectra of ST-LCP and (b) anti-site defect concentration of HT-LCP and ST-LCP.

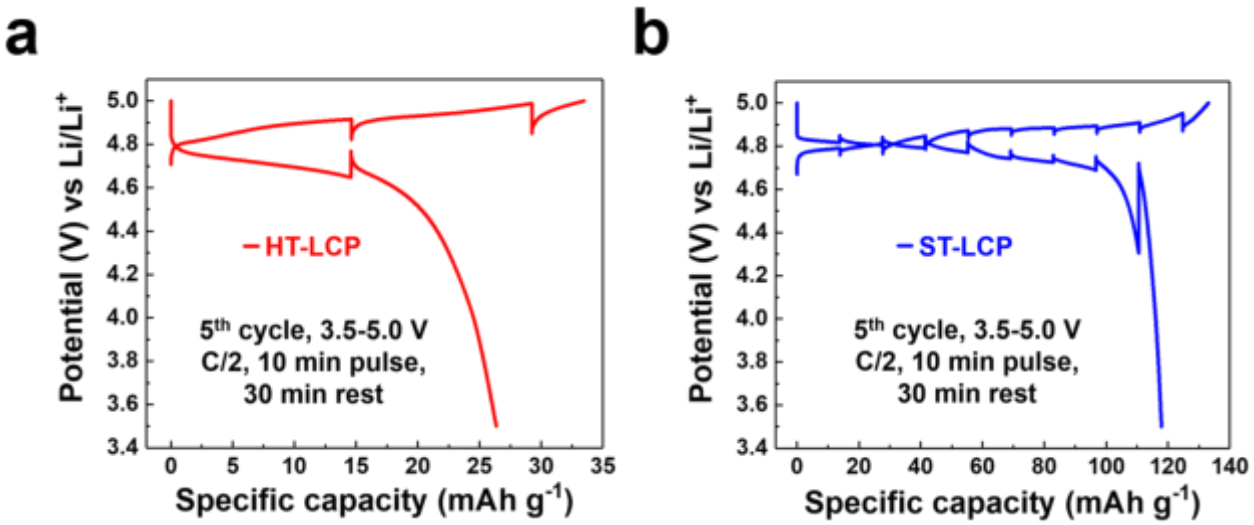


**Figure A.3.9.** Voltage profiles of (a) HT-LCP and (b) ST-LCP as a function of the specific capacity upon charge and discharge.

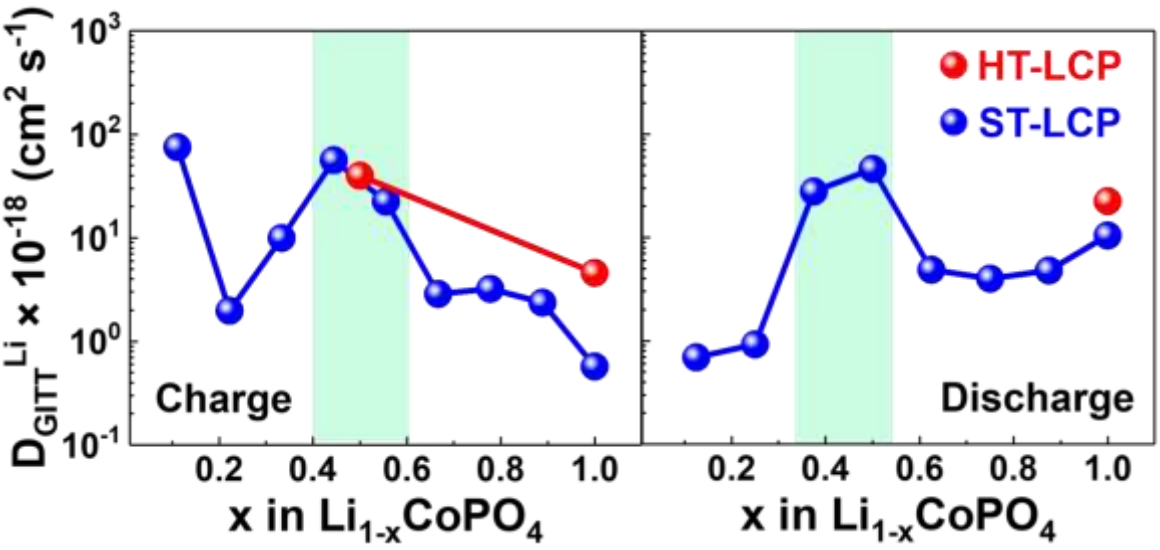


**Figure A.3.10.** Li-ion diffusion coefficient of HT-LCP and ST-LCP upon (a) charge and (b) discharge.

Li-ion diffusion coefficient extracted from the voltage relaxation profiles of both HT-LCP and ST-LCP is presented as a function of the degree of Li-ion storage upon cycling. It is well-established that Li-ion diffusion coefficient ($D_{GITT}{}^{Li}$) in solid phase is calculated by the following formula for non-spherical particles,

$$D_{GITT}{}^{Li} = \frac{4}{\pi\tau}\left(\frac{n_M V_M}{S}\right)^2\left(\frac{\Delta V_s}{\Delta V_t}\right)^2 \quad \text{(S1)}$$

where $n_M$ and $V_M$ are the number of mole (mol) and molar volume ($cm^3$ $mol^{-1}$) of active material, respectively, $S$ is the cell interfacial area ($cm^2$), and $\tau$ is the time duration (s) of the pulse.[2, 3]

Notably, three distinct regions of Li-ion diffusion coefficients in ST-LCP as a function of Li content are clearly observed. $D_{GITT}{}^{Li}$ is seen to be ~$10^{-18}$ $cm^2$ $s^{-1}$ at fully lithiated state increasing to near $10^{-16}$ $cm^2$ $s^{-1}$ at nearly 50 % Li content decreasing with further delithiation between $10^{-18}$ and $10^{-16}$ $cm^2$ $s^{-1}$. We postulate that the middle region relates to the intermediate phase, $Li_{2/3}(Co^{2+})_{2/3}(Co^{3+})_{1/3}PO_4$, which is known to exist experimentally and theoretically only in Olivine system with Co rather than other polyanionic compounds such as LFP.[4-6] In particular, this tendency aligns with the outcomes of rising mass transfer overpotential induced by the phase boundary interface that occurs throughout the phase transition process upon the Li-ion intercalation process.[6] In turn, larger activation energy is required in a process that deviates from the defined states to drive the energetically unfavorable Li-ion diffusion resulting in almost two orders of magnitude lowered Li-ion diffusion coefficient values.

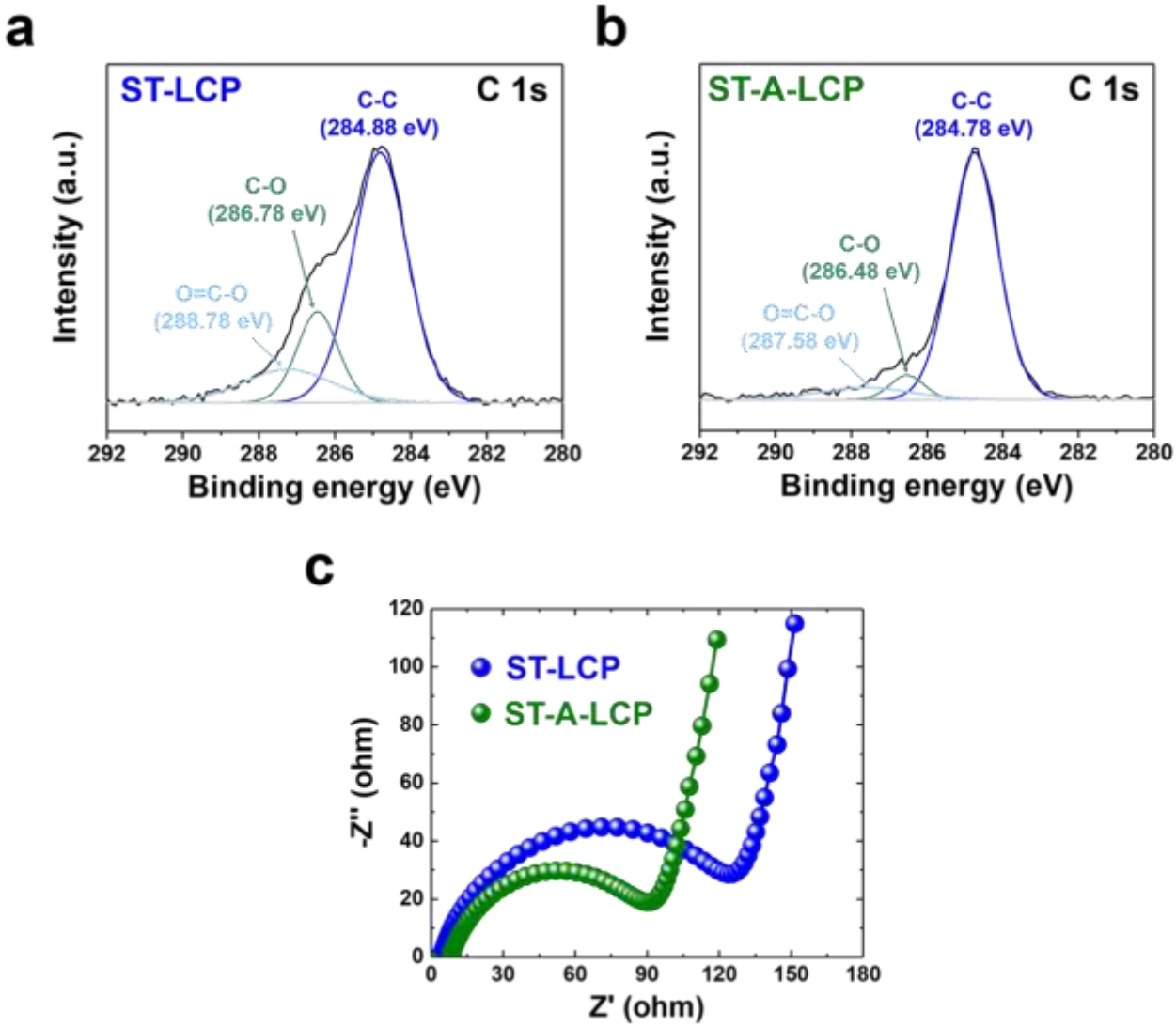


**Figure A.3.11**. (a-b) XPS C 1s spectra of pristine ST-LCP and ST-A-LCP powder and (c) Nyquist plots of pristine ST-LCP and ST-A-LCP electrodes before cycling test.

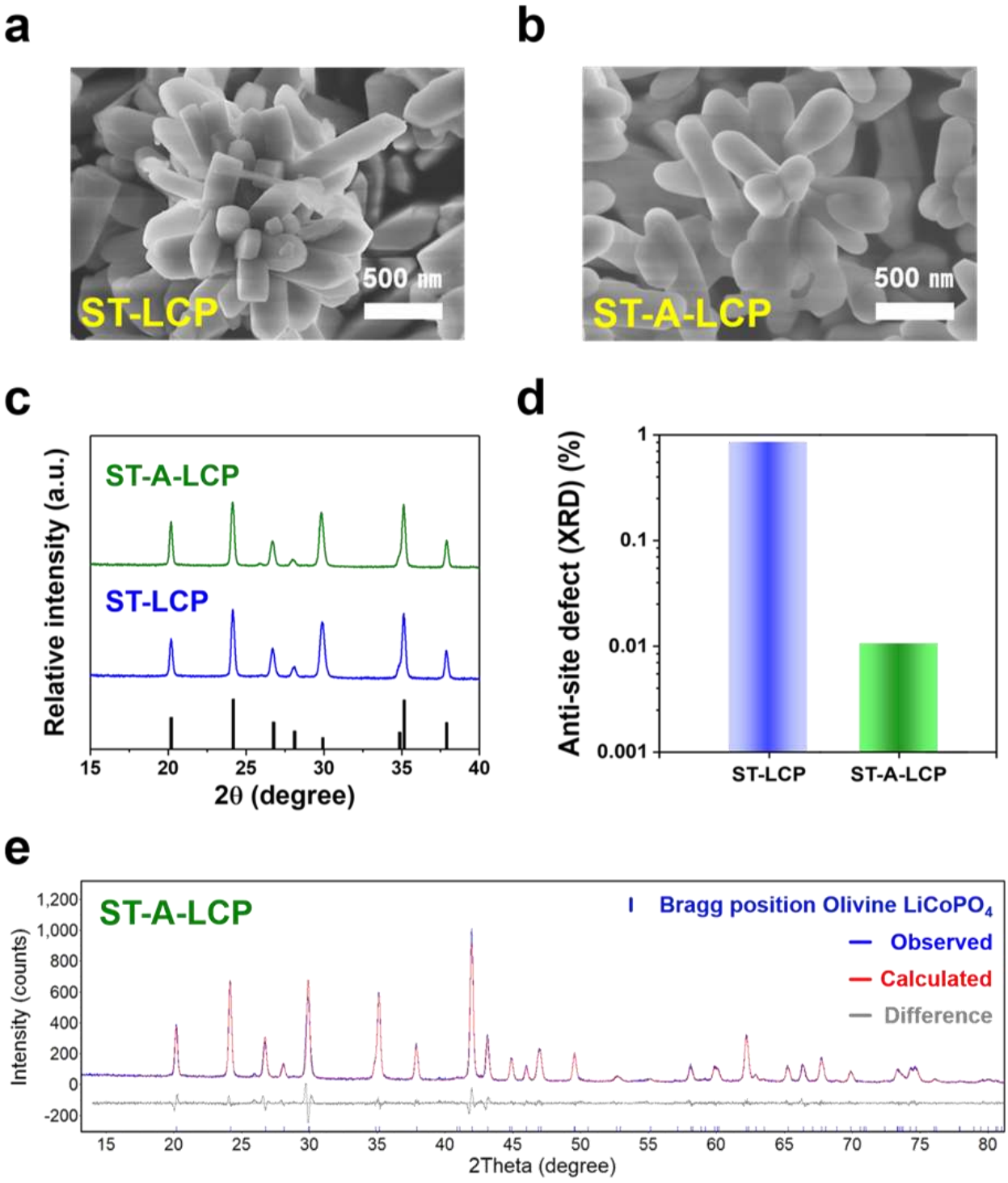


**Figure A.3.12.** Influence of Ar-annealing treatment on morphology and structure: (a-b) SEM images, (c) XRD pattern, (d) anti-site defect concentration of ST-LCP and ST-A-LCP; (e) Rietveld refinement of ST-A-LCP.

**Table A.3.2.** Refined XRD data for ST-A-LCP.

| | **ST-A-LCP** |
|---|---|
| *a* (Å) | 10.1965658 |
| *b* (Å) | 5.9247683 |
| *c* (Å) | 4.6996231 |
| Unit cell volume ($Å^3$) | 283.91 |
| Grain size (nm) | 66.4 |
| Anti-site defect concentration (%) | 0.0106 |
| $R_{wp}$ (%) | 12.740 |

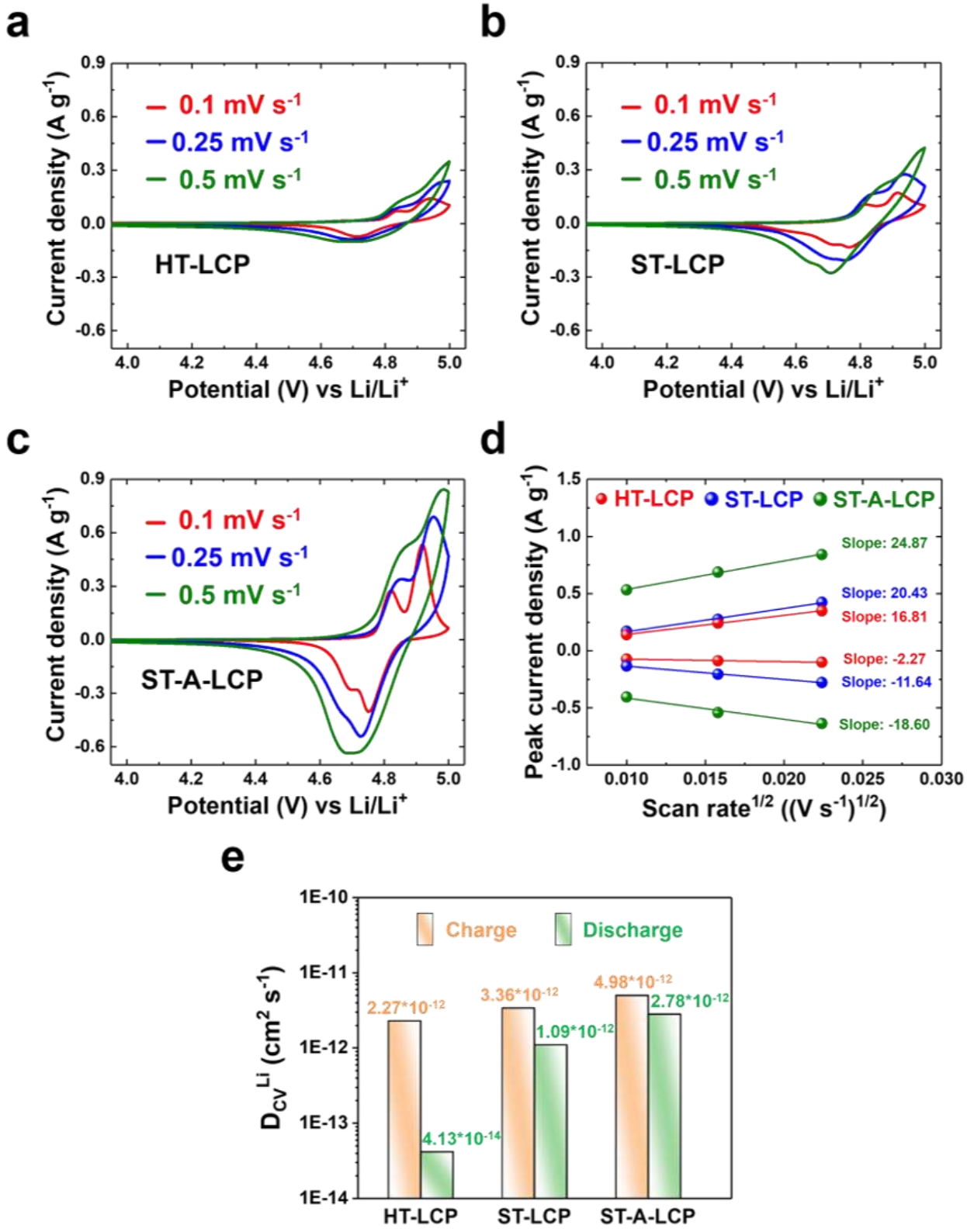


**Figure A.3.13.** (a-c) CV plots within the voltage range 3.5-5.0 V vs. $Li/Li^+$ at various scan rates of 0.1, 0.25, and 0.5 mV $s^{-1}$; (d) comparison of peak current density as a function of the square root of the scan rate; (e) calculated Li-ion diffusion coefficient of HT-LCP, ST-LCP, and ST-A-LCP upon charge and discharge based on CV results.

To further elaborate the enhanced Li-ion diffusivity, we conducted also CV tests with different scan rates (0.1, 0.25, and 0.5 mV $s^{-1}$). Figure A.3.13a-c reveals that the redox peak currents and overpotentials increase with faster scan rates. In addition, the linear relation between redox peak current ($I_P$) and the square root of the scan rate ($v^{1/2}$) is shown in Figure A.3.13d: The fitted slopes of HT-LCP are 16.81 (Charge) and -2.27 (Discharge); that of ST-LCP are 20.43 (Charge) and -11.64 (Discharge); that of ST-A-LCP are 24.87 (Charge) and -18.60 (Discharge), respectively.

With these linear fitted slopes, Li-ion diffusion coefficient values (${D_{CV}}^{Li}$) can be calculated following the Randles-Ševčík equation[7],

$$I_P = 2.69 \times 10^5 \times n^{3/2} \times S \times C \times ({D_{CV}}^{Li})^{1/2} \times v^{1/2} \quad \text{(S2)}$$

where $I_P$ is the redox peak current density, $n$ is the number of electrons involved in the redox reaction, $S$ ($cm^2$) is the surface area of the electrode, $C$ (mol $cm^{-3}$) is the concentration of Li ions in the electrode, $D$ ($cm^2$ $s^{-1}$) is the diffusion coefficient, $v$ (V $s^{-1}$) is the scan rate, and the constant with a value of $2.69 \times 10^5$ has the unit of C $mol^{-1}$ $v^{-1/2}$.

In Figure A.3.13e, the determined diffusion coefficients of ST-LCP ($3.36 \times 10^{12}$ $cm^2$ $s^{-1}$ upon charge and $1.09 \times 10^{12}$ $cm^2$ $s^{-1}$ upon discharge) are higher than those of HT-LCP ($2.27 \times 10^{12}$ $cm^2$ $s^{-1}$ upon charge and $4.13 \times 10^{14}$ $cm^2$ $s^{-1}$ upon discharge). This enhancement is attributed to the benefits of solvent modification from $H_2O$ to EG solvents, which provided both morphological and structural advantages. Furthermore, the diffusion coefficient values of ST-A-LCP further increase up to $4.98 \times 10^{12}$ $cm^2$ $s^{-1}$ and $2.78 \times 10^{12}$ $cm^2$ $s^{-1}$ upon charge and discharge due to its nearly defect-free structure.

The determination of Li-ion diffusion coefficient is crucial for understanding electrode material performance, with GITT and CV serving as primary analytical methods. GITT measures Li-ion diffusion under near-equilibrium condition by applying a small current pulse to the electrode and allowing the system to relax under open-circuit conditions. The relaxation profile of the potential over time reflects the diffusion of Li-ions into the bulk material, and the diffusion coefficient is calculated using Fick's second law. This method captures the equilibrium behavior of Li-ion diffusion and is particularly ideal for studying slow diffusion processes over extended timescales. The highly reliable accuracy of GITT originates from isolating the diffusion process and avoiding the influence of non-diffusion-related factors.

In contrast, CV measures the current response during potential sweeps, reflecting not only Li-ion diffusion but also capacitive effects and surface faradaic reaction kinetics. Additionally, the rapid nature of CV experiments may over-emphasize surface-related processes and transient phenomena, which as consequence can lead to an overestimation or underestimation of the diffusion coefficient compared to GITT.

Based on the above discussion and our comprehensive analysis of Li-ion diffusion coefficients, we would conclude that the diffusion coefficient values calculated by GITT and CV are inherently different. However, the consistent trend of improved Li-ion diffusivity observed through CV strongly validates our GITT results, particularly during the discharging process.

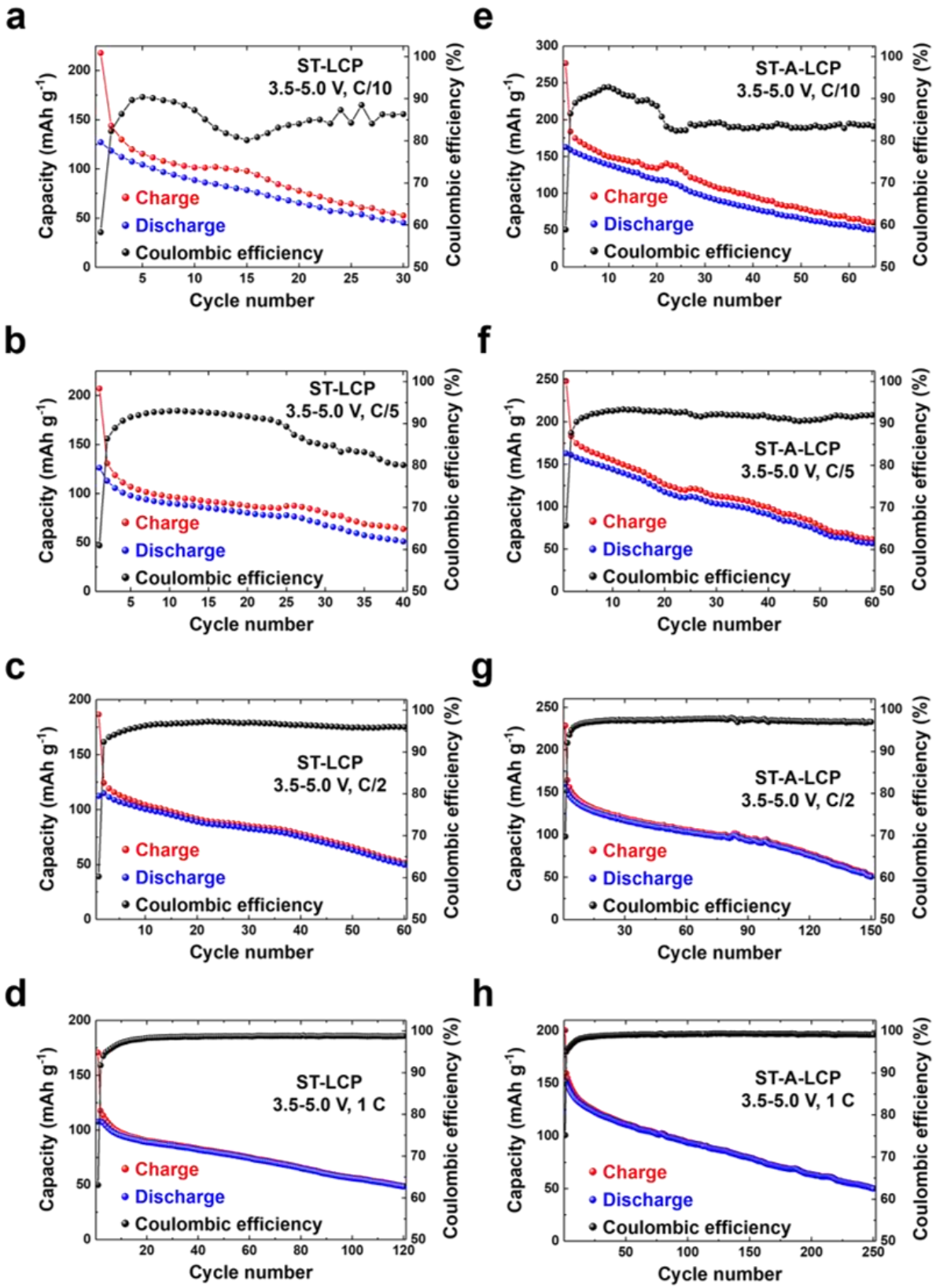


**Figure A.3.14** Capacity retention and Coulombic efficiency of ST-LCP and ST-A-LCP during cycling within the voltage range 3.5-5.0 V vs. $Li/Li^+$ at different C-rates.

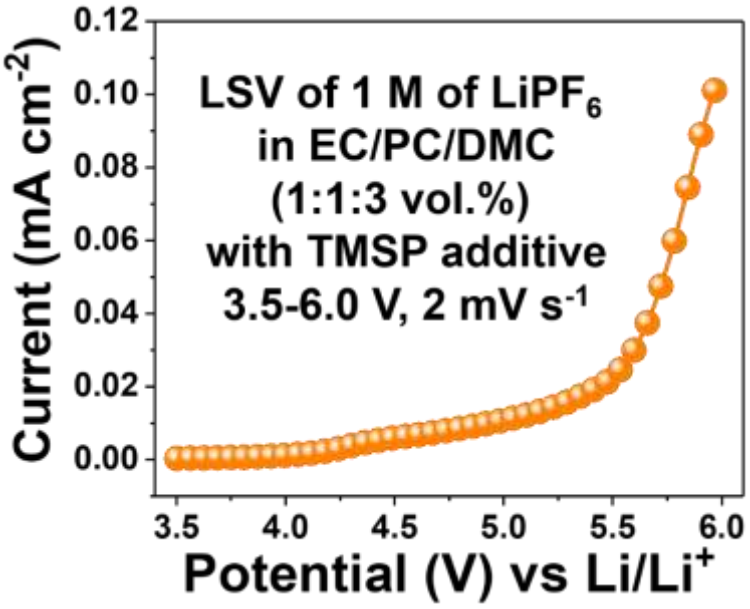


**Figure A.3.15.** Linear sweep voltammetry (LSV) analysis of our electrolyte with the composition, 1 M of $LiPF_6$ in EC/PC/DMC (1:1:3 vol.%) with 2 wt.% TMSP additive.

**Reference A.3**

1. K.-C. Wu, C.-M. Hsieh, B. K. Chang, First principles calculations on lithium diffusion near the surface and in the bulk of Fe-doped $LiCoPO_4$. *Physical Chemistry Chemical Physics* **2022,** *24* (2), 1147-1155.
2. Z. Shen, L. Cao, C. D. Rahn, C.-Y. Wang, Least Squares Galvanostatic Intermittent Titration Technique (LS-GITT) for Accurate Solid Phase Diffusivity Measurement. *Journal of The Electrochemical Society* **2013,** *160* (10), A1842-A1846.
3. A. Nickol, T. Schied, C. Heubner, M. Schneider, A. Michaelis, M. Bobeth, G. Cuniberti, GITT analysis of lithium insertion cathodes for determining the lithium diffusion coefficient at low temperature: Challenges and pitfalls. *Journal of The Electrochemical Society* **2020,** *167* (9), 090546.
4. F. C. Strobridge, R. J. Clément, M. Leskes, D. S. Middlemiss, O. J. Borkiewicz, K. M. Wiaderek, K. W. Chapman, P. J. Chupas, C. P. Grey, Identifying the structure of the intermediate, $Li_{2/3}CoPO_4$, formed during electrochemical cycling of $LiCoPO_4$. *Chemistry of Materials* **2014,** *26* (21), 6193-6205.
5. M. Kaus, I. Issac, R. Heinzmann, S. Doyle, S. Mangold, H. Hahn, V. S. K. Chakravadhanula, C. Kübel, H. Ehrenberg, S. Indris, Electrochemical delithiation/relithiation of $LiCoPO_4$: A two-step reaction mechanism investigated by *in situ* X-ray diffraction, *in situ* X-ray absorption spectroscopy, and *ex situ* $^7Li/^{31}P$ NMR spectroscopy. *The Journal of Physical Chemistry C* **2014,** *118* (31), 17279-17290.
6. M. G. Palmer, J. T. Frith, A. L. Hector, A. W. Lodge, J. R. Owen, C. Nicklin, J. Rawle, *In situ* phase behaviour of a high capacity $LiCoPO_4$ electrode during constant or pulsed charge of a lithium cell. *Chemical Communications* **2016,** *52* (98), 14169-14172.
7. J. Hu, W. Li, Y. Duan, S. Cui, X. Song, Y. Liu, J. Zheng, Y. Lin, F. Pan, Single-particle performances and properties of $LiFePO_4$ nanocrystals for Li-ion batteries. *Advanced Energy Materials* **2017,** *7* (5), 1601894.

## A.4. Supplementary Information – Chapter 5

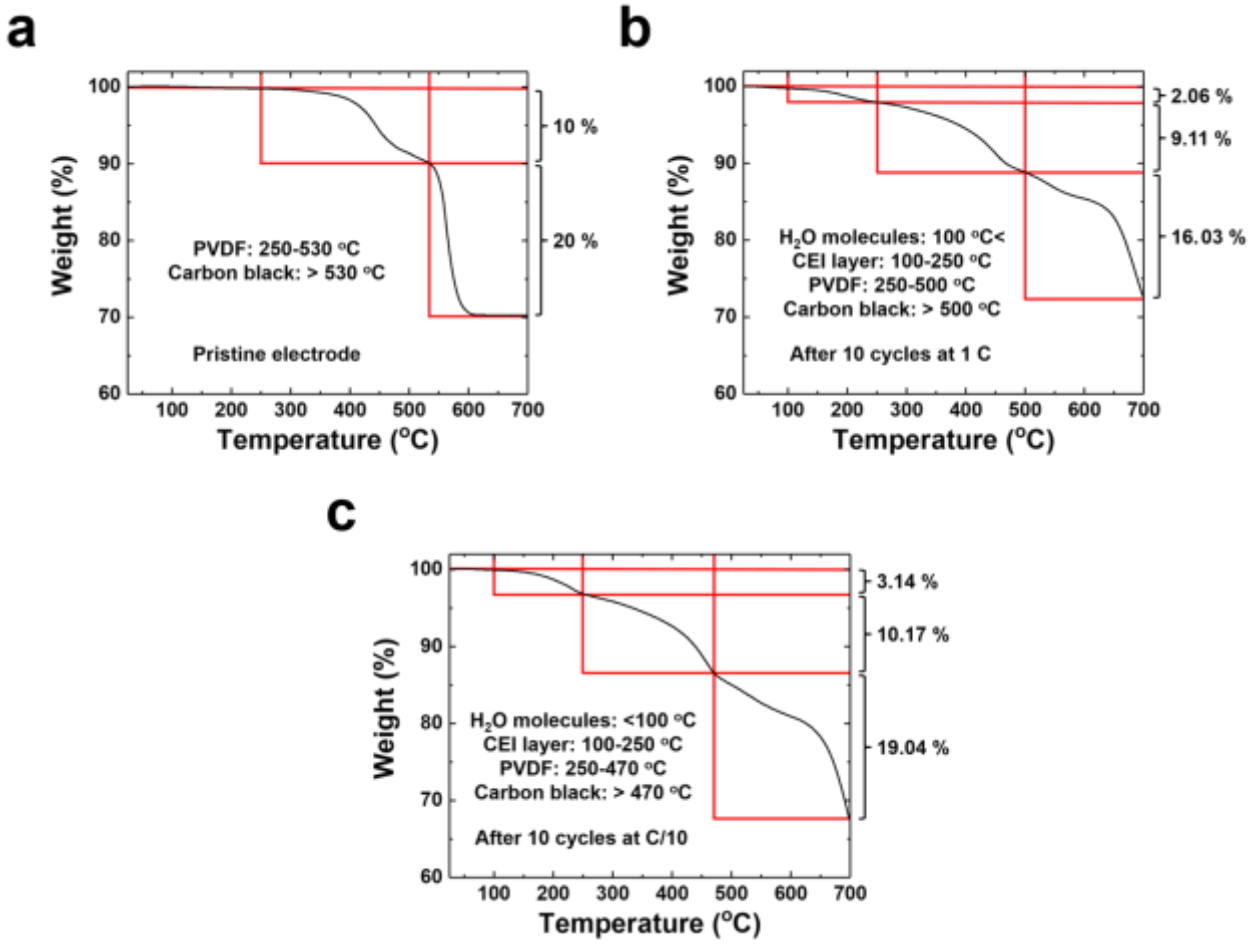


**Figure A.4.1.** TGA curves of (a) pristine and cycled electrodes after 10 cycles at (b) 1 C and (c) C/10 over the whole temperature range up to 700 °C**.**

**Table A.4.1.** Summary of the Coulombic efficiency and standard deviation values of ST-A-LCP at different C-rates.

| C-rates | Minimum | Maximum | Range | Mean value |
|---|---|---|---|---|
| C/10 | 58.89 | 92.74 | 33.85 | 85.12 |
| C/5 | 65.72 | 93.37 | 27.65 | 91.53 |
| C/2 | 69.79 | 97.96 | 28.17 | 97.05 |
| 1 C | 75.22 | 99.31 | 24.09 | 98.57 |

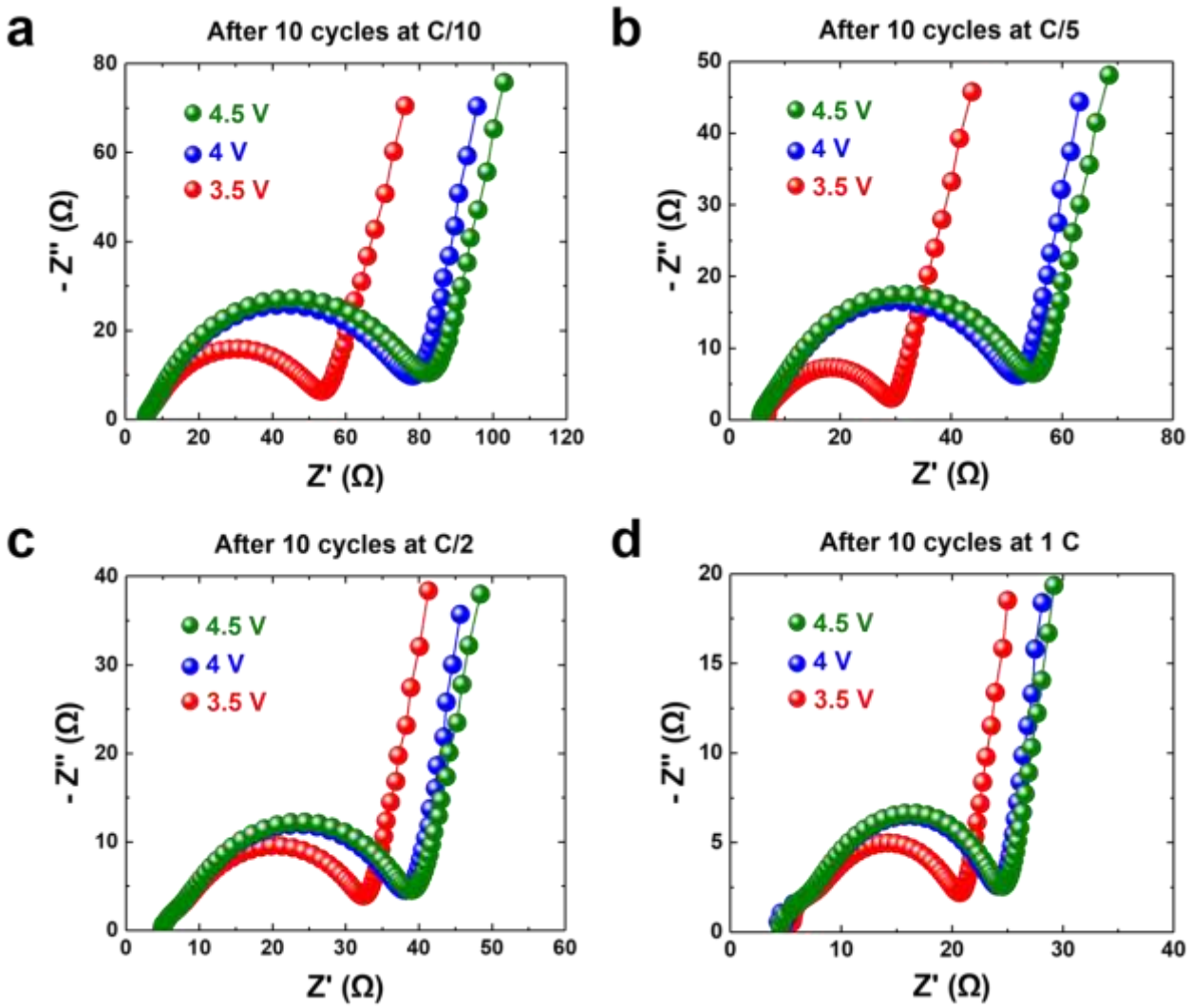


**Figure A.4.2.** Nyquist plots corresponding to the cycled ST-A-LCP electrodes after 10 cycles measured under 3.5, 4, 4.5 V vs. $Li/Li^+$ forward bias.

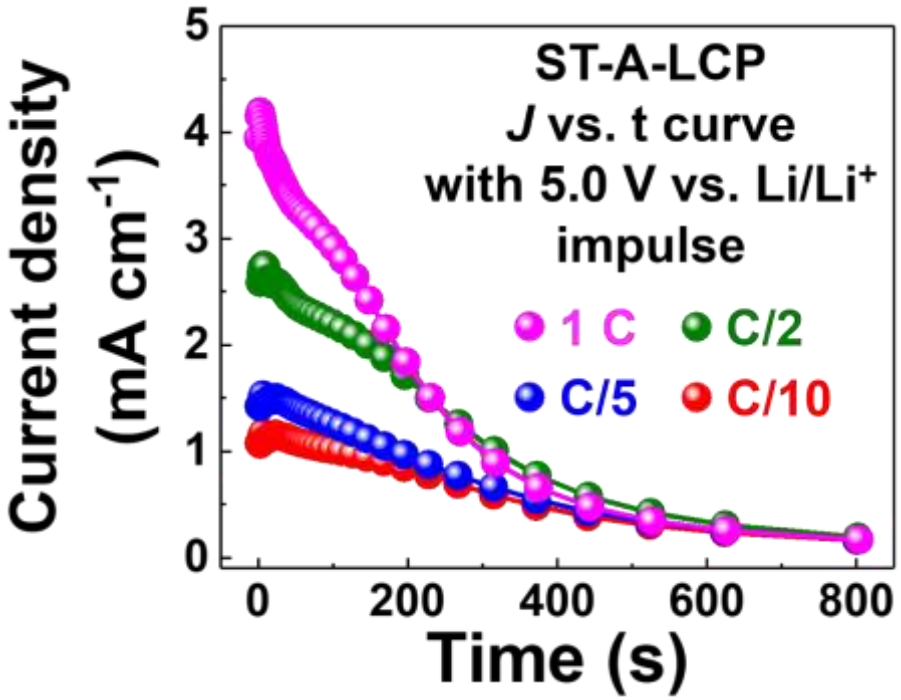


**Figure A.4.3.** Current density vs. time (*J-t*) for cycled ST-A-LCP electrodes at different C-rates after 10 cycles, measured from the Nyquist plot with 5.0 V vs. $Li/Li^+$ impulse.

**Table A.4.2.** XPS peak data summary of pristine ST-A-LCP electrodes.

| Peak | Bond | Binding energy (eV) | FWHM (eV) | Atomic % |
|---|---|---|---|---|
| C 1s | C-C & C-H | 284.75 | 0.81 | 54.5 |
| | C-O | 285.70 | 1.24 | 14.34 |
| | C-F | 286.69 | 1.36 | 13.00 |
| | C=O | 287.73 | 1.34 | 2.86 |
| | O-C=O | 288.98 | 1.39 | 2.76 |
| | $CH_2$-$CF_2$ | 291.09 | 1.72 | 12.54 |
| O 1s | C=O & O-C=O | 531.85 | 1.89 | 96.05 |
| | C-O | 533.69 | 1.16 | 3.95 |
| F 1s | Li-F & Co-F | 685.37 | 0.86 | 0.65 |
| | C-F | 687.93 | 1.81 | 97.11 |
| | $CH_2$-$CF_2$ | 690.21 | 2.43 | 2.24 |

**Table A.4.3.** XPS peak data summary of ST-A-LCP electrodes after 10 cycles at 1 C.

| Peak | Bond | Binding energy (eV) | FWHM (eV) | Atomic % |
|---|---|---|---|---|
| C 1s | C-C & C-H | 284.78 | 1.27 | 49.16 |
| | C-O | 285.88 | 0.88 | 11.83 |
| | C-F | 286.5 | 1.00 | 12.24 |
| | C=O | 287.36 | 1.23 | 5.94 |
| | O-C=O | 288.62 | 1.77 | 5.03 |
| | $CH_2$-$CF_2$ | 290.47 | 1.32 | 15.8 |
| O 1s | C=O & O-C=O | 531.84 | 1.75 | 67.66 |
| | C-O | 533.28 | 2.07 | 32.34 |
| F 1s | Li-F & Co-F | 686.34 | 0.81 | 1.69 |
| | C-F | 687.76 | 1.81 | 98.31 |
| | $CH_2$-$CF_2$ | 689.44 | 0.50 | 0 |

**Table A.4.4.** XPS peak data summary of ST-A-LCP electrodes after 10 cycles at C/10.

| Peak | Bond | Binding energy (eV) | FWHM (eV) | Atomic % |
|---|---|---|---|---|
| C 1s | C-C & C-H | 284.78 | 1.15 | 38.04 |
| | C-O | 285.82 | 1.22 | 19.01 |
| | C-F | 286.64 | 1.17 | 15.08 |
| | C=O | 287.44 | 1.33 | 8.33 |
| | O-C=O | 288.94 | 2.08 | 6.38 |
| | $CH_2$-$CF_2$ | 290.72 | 1.26 | 13.17 |
| O 1s | C=O & O-C=O | 531.57 | 2.04 | 59.54 |
| | C-O | 533.19 | 2.24 | 40.46 |
| F 1s | Li-F & Co-F | 685.44 | 1.94 | 6.16 |
| | C-F | 687.55 | 1.60 | 93.63 |
| | $CH_2$-$CF_2$ | 689.57 | 0.54 | 0.21 |

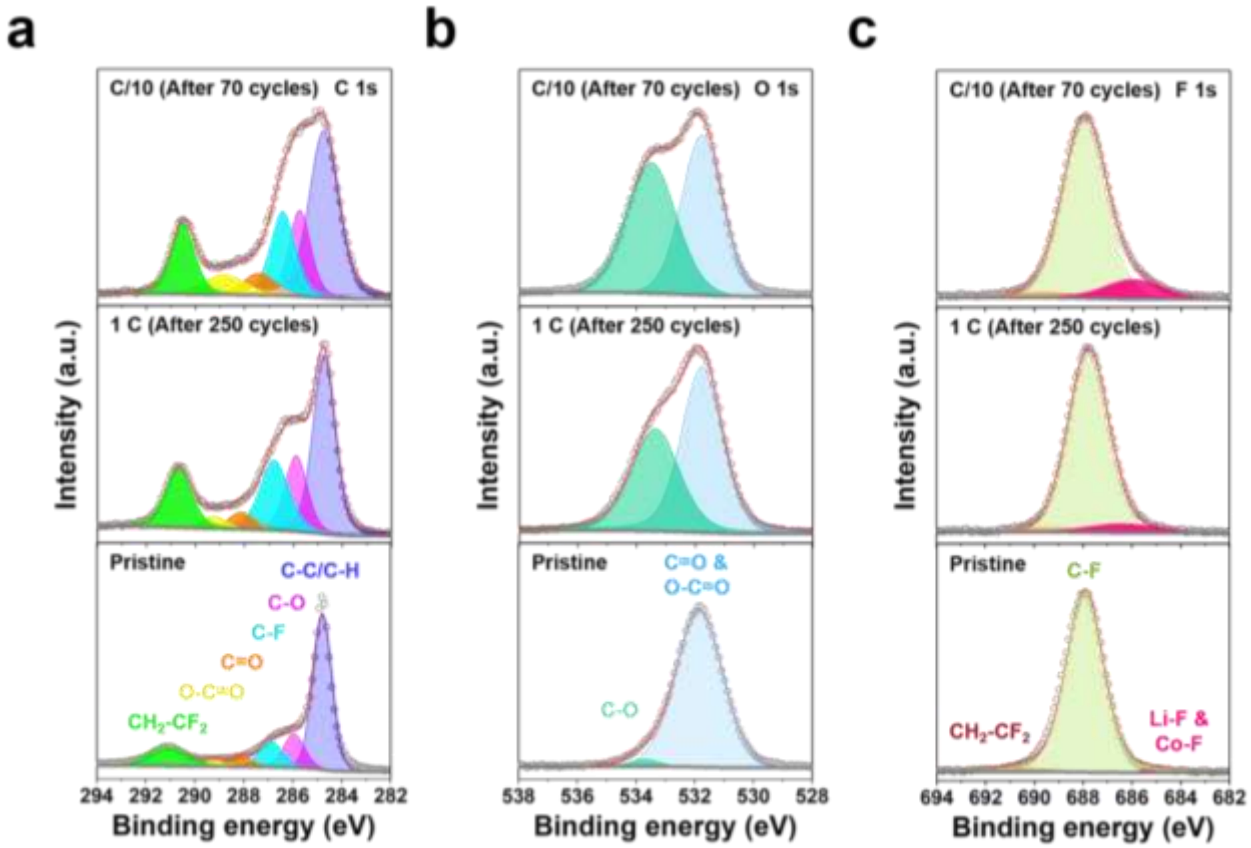


**Figure A.4.4.** XPS spectra of ST-A-LCP electrodes in different cycling states (a) C 1s, (b) F 1s, and (c) O 1s.

**Table A.4.5.** XPS peak data summary of ST-A-LCP electrodes after 250 cycles at 1 C.

| Peak | Bond | Binding energy (eV) | FWHM (eV) | Atomic % |
|---|---|---|---|---|
| C 1s | C-C & C-H | 284.75 | 1.07 | 39.62 |
| | C-O | 285.88 | 1.09 | 17.19 |
| | C-F | 286.78 | 1.38 | 20.15 |
| | C=O | 288.13 | 1.19 | 4.18 |
| | O-C=O | 289.23 | 1.14 | 2.95 |
| | $CH_2$-$CF_2$ | 290.67 | 1.29 | 15.90 |
| O 1s | C=O & O-C=O | 531.78 | 1.64 | 57.97 |
| | C-O | 533.35 | 1.93 | 42.03 |
| F 1s | Li-F & Co-F | 686.38 | 3.2 | 3.82 |
| | C-F | 688.00 | 1.89 | 96.18 |
| | $CH_2$-$CF_2$ | 690.90 | 0.62 | 0 |

**Table A.4.6.** XPS peak data summary of ST-A-LCP electrodes after 70 cycles at C/10.

| Peak | Bond | Binding energy (eV) | FWHM (eV) | Atomic % |
|---|---|---|---|---|
| C 1s | C-C & C-H | 284.76 | 1.41 | 40.38 |
| | C-O | 285.74 | 1.06 | 15.70 |
| | C-F | 286.43 | 1.19 | 17.18 |
| | C=O | 287.39 | 1.56 | 5.85 |
| | O-C=O | 288.81 | 1.98 | 6.80 |
| | $CH_2$-$CF_2$ | 290.5 | 1.17 | 14.09 |
| O 1s | C=O & O-C=O | 531.76 | 1.65 | 49.86 |
| | C-O | 533.49 | 2.02 | 50.14 |
| F 1s | Li-F & Co-F | 686.55 | 1.79 | 14.07 |
| | C-F | 687.92 | 1.97 | 85.93 |
| | $CH_2$-$CF_2$ | 689.33 | 0.50 | 0 |

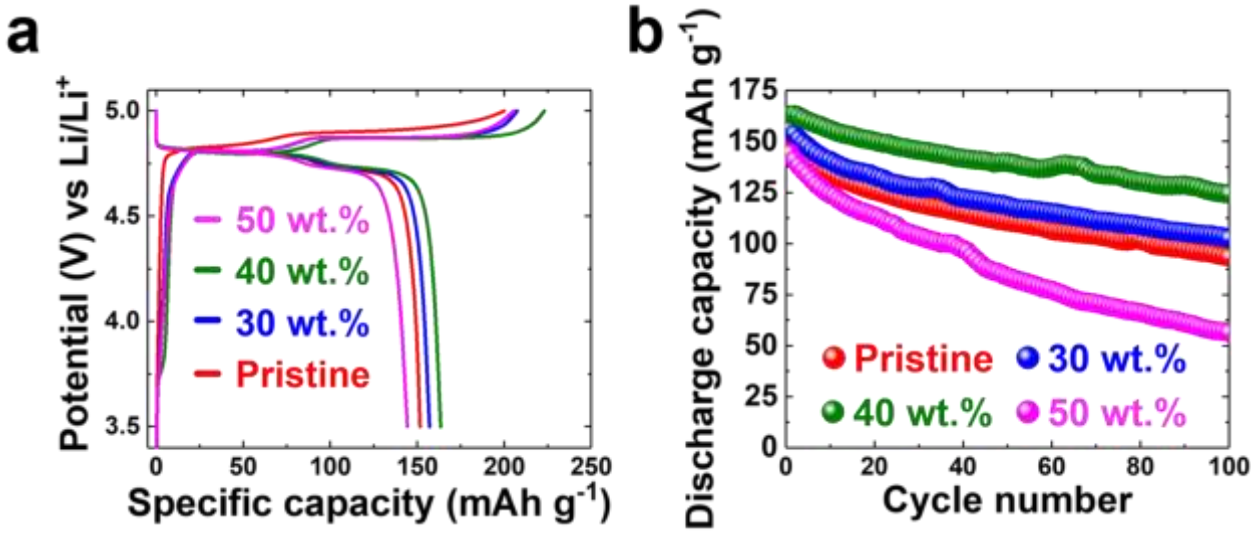


**Figure A.4.5.** Electrochemical evaluations on the effect of sucrose-derived RGO layer via (a) galvanostatic charge-discharging and (b) capacity retention of ST-R-LCP with different amount of sucrose, measured within the voltage range 3.5-5.0 V vs. $Li/Li^+$ at 1 C.

**Table A.4.7.** XPS peak data summary of ST-R-LCP powder.

| Peak | Bond | Binding energy (eV) | FWHM (eV) | Atomic % |
|---|---|---|---|---|
| C 1s | C=C & C-C | 284.77 | 1.26 | 52.82 |
| | C-OH | 285.33 | 1.43 | 20.93 |
| | C-O-C | 286.53 | 1.31 | 9.18 |
| | C=O | 289.32 | 1.86 | 3.99 |
| | COOH | 291.17 | 3.51 | 6.20 |
| | π- π | 287.76 | 1.64 | 6.87 |
| O 1s | P-O & C=O | 531.23 | 1.02 | 4.20 |
| | COOH | 532.28 | 1.56 | 43.76 |
| | C-OH | 533.35 | 1.38 | 30.60 |
| | C-O-C | 534.20 | 1.81 | 21.43 |

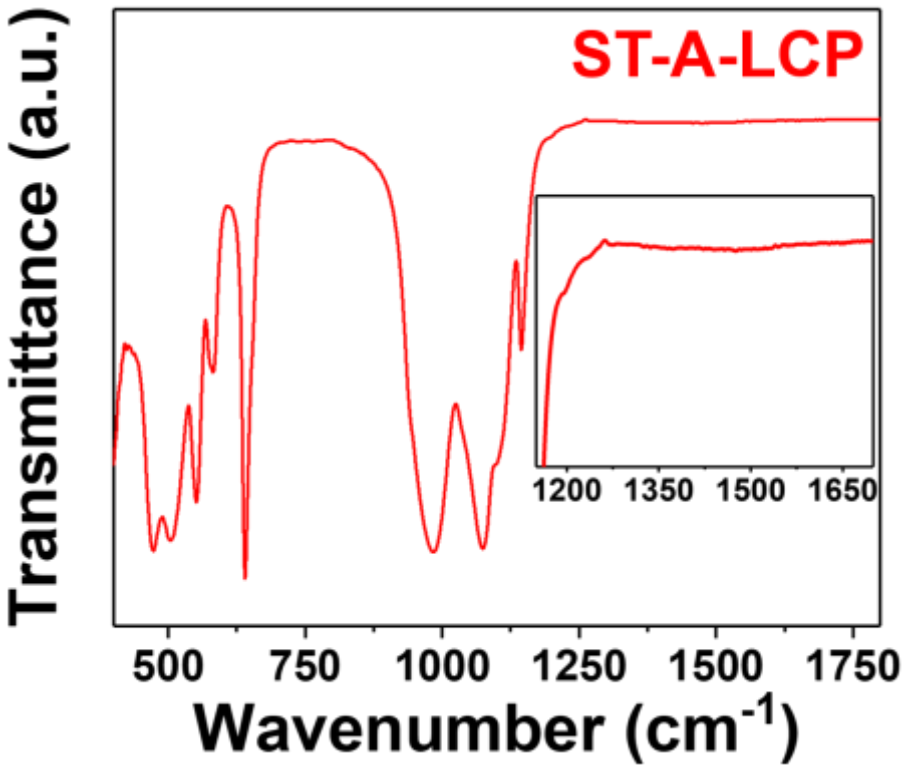


**Figure A.4.6.** FT-IR spectrum of ST-A-LCP.

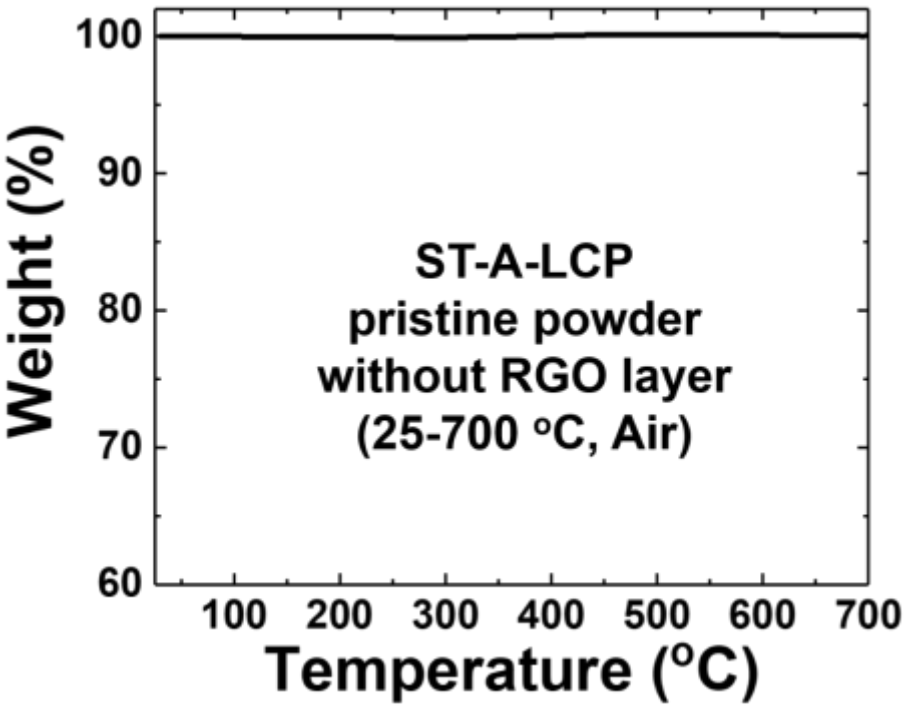


**Figure A.4.7.** TGA curves of pristine ST-A-LCP powder without RGO layer over the whole temperature range up to 700 °C.

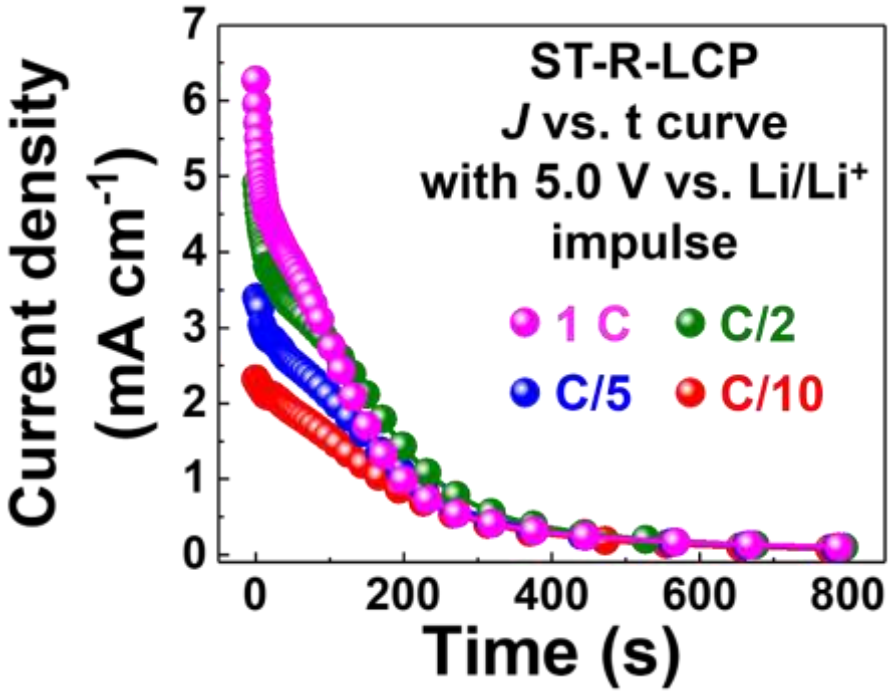


**Figure A.4.8.** Current density vs. time (*J*-t) for cycled ST-R-LCP electrodes at different C-rates after 10 cycles, measured from the Nyquist plot with 5.0 V vs. $Li/Li^+$ impulse.

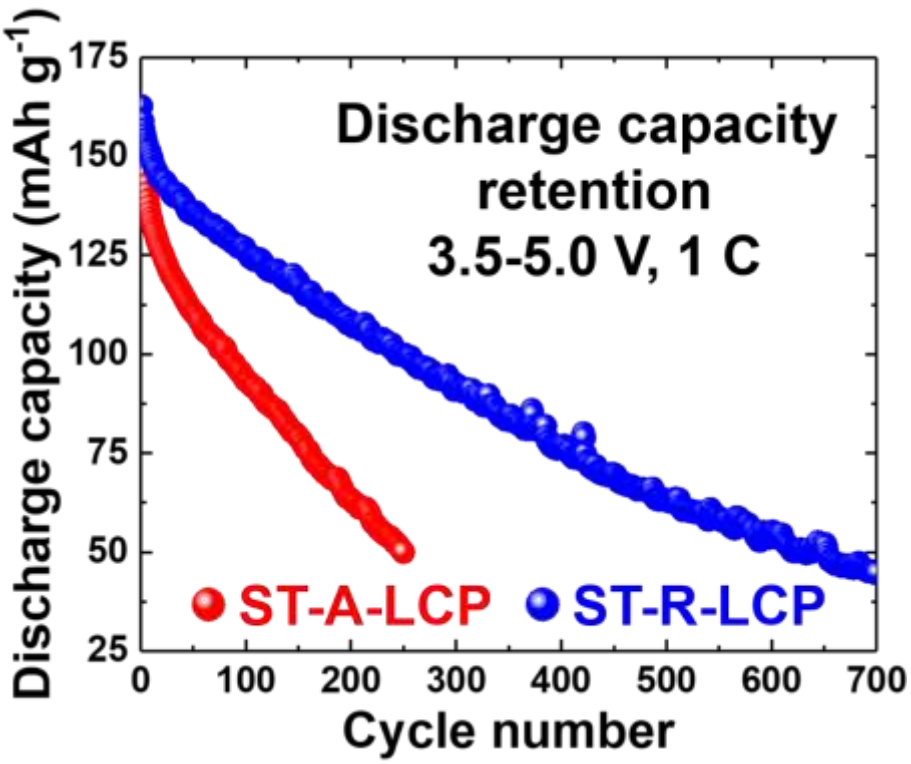


**Figure A.4.9.** Comparison of discharge capacity retention of ST-A-LCP and ST-R-LCP at 1 C.

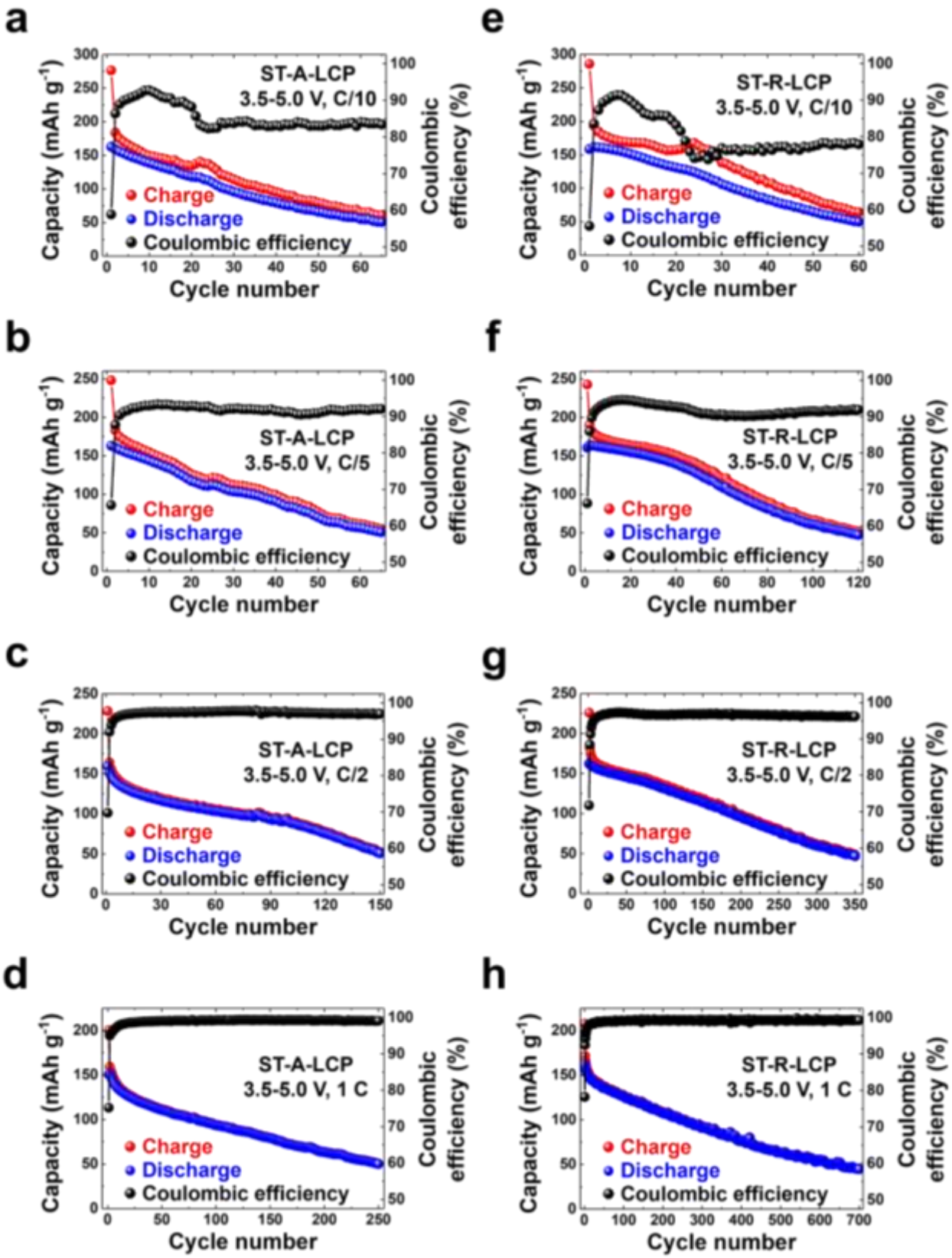


**Figure A.4.10.** Capacity retention and Coulombic efficiency of ST-A-LCP and ST-R-LCP during cycling within the voltage range 3.5-5.0 V vs. $Li/Li^+$ at different C-rates.

**Table A.4.8.** Summary of the Coulombic efficiency and standard deviation values of ST-R-LCP at different C-rates.

| C-rates | Minimum | Maximum | Range | Mean value |
|---|---|---|---|---|
| C/10 | 55.54 | 91.36 | 35.81 | 79.90 |
| C/5 | 66.25 | 94.64 | 28.39 | 91.58 |
| C/2 | 71.79 | 97.33 | 25.54 | 96.52 |
| 1 C | 78.25 | 99.82 | 21.57 | 99.10 |

**Table A.4.9.** XPS peak data summary of pristine ST-R-LCP electrodes**.**

| Peak | Bond | Binding energy (eV) | FWHM (eV) | Atomic % |
|---|---|---|---|---|
| C 1s | C-C & C-H | 284.81 | 0.87 | 62.89 |
| | C-O | 285.72 | 0.75 | 7.60 |
| | C-F | 286.40 | 0.97 | 7.66 |
| | C=O | 287.06 | 1.33 | 6.66 |
| | O-C=O | 288.78 | 2.49 | 5.40 |
| | $CH_2$-$CF_2$ | 291.13 | 1.63 | 9.79 |
| O 1s | C=O & O-C=O | 531.86 | 1.45 | 78.74 |
| | C-O | 533.25 | 1.88 | 21.26 |
| F 1s | Li-F & Co-F | 685.84 | 0.52 | 0.48 |
| | C-F | 687.98 | 1.78 | 97.70 |
| | $CH_2$-$CF_2$ | 689.73 | 1.90 | 1.82 |

**Table A.4.10.** XPS peak data summary of ST-R-LCP electrodes after 700 cycles at 1 C.

| Peak | Bond | Binding energy (eV) | FWHM (eV) | Atomic % |
|---|---|---|---|---|
| C 1s | C-C & C-H | 284.75 | 0.94 | 35.94 |
| | C-O | 285.93 | 1.27 | 17.20 |
| | C-F | 286.76 | 1.21 | 18.26 |
| | C=O | 287.71 | 1.11 | 3.68 |
| | O-C=O | 289.11 | 2.09 | 5.85 |
| | $CH_2$-$CF_2$ | 290.96 | 1.27 | 19.07 |
| O 1s | C=O & O-C=O | 531.91 | 1.71 | 57.92 |
| | C-O | 533.59 | 1.99 | 42.08 |
| F 1s | Li-F & Co-F | 685.95 | 1.6 | 18.94 |
| | C-F | 688.00 | 1.84 | 80.94 |
| | $CH_2$-$CF_2$ | 690.58 | 0.51 | 0.12 |

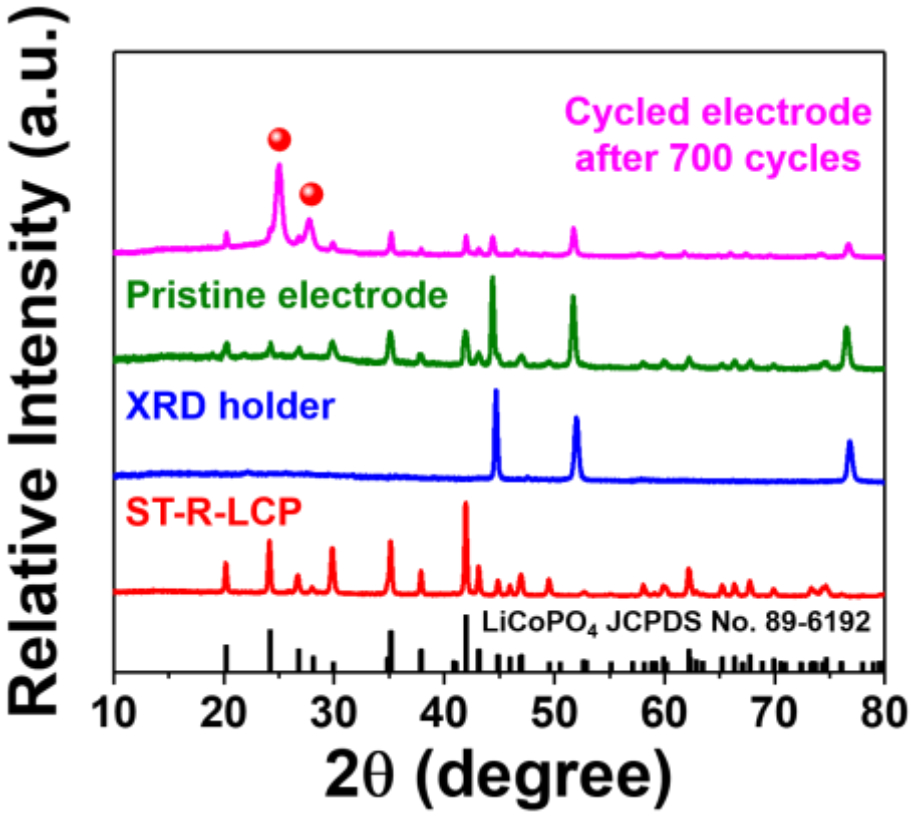


**Figure A.4.11.** XRD patterns of pristine ST-R-LCP powder, aluminium XRD holder, ST-R-LCP pristine electrode, and cycled ST-R-LCP electrode after 700 cycles at 1 C.

**Table A.4.11.** Refined XRD data for ST-R-LCP.

| ST-R-LCP | |
|---|---|
| *a* (Å) | 10.1946686 |
| *b* (Å) | 5.9216008 |
| *c* (Å) | 4.7015127 |
| Unit cell volume (Å$^3$)volume (Å$^3$) | 283.82 |
| Grain size (nm) | 67.3 |
| Anti-site defect concentration (%) | 0.4439 |
| $R_{wp}$ (%) | 13.278 |

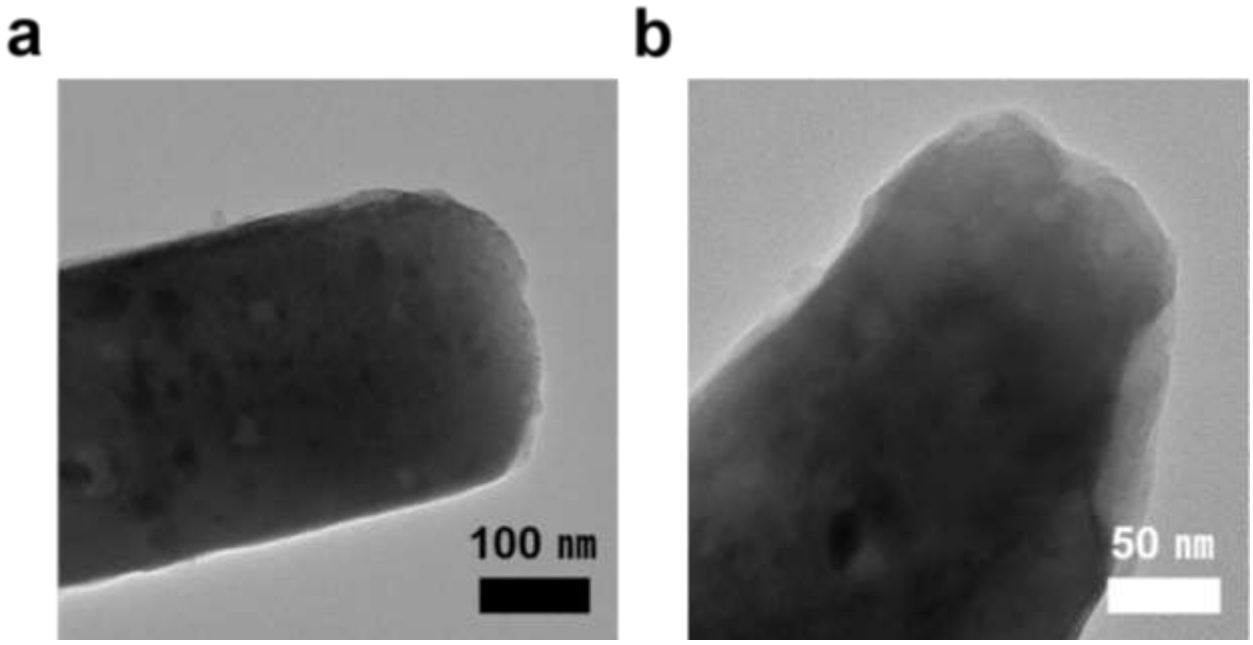

**Figure A.4.12.** HRTEM images of (a) ST-R-LCP and (b) ST-A-LCP samples after 100 cycles at 1 C.

**Table A.4.12.** XPS peak data summary of collected separator from the battery with ST-A-LCP cathode after 100 cycles at 1 C.

| Peak | Bond | Binding energy (eV) | FWHM (eV) | Atomic % |
|---|---|---|---|---|
| Co 2p $_{3/2}$ | $Co^{3+}$ | 780.94 | 2.27 | 14.84 |
| | $Co^{2+}$ | 782.39 | 3.37 | 27.16 |
| | $Co^{3+}$ Sat. | 785.71 | 3.37 | 16.06 |
| | $Co^{2+}$ Sat. | 788.76 | 3.37 | 8.88 |
| Co 2p $_{1/2}$ | $Co^{3+}$ | 796.95 | 2.33 | 5.73 |
| | $Co^{2+}$ | 797.77 | 2.56 | 10.39 |
| | $Co^{3+}$ Sat. | 800.71 | 3.37 | 8.58 |
| | $Co^{2+}$ Sat. | 804.06 | 3.37 | 8.36 |

***Sat.: Satellite**